Principle of vibroacoustic subtractive modelling and application to the prediction of the acoustic radiation of partially coated submerged cylindrical shells

Florent Dumortier

N°d'ordre NNT : 2021LYSEI082

THESE de DOCTORAT **DE L'UNIVERSITE DE LYON**
opérée au sein de
l'INSA de Lyon

Ecole Doctorale N° 162
Mécanique – Energétique – Génie Civil - Acoustique

Spécialité discipline de doctorat : Acoustique

Soutenue publiquement le 30/11/2021, par :
Florent Dumortier

Principle of vibroacoustic subtractive modelling and application to the prediction of the acoustic radiation of partially coated submerged cylindrical shells

---

Devant le jury composé de :

Ouisse, Morvan	Professeur, FEMTO-ST, ENSMM	Président
Guasch, Oriol	Professeur, La Salle, URL	Rapporteur
Kessissoglou, Nicole	Professeure, UNSW	Rapporteure
Audoly, Christian	HdR, Naval Group Research	Examinateur
Maxit, Laurent	Maître de Conférences HdR, INSA Lyon	Directeur de thèse
Meyer, Valentin	Docteur, Naval Group Research	Co-encadrant

Département FEDORA – INSA Lyon - Ecoles Doctorales

SIGLE	ECOLE DOCTORALE	NOM ET COORDONNEES DU RESPONSABLE
CHIMIE	**CHIMIE DE LYON** **https://www.edchimie-lyon.fr** Sec. : Renée EL MELHEM Bât. Blaise PASCAL, 3e étage secretariat@edchimie-lyon.fr	**M. Stéphane DANIELE** C2P2-CPE LYON-UMR 5265 Bâtiment F308, BP 2077 43 Boulevard du 11 novembre 1918 69616 Villeurbanne **directeur@edchimie-lyon.fr**
E.E.A.	**ÉLECTRONIQUE, ÉLECTROTECHNIQUE, AUTOMATIQUE** **https://edeea.universite-lyon.fr** Sec. : Stéphanie CAUVIN Bâtiment Direction INSA Lyon Tél : 04.72.43.71.70 secretariat.edeea@insa-lyon.fr	**M. Philippe DELACHARTRE** INSA LYON Laboratoire CREATIS Bâtiment Blaise Pascal, 7 avenue Jean Capelle 69621 Villeurbanne CEDEX Tél : 04.72.43.88.63 **philippe.delachartre@insa-lyon.fr**
E2M2	**ÉVOLUTION, ÉCOSYSTÈME, MICROBIOLOGIE, MODÉLISATION** **http://e2m2.universite-lyon.fr** Sec. : Sylvie ROBERJOT Bât. Atrium, UCB Lyon 1 Tél : 04.72.44.83.62 secretariat.e2m2@univ-lyon1.fr	**M. Philippe NORMAND** Université Claude Bernard Lyon 1 UMR 5557 Lab. d'Ecologie Microbienne Bâtiment Mendel 43, boulevard du 11 Novembre 1918 69 622 Villeurbanne CEDEX **philippe.normand@univ-lyon1.fr**
EDISS	**INTERDISCIPLINAIRE SCIENCES-SANTÉ** **http://ediss.universite-lyon.fr** Sec. : Sylvie ROBERJOT Bât. Atrium, UCB Lyon 1 Tél : 04.72.44.83.62 secretariat.ediss@univ-lyon1.fr	**Mme Sylvie RICARD-BLUM** Institut de Chimie et Biochimie Moléculaires et Supramoléculaires (ICBMS) - UMR 5246 CNRS - Université Lyon 1 Bâtiment Raulin - 2ème étage Nord 43 Boulevard du 11 novembre 1918 69622 Villeurbanne Cedex Tél : +33(0)4 72 44 82 32 **sylvie.ricard-blum@univ-lyon1.fr**
INFOMATHS	**INFORMATIQUE ET MATHÉMATIQUES** **http://edinfomaths.universite-lyon.fr** Sec. : Renée EL MELHEM Bât. Blaise PASCAL, 3e étage Tél : 04.72.43.80.46 infomaths@univ-lyon1.fr	**M. Hamamache KHEDDOUCI** Université Claude Bernard Lyon 1 Bât. Nautibus 43, Boulevard du 11 novembre 1918 69 622 Villeurbanne Cedex France Tél : 04.72.44.83.69 **hamamache.kheddouci@univ-lyon1.fr**
Matériaux	**MATÉRIAUX DE LYON** **http://ed34.universite-lyon.fr** Sec. : Yann DE ORDENANA Tél : 04.72.18.62.44 yann.de-ordenana@ec-lyon.fr	**M. Stéphane BENAYOUN** Ecole Centrale de Lyon Laboratoire LTDS 36 avenue Guy de Collongue 69134 Ecully CEDEX Tél : 04.72.18.64.37 **stephane.benayoun@ec-lyon.fr**
MEGA	**MÉCANIQUE, ÉNERGÉTIQUE, GÉNIE CIVIL, ACOUSTIQUE** **http://edmega.universite-lyon.fr** Sec. : Stéphanie CAUVIN Tél : 04.72.43.71.70 Bâtiment Direction INSA Lyon mega@insa-lyon.fr	**M. Jocelyn BONJOUR** INSA Lyon Laboratoire CETHIL Bâtiment Sadi-Carnot 9, rue de la Physique 69621 Villeurbanne CEDEX **jocelyn.bonjour@insa-lyon.fr**
ScSo	**ScSo*** **https://edsciencessociales.universite-lyon.fr** Sec. : Mélina FAVETON INSA : J.Y. TOUSSAINT Tél : 04.78.69.77.79 melina.faveton@univ-lyon2.fr	**M. Christian MONTES** Université Lumière Lyon 2 86 Rue Pasteur 69365 Lyon CEDEX 07 **christian.montes@univ-lyon2.fr**

*ScSo : Histoire, Géographie, Aménagement, Urbanisme, Archéologie, Science politique, Sociologie, Anthropologie

Abstract

The research on the vibroacoustic behavior of cylindrical shells has been of great interest in the industry for its applications in the naval and aeronautics domains. The application of a coating on submerged cylindrical shells allows reducing the noise radiated and scattered by the shell and finds great utility in the necessity of acoustic furtivity and stealth of submarine vehicles. The coatings applied on underwater structures are viscoelastic materials that can generally be decomposed into two categories. Decoupling coatings isolate the hull from the surrounding medium and reduce the radiated noise to serve as a protection against passive sonars, while anechoic coatings serve as a protection against active sonars by reducing the acoustic scattering from the hull. If fully coated cylindrical shells have been intensively studied in the literature, few works can be found on partially coated cylindrical shells. Modelling the vibroacoustic behavior of such structures may be useful for predicting the impact of missing coating tiles, or for studying cylindrical shells with several kinds of coatings. Compared to fully coated cylindrical shells, the loss of axisymmetry induced by the partial coating leads to a coupling of the circumferential orders of the submerged shell, leading to prohibitive calculation costs for numerical methods and an impossibility of applying classical semi-analytical methods.

In this work, a subtractive modelling approach is developed to circumvent this issue. It is based on a reverse formulation of the Condensed Transfer Function method, a substructuring approach that has already proven its ability in dealing with complex vibroacoustic problems. Considering this subtractive modelling approach, the partially coated cylindrical shell can be studied from the model of a fully coated cylindrical shell, from which a model of the missing part of the coating is removed. The theoretical framework of the method is explored for 1-D and 3-D problems before being applied to analytical test cases to evaluate the accuracy of the method. Numerical errors are then introduced in the models to explore the sensitivity of the method to model errors. Finally, the subtractive modelling approach is applied to the practical case of interest, which is the partially coated cylindrical shell.

Résumé

La recherche sur le comportement vibroacoustique des coques cylindriques est d'un grand intérêt dans un contexte industriel, pour ses applications dans les domaines naval et aéronautique. Afin de limiter le bruit rayonné et diffusé par les coques, et dans un contexte de grande nécessité de furtivité acoustique et de discrétion des navires sous-marins, des revêtements peuvent être appliqués sur la surface de la coque. Les revêtements que l'on peut trouver sur des structures sous-marines sont des matériaux viscoélastiques que l'on peut généralement séparer en deux grandes catégories. D'un côté, les matériaux de masquage permettent d'isoler la coque résistante du milieu environnant, servant ainsi de protection face aux sonars passifs. D'un autre côté, les matériaux anéchoïques ont pour but de protéger le sous-marin face aux sonars actifs en limitant au maximum la réflexion des ondes provenant de l'extérieur. Si l'on peut trouver dans la littérature de nombreuses recherches s'intéressant aux coques cylindriques entièrement revêtues, peu de travaux ont été effectués sur les coques partiellement revêtues. Modéliser le comportement vibroacoustique de telles structures pourrait s'avérer utile afin de prédire l'impact des zones de revêtement manquantes, ou pour étudier des coques cylindriques présentant plusieurs types de revêtement différents. Par rapport à une coque entièrement revêtue, la perte de l'axisymétrie induite par le revêtement partiel entraîne un couplage des ordres circonférentiels de la coque en eau, ce qui conduit à des calculs très lourds limitant la possibilité d'utiliser les méthodes numériques classiques, tout en rendant impossible l'application des méthodes semi-analytiques usuellement utilisées pour étudier les coques cylindriques.

Dans cette thèse, une approche de modélisation soustractive est développée afin de remédier à ce problème. Elle se base sur une formulation inversée de la méthode des fonctions de transfert condensées (CTF, Condensed Transfer Function), une approche de sous-structuration ayant déjà montré sa capacité pour étudier et modéliser des systèmes vibroacoustiques complexes. Grâce à cette approche de modélisation soustractive, une coque cylindrique partiellement revêtue pourrait être modélisée en partant d'un modèle de la coque cylindrique intégralement revêtue, auquel on enlèverait un modèle de la partie manquante du revêtement. Les principes théoriques de la méthode sont dans un premier temps explorés sur des problèmes 1-D et 3-D, avant d'être appliqués à des cas tests permettant d'évaluer

l'efficacité et la précision de la méthode. Des erreurs numériques sont ensuite introduites afin d'évaluer la sensibilité de la méthode aux erreurs de modèle. Enfin, l'approche de modélisation soustractive est appliquée au cas d'intérêt initial, correspondant à la coque cylindrique partiellement revêtue.

N.B. : le manuscrit étant rédigé en anglais, un résumé étendu en français peut être consulté en annexe E.

Remerciements

Il est commun de penser qu'une thèse de doctorat est un travail individuel par essence. Cette affirmation est pourtant on ne peut plus éloignée de la réalité, et il est certain que je n'aurais pas pu mener tous ces travaux seul.

Je tiens donc à grandement remercier, en premier lieu, mon directeur de thèse Laurent Maxit. Tout d'abord pour m'avoir fait confiance et avoir cru en moi pour mener à bien ce projet. Et ensuite pour sa sympathie, sa disponibilité durant ces 3 années de thèse, et pour avoir été un excellent encadrant qui a su me donner les clés pour avancer et pour surmonter les difficultés rencontrées. Un grand merci également à mon encadrant Valentin Meyer, qui a été d'un grand soutient lors de périodes de doutes, et qui est très largement à créditer pour la réussite de ce projet. Je tiens également à remercier Nicole Kessissoglou et Orial Guasch pour avoir accepté de rapporter la thèse, ainsi que Morvan Ouisse pour avoir présidé le jury, et enfin Christian Audoly pour avoir accepté notre invitation de participer au jury, et pour ses conseils précieux sur mon manuscrit de thèse.

Une grande partie de ces 3 ans de travail a été effectuée au LVA, et il va sans dire que la bonne ambiance dans le laboratoire constitue une part non négligeable dans les bons souvenirs que je garderai de cette époque. Un grand merci donc à Luc pour tous ces moments de gwap, à Coco toujours là, à Krist pour les jams au G, et à tous les doctorants et post-doctorants du labo : Yasmine, Alice, Nicolas, Gianluigi, Matthieu, Xavier, Valentin, Augustin, Giorgio, Emmanuel, Phileas, Sanae, Xiaowen, Adrien, Simon, et tous les autres que j'ai pu croiser durant ces 3 ans. Je n'oublie pas tous les permanents avec qui il fut toujours agréable de discuter. J'aurai évidemment une pensée pour les membres du CEMIS qui m'ont très bien accueilli à Naval Group durant les derniers mois de thèse, et pour ces pauses bienvenues au Barrio.

J'ai eu la chance de pouvoir compter sur un superbe groupe d'amis qui n'ont rendu ces 3 années supplémentaire que bien meilleures, avec tous ces bons moments passés et ces fous rires : merci donc à Aymeric, Clara, Colin, Hugo, Juliette, Mathilde, Maxime, Pierre, Romain, Tommy et Vitória. Un grand merci aussi aux membres de mes groupes Pharnal et Talvienkeli, pour toutes les répètes, concerts, et moments de franche rigolade qui ont agrémenté ces 3 ans.

Enfin, mon dernier remerciement ira à ma famille, et en particulier à ma soeur ainsi qu'à mes parents, pour avoir toujours cru en moi, pour avoir toujours été là pour moi dans les bons comme dans les mauvais moments, et parce que je sais à quel point il est précieux d'avoir une famille comme cela.

Contents

List of Figures

List of Tables

Acronyms

BEM	Boundary Element Method.
CAA	Circumferential Admittance Approach.
CF	condensation function.
CMS	Component Mode Synthesis.
CTF	Condensed Transfer Function.
DEA	Dynamic Energy Analysis.
DGM	Direct Global Matrix.
DoF	Degree of Freedom.
EFEA	Energy Finite Element Analysis.
EMT	Effective Medium Theory.
FEM	Finite Element Method.
FRF	Frequency Response Function.
LFAT	Love's First Approximation Theory.
LRPC	Locally Resonant Phononic Crystal.
PML	Perfectly Matched Layer.
PTF	Patch Transfer Function.
rCTF	reverse Condensed Transfer Function.
RRA	Reverse Receptance Approach.
SEA	Statistical Energy Analysis.
SmEdA	Statistical modal Energy distribution Analysis.
TBL	Turbulent Boundary Layer.
TMM	Transfer Matrix Method.
WE	Wave-enveloppe.

Nomenclature

Capital Roman Letters

$\tilde{\mathbf{P}}$	Blocked pressure vector
$\mathbf{F}$	Force vector
$\mathbf{H}$	Condensed Transfer Function matrix
$\mathbf{K}^*$	Complex value of the stiffness matrix to account for the damping
$\mathbf{K}$	Stiffness matrix
$\mathbf{M}$	Mass matrix
$\mathbf{P}$	Pressure vector
$\mathbf{Q}$	Volume velocity vector
$\mathbf{R}$	Fluid-structure interaction matrix
$\mathbf{U}$	Displacement vector
$\mathbf{Z}$	Condensed impedance matrix
$\mathbf{Z}(M)$	Point condensed impedance vector
E	Young's modulus of the cylindrical shell
F	Radial force exerted on the shell
G	Green function
H	Transfer function
$H_n^{(1)}$	Hankel function of the first kind and of order n
$H_n^{(2)}$	Hankel function of the second kind and of order n
J_n	Bessel function of the first kind and of order n
L_f	Axial force exerted on the shell
L_i	Length of the rod i
L_p	Sound Pressure Level
M_T	Tangential moment exerted on the shell
N	Number of condensation functions
N_L	Maximal degree of the associated Legendre polynomial
N_{max}	Maximal circumferential wavenumber
P_i	Amplitude of the acoustic plane wave
P_n	Legendre polynomial

P_n^m	Associated Legendre polynomial
Q	Volume velocity flow
Q_i	Amplitude of the monopole source
R	Radius of the cylindrical shell
S	Surface of the finite cylindrical shell
S_n	Struve function
T	Tangential force exerted on the shell
U	Axial displacement of the shell
V	Tangential displacement of the shell
V_0	Uniform radial velocity of the shell
W	Radial displacement of the shell
W_a	Radiated power
Z_0	Acoustic impedance
Z_c	Coating impedance
Z_f	Fluid loading impedance
Z_R	Radiation impedance of a baffled circular piston
Z_s	Impedance of the cylindrical shell

Lower-case Roman Letters

j	Unit imaginary number
a	Sphere radius
a_p	Radius of the circular piston
c_f	Sound speed in the fluid
c_p	Rubber sound speed
c_s	Longitudinal waves celerity in the shell
d	Size of the patch
d_e	Size of the elements of the FEM model
d_{segm}	Size of the segments
f_c	Critical frequency of the shell
f_r	Ring frequency of the shell
h	Thickness of the cylindrical shell
$h_n^{(1)}$	Spherical Hankel function of the first kind and of order n
$h_n^{(2)}$	Spherical Hankel function of the second kind and of order n
h_p	Rubber thickness
j_n	Spherical Bessel function of the first kind and of order n
k_f	Acoustic wavenumber in the fluid
k_l	Wavenumber of the longitudinal waves in the shell

k_r	Radial wavenumber
k_s	Flexural wavenumber of a plate of same thickness as the shell
k_x	Axial wavenumber
n	Circumferential wavenumber
p	Pressure
p_0	Reference sound pressure
p_d	Double layer potential
p_s	Single layer potential
r	Radial coordinate
u	Normal velocity
x	Axial coordinate
y_n	Spherical Bessel function of the second kind and of order n

Capital Greek Letters

Δ	Laplacian operator
$\mathbf{\Delta}$	Vibroacoustic excitation vector
$\mathbf{\Lambda}$	Condensed pressure and radial velocity vector
$\mathbf{\Phi}$	Modal basis
Ω	Decoupling interface
Ω_s	Patch area
Π	Power flow exchanged between two subsystems
$\tilde{\tilde{\Delta}}$	Determinant of the spectral Flügge matrix taking into account the fluid impedance

Lower-case Greek Letters

β	Shell thickness parameter
β^{ij}	Intermodal coupling loss factor between two subsystems
$\boldsymbol{\xi}$	Vibroacoustic unknown vector
χ	Fraction of the fluid impedance
δS_n	Area around the node n
δ	Dirac delta distribution
η	Loss factor in the fluid
η_s	Structural damping coefficient
η_{ij}	Coupling loss factor between two subsystems
λ	Wavelength
λ_f	Acoustic wavelength in the exterior fluid
λ_p	Acoustic wavelength in the rubber
λ_s	Flexural wavelength
$\delta\mathbf{U}$	Velocity jump vector

μ	Layer of dipole sources
ν	Layer of monopole sources
ν_p	Rubber loss factor
ν_s	Poisson's ratio of the cylindrical shell
ω	Angular frequency
ω_c	Central angular frequency in the frequency band of interest
ϕ	Azimutal angle
$\psi_{n,m}$	Spherical harmonics
ρ_f	Fluid density
ρ_p	Rubber density
ρ_s	Density of the cylindrical shell
σ	Radiation efficiency of a cylindrical shell
θ	Tangential coordinate
φ	Tangential rotation
φ^j	Condensation function
ξ	Time-averaged total energy
k_p	Acoustic wavenumber in the rubber

Symbols and accents

$\bullet'$	Derivative with respect to the argument
$\langle \bullet, \bullet \rangle$	Scalar product
$\tilde{\tilde{\bullet}}$	Quantity in the spectral domain (2D Fourier transform)
$\underline{\bullet}$	Reduced matrix

Introduction

Context

The work presented in this thesis was funded by Naval Group, a french industrial specialized in the design and realization of naval vessels, including submarines. It was conducted in collaboration with the Laboratoire Vibrations Acoustique (LVA) of INSA de Lyon.

In the naval industrial context, modelling the vibroacoustic behavior of submerged cylindrical shells has been a challenging issue for the last decades. In the civil area, there is a growing interest in limiting the noise emitted by naval vehicles for environmental protection matters, and for enhancing the detection performance of Sonar arrays that can be embedded on ships for fisheries research. Concerning military applications, the ongoing acoustic warfare has led to strict requirements regarding the acoustic performances of submarine hulls, and the increasing performances of the Sonar antennas induces the need of modelling the systems over a large frequency range (from several Hz to several kHz depending on the application). In particular, three main operational capabilities arise from different kinds of excitation of the hull:

ACOUSTIC DISCRETION: when the hull is subjected to internal mechanical (presence of floors, engine foundations or pumps) or acoustical (reverberant field) excitations, the radiated noise of the vehicle in the far-field can be detected by passive sonars listening to the sea with a hydrophone array (see figure 1a). That noise must hence remain as low as possible.

ACOUSTIC STEALTH: when the hull is subjected to an external acoustical excitation (a plane wave), the scattered pressure field induced by the acoustic wave impacting the hull can be detected and measured by active sonars (see figure 1b). It is thus necessary to minimize this scattered field as much as possible, in order to reduce the acoustic target strength of the vehicle.

SONAR PERFORMANCES: the hull of a submarine vehicle is often equiped with an array of hydrophones in order to detect and localize other naval vehicles. However, the turbulences induced by the vehicle moving into the fluid domain or the internal

mechanical and acoustical sources can increase the self-noise in the near-field of the vehicle, which disturbs the measurements of the embedded sonar array. This near-field radiated pressure must hence be controlled as much as possible in order to have a high signal-to-noise ratio, both for passive and active sonar situations.

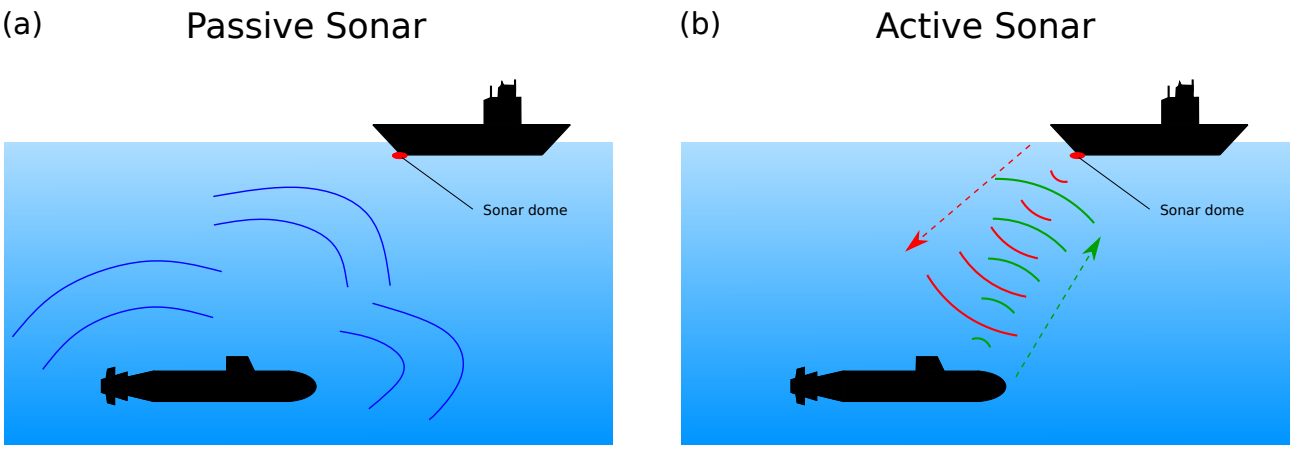

Figure 1: (a) Passive Sonar. (b) Active Sonar.

In order to reduce the radiated noise and scattered pressure field of the hull, and to be as efficient as possible concerning those operational capabilities, acoustic coatings can be applied on the hull's surface. These coatings consist in viscoelastic materials and can be separated into two main categories:

ANECHOIC COATINGS: by absorbing the incoming acoustic waves, anechoic coatings reduce the scattering from the hull and hence serve as a protection again active sonars. They are used to reduce the vehicle's *target strength*.

COMPLIANT COATINGS: by isolating the hull from the surrounding medium, compliant (or decoupling) coatings reduce the noise radiated by the hull and hence serve as a protection against passive sonars while reducing the self-noise. They are used to improve the *acoustic stealth* and the *sonar performances*.

While many works have been conducted in the literature concerning acoustic coatings and fully coated cylindrical shells, less attention has been paid to the case of partially coated cylindrical shells. Compared to a fully coated shell, the loss of the axisymmetry introduced by the partial coating induces a coupling of the circumferential orders of the submerged shell, making unusable the semi-analytical methods usually employed to study cylindrical shells. Hence, the few studies available in the literature on this topic are reduced to low-frequencies or to simplified models regarding the modelling of the coating or the shell (as it will be highlighted in the state of the art review of this thesis).

Yet, being able to study a partially coated cylindrical shell in a wide range of frequencies is an important issue in an industrial context. Indeed, one could be interested in quantifying the impact of missing tiles at the surface of the shell, as illustrated in figure 2a. Besides, the two categories of coatings are generally simultaneously applied on a submarine hull. Anechoic coatings can be found on the flank of the hull and on the sail (which does not belong to the pressure hull), while decoupling coatings are applied everywhere else as illustrated in figure 2b. This non-axisymmetric configuration of the hull constitutes a particular case of partial coating that must be addressed as it answers to industrial needs. Furthermore, some particular areas of the hull are more challenging for the application of coatings and their impact on the vibroacoustic behavior must be quantified as well. Notably, for self-noise applications, it could be of interest to model the effect of un-joined coating tiles on the performances of the sonar array. Finally, one could find a physical or economical interest in applying coating solutions only on targeted areas of the shell.

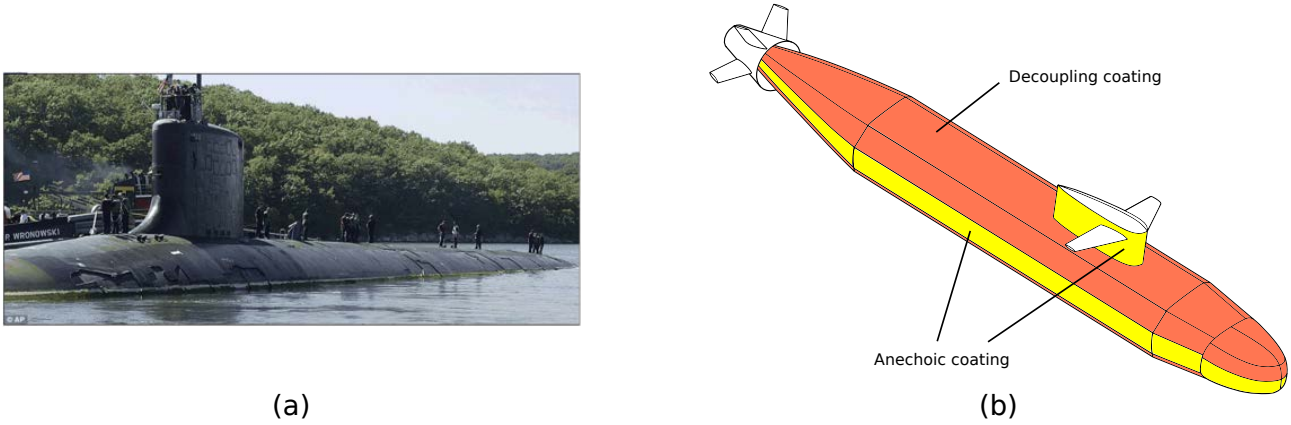

Figure 2: (a) Submarine hull with missing coating tiles. (b) Schematic view of a submarine hull covered with decoupling and anechoic coatings.

Objective of the thesis

The aim of this thesis is to develop a numerical method capable of modelling a partially coated cylindrical shell in a wide range of frequencies, with a reasonable computational cost meeting industrial needs. This method should be able to take into account different geometries of the shell, including internal frames such as stiffeners, bulkheads or floors, and present the possiblity of considering not only partial coating, but also the presence of two different kinds of coating materials at the surface of the shell. The past collaborations between INSA de Lyon and several industrial partners of the naval domain allowed the development of vibroacoustic models of submerged cylindrical shells, either with internal substructures, multilayered coatings, or both. However, these models were limited to axisymmetric systems. Besides, the usual analytical and semi-analytical methods available in the literature showed

their limitations in dealing with non-axisymmetric systems due to the coupling of the circumferential orders. In order to utilize existing models and to circumvent the limitations of the existing methods, a new lead is explored in this work: subtractive vibroacoustic modelling. Using this concept, the partially coated cylindrical shell can be studied from an existing model of the fully coated shell, from which the missing part of the coating is removed and replaced by water, as illustrated in figure 3.

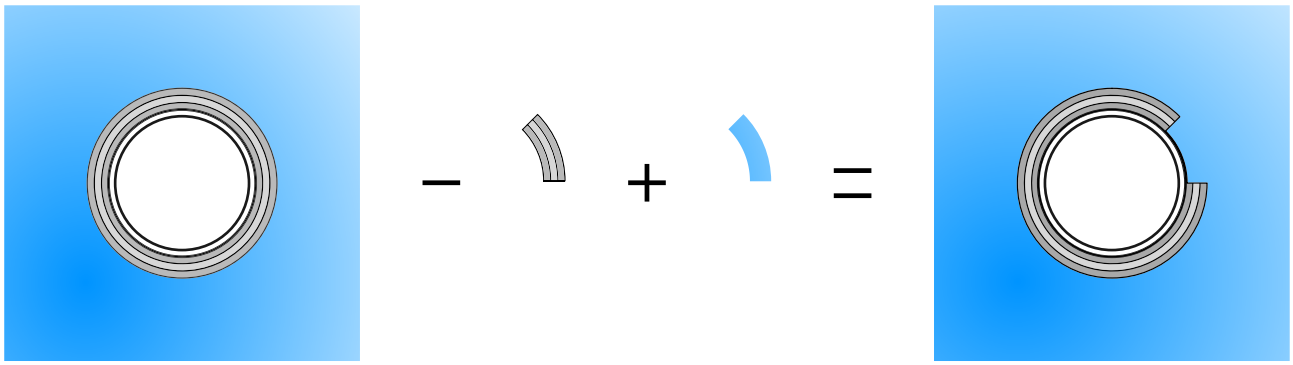

Figure 3: Studying a partially coated cylindrical shell using subtractive vibroacoustic modelling.

The subtractive modelling approach proposed in this thesis will be based on a reverse formulation of the Condensed Transfer Function (CTF) method, a substructuring approach initially developed to couple subsystems along lines or surfaces. After having established the principles of this approach named the reverse Condensed Transfer Function (rCTF) method, applications on academic test cases will be carried out. They will allow to validate numerically the proposed approach, to study its validity range and to evaluate its performances. Finally, as a first example of naval application, the rCTF approach will be applied to simulate the behavior of a partially coated cylindrical shell.

In the next chapter, a review of the literature is proposed on the three topics related to this work: the acoustic radiation of submerged cylindrical shells, the modelling of acoustic coatings for naval applications, and the numerical methods in vibroacoustics, including substructuring and decoupling approaches. Following this analysis, the methodology and organization of the document will be presented.

Chapter 1

Literature review

The aim of this chapter is to give a comprehensive overview of the literature concerning three topics in relation with the problem presented in the introduction. Firstly, the vibroacoustic problem of a bare cylindrical shell is addressed, starting from the *in vacuo* case to more complex configurations, with the influence of fluid loading and internal structures such as stiffeners. Then, the second part deals with the different kinds of coatings that can be considered and the studies that have been carried out so far on partial coating. In the third part, numerical methods used to solve vibroacoustic problems will be presented with their advantages and limitations. It can be underlined that some mathematical developments will be proposed in this chapter, as they will serve as a basis for the next chapters. Finally, the methodology of this work and the organization of the document will be presented.

1.1 Vibroacoustic behavior of cylindrical shells

1.1.1 *In vacuo* cylindrical shells

The vibroacoustic behavior of cylindrical shells has been studied with great interest over the last decades, particularly for its industrial applications such as aeronautics and naval domains. In his book published in 1972, Leissa [1] compiled a great part of the work that had been done on the vibrational behavior of thin shells so far, and particularly the principal assumptions and theories. A first theory on the vibrations of thin elastic shells was derived by Love [2] and exhibited hypothesis known as the Love's First Approximation Theory (LFAT) :

- the shell is thin, meaning that its thickness is small compared to its other dimensions;
- the deflections of the shell are small, meaning that the second- and higher-order magnitude in the strain-displacement relations may be neglicted compared to first-order terms;
- the transverse normal stress is negligible compared to the other normal stress components;

- normals to the underformed middle surface remain straight and normal to the deformed middle surface, and suffer no change in dimensions.

Following these postulates, other thin shell theories have emerged, and particularly thin cylindrical shell theories. We can state the Donnell-Mushtari's theory, the Sanders' theory or the Flügge's theory. Ruotolo [3] showed that Donnell's theory exhibits high errors in the evaluation of the eigenfrequencies of the structure and does not fit well with internal stiffeners. On the contrary, Flügge's theory [4–6] has proven its convenience and accordance with other theories and will be used in this work. Let us consider an *in vacuo* infinitely long cylindrical shell, of radius R and thickness h, as in figure 4. The shell material is assumed to be elastic and isotropic, and is characterized by its Young's modulus E, density ρ_s and Poisson's ratio ν_s. The shell is considered as thin, meaning that $R \gg h$.

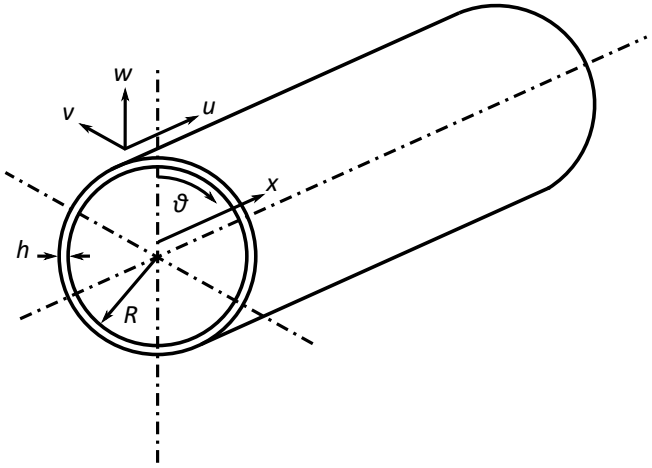

Figure 4: Infinite cylindrical shell and associated coordinate system

Let us define U, V and W, which are the axial, tangential and radial displacements of the shell, respectively. L_f, T and F are respectively the axial, tangential and radial forces exerted on the shell by a point force, and M_T is the tangential moment exerted on the shell by the external load. As we are in harmonic regime, the time dependence $e^{j\omega t}$ (with $j^2 = -1$, ω the pulsation and t the time) is omitted. The vibrational behavior of the shell is described by the Flügge's equations as follows

$$\begin{aligned}\left[R^2\frac{\partial^2}{\partial x^2} + \left(1+\beta^2\right)\frac{1-\nu}{2}\frac{\partial^2}{\partial\theta^2} - \rho R^2\frac{1-\nu^2}{E}\frac{\partial^2}{\partial t^2}\right]U + \left[R\frac{1+\nu}{2}\frac{\partial^2}{\partial x\partial\theta}\right]V \\ + \left[R\nu\frac{\partial}{\partial x} - \beta^2R^3\frac{\partial^3}{\partial x^3} + \beta^2R\frac{1-\nu}{2}\frac{\partial^3}{\partial x\partial\theta^2}\right]W = -\frac{\left(1-\nu^2\right)R^2}{Eh}L_f\delta(x)\delta(\theta)\end{aligned} \tag{1.1a}$$

$$\begin{aligned}\left[R\frac{1+\nu}{2}\frac{\partial^2}{\partial x\partial\theta}\right]U + \left[R^2\left(1+3\beta^2\right)\frac{1-\nu}{2}\frac{\partial^2}{\partial x^2} + \frac{\partial^2}{\partial\theta^2} - \rho R^2\frac{1-\nu^2}{E}\frac{\partial^2}{\partial t^2}\right]V \\ + \left[\frac{\partial}{\partial\theta} - \beta^2R^2\frac{3-\nu}{2}\frac{\partial^3}{\partial x^2\partial\theta}\right]W = -\frac{\left(1-\nu^2\right)R^2}{Eh}T\delta(x)\delta(\theta)\end{aligned} \tag{1.1b}$$

$$\left[R\nu\frac{\partial}{\partial x}-\beta^2R^3\frac{\partial^3}{\partial x^3}+\beta^2R\frac{1-\nu}{2}\frac{\partial^3}{\partial x\partial\theta^2}\right]U+\left[\frac{\partial}{\partial\theta}-\beta^2R^2\frac{3-\nu}{2}\frac{\partial^3}{\partial x^2\partial\theta}\right]V$$
$$+\left[1+\beta^2\left(R^4\frac{\partial^4}{\partial x^4}+2R^2\frac{\partial^4}{\partial x^2\partial\theta^2}+\frac{\partial^4}{\partial\theta^4}\right)+\rho R^2\frac{1-\nu^2}{E}\frac{\partial^2}{\partial t^2}+\beta^2\left(1+2\frac{\partial^2}{\partial\theta^2}\right)\right]W \tag{1.1c}$$
$$=\frac{\left(1-\nu^2\right)R^2}{Eh}\left(F\delta(x)-M_T\delta'(x)\right)\delta(\theta)$$

where δ and δ' respectively correspond to the Dirac distribution and its derivative, and $\beta=\frac{h}{R\sqrt{12}}$ is the shell thickness parameter. The natural damping of the shell can be accounted for by adding a complex part with a loss factor η_s to the Young's modulus of the shell $E^*=E(1+\mathrm{j}\eta_s)$.

In order to study cylindrical shells, it can be more convenient to write the equations of motion in the wavenumber domain, as it has been completely described by Skelton [7]. In cylindrical coordinates, any physical field $f(r,\theta,x)$ can be expressed using a Fourier series decomposition along coordinate θ and a Fourier transform along coordinate x as follows

$$f(r,\theta,x)=\frac{1}{2\pi}\sum_{n=-\infty}^{n=+\infty}\mathrm{e}^{\mathrm{j}n\theta}\int_{-\infty}^{+\infty}\tilde{\tilde{f}}(r,n,k_x)\mathrm{e}^{\mathrm{j}k_xx}\,\mathrm{d}k_x \tag{1.2}$$

where k_x is the axial wavenumber, and n is the circumferential order. The associated spectral quantity $\tilde{\tilde{f}}(r,n,k_x)$ is given by the 2D Fourier transform

$$\tilde{\tilde{f}}(r,n,k_x)=\frac{1}{2\pi}\int_0^{2\pi}\int_{-\infty}^{+\infty}f(r,\theta,x)\mathrm{e}^{-\mathrm{j}(n\theta+k_xx)}\,\mathrm{d}x\,\mathrm{d}\theta \tag{1.3}$$

The Flügge system in Eq. (1.1) can hence be rewritten in the spectral domain as follows

$$\begin{bmatrix}\tilde{\tilde{Z}}_{UU}&\tilde{\tilde{Z}}_{UV}&\tilde{\tilde{Z}}_{UW}\\ \tilde{\tilde{Z}}_{UV}&\tilde{\tilde{Z}}_{VV}&\tilde{\tilde{Z}}_{VW}\\ \tilde{\tilde{Z}}_{UW}&\tilde{\tilde{Z}}_{VW}&\tilde{\tilde{Z}}_{WW}\end{bmatrix}\begin{bmatrix}\tilde{\tilde{U}}\\ \tilde{\tilde{V}}\\ \tilde{\tilde{W}}\end{bmatrix}=\frac{\left(1-\nu^2\right)R^2}{Eh}\begin{bmatrix}-\tilde{\tilde{L}}_f\\ -\tilde{\tilde{T}}\\ \tilde{\tilde{F}}+jk_x\tilde{\tilde{M}}\end{bmatrix} \tag{1.4}$$

The spectral expressions of the Flügge's operator and the spectral displacements are given in Appendix A, and their value in the physical space can be retrieved using the inverse Fourier operation described in Eq. (1.2).

Studying cylindrical shells exhibits characteristic frequencies at which the properties of the shell show a change in behavior [8] and particularly in the radiation efficiency. The radiation efficiency σ corresponds to the ratio between the actual far-field radiated power W_a and the power that would be radiated by a cylindrical shell having the same radiating surface S and an uniform radial velocity V_0 [9]

$$\sigma=\frac{W_a}{\rho_fc_fSV_0^2} \tag{1.5}$$

where ρ_f is the fluid density and c_f the sound speed in the fluid. This value is particularly high around the ring frequency of the shell f_r, at which the longitudinal wavelength equals the circumference of the shell [10, 11]. This frequency is given by the following relation[11]

$$f_r = \frac{c_s}{2\pi R} \tag{1.6}$$

where c_s is the celerity of the longitudinal waves in the shell

$$c_s = \sqrt{\frac{E}{(1-\nu_s^2)\,\rho_s}} \tag{1.7}$$

Above the ring frequency, the radial displacements are weakly coupled from longitudinal and tangential displacements, and it can be considered that the cylindrical shell behaves like a plate [12]. On the other hand, the critical frequency f_c is the frequency at which the acoustic wavenumber $k_f = \omega/c_f$ in the medium is the same as the flexural wavenumber of an equivalent plate of thickness h, and is defined as [8]

$$f_c = \frac{c_f^2\sqrt{12}}{2\pi h c_s} \tag{1.8}$$

The coincidence frequency corresponds to the maximum value of the radiation efficiency, that tends to 1 above f_c (supersonic domain) and is lower under f_c (subsonic domain).

1.1.2 Effect of heavy fluid loading

In order to study the behavior of submerged structures or fluid-filled structures, the effect of fluid loading must be investigated. Compared to *in vacuo* shells, shells surrounded by an acoustic medium present lower natural frequencies, due to an accession to inertia and dissipation of energy by radiation, as it has been highlighted by Junger and Garrelick [13]. The effect of fluid loading can be accounted for by adding a pressure reaction in the right-hand side of the third equation of the Flügge's system (Eq. (1.1c)). In this work, we will only consider external pressure, meaning that the internal pressure will not be taken into account (i.e. there is no acoustic domain inside the shell). Eq. (1.1c) hence becomes

$$\begin{aligned}
&\left[R\nu\frac{\partial}{\partial x} - \beta^2 R^3\frac{\partial^3}{\partial x^3} + \beta^2 R\frac{1-\nu}{2}\frac{\partial^3}{\partial x\partial\theta^2}\right]\mathbf{U} + \left[\frac{\partial}{\partial\theta} - \beta^2 R^2\frac{3-\nu}{2}\frac{\partial^3}{\partial x^2\partial\theta}\right]\mathbf{V} \\
&+ \left[1 + \beta^2\left(R^4\frac{\partial^4}{\partial x^4} + 2R^2\frac{\partial^4}{\partial x^2\partial\theta^2} + \frac{\partial^4}{\partial\theta^4}\right) + \rho R^2\frac{1-\nu^2}{E}\frac{\partial^2}{\partial t^2} + \beta^2\left(1 + 2\frac{\partial^2}{\partial\theta^2}\right)\right]\mathbf{W} \\
&= \frac{(1-\nu^2)\,R^2}{Eh}\left(F\delta(x)\delta(\theta) - M_T\delta'(x)\delta(\theta) - p(x,\theta)\right)
\end{aligned} \tag{1.9}$$

In the fluid medium, the pressure p in Eq. (1.9) satisfies the homogeneous Helmholtz equation [8]

$$\Delta p(r,\theta,x) + k_f^2 p(r,\theta,x) = 0 \tag{1.10}$$

where $\Delta = (\partial^2/\partial x^2) + (\partial^2/\partial r^2) + (1/r)(\partial/\partial r) + (1/r^2)(\partial^2/\partial\theta^2)$ is the Laplacian operator in cylindrical coordinates, and k_f is the acoustic wavenumber. The radiated far-field pressure verifies the Sommerfeld radiation condition [14], while the kinematic condition at the cylindrical interface between the shell and the fluid medium satisfies the Euler condition

$$\begin{cases} \lim\limits_{r\to\infty} r\left(\mathrm{j}k_f p + \frac{\partial p}{\partial r}\right) = 0 \\ \frac{\partial p}{\partial r}(R,\theta,x) = \rho_f \ddot{W}(\theta,x), \end{cases} \tag{1.11}$$

Applying a 2D Fourier transform as in Eq. (1.3) to Eqs. (1.10) and (1.11) allows solving the problem in the wavenumber domain. The spectral pressure can be expressed in terms of the spectral radial displacement of the shell $\tilde{\tilde{W}}$ as well as the spectral fluid "impedance" $\tilde{\tilde{Z}}_f$ (defined as the spectral pressure over the spectral displacement)

$$\tilde{\tilde{p}}(R,n,k_x) = \tilde{\tilde{Z}}_f(R,n,k_x)\tilde{\tilde{W}}(n,k_x) \tag{1.12}$$

with the spectral fluid impedance being:

$$\tilde{\tilde{Z}}_f(R,n,k_x) = \frac{\rho_f\omega^2}{k_r}\frac{H_n^{(2)}(k_r R)}{H_n^{(2)'}(k_r R)} \tag{1.13}$$

where $k_r^2 = k_f^2 - k_x^2$. $H_n^{(2)}$ and $H_n^{(2)'}$ are the Hankel function of the second kind and of order n and its derivative with respect to its argument, respectively. The relation in Eq. (1.12) can be injected into the spectral Flügge's system accounting the fluid loading, yielding a linear system that can be solved by inverting the Flügge's operator. The results are explicited by Maxit and Ginoux [15] and given in Appendix A. The resolution of this system of equations give us the spectral radial displacement $\tilde{\tilde{W}}$, which allows deducing the spectral pressure at any distance r from the shell. The radiated pressure for a point (r,θ,x) can then be estimated by applying a 2D inverse Fourier transform

$$p(r,\theta,x) = \frac{1}{2\pi}\sum_{n=-\infty}^{n=+\infty} \mathrm{e}^{\mathrm{j}n\theta}\int_{-\infty}^{+\infty}\frac{\rho_f\omega}{k_r}\frac{H_n^{(2)}(k_r r)}{H_n^{(2)'}(k_r R)}\tilde{\tilde{W}}(k_x,n)e^{jk_x x}dk_x \tag{1.14}$$

The far field radiated pressure ($r \gg \frac{2\pi}{k_f}$) can be computed using the stationary phase theorem based on an asymptotic value of the Hankel function for large arguments. With θ being the circumferential angle and ϕ the azimutal angle, the stationary phase theorem yields

$$p(r,\phi,\theta) = \sum_{n=-\infty}^{\infty}\frac{2\mathrm{j}\rho_f\omega^2}{rk_f\cos\phi}\frac{\tilde{\tilde{W}}(-k_f\sin\phi,n)}{H_n^{(2)'}(rk_f\cos\phi)}e^{-\mathrm{j}rk_f+\mathrm{j}n\left(\theta+\frac{\pi}{2}\right)}, \quad r \gg \frac{2\pi}{k_f} \tag{1.15}$$

Here, the developments have been presented considering an infinite cylindrical shell. However, in practice, finite shells are of interest, especially when industrial applications are considered. Different models of finite cylindrical shells extended by cylindrical rigid baffles have been developed in the past. Using a similar approach based on Fourier integrals, Sandman [16] evaluates the fluid radiation loading exhibited by the vibrating modes of a finite cylindrical shell. Harari and Sandman [10] use a modal approach to study the vibratory response of laminated shells both *in vacuo* and embedded in an acoustic medium. They find that the presence of the fluid induces cross-modal coupling on the response of the shell. This modal coupling is further investigated by Stepanishen [17], by combining the Fourier integral approach with a Green's integral equation representation of the acoustic loading on the shell. A modal analysis is also used by Laulagnet and Guyader [18] to compute the radiated power and shell quadratic velocity of cylindrical shells loaded by light and heavy fluids. They exhibit that for heavy fluid loading, strong power radiation is obtained for low radiation efficiency and small power radiated by strong radiation efficiency, as opposed to what was observed for light fluid loading. Photiadis [19] studies the response on and near the surface of a fluid-loaded infinite cylindrical shell excited by a ring drive, for frequencies below the ring frequency of the shell. His objective is to gain an understanding of the individual components of the Green's function of the system, which takes into account the acoustic wave emanating from the drive and evanescent surface waves propagating along the cylinder. The understanding of these propagating waves is also studied by Sinha *et al.*, both analytically and experimentally [20, 21], to serve as a basis to study more complex phenomena.

1.1.3 Shells with internal axisymmetric structures

In industrial applications, such as naval or aeronautical domains, the shells are reinforced by axisymmetric structures called stiffeners, in order to strengthen the hull against buckling or hydrostatic pressure in case of submerged shells as studied here. They are also a means to reduce the thickness of the shell, and thus its weight. Other axisymmetric structures are encountered in submarine shells such as bulkheads between the different compartments and at the ends of the pressure hull. It is therefore necessary to predict their influence on the vibroacoustic behavior of the shell. The case of *in vacuo* ring-stiffened cylindrical shells is studied by Galletly [22] using Lagrange's equations to derive the dynamic equations of the system. Compared to an unstiffened shell, it is shown that the stiffened case exhibits an increase in the frequencies of vibration of the structure. Sewall and Naumann [23] compare analytical and experimental results for cylindrical shells with and without longitudinal stiffeners, using a Rayleigh-Ritz procedure for the analytical calculation. The conclusion is similar to the study of Galletly, and they also show that the stiffeners properties can be

averaged over the shell surface when the rings are closely spaced (when the wavelength of vibration is much greater than the stiffeners spacing), hence limiting its validity. In order to overcome this limitation, Mead and Bardell [24] study axially and circumferentially stiffened shells by reducing them to a one-dimensional periodic system. Wah and Hu [25] propose a different approach, valid for evenly spaced ring stiffeners and not based on energy methods, where the stiffeners are considered as discrete members, allowing to find an exact solution for the inter-ring shell motion. They find that the inter-ring displacements depend on the ring spacing, their stiffness in comparison with that of the shell, but also strongly on the circumferential wavenumber. Using the Finite Element Method (FEM) (which will be presented in section 1.3.1), Al-Najafi and Warburton [26] allow themselves to study the influence of parameters such as non-periodic stiffeners spacing, different cross-sections among the stiffeners, or the eccentricity of the ring centroid relative to the shell middle surface.

The far-field acoustic radiation from a fluid-loaded stiffened shell excited by a point force is studied by Burroughs [27], by adding to the solution for the unsupported cylinder, the effect of the sets of rings. It is concluded that the radiation pattern appears like an array of ring radiators, thus highlighting the influence of the stiffeners. It is also emphasized that structural damping reduces the area over which radiation occurs, which reduces the peaks and valleys in the acoustic radiation. This study is extended to different kinds of driving mechanisms [28] and the single radial drive shows itself to produce the greater acoustic radiation per pound of input force. Finite ring stiffened cylindrical shells were also greatly studied by Laulagnet and Guyader [29], for both light and heavy fluid loading. The effect of the stiffeners is studied in terms of radiated power, shell quadratic velocity and radiation coefficient. The calculation is derived using a Green's integral approach as described in [17], for frequencies below the ring and coincident frequencies of the shell. The stiffeners have a strong effect on the quadratic velocity of the shell in water, but less on the radiated power, due to their influence on phenomena controlled by high circumferential order modes. It is also shown that increasing the damping of the stiffeners is mostly inefficient in reducing the radiated noise. This method is however limited to low frequencies due to the difficulty of estimating numerically the modal radiation impedances. Yan *et al.* [30, 31] analyze the vibrational power flow propagation in an infinite ring-stiffened cylindrical shell immersed in heavy fluid by using a space-harmonic method, allowing themselves to expand the response of the periodic structure to harmonic excitations in the terms of a series of space harmonics. They compare results for stiffened and unstiffened shells and come to a conclusion that the stiffeners mainly have a great influence at middle frequencies due to their spacing comparable to the shell wavelength along axial direction, but less at low and high frequencies.

Caresta and Kessissoglou [32] use a semi-analytical method to study the influence of bulkheads, ring-stiffeners and fluid loading on the structural and acoustic responses of a finite cylindrical shell. The stiffeners are accounted for by averaging their properties over the surface of the cylindrical shell, while bulkheads and end plates are modelled as thin circular plates. The results are compared to a coupled FEM/BEM reference calculation. Maxit and Ginoux [15] propose a substructuring approach called the Circumferential Admittance Approach (CAA) to study non-periodically stiffened cylindrical shells in a wide frequency range. The contributions from the fluid loaded shell and those from the stiffeners and internal bulkheads are studied separately before assembling the results using transfer functions. The stiffeners are described using a FEM model while the fluid loaded shell is studied using an accelerated spectral resolution of the Flügge's equations in the wavenumber domain. The results in terms of vibratory field of the shell and radiated pressure field are very satisfactory compared to existing methods, while the computational time is improved.

1.2 Acoustic coatings for naval applications

With the ongoing necessity of acoustic stealth and furtivity of submarine hulls, much attention has been given in the past decades to the study of acoustic coatings in order to reduce the acoustic radiation and scattering of submerged structures. As described in the Introduction, the coatings applied on underwater structures are viscoelastic materials that can generally be decomposed into two main categories:

- Anechoic coatings serve as a protection against active sonars by reducing the acoustic scattering from the hull;
- Compliant or decoupling coatings isolate the hull from the surrounding medium and reduce the radiated noise to serve as a protection against passive sonars.

A review of such coatings will be given in this section, with the numerical methods to model them.

1.2.1 Modelling acoustic coatings

With the generalization of applying acoustic coatings to increase the furtivity of submarine hulls emerged the necessity of correctly modelling such coatings. This challenge has been addressed by many researchers over the past decades and some of the methods to model acoustic coatings will be presented in this section.

1.2.1.1 The locally reacting material approach

To study the radiation, reflection and transmission of an infinite plane panel coated on its two surfaces with a compliant coating and immersed in a fluid medium, Maidanik and Tucker [33] develop a method where the coating is considered as a locally reacting material. Such a material is characterized by a constant complex stiffness and with no thickness, and for which the thickness deformation at a given position depends on the surface acoustic pressure at this position only. This way of modelling a compliant coating has been widely used in the past decades and is still taken under consideration today in certain studies [34]. One of the reasons is that it is relatively easy to implement and gives good insights in the global behavior of the coated structure. To complete the study of Maidanik and Tucker, Crighton [35] observes that decoupling coatings reduce the subsonic wave pressure field and the acoustic field with negligible change in the structural response of the panel either close to or far from the excitation. These studies were carried out with plane membranes as backing structures of the coating. Membranes differ from thin plates in the fact that they do not support shear and are thus easier to handle and the physical interpretations are easier to obtain. Foin *et al.* [36] study the acoustic behavior of a finite, baffled elastic plate-compliant coating system, using a locally reacting material as coating, with the aim to derive a global vibratory indicator to represent the acoustic efficiency of the decoupling treatment, independently of the plate dimensions.

The literature on cylindrical shells covered with compliant coatings is also very significant, and we owe to Laulagnet and Guyader a great amount of knowledge on this topic. In [37] they study the acoustic radiation from a finite cylindrical shell covered with a compliant coating. The shell is closed at its two ends by rigid baffles, and the compliant coating is modelled using a reacting material. They evaluate the power radiated by the shell, and the shell radial quadratic velocity with and without compliant coating, and for several values of the stiffness and loss factor of the coating. It is found that a global reduction of power radiation is observed with the presence of a compliant coating, and this reduction increases with the stiffness and loss factor of the coating. The work of Laulagnet and Guyader is extended by Cuschieri and Feit [38] to consider the scattering from a coated cylindrical shell, that is to say that the external force is an external acoustic plane wave instead of a mechanical drive force applied on the shell. For the radiation problem, the radial velocity at the interface between the coating and the exterior fluid can be expressed using Z_s, Z_f and Z_c which are the impedances of the shell, the fluid and the coating, respectively ([38])

$$\dot{W}_a = \frac{F}{Z_f + Z_s + \frac{Z_s Z_f}{Z_c}} \tag{1.16}$$

where F is the excitation force. A simplified form of the impedance Z_c of the coating "can be

taken to be simply that of the decoupling layer, that is the coating has only radial stiffness" ([38, 39])

$$Z_c = -\mathrm{j}\rho_f c_f \chi(1 + \mathrm{j}\eta) \tag{1.17}$$

with ρ_f being the density of the fluid, c_f acoustic wave speed in the fluid, χ the fraction of the fluid impedance and η the damping term. If the scattering problem is considered and the excitation is a plane wave of amplitude P_i, the radial velocity at the interface between the coating and the exterior fluid is

$$\dot{W}_a = \frac{P_i}{Z_f + \frac{Z_s Z_c}{Z_s + Z_c}} \tag{1.18}$$

From the expressions in Eqs. (1.16) and (1.18), we can notice that, for the radiation problem, the coating can be seen as being mounted in series with the exterior fluid and in parallel with the shell, while for the scattering problem, the coating can be seen as being mounted in series with the shell and in parallel with the exterior fluid. This highlights the significant difference of behavior whether the considered problem is the radiation or the scattering. Besides, as the coating is softer than the shell, the term $\frac{Z_s Z_c}{Z_s + Z_c}$ in Eq. (1.18) can become negligible compared to Z_f, which leads to results showing no substantial differences between the coated and uncoated shells for the scattering problem. This behavior exhibits the properties of decoupling coatings, used in industrial applications for reducing the radiation but not necessarily the scattering, for which anechoic coatings are used.

1.2.1.2 Three-dimensional theory of elasticity

As stated before, using the locally reacting material model to describe acoustic coatings is easy to implement, but it is however limited in a physical point of view. This method does not correctly describe the three-dimensional behavior of the layer as it does not allow for wave effects in the layer nor calculating its hydrostatic compressibility factor. To capture all the physical phenomena involved in the coating, it can hence be necessary to use a three-dimensional theory of elasticity. We can cite the work of Keltie [40] who studies the response of a compliant coating attached to an infinite thin plate and impacted by an acoustic plane wave. The study is carried in two dimensions and the compliant coating is described using longitudinal and shear potentials, and the objective is to get an understanding of the dynamic processes affecting the coating response, in order to embed an array of sensors in the coating. Berry *et al.* [41] investigate the three-dimensional theory of elasticity on a finite bending plate with a compliant coating, embedded in a infinite rigid baffle, and excited by a point force. A comparison is made with the locally reacting model taken from [36] which exhibits the differences between the two models.

In [42], Hull and Welch develop an analytical model of a rib-stiffened thick plate assembly, comprising a steel backing plate and an acoustic coating, both described using the three-dimensional Navier-Cauchy equations of motion. The model aims at being more accurate for high wavenumbers and frequencies, where thin-plate theories generally used fail. The results can be compared in low frequency and low wavenumber to a fluid-loaded, ribbed, Bernoulli-Euler thin plate model previously developed in [43–45], and show very good agreement. It is also found that the ribs have a significant impact of the structural acoustic response of the system. However, Remillieux and Burdisso [46] compare these results to a FEM formulation and find that the results presented by Hull and Welch in [42] are partially incorrect due to an inappropriate chosen number of modes. It must be mentioned that the FEM calculation is much more time consuming than the analytical one, the time ratio between the two studies being 140. This highlights the accuracy of the FEM method, but also its limitations due to prohibitive calculation costs, which will be further explored in section 1.3.1. The study is then extended to the analysis of void inclusions in the elastic layer, as a first step towards the incorporation of a sensor array in the coating.

Concerning cylindrical shells, the behavior of such structures is often studied using multilayer shell theories. In [47], Markus investigates the case of a cylindrical shell coated with a viscoelastic material, either on one side or on both sides of the shell. Gaunaurd [48] studies the scattering of a plane wave by a hollow coated cylinder immersed in a heavy fluid and filled by a light fluid. Each medium is considered as a layer and the equations of motion in the layers are solved by matching ten boundary conditions at the fluid-solid and solid-solid interfaces. Schmidt and Jensen [49] study wave propagations in multilayered viscoelastic media by developing a Direct Global Matrix (DGM) approach, based on continuity and equilibrium relations at the interfaces between the layers. The approach is then applied to cylindrically layered shells excited by ring forces [50], and the stability of the method is improved by using new representations of the potentials in each layer. Laulagnet and Guyader [51] study the radiation of a finite cylindrical shell where the coating is described using Navier's equations to take into account the Young's modulus, Poisson's ratio and mass density of the coating. In order to solve these equations in the low frequency domain, the transverse displacement in the coating is described by the means of an asymptotic expansion to account for the finite character of the shell. Significant insights are obtained from this study that could not be derived using the locally reacting material theory in [37]. The shell exhibits an antiresonance phenomenon due to the presence of the coating, and a wave conversion phenomenon is described in the coating, explaining the observed noise reduction. It is suggested that, in order to improve the noise reduction as much as possible, the hydrostatic compressibility factor must be high enough, while the Young's modulus and density of the

layer must be as low as possible. Cuschieri [52] use the multilayer shell theory to study an infinite cylindrical shell with a compliant coating using a three-dimensional description of the coating. Radiation and scattering are studied, and the shell surface velocity response Green's function is obtained. In their book, Skelton and James [7] propose a mathematical framework for planar, spherical and cylindrical layered media, with a procedure close to the DGM approach where dynamic stiffness matrices for each layer must be obtained. The procedure for an infinite cylindrically layered medium as in figure 5a will be presented here, with an example of how to obtain the dynamic stiffness matrix of a fluid layer.

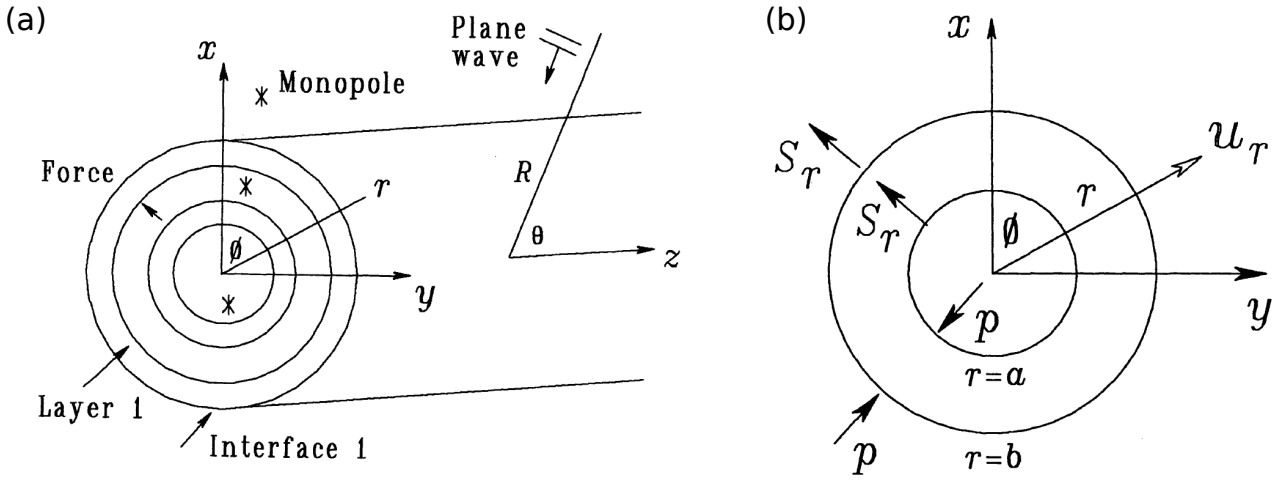

Figure 5: (a) Cylindrically layered medium [7]. (b) Layer of acoustic fluid [7].

In a fluid layer as presented in figure 5b, the pressure satisfies the homogeneous Helmholtz equation in Eq. (1.10) between the inner and outer radii a and b, respectively. The problem is solved in the spectral domain by the means of a 2D Fourier tranform introduced in Eq. (1.3). The solution can be expressed in terms of Bessel functions as

$$p(r,n,k_x) = A_1 J_n(k_r r) + A_2 H_n^{(1)}(k_r r) \tag{1.19}$$

where J_n is the Bessel function of the first kind and of order n, and $H_n^{(1)}$ is the Hankel function of the first kind and of order n. A_1 and A_2 are arbitrary constants of integration. The pressure and normal radial velocities at the inner and outer boundaries can be linked using the Euler relation

$$\frac{\partial p}{\partial r}(r,n,k_x) = \rho\omega^2 u_r(r,n,k_x) \tag{1.20}$$

By combining Eqs. 1.19 and 1.20, the pressure at the inner and outer boundaries can be expressed by solving the following system

$$\begin{pmatrix} p(b,n,k_x) \\ p(a,n,k_x) \end{pmatrix} = \frac{\rho\omega^2}{k_r W} \begin{pmatrix} a_{11}(n,k_x) & a_{12}(n,k_x) \\ a_{21}(n,k_x) & a_{22}(n,k_x) \end{pmatrix} \begin{pmatrix} u_r(b,n,k_x) \\ u_r(a,n,k_x) \end{pmatrix} \tag{1.21}$$

where

$$\begin{aligned} W &= J_n'(k_r b) H_n^{(1)'}(k_r a) - H_n^{(1)'}(k_r b) J_n'(k_r a) \\ a_{11} &= J_n(k_r b) H_n^{(1)'}(k_r a) - H_n^{(1)}(k_r b) J_n'(k_r a) \\ a_{22} &= J_n'(k_r b) H_n^{(1)}(k_r a) - H_n^{(1)'}(k_r b) J_n(k_r a) \\ a_{12} &= -2\mathrm{j}/\pi k_r b, \quad a_{21} = 2\mathrm{j}/\pi k_r a \end{aligned} \tag{1.22}$$

Finally, in terms of spectral surface tractions, $S_r(b,n,k_x) = -p(b,n,k_x)$ and $S_r(a,n,k_x) = p(a,n,k_x)$, the spectral dynamic stiffness matrix equation is

$$[D(n,k_x)] \begin{pmatrix} u_r(b,n,k_x) \\ u_r(a,n,k_x) \end{pmatrix} = \begin{pmatrix} S_r(b,n,k_x) \\ S_r(a,n,k_x) \end{pmatrix} \tag{1.23}$$

where the elements of $[D(n,k_x)]$ are

$$\begin{aligned} d_{11} &= -(\rho\omega^2/k_r W) a_{11}(n,k_x), \quad d_{12} = -(\rho\omega^2/k_r W) a_{12}(n,k_x) \\ d_{21} &= (\rho\omega^2/k_r W) a_{21}(n,k_x), \quad d_{22} = (\rho\omega^2/k_r W) a_{22}(n,k_x) \end{aligned} \tag{1.24}$$

This dynamic stiffness matrix $[D(n,k_x)]$ is required for the assembly procedure. The processus of obtaining the dynamic stiffness matrix is the same for elastic isotropic, anisotropic and viscous fluid layers. Once the dynamic stiffness matrices have been obtained for all the layers of the cylindrically layered medium, the assemblage of the M layers together with the interior and exterior media results in the following system

$$[Z(n,k_x)] \{u(n,k_x)\} = \{E(n,k_x)\} \tag{1.25}$$

where $[Z(n,k_x)]$ is the assembly matrix of the dynamic stiffness matrices of all the layers. The size of $[Z(n,k_x)]$ is $3(M+1) \times 3(M+1)$. $\{u(n,k_x)\}$ is a $3(M+1)$ column vector containing the spectral displacements at the $(M+1)$ interfaces, while $\{E(n,k_x)\}$ is a $3(M+1)$ column vector of spectral excitations and depends on the nature of the excitation (mechanical, monopole, plane wave...). Once the spectral displacements have been obtained, the displacements in the physical space can be retrieved by applying an inverse 2D Fourier transform as defined in Eq. (1.2).

The method developped by Skelton and James can be applied for any number and nature of layers, including anisotropic elastic and viscous fluid layers as evoked earlier. The problem of anisotropy is also addressed by Chen *et al.* [53] and Dutrion [54] by discretizing each anisotropic layer into several isotropic sublayers. Dana *et al.* [55] study the response of a fluid-loaded multilayered cylindrical shell excited by an acoustic plane wave, where the layers can either be fluid or solid. Each layer is characterized by a transfer matrix instead of a dynamic stiffness matrix used for example in the Skelton approach [7]. The transfer matrix of the assembly may be evaluated by multiplying the layer transfer matrices as usually done with the well known Transfer Matrix Method (TMM). However, it has been shown that

convergence issues appear at high frequencies, for large thicknesses of the layers (i.e. the so called *large fd problems*). To overcome this issue, a procedure assembly of the transfer matrix similar to the one of the DGM method is considered. The proposed approach shows a good numerical stability over both a wide range of axial wavenumbers and circumferential orders, but also the ability to consider intermediate fluid layers.

1.2.2 Technologies for acoustic coatings

1.2.2.1 Different kinds of technologies

In order to optimize the radiation and scattering reduction of acoustic coatings, several kinds of technologies have been developed. The review drawn in this paragraph does not aim at being fully exhaustive, as the recent advances in this domain are wide, and this topic could take as much as an entire dedicated chapter. For a deeper analysis of these different designs, the reader can refer to the works of Méresse [56] and Roux [57]. The most widespread technology, that is used for anechoic applications, is the "Alberich" coating. Such coatings were developed by Meyer [58] and consist of a viscoelastic coating in which periodically distributed air cavities are included. When these coatings are excited by an acoustic wave, these inclusions introduce resonances in the rubber and the energy scattered by the cavities is absorbed by the material. Gaunaurd [59] studies the acoustic absorption of an Alberich coating composed of a multiperforated rubber layer bonded to a rigid backing and covered with a nonperforated rubber layer. The study is carried out by isolating a cavity, hence reducing the problem to a one-dimensional model of a lossy viscoelastic ring. He highlights a resonance mechanism associated with the radial motion of the cylinder ring, while Lane [60] focuses on the drum-like resonance of the cover layer having a higher influence on the anechoic performance of the coating. While the inclusions in the previously cited studies are all cylindrical, Gaunaurd *et al.* [61, 62] investigate spherical inclusions, allowing for an easier analytical treatment of the resonance scattering theory. It is worth mentioning that the methodology to predict the dynamic behavior of Alberich coatings in the evoked studies is based on the Effective Medium Theory (EMT). A unified treatment of this theory is developped in [63], and the principle lies in determining effective values of the sound speed and compressional waves attenuation in inhomogeneous media. Experimental investigations are conducted by Audoly [64] on test panels made with viscoelastic materials containing resonant cavities. The comparison with EMT exhibits differences that can be explained by two principal facts: the interaction between the inclusions is not taken into account in the EMT, and the experimentations are conducted on finite panels while the EMT relies on the asumption of infinite panels. According to Audoly, coatings with periodic inclusions such as Alberich coatings are better described using FEM formulations, as the periodicity of the

structure allows studying only one period using Bloch type relations on the boundaries of the structure to simulate the periodicity [65]. The sound transmission in the rubber is studied by Hladky-Hennion and Decarpigny in [65], while Langlet *et al.* [66] calculate the effective wavenumber of the medium using the same code.

The characteristics of elastomers correspond to the need of dissipating vibratory energy, but the celerity of longitudinal waves in these materials is often close to the one of water, hence meaning a problematic acoustic transparency when immerged in water. To this end, micro-cavities or soft-wall micro-balloons can be included in the elastomer, forming the family of micro-inclusion materials. The micro-inclusions allow reducing the celerity of longitudinal waves in the material, which can be tuned depending on the application (decoupling or anechoic). The size of the inclusions, particularly for low-frequencies, are very small compared to the wavelength, which means that the material can be considered as homogeneous [67]. Similar effective medium theories as the ones used for Alberich coatings can be used to describe such materials [68]. However, for higher frequencies, the micro-inclusions can resonate and the material can no longer be considered as homogeneous [69]. Materials exhibiting such characteristics of resonant inclusions can be considered as belonging to the category of meta-materials. Although the definition of meta-materials is not always clear, they can be considered as materials which exhibit unusual properties, with values or strong variations with frequency of the constitutive acoustic parameters not found in conventional materials [57]. A thorough review of meta-materials is carried out by Ma and Sheng in [70]. Solid resonant inclusions have been investigated by Liu *et al.* [71] by inserting in a relatively rigid matrix a steel sphere embedded in an elastically soft material. Contrary to air or void inclusions, this kind of material is not constrained by the increase in hydrostatic pressure, but the increase of density due to the steel core renders it inapplicable for decoupling use. It can hence only be used as an anechoic coating. In [72], Wen *et al.* use the FEM to study the same material. Two peaks of absorption are observed, the first one corresponding to the spring-mass like system exhibited by the core in the soft material, and the second one corresponding to the conversion of longitudinal waves into transversal wave along the soft material. Another kind of designs, that must be distinguished from meta-materials, are phononic crystals. Phononic crystals exhibit periodic properties, while for meta-materials the inclusions can be randomly distributed [57]. Phononic crystals can also be constituted by resonant inclusions, and the medium is thus referred to as Locally Resonant Phononic Crystal (LRPC). Alberich types anechoic coatings are a particular case of LRPC. The concept of phononic crystal is studied by Kushwaha *et al.* [73] by including aluminium cylinders in a nickel matrix, and they highlight the presence of an absolute frequency band gap in which no eigenfrequency is permitted in the material. Leroy *et al.* [74, 75] design

a phononic crystal consisting of gas bubbles in a viscoelastic matrix. A simple model is developed in good accordance with experimental results.

1.2.2.2 Inclusion of coating technologies in vibroacoustic models

If the technologies evoked in section 1.2.2.1 are designed to improve the performances of acoustic coatings, it is of paramount importance to study their behavior in vibroacoustic contexts, that is when they are backed by a solid structure. To this end Meng *et al.* [76] use the FEM to analyse acoustic performances of several kinds of coatings, including Alberich coatings, backed by a steel plate. It is found that, in addition to the aforementioned inclusion resonances, the longitudinal resonance of the anechoic layer and the steel slab induce a new absorption peak, meaning that the steel plate enhances the performances of the anechoic coating. A similar study is conducted by Zhou *et al.* [77] with a particular interest given to the incident angle of the plane wave. On the topic of Alberich coatings, Ivansson [78] studies coatings with sperical inclusions and backed by a steel plate using a semi-analytical method, where an analogy is used between sound scattering by cavities in the rubber and electron scattering by atoms in a lattice. The absorption loss of each isolated cavity is corrected by a factor to account for the coupled effect of the different cavities, hence giving an increased level of physical understanding of the phenomenon than the paper of Gaunaurd [59]. This method, named Multiple Layer Scattering (MLS), is extended to non-spherical scatterers for the investigation of superellipsoidal cavities [79] or infinite cylindrical cavities [80]. It is found that, for infinite cylindrical cavities, with axes in a lateral direction, the thickness of the coating can be reduced by a factor three without losing absorption performances, and mixing cavities of differents sizes can be favorable.

Sharma *et al.* [81] develop a semi-analytical model of a coating with a single periodic layer of cylindrical voids and apply the method for the case of such a coating with a steel backing plate. The theory is compared with a FEM calculation and shows very good agreements for several numbers of layers of voids and several void diameters. Later on, they investigate similar technologies with hard inclusions [82], and the homogenisation theory is used to result in a mulilayered medium. The comparison with a FEM calculation highlights the independant effects of the cylindrical voids and steel cylinders on the two observed absorption peaks. Ke *et al.* [83] use the FEM approach coupled to a Newton's iterative method to evaluate the performances of an anechoic layer attached to a steel plate, and apply later the method to a steel spherical shell. However, it must be emphasized that, for most of the technologies evoked in section 1.2.2.1, ongoing researchs focus on the acoustic characteristics of such materials, hence the available literature on their application in a vibroacoustic model is not substantial.

1.2.3 Influence of partial coating

While a massive amount of research on coated surfaces exists in the literature, and especially coated cylindrical shells, little attention has been given to partial coating. For cylindrical shells, breaking the axisymmetry increases substantially the computational costs. While most analytical methods that have been presented cannot deal with this situation due to their lack of versatility, numerical methods such as FEM are limited to low frequencies due to their high computational cost at mid and high frequencies. Nevertheless, some authors investigated the case of partial coating. Ferri *et al.* [84] study the scattering of a plane wave by finite and infinite partially coated cylindrical shells. The coated and uncoated surfaces are modeled by assuming that the specific local impedance is constant along arcs of cylindrical surfaces. The effect of partial coating is thus accounted for as an impedance discontinuity at the adjacent regions between coated and uncoated surfaces. Laulagnet and Guyader [85] investigate the effect of circumferential partial coating on the sound radiation from a cylindrical shell (see figure 6). The decoupling coating is modelled as a locally reacting material as described in section 1.2.1.1, which means that the results cannot be as accurate as wished due to the lack of accuracy of this method. The effects are observed in terms of quadratic velocity of the shell and of the coating, and of far-field radiated power. It is found that, compared to full coating, partial coating increases substantially the acoustic radiation. For cases where the shell is coated on only 10% of its circumference, partial coating even induces a higher radiation factor than for the case of the bare shell, and this effect is observed well below the coincidence frequency.

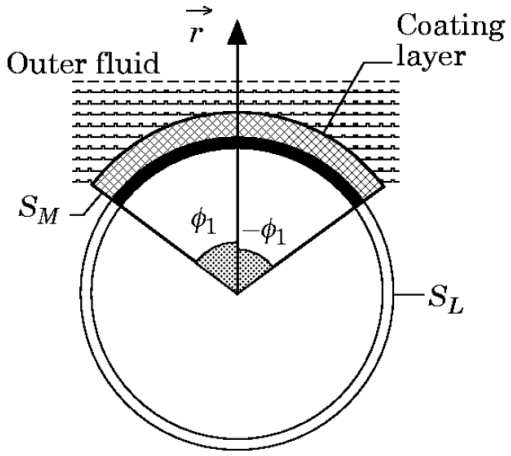

Figure 6: Cross-section of a partially coated cylindrical shell [85].

Similar conclusions are drawn by Cuschieri and Feit [38] when they evaluate the near- and far-field radiation and the scattering from partially coated cylindrical shell, using the locally reacting material theory to model the coating. In addition, they exhibit the influence of the edge smoothness on the strength of the radiated acoustic field. Both papers highlight

the influence of the loss of axisymmetry in those results. More recently, Liu *et al.* [86] studied a finite cylindrical shell partially covered along its length, which means that they do not break the axisymmety. Their conclusion is different than in the previous papers, and this highlights the influence of the axisymmetry of the acoustic response of cylindrical shells.

1.3 Numerical methods in vibroacoustics and naval applications

Simple vibroacoustic problems can be addressed by solving by an analytical way the equations of motion of the structure or the equations of propagation in the medium. However, when the problems become more complex, it is not always possible to derive an analytical formulation. Numerical methods in vibroacoustics have emerged with this need of modelling complex problems, for which analytical formulations are no longer available. Several methods have been developed, covering a wide range of frequencies. Among those methods, elements based methods are very accurate but also time consuming and therefore restricted to low frequencies. On the other hand, energy-based methods allow studying vibroacoustic problems at high frequencies. Finally, substructuring methods can be used to extend the domain of application of low-frequency methods towards higher frequencies. In this section, an overview of these methods will be presented.

1.3.1 Element-based methods

1.3.1.1 The Finite Element Method

(a) Principle

The Finite Element Method (FEM) is one of the most common ways to solve engineering problems, with a wide range of applications over multiple domains. In particular, it has been widely used in vibroacoustics for its ability in dealing with problems exhibiting complex geometrical situations [87]. The original problem is transformed into an equivalent integral formulation, and the partial differential equations are solved by discretizing the domain into small subdomains called finite elements. Each element contains a certain amount of nodes depending on its shape, at which the field variables are calculated. The mass and stiffness matrices, noted respectively $\mathbf{M}$ and $\mathbf{K}$, are defined and the FEM model is obtained for an angular frequency ω via the following expression

$$\left(\mathbf{K}^{*} - \omega^{2}\mathbf{M}\right)\mathbf{U} = \mathbf{F} \tag{1.26}$$

In Eq. (1.26), $\mathbf{U}$ represents the unknown vector and is marked here as a displacement

vector, while $\mathbf{F}$ corresponds to the vector of external forces, as it is usually written for a structural problem. For the case of an acoustic problem, the unknown vector would be a pressure vector, while the external forces vector could take several forms depending on the acoustic excitation. In order to introduce damping in the model, the stiffness matrix can take a complex value $\mathbf{K}^* = \mathbf{K}(1 + j\eta)$, with η being the damping value. The system in Eq. (1.26) can be solved directly by inverting the dynamic matrix $\left(\mathbf{K}^* - \omega^2\mathbf{M}\right)$. This process is very accurate, but also very time consuming for large systems. The computational efforts induced by the direct resolution can be reduced by using a modal expansion technique. The eigenfrequencies of the problem are calculated by solving the eigenvalue problem

$$\omega_n^2 \mathbf{M}\boldsymbol{\Phi}_n = \mathbf{K}\boldsymbol{\Phi}_n \tag{1.27}$$

with ω_n being the eigenfrequencies and $\boldsymbol{\Phi}_n$ the associated mode shapes. The frequency response of the system can be calculated as a linear combination of the modes associated with the eigenvalues. The resulting sum is theoretically infinite, but in practice, it is truncated to a finite value N_m, determined by the modes having a resonance frequency until 1.5 times the maximal frequency of interest. It yields

$$\mathbf{U} = \sum_{n=1}^{N_m} a_n \boldsymbol{\Phi}_n \tag{1.28}$$

where a_n is the modal amplitude and can be calculated from the reduced mass matrix $\underline{\mathbf{M}} = \boldsymbol{\Phi}^T\mathbf{M}\boldsymbol{\Phi}$, the reduced stiffness matrix $\underline{\mathbf{K}} = \boldsymbol{\Phi}^T\mathbf{K}\boldsymbol{\Phi}$ and the reduced force vector $\underline{\mathbf{F}} = \boldsymbol{\Phi}^T\mathbf{F}$

$$a_n = \left(\underline{\mathbf{K}}(1 + j\eta) - \omega_n^2\underline{\mathbf{M}}\right)^{-1} \underline{\mathbf{F}} \tag{1.29}$$

The reduced system is much faster to compute, but has a poor convergence outside of resonance peaks because of the basis truncation. To circumvent this issue, Rubin [88] proposes to take into account the contribution of neglected modes, called residual modes. This technique has proven to have a better convergence than the modal expansion method alone, with a calculation time that remains low compared to the direct inversion of the dynamic matrix.

It must be emphasized that the size of the discretization follows a wavelength-based criterion. In industrial applications, a criterion of 6 elements per wavelength (the nature of which depends on the considered problem) is generally retained. This assumption clearly exhibits the frequency limitations of the method, as prohibitive calculation costs will shortly be met as the frequency of the study will increase.

In the case of fluid-structure coupling for vibroacoustic problems, the FEM problem that must be solved has to take into account both the displacement field of the structure (a shell

for example) and the pressure field in the acoustic cavity (i.e. a bounded fluid domain). The coupled problem is stated as [89]

$$\left(-\omega^2 \begin{bmatrix} \mathbf{M}_S & 0 \\ \rho_s \mathbf{R}^T & \mathbf{M}_F \end{bmatrix} + \begin{bmatrix} \mathbf{K}_S & -\mathbf{R} \\ 0 & \mathbf{K}_F \end{bmatrix}\right) \begin{Bmatrix} \mathbf{U} \\ \mathbf{P} \end{Bmatrix} = \begin{Bmatrix} 0 \\ 0 \end{Bmatrix} \tag{1.30}$$

where $\mathbf{M}_S$ and $\mathbf{K}_S$ are the mass and stiffness matrices of the structure, respectively, $\mathbf{M}_F$ and $\mathbf{K}_F$ are the mass and stiffness matrices of the fluid, respectively, ρ_s is the shell density, and $\mathbf{R}$ is the Fluid-Structure Interaction matrix. It is worth noticing that this pressure/displacement formulation yields non-symmetric matrices, despite the conservative nature of the mechanical coupling. When the acoustic domain is unbounded, the FEM is not well indicated. Methods to study infinite domains will be investigated in the next section.

(b) The component mode synthesis

Following earlier works dealing with matrix methods for structural analysis, Hurty [90] proposes to study complex structural systems by dividing them into interconnected components treated separately. This method is called the Component Mode Synthesis (CMS), and is "a technique to simplify the analysis of complicated finite element models" [91]. Several kinds of displacement modes (rigid-body modes, constraint modes and normal modes) are considered to evaluate the displacements of the separate components and the mass, stiffness and damping matrices of the complete systems can be obtained, as well as the response of the system. Similarly to this method, Gladwell [92] develops a method, called branch mode analysis, in order to calculate the natural frequencies and principal modes of a system with many degrees of freedom. The principle of the method is to impose a sequence of sets of constraints such that, when a set is imposed, only one component of the system, called branch, can vibrate, the other ones remaining fixed or vibrating as rigid bodies. This allows determining natural frequencies and principal modes of these branches. These branch modes are then introduced into a Rayleigh-Ritz procedure to determine the natural frequencies and modes of the whole system. This method is particularly appropriate for systems consisting of a main structure linked to secondary systems, but is restricted due to the fact that the boundary between the substructures is assumed to be rigid, condition that is not always met in general. To circumvent this issue, Craig and Bampton [93] propose a fixed interface method based on the component mode synthesis method developed by Hurty. The approach however differs from the previous one as all the boundary freedoms are treated alike rather than being separated into determinate and indeterminate constraints. This difference leads to an easier formulation of substructures problems and shortens computing times. Alternatively, Rixen [94] develops a free-interface method dual to the Craig-Bampton fixed interface method. The

substructures are assembled through interface forces instead of displacements and injected into a FEM code as macro-elements. Finally, one can cite hybrid methods like the one proposed by MacNeal [95] where fixed and free connections can be retained between the substructures. This method is interesting in the sense that the boundary conditions may be selected to optimize accuracy.

1.3.1.2 The Boundary Element Method

(a) Principle

Exterior problems with infinite domains can be studied using the Boundary Element Method (BEM) instead of FEM. Contrary to the FEM where all the domain must be discretized, only the boundary of the domain is discretized when using the BEM, hence reducing by one dimension the considered problem [96]. The Sommerfeld radiation condition, introduced in Eq. (1.11) and of paramount importance for exterior radiation problems, is automatically satisfied by the equations exhibited by the BEM. There are classically two ways of solving a BEM problem: the direct and indirect formulations.

The direct BEM formulation is based on the resolution of the Helmholtz equation defined in Eq. (1.10) by the means of an integral formulation and the use of the Green's function. Let us consider a solid structure bounded by a closed surface S, embedded in an infinite homogeneous acoustic medium Ω. The free-space Green's function $G(r,q)$ is introduced and verifies the following equation [97]

$$\Delta G(r,q) + k_f^2 G(r,q) = -\delta(|r-q|), \quad (r,q) \in \Omega \tag{1.31}$$

where δ is the Dirac delta function and $|\bullet|$ denotes the cartesian distance. The free-space Green's function represents the effect at point q of a unit point source located at point r and radiating into the medium, satisfies the Sommerfield radiation condition, and is given in three dimensions by

$$G(r,q) = \frac{e^{jk_f|r-q|}}{4\pi|r-q|} \tag{1.32}$$

The application of the Green's Second Theorem enables one to obtain the direct formulation of the BEM

$$c(r)p(r) = \int\int_S \left[p(r)\frac{\partial G}{\partial n}(r,q) - G(r,q)\frac{\partial p}{\partial n}(r) \right] \mathrm{d}S \tag{1.33}$$

with n being the normal exterior to the closed surface S, and $c(r)$ is a coefficient depending on the receptor's location

$$c(r) = \begin{cases} \frac{1}{2}, & r \in S \\ 1, & r \in \Omega \end{cases} \tag{1.34}$$

The indirect BEM formulation is based on layer potentials, as it has been shown by Filippi that the solution of the Helmholtz equation can take the form of a linear combination of simple layer and double layer potentials [98]

$$p(r) = \alpha p_s(r) + \beta p_d(r) \tag{1.35}$$

where α and β are constant complex coefficients. The simple layer potential $p_s(r)$ is a potential due to a layer of monopole sources, and represents a velocity jump at the crossing of the surface S. It is given by

$$p_s(r) = \int\int_S \nu(q) G(r,q)\, \mathrm{d}S \tag{1.36}$$

where $\nu(q)$ is the layer of monopole sources. The double layer potential $p_d(r)$ is a potential due to a layer of dipole sources, and represents a pressure jump between the interior side and the exterior side of the surface S. It is given by

$$p_s(r) = \int\int_S \mu(q) \frac{\partial G}{\partial n}(r,q)\, \mathrm{d}S \tag{1.37}$$

where $\mu(q)$ is the layer of dipole sources. It must be emphasized that the direct and indirect formulations of the BEM are equivalent, as it has been formally demonstrated by Brebbia and Butterfield [99]. As for the FEM, the size of the discretization of the boundary follows a wavelength-based criterion, which is equivalent to the FEM criterion as the generally adopted criterion yields 6 elements per wavelength at the highest considered frequency, where the wavelength corresponds for a vibroacoustical problem to the smaller value between the acoustic wavelength in the fluid medium and the flexural wavelength of the structure.

(b) Alternative methods

Additionnally to the BEM, other methods have been developed to study the acoustic radiation in unbounded domains. For example, the Perfectly Matched Layer (PML) approach, initially derived for electromagnetic fields [100], is well adapted to emulate the Sommerfeld radiation condition by absorbing all the incoming waves propagating towards infinity and by dissipating their energy. Such layers can be implemented in FEM codes such as in the COMSOL Multiphysics® 5.6 [101] software with the Acoustics module. The PML layer must be meshed in the same way as the rest of the model, and its size is determined by the

acoustic wavelength at the smallest considered frequency, which means that studies in the low frequency range exhibit very large PML thicknesses.

Besides, Infinite Elements have been considered as an adaptation of the FEM method to the propagation in infinite domains [102]. A series of shape functions analogous the Lagrange polynomials, including an exponential decay term, are used. Variants of this method have emerged, and we can notably cite the Wave-enveloppe (WE) method, in which complex conjugates of the element shape functions are used as weighting functions in a Petrov-Galerkin procedure [103, 104].

1.3.1.3 Naval applications

The methods presented subsections 1.3.1.1 and 1.3.1.2 present the advantage of being able to deal with complex systems. They have hence been widely applied in naval applications, to study for example immersed cylindrical shells.

Zhou and Joseph [105] study the acoustic radiation from a fluid-loaded stiffened cylindrical shell using the BEM to model the acoustic medium, for which the results are used as an entry in a FEM calculation to model the cylindrical shell. The results are compared to experimental investigations from Chen and Schweikert [106]. The results show a good agreement, but are limited to low frequencies (250 Hz for a diameter of the shell of 1.25 m) due to the substantial computational cost of the numerical calculations. As already evoked in subsection 1.1.3, Caresta and Kessissoglou [32] use a coupled FEM/BEM calculation as a reference to study in the low-frequency range a finite stiffened cylindrical shell immersed in heavy fluid and under axial load, where both ends of the cylinder are closed by circular plates. Their semi-analytical model also incorporates internal bulkheads to account for the separation of the different areas in a submarine hull. The cylinder is extended by two semi-infinite rigid baffles, hence the scattering at the finite ends is not taken into account. In later studies [107, 108], they close the shell using truncated conical shells, and evaluate the influence of these ends. They also show that the far-field radiated sound is greater in the case of a radial load compared to an axisymmetric excitation of the hull due to the circumferential bending modes from $n = 1$. To calculate the surface and far-field radiated pressures, they use a direct BEM formulation. Merz *et al.* [109, 110] use a hybrid FEM/BEM method to simulate the vibro-acoustic response of a submarine hull due to propeller forces. The hull is described by a FEM model, while the surrounding fluid is modelled by BEM. The study is limited to the low frequencies (i.e. under 100 Hz) due to the size of the model, which would require prohibitive computational costs at higher frequencies. Once again, the size of the model limits the frequency range of the study, which does not go beyond 100 Hz. A coupled FEM/BEM method used with a Krylov subspace model order reduction allows considering the study of the radiation from a fluid-loaded cylindrical shell closed at each end by hemispherical end

caps by Peters *et al.* [111]. The computational effort required from a fully coupled FEM/BEM method is limited by the model order reduction and the conclusions drawn from their study are very satisfaying and allow considering more complex physical problems in future studies.

FEM coupled with a PML layer is used by Zampolli *et al.* [112] to study the radiation and scattering by axially symmetric objects subject to non-symmetric loading. This technique can be applied to any structure within this scope, including cylindrical shells. In order to circumvent the low-frequency issues of the PML layer, a wavelength-dependent rescaling of the PML is used, enabling keeping a single thickness of the absorbing layer where the size of the mesh is adapted to the corresponding frequency band.

1.3.2 Energy-based methods

1.3.2.1 The Statistical Energy Analysis

The approaches presented in section 1.3.1 are a good way to estimate the eigenvalues of complex systems, but in practice, they are limited in frequency and cannot be used at mid and high frequencies. For example, for the CMS presented in subsection 1.3.1.1, the solution obtained is only an approximation of the actual eigensolution of the original structure [113]. This is partly due to the fact that the theoretically infinite modal basis must be truncated to a finite number of modes, leading to convergence issues, particularly when frequency increases. Furthermore, such deterministic methods are very sensitive to the input parameters, and a slight change can induce very large dispersions in the response, as described by Guyader [114]. Following these statements, Statistical Energy Analysis (SEA) methods have been developed to address the necessity of predicting average noise and vibration levels in various frequency bands of complex systems containing substructures [115]. The approach is first evoked by Lyon and Maidanik [116] without employing the term SEA. The wave based approach employed in [116] is balanced by a modal approach described by Smith [117], but the two approaches give the same results. The method has been vastly investigated and is thorougly described by Burroughs *et al.* [115] and Maxit [118]. It describes the power flow exchanged between two subsystems of a complex system. Let us consider two subsystems which may be driven, dissipate energy through internal viscous damping and there is a conservative interchange of energy between them [119]. If, in the considered frequency band, are included N_1 resonant modes for subsystem 1 and N_2 resonant modes of subsystem 2, and considering that one mode of one subsystem is not coupled with modes of the same subsystem but is coupled by gyroscopic elements with the modes of the other subsystem [120], the power flow exchanged by the two subsystems reads

$$\Pi_{1-2} = \omega_c \eta_{12} \left(\xi_1 - \frac{N_1}{N_2} \xi_2 \right) \tag{1.38}$$

where ω_c is the central angular frequency of the frequency band of interest, ξ_1 and ξ_2 represent the time-averaged total energies of subsystems 1 and 2, respectively, and η_{12} is the coupling loss factor. The latter can be expressed as

$$\eta_{12} = \frac{\sum_{p=1}^{N_1} \sum_{q=1}^{N_2} \beta_{pq}^{12}}{N_1 \omega_c} \tag{1.39}$$

with β_{pq}^{12} being the intermodal coupling factor. The difficulty of applying the SEA lies in the evaluation of the coupling loss factors. Besides, the SEA is based on several assumptions, some of which are [119]

- subsystems and coupling mechanisms are assumed linear;
- only statistically independent, stationary driving forces are applied to the subsystems;
- the driving forces have flat spectra compared with the frequency responses of the subsystems;
- the coupling between the subsystems is conservative and weak;
- modes are statistically independant within subsystems which implies that the modal components of the driving forces should all be directly proportional to the overall driving force levels;
- the damping is light compared with the frequency bandwidth.

The concept of SEA leads to a new scientific method applied to sound and vibration, as it proposes an energetic description of the systems [121]. One of the particularities of the SEA is to be efficient in the high frequency range where no other numerical tool is available, but it comes with the loss of details in description of the behavior of the system [122].

1.3.2.2 Alternative methods

To circumvent some issues related to the range of validity of the SEA, Maxit [118] and Guyader [123] extend the method to subsystems with non-uniform modal energy distribution by developing the Statistical modal Energy distribution Analysis (SmEdA). This method improves energy prediction compared to SEA in certain typical configurations. The SEA is also coupled with deterministic methods such as FEM or CMS [124] to find applications in a wider range of frequencies. In [125], the partioning of complex dynamic systems into local and global sets of degrees of freedom enables the use of SEA for the local components and deterministic methods (FEM, fuzzy structure theory) for the global components. A test case application on coupled rods yields very good results form low to high frequency excitation.

Hybrid SEA/FEM methods can also be used to find the coupling loss factors necessary to apply the SEA [120, 126, 127], or to model systems comprising of subsystems with long wavelength behavior (where FEM is used) and short wavelength behavior (where SEA is used) [128].

The Dynamic Energy Analysis (DEA) [129] is proposed in order to enhance the range of applicability of standard SEA, by interpolating SEA and full ray tracing technique. The SEA is then improved by using the BEM for the spatial variable which leads to large efficiency gains [130]. One can also cite the Energy Finite Element Analysis (EFEA) [131–133], which offers an improved alternative to the SEA for simulating the structural-acoustic behavior of large-scale structures. It is based on deriving governing differential equations in terms of energy density variables and employing a FEM approach for solving them numerically.

1.3.2.3 Naval applications

The SEA method has been widely used in the naval domain for its ability in giving results in high-frequency ranges. For example, in [134], a finite cylindrical shell whose dimensions correspond to those of a submarine hull is studied in a wide frequency range. A coupled FEM/BEM method is used for the low frequencies (with the model described in [111]), while the SEA is used above 200 Hz. In order to bridge the frequency gap between the two models, a substructuring method, the CTF (which will be developed in more details in sections 1.3.3.4 and 3.1), is used. Determining the self noise of a submarine hull in the high-frequency range is also crucial in order to quantify the acoustic detection performance of a sonar system. The SEA can be used for such study [135] and allows estimating that, at high speeds, the flow noise can be supposed to be the main contribution of self noise. SEA [136] or SmEdA [137] have been used to study the radiation efficiency of cylindrical shells. In the latter, the SmEdA provides better results than the SEA compared to experimental investigations due to a more precise estimation of the coupling loss factors. Fluid-loaded stiffened cylindrical shells can also be studied using the EFEA method in [138]. They use the periodic properties of the structure due to the regular spacing of the stiffeners and consider the fluid loading as an added mass with radiation effects.

The SEA can also be used to study the efficiency of decoupling coatings (as described in section 1.2) at high frequencies [139]. The difficulty in estimating the efficiency of the decoupling coating using the SEA lies in the necessity of introducing some parameters in the SEA model (such as the added mass of the plate). Similarly, partial covering of a cylindrical shell with a decoupling coating has been studied with SEA [140]. The leak effect observed with an analytical calculation in [85] is found back in this study and shows that the SEA can be used to study such structures at high frequencies (as the SEA calculation in the low frequency range does not show accurate results compared to the analytical one). These

studies demonstrate that the SEA and its derivatives can be a powerful tool to study complex structures in a frequency range where other methods fail to give results with reasonable computation costs. However, it must be emphasized that, for naval applications, the weak coupling asumption of the SEA is often hardly verifiable. As an outcome, studying the heavy fluid-structure interaction using SEA can lead to inaccurate results due to the added mass and added stiffness effects of the heavy fluid [141].

1.3.3 Substructuring methods based on admittance concepts

In order to overcome the frequency limitations of the element-based methods presented in section 1.3.1, substructurings methods based on admittance concepts have been developed. They allow studying complex systems by separating them into several substructures that can be linked using frequency transfer functions. In theory, these methods show no frequency dependency and can then be applied over a larger frequency domain, especially at mid frequencies. They can thus constitute a bridge between the elements-based methods presented in section 1.3.1 and the energy-based methods presented in section 1.3.2, as it was evoked in [134].

1.3.3.1 The admittance method

The admittance method, also called mobility method, is a kind of substructuring method, where subsystems are coupled via transfer functions based on mechanical continuity between the subsystems. It has hence no theoretical frequency limitations. This method is initially derived from electrical concepts by Firestone [142], and the concept of mobility is defined as the ease of motion, meaning the ratio of the velocity accross an element to the force through an element. One must precise that hypothesis of linear structures and harmonic excitations are necessary assumptions to apply admittance concepts. The origins of the method are presented by Gardonio and Brennan [143], from the original concepts emanating from the electrical field to the more recent advances and applications of the method in the end of the 20^{th} century. Rubin [144] is the first to define admittance matrices to account for several coupling points and degrees of freedom. This allows defining point-admittances for diagonal terms of the matrix and cross- of transfer-admittances for extra-diagonal terms of the matrix. The impedance matrix can be defined similarly, with the difference that the impedance represents the effect upon the resultant force of the application of a velocity [145]. The impedance can hence be seen as the inverse of the admittance, as admittance is a concept which sums velocity responses while impedance is a concept that sums force responses. It is worth noticing that these transfer functions can be characterized by different means (analytical, numerical or experimental), thus giving these methods a useful versatility.

The formalism for multi-point coupled structures is established by Petersson and Plunt [146, 147] and effective point or overall mobilities are defined to reduce the calculations and measurements by taking into account the contributions of all the coupling points into the response at a single point of the structure, and determining contributions of extra-diagonal terms that can be neglected. Petersson [148, 149] uses this theory to predict the response of two plates perpendicularly assembled and the influence of each plate of the point mobilities at the intersection. The admittance method is also used by Wilken and Soedel [150] to study the modal characteristics of ring-stiffened cylindrical shells. A similar study, where the stiffeners are replaced by welded circular plates, is proposed by Huang and Soedel [151]. Line admittances are defined from responses of the plate and the shell to line forces distributed along the interface, and the results show a good agreement with numerical simulations obtained via FEM. The approach is also extended to weakly-coupled structural-acoustic systems by Kim and Brennan [152].

1.3.3.2 The Circumferential Admittance Approach

The Circumferential Admittance Approach (CAA) is developped by Maxit [153] as an extension of the classical admittance approach to axisymmetric line coupled subsystems. It allows studying for example the vibro-acoustic behavior of fluid-loaded cylindrical shells non-periodically stiffened by internal frames (that can be stiffeners or bulckheads) as in [15]. An example of such a stiffened cylindrical shell, with an associated radial displacement field at the surface of the shell for a point force excitation, is illustrated in figure 7. This method can be extended to scattering from such structures [154], or by taking into account random excitations such as Turbulent Boundary Layers (TBLs) [155]. The principle is to consider the non-stiffened shell as a first subsystem and the internal structures as multiple individual subsystems. The circumferential admittances, that are the necessary transfer functions for the application of the method, can be calculated using the FEM for the internal structures, and using a spectral approach as described in section 1.1.2 for the cylindrical shell. The method is also valid for fluid-filled stiffened cylindrical shells, as it has been applied to study the spatial coherence and vibratory fields induced by a TBL in fluid-filled pipes [156], or to detect acoustic leaks in sodium water heat exchangers using a beamforming technique [157].

1.3.3.3 The Patch Transfer Function method

The Patch Transfer Function (PTF) method is an extension of the admittance method to subsystems that are coupled along surfaces. The method is introduced by Ouisse *et al.* [158] and consists in partitioning the coupling surface between the subsystems into elementary surfaces called patches that are successively excited to build the transfer matrix. The size of the patches is defined following a criterion equivalent to the Nyquist-Shannon sampling

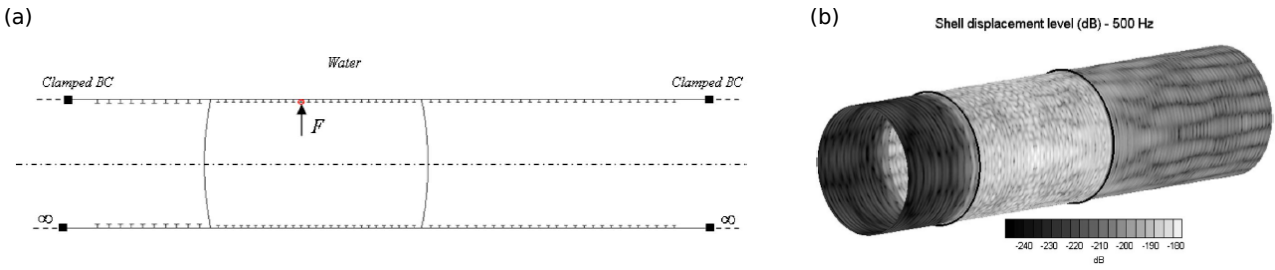

Figure 7: (a) Stiffened cylindrical shell comprising three sections with various stiffeners spacing and cross-sections, separated by spherical bulkheads [15]. (b) Example of a radial displacement field at 500 Hz at the surface of the shell, when a radial point force is applied on a stiffener [15].

theorem [159], which means that the maximum size of a patch should be half the smallest wavelength of the problem. It is hence much less restrictive than the FEM criterion evoked in section 1.3.1.1. Once the transfer matrix has been obtained, the Patch Transfer Functions (PTFs) are assembled using the superposition principle valid for linear passive systems along with continuity relations.

This method has been widely studied in literature because of its various industrial applications. In the automotive industry, Ouisse *et al.* use the PTF method to calculate the noise radiated through openings of the engine cavity of a car, while Veronesi *et al.* [160] investigate the vibro-acoustic properties of porous materials present in automotive vehicles for lightweight purpose after having studied coupled vibro-acoustic problems [161]. Chazot and Guyader [162, 163] use the PTF method to calculate the transmission loss of double panels that can be filled with air or with porogranular materials. The PTF method is also used for the study of micro-perforated panel liners in complex vibro-acoustic environments [164–166]. An inverse PTF method is also studied for source identification applications [167–169]. The convergence of the method was improved by Aucejo *et al.* [170] for the case of strong vibro-acoustic coupling by using residual mode shapes in the cavity when the different subsystems are computed using FEM. In particular, it was found that the criterion yielding 2 patches per acoustic wavelength may not be sufficient in the case of strong coupling. Maxit *et al.* [171] hence propose to partition the subdomains outside the acoustic near-field of the structure to keep the initial criterion for the size of the patches. This work is then applied to the sound transmission from a bulkhead through ballast compartments in a submarine, for which an illustration is proposed in figure 8.

1.3.3.4 The Condensed Transfer Function method

As a generalization of both the CAA and PTF methods, Meyer *et al.* [172] develop a substructuring approach called the Condensed Transfer Function (CTF) method to couple subsystems along lines or surfaces. For the case of a structural system, the displacements and forces at the

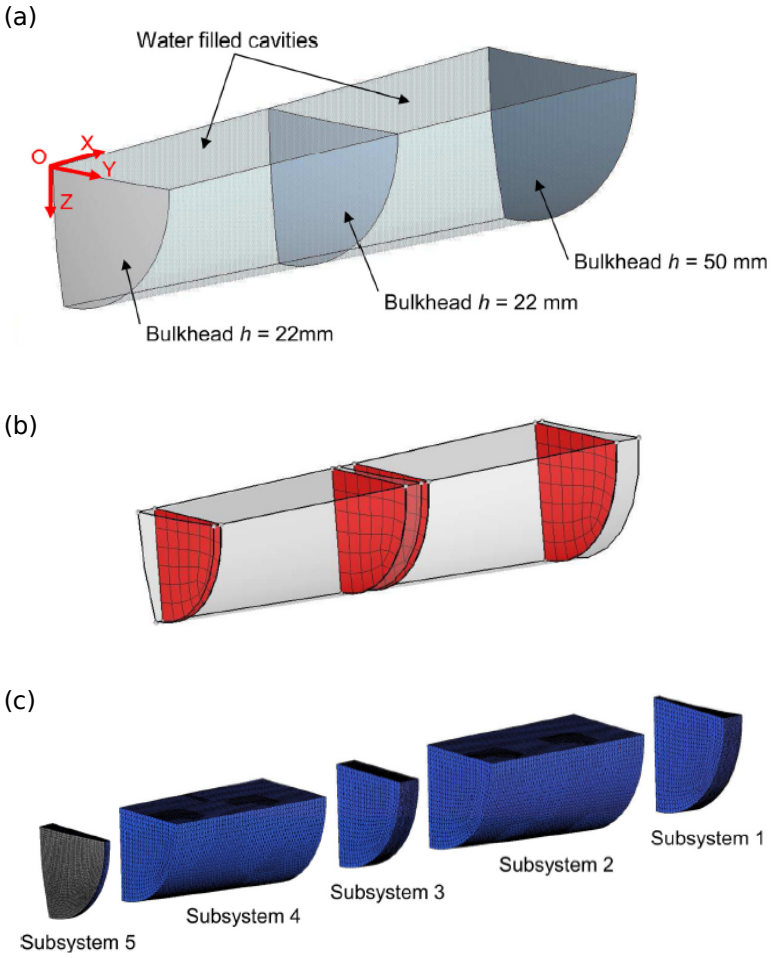

Figure 8: (a) View of the ballast compartments of a submarine hull, separated by bulkheads [171]. (b) Definition of the patches at the different interfaces ballast compartment-bulkhead [171]. (c) FEM model definition of the different subsystems constituting the PTF model [171].

junctions of the subsystems are decomposed into a set of orthonormal functions, called the condensation functions, that can take various forms: gate functions, complex exponentials or Chebyshev polynomials for example. The PTF method can hence be seen as a particular case of the CTF method where the condensation functions are 2D gate functions. It is also more general than the CAA as it can be applied to non-axisymmetric systems. This method will be vastly investigated in this work, and a clear formalism will be developped for the case of acoustic subsystems in section 3.1.

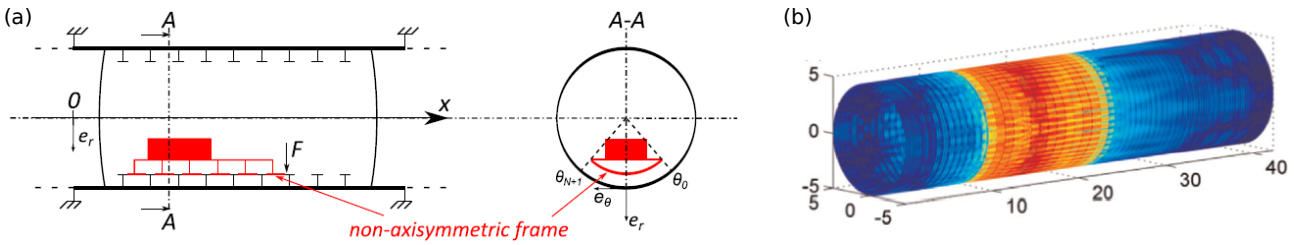

Figure 9: (a) Cylindrical shell stiffened by non-axisymmetric internal frames [173]. (b) Example of radial displacement field at 1000 Hz at the surface of the shell, when a radial point force is applied on a stiffener bounded to the non-axisymmetric frame [173].

The CTF method finds applications in various industrial domains, especially the naval domain where it has been used to study the acoustic radiation [173] and scattering [174] of submerged stiffened cylindrical shells with non-axisymmetric internal substructures such as floors (see figure 9a). The study of the axisymmetric structure can be done using the CAA, while the incorporation of non-axisymmetric internal substructures is taken care of using the CTF method. An example of the radial displacement field at the surface of the shell for a mechanical point force applied on a stiffener is shown at 1000 Hz in figure 9b. Hu *et al.* [175, 176] use the CTF method to model a panel-cavity system in mid and high frequencies. They use complex exponential functions as condensation functions and improve the convergence of the method using a piecewise calculation scheme. Later on, Hu *et al.* [177] also use the CTF method to study double skin façade systems.

1.3.4 Decoupling procedures

While the substructuring methods presented in this chapter are based on the coupling of subsystems, it can sometimes be necessary to decouple subsystems. Such decoupling procedures could be useful to evaluate the effect of a default in a system or to account for complex geometries without having to use computationally intensive methods such as FEM. As far as the author knows, Soedel and Soedel [178] are the first to subtract systems by using a reverse formulation of the admittance method. When measuring transfer functions of an automotive suspension system, their aim is to suppress the contribution of an auxiliary airspring necessary to hold the suspension system in position (see figure 10).

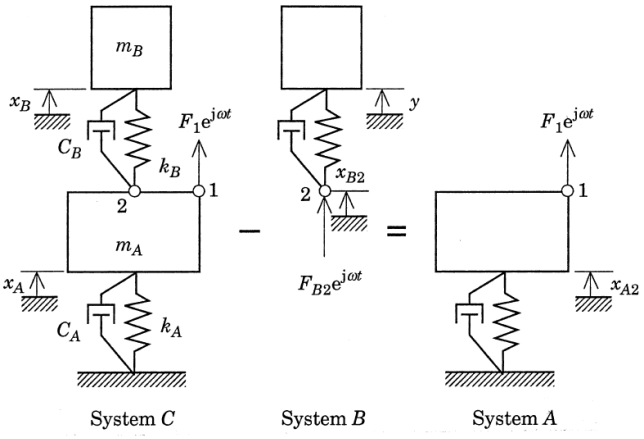

Figure 10: Decoupling in an automotive suspension system [178].

While the examples presented concern discrete systems, they affirm that the receptance subtraction will also work for continuous systems. Gontier and Bensaibi [179] try to identify the influence of bolted or insulating joints in structural elements by subtracting the dynamic behavior of a known part (for example a beam, a plate or a shell) from the measured behavior of the whole structure. The analysis is carried out in the time domain and is called modal

subtracting. It was observed that the procedure was highly sensitive to approximations in the modal description of the known structure, but the results show satisfying performances even for measurement noise levels over 5%.

Decoupling procedures have been widely investigated by D'Ambrogio and Fregolent [180–182] in an experimental context, to estimate the Frequency Response Functions (FRFs) of a part of interest (which will be called subsystem A for the sake of clarity) from the FRFs of the global large system (which will be called system A+B) and a physical model of a part to be removed (which will be called subsystem B). The natural frequencies of the decoupled subsystem A are then deduced. The effect of modal truncation, which is due to the fact that only a limited number of modal parameters can be identified experimentally for the global system A+B, is observed on the accuracy of prediction of the natural frequencies of the decoupled subsystem A. It is found that the number of modes must be correctly chosen because a model truncated to a insufficient number of modes leads to an increase of the predicted natural frequencies. However, in practice, identifying a sufficient number of modes from measurement data can be challenging. Besides, in order to match the Degree of Freedoms (DoFs) of the global system A+B (determined experimentally) and of the removed subsystem B (determined using a FEM model), an expansion of the coupling DoFs of the global system A+B must be performed, and the effect of this expansion on the prediction of the natural frequencies of the decoupled subsystem A is quantified as well. It is important to mention that this study is carried out with point-coupled discrete substructures, and that the final outcome is to determine the natural frequencies of the decoupled subsytem A. There is no emphasis in the vibratory reponse of the decoupled subsystem A at a given point of the subsystem. In [181], they study the drive-point mobility of the decoupled subsystem A at the coupling DoFs from data regarding the global system A+B and the removed subsystem B. They identify that the lack of measured DoFs produces ill-conditioning at the neighbourhood of the natural frequencies. This can be corrected by taking into account internal DoFs of the global system A+B in the measured FRF (i.e. DoFs that are not located at the coupling interface), and the comparison of the decoupling results with a reference calculation for a simple test case exhibits excellent results. In [182], the decoupling problem is revisited in the general framework of frequency based substructuring by adding to the global structure A+B a fictitious subsystem which is the negative of the removed subsystem B that was considered in [180, 181]. A dual domain decomposition is performed by taking into account the total set of DoFs (i.e. the coupling DoFs and the internal DoFs of the global system A+B) in order to predict the drive-point mobility at the coupling DoFs of the decoupled subsystem A. It must be emphasized that the reponses are computed at the coupling DoFs only, and that the response at any point of the decoupled subsystem A is not of interest in these studies.

Still from an experimental point of view, Sjövall and Abrahamsson [183] address the problem of substructure idenfication by performing measurements of a large system A+B in which the system to be identified constitutes the subsystem A. A validation is proposed by reassembling the subsystems A and B and comparing with the initial large system A+B. They identify that the inversion of the problem can exhibit ill-conditioned matrices, which will result in a failed procedure if the frequency of general anti-resonances for the global system A+B appear near a frequency where the removed subsystem B has a regular resonance. This issue can be corrected in the same way as shown by D'Ambrogio and Fregolant [181] by taking non-interface DoFs in addition to the coupling DoFs. Voormeeren and Rixen [184] develop a mathematical framework for the dual formulation of the decoupling problem, before applying it on an academic test case and an experimental case study. These studies are restricted to discrete substructures with point coupling, and the responses are calculated at the coupling interfaces between the subsystems. Tuysuz and Altintas [185] use a similar decoupling procedure for the updating of thin-walled workpiece structures from which material is removed by machining. It is shown that the updated FRFs are predicted 20 times faster than a full order FEM analysis.

In [186], virtual decoupling is performed on vibroacoustical systems. The aim of the paper is to build an equivalent vibroacoustical system capable of representing the same behavior as an experimentally measured one, in order to perform decoupling calculations on this equivalent system. These calculations have the objective of identifying, from the coupled modes of the vibroacoustical system, which modes are governed by the structural or acoustic part. This study is also a means of validating the uncoupled numerical models used in early design stages of vibroacoustical systems. The procedure is based on the identification of the complex modes of the vibroacoustical system, by the use of an extension of the least-square complex frequency-domain to non-symmetrical cases (as the vibroacoustic formulation is non-symmetrical by nature, see for instance Eq. (1.30)). A QR reduction technique is then used in order to reduce the number of DoFs in the system (and hence reduce the calculation costs and complexity of the procedure). The obtained modes are subsequently optimized using the properness enforcement method, and, if necessary, an original mini-FRF method, in order to reduce the sensitivity of the inverse method to measurement noise. Finally, a modal assurance is proposed to filter the redundant modes, and obtain a physical configuration of the structural and acoustic DoFs. The procedure is firstly tested on a simulated case, allowing the idenfication of each step and the potential blocking points of the method. It is then applied on an experimental setup consisting in an acoustic cavity closed by an aluminum plate. The plate is then replaced by a marble cover to have a reference calculation on the acoustic cavity alone, allowing the validation of the proposed procedure. It must be emphasized that

the nature of this work is to identify, in a coupled vibroacoustic system, which modes are governed by the acoustic or structural part of the system. In that sense, the study conducted in [186] differs from the other decoupling studies presented in this section, and from the primary point of interest of the present thesis that will be developed in the next chapters. However, this study gives a significant insight on the potential applications of decoupling procedures in vibroacoustics.

Decoupling procedures have also been addressed from a numerical point of view, for example by Huang and Ting [187] who propose a Reverse Receptance Approach (RRA) similar to the study of Soedel and Soedel [178]. They use this technique to predict the natural frequencies and modes of an annular plate consisting of two circular plates deducted from one another, with several kinds of boundary conditions (figure 11). It is found that the diameter ratio between the initial and deducted plates plays a key role in the convergence of the results, and the errors between the RRA and theoretical calculations remain under 1% when the ratio is under 0.4. Similar studies are conducted by Huang for the analysis of grooved plates [188, 189] or circular holes in rectangular plates [190], or by Cho and coworkers [191, 192] on rectangular plates with arbitrary openings. These studies are also interesting in the fact that they exhibit line coupling and are hence not restricted to discrete subsystems.

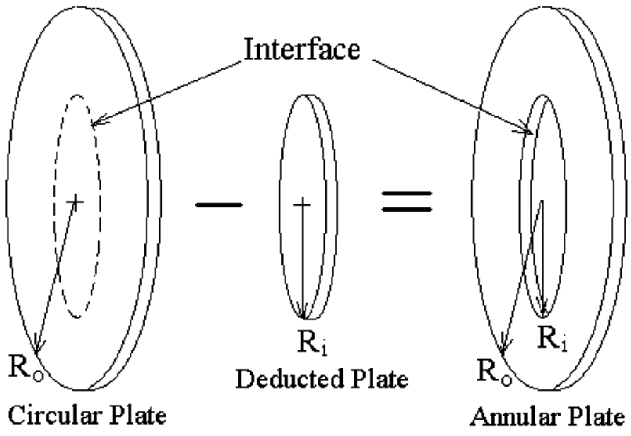

Figure 11: Decoupling of circular plates [187].

1.4 Methodology and document organization

The aim of the present work is to develop a subtractive modelling approach, based on both substructuring and decoupling methods, which can be applied to study the acoustic radiation of a partially coated cylindrical shell immersed in water. Indeed, the literature on fully coated shells is comprehensive, but less attention has been paid to the problem of partial coating, as it has been emphasized in the literature review. Compared to fully coated cylindrical shells, the loss of axisymmetry induced by partial coating makes classical semi-analytical

methods unusable. Element-based methods such as FEM and BEM allow studying such systems, but their substantial computational cost at mid and high frequencies makes them unadapted to an industrial context. On the other hand, substructuring methods have proven to be able to deal with such problems. In particular, the CTF method has shown its ability in coupling non-axisymmetric subsystems, in order to study either mechanical, acoustical or vibroacoustical problems with challenging geometries.

Based on the CTF method and on the concept behind decoupling procedures, a new subtractive substructuring method, called the reverse Condensed Transfer Function (rCTF) method, is developed to decouple systems along lines or surfaces. The main objective of the rCTF method is to be able to predict the response at any point of the decoupled subsystem, and not only at the decoupling interface.

The investigations concerning the development of this new technique have been decomposed into 4 steps, each of which constitutes a chapter of the thesis. A first investigation on subtractive modelling is carried out by considering a 1-D mechanical problem consisting in the decoupling of vibrating rods. The receptances of the decoupled structure are computed from information concerning the initial and removed rods. Two approaches, a local one and a global one, are explored, and the responses at the decoupling point are studied. These investigations are described in chapter 2, and the results are used as a first insight on the potentials of subtractive modelling.

The theoretical formulation of the rCTF method can then be developed, at first for an acoustical problem, and its foundations are laid. On the basis of a reverse formulation of the CTF method, a subtracted subsystem can be removed from a global system, and the procedure to obtain the response at any point of the decoupled subsystem is proposed. As for the CTF method, the rCTF method is based on the definition of condensation functions. These condensation functions are then used to compute the Condensed Transfer Functions (CTFs) of the initial (sub)systems. These developments are presented in chapter 3, in which a first application of the rCTF method is carried out on an academic test case consisting in the scattering of an acoustic plane wave by a rigid sphere in an infinite water medium. The Condensed Transfer Functions are at first computed from analytical models of the initial (sub)systems, with two types of condensation functions investigated. These models can be described either by the local or the global decoupling forms of chapter 2, and both approaches are explored.

If, in chapter 3, the CTFs are computed from analytical models, in practice, numerical models must be considered, especially for the removed subsystem. Differences can then appear between the representations of the initial global system and of the subtracted subsystem, which can induce errors in the response of the final, target subsystem. The procedure to

compute the CTFs from numerical models must hence be developed, in order to evaluate the sensitivity of the method to numerical errors. These investigations are carried out in chapter 4, and applied to the same test case as in chapter 3. The advantages and drawbacks of the local and global rCTF approaches are then discussed in order to select the more relevant one for the industrial application.

Once the theoretical fundaments of the approach have been established, and the method has been applied to several test cases to evaluate its accuracy and sensitivity to model errors, it can be used to study the radiation of a partially coated cylindrical shell immersed in water. To this end, a global system consisting in a fully coated cylindrical shell is considered, from which the missing part of the coating is removed (as illustrated in figure 12). The CTFs of the fully coated cylindrical shell are computed considering a semi-analytical spectral approach, where the shell is described by the Flügge's equations and the coating is modelled as an equivalent fluid having acoustic properties close to decoupling coatings. The CTFs of the missing part of the coating are calculated from a FEM model. These calculations are performed in chapter 5, before re-coupling the obtained decoupled subsystem to a FEM model of the water occupying the missing part of the coating. The influence of partial coating on the radiation from the shell is then discussed for different configurations regarding the position of the excitation and the angular spreading of the coating.

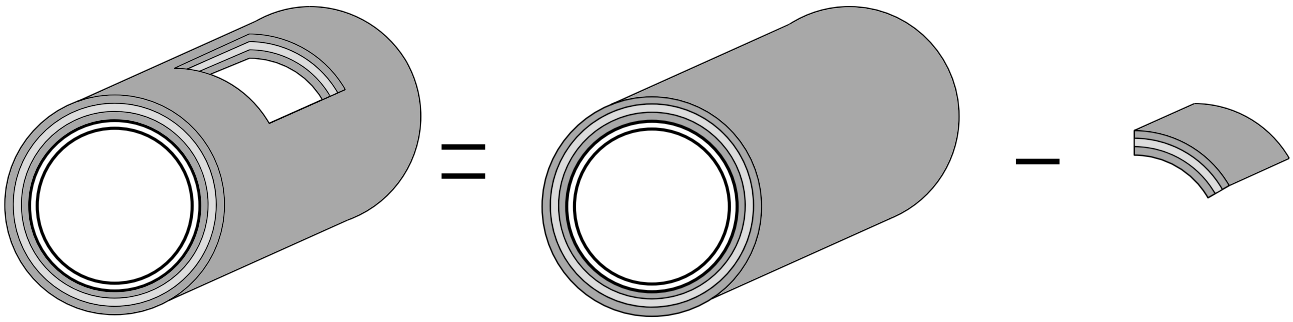

Figure 12: Example of application of the rCTF method: modelling of a partially coated cylindrical shell.

Chapter 2

Subtractive modelling on a one-dimensional mechanical system

In this chapter, a first investigation is carried out on subtractive modelling by exploring the decoupling of a master rod by a subtracted rod using receptance formulations such as in [178]. The principle of this investigation is illustrated in figure 13.

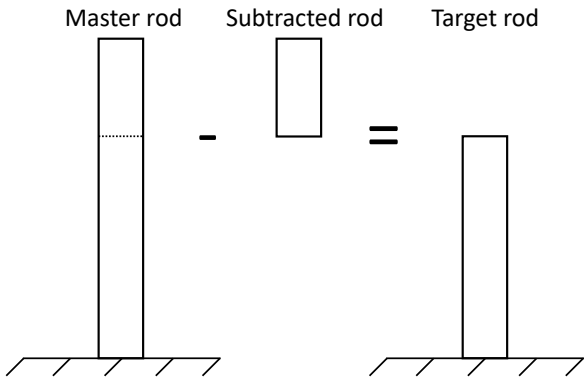

Figure 13: Principle of the decoupling of rods.

The aim of this investigation is to obtain a good insight on the feasibility of subtractive modelling, and its sensitivity to model errors. The focus is brought out on the estimation of the receptances of the target rod from the ones of the master and subtracted ones. Model errors will be introduced by considering 2 types of models to represent the master and subtrated rods: an analytical one and a FEM one. Two formulations are explored in this chapter:

- A local approach where the master rod is disassembled at one of its ends by the substracted rod, leading to a single point-decoupling equation. This approach will be developed in section 2.1.
- A global approach where the master rod is disassembled at an intermediary position by the subtracted rod, leading to a matrix decoupling formulation. This approach will be developed in section 2.2.

A part of this chapter is based on the article "First investigations on subtractive modeling with the condensed transfer functions method", published in *Forum Acusticum, Dec 2020, Lyon, France*.

2.1 First approach: local decoupling

2.1.1 Direct and reverse formulations of the receptance approach

Let us consider three vibrating elastic rods as shown in figure 14, only subjected to traction and compression. The rod 1+2 consists in the assembling of the rods 1 and 2. One of its ends is supposed clamped whereas the other one is free. The direct formulation of the receptance approach consists in writing the receptance μ_{11} of the rod 1+2 at the point 1 from the receptances α_{11} and β_{11} of the rods 1 and 2, respectively, at the same point.

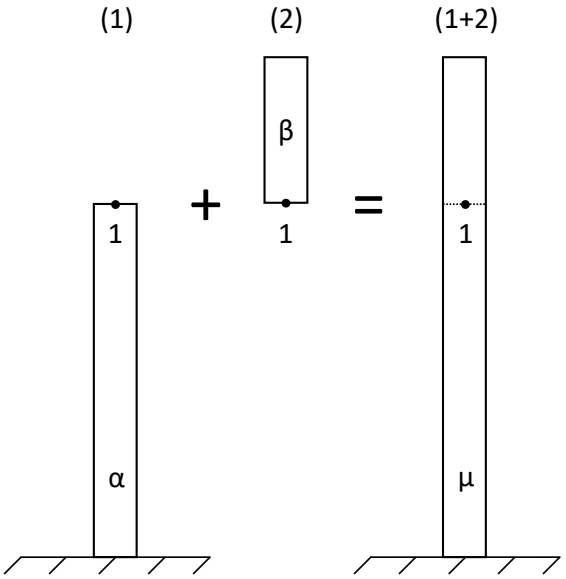

Figure 14: Coupling of rods.

It is reminded that the receptance of the rod 1+2, μ_{ij}, represents the ease of motion of the structure at point i when it is subjected to a harmonic point force at point j

$$\mu_{ij} = \frac{U_i}{F_j} \tag{2.1}$$

where F_j is the amplitude of the harmonic longitudinal force applied at point j at the angular frequency ω and U_i is the amplitude of the longitudinal displacement response at point i. One has to keep in mind that μ_{ij} is a complex value, taking into account the phase shift between the force at point j and the displacement at point i. When the points i and j are the same, the receptance is referred to as "direct receptance" while it is referred to as "cross receptance" when they differ.

Based on the reciprocity principle [193], the receptances are symmetric, which means that they remain the same if the point of excitation and the point of response are exchanged: $\mu_{ij} = \mu_{ji}$. The definition of the receptances, which has been presented here for the master rod is extended for the receptances of the rod 1 and 2, α_{ij} and β_{ij}, respectively.

In order to obtain the receptance μ_{11} as a function of α_{11} and β_{11}, a harmonic longitudinal force, F_1^{1+2}, is prescribed at point 1 of the rod 1+2. The longitudinal displacement at the same point, U_1^{1+2} should then be evaluated by assembling the rods 1 and 2. As a first step, we consider that the two rods are uncoupled. The longitudinal forces, F_1^1 and F_1^2 are supposed to be applied at point 1 on each of the two rods 1 and 2, respectively. Taking into account the linear vibratory behavior of the rods, the displacements at point 1 for these two rods can be written

$$\begin{cases} U_1^1 = \alpha_{11} F_1^1 \\ U_1^2 = \beta_{11} F_1^2 \end{cases} \tag{2.2}$$

As a second step, the displacement continuity and force equilibrium between the two rods at the coupling point yield the following relations

$$\begin{cases} U_1^1 = U_1^2 = U_1^{1+2} \\ F_1^1 + F_1^2 = F_1 \end{cases} \tag{2.3}$$

Introducing Eq. (2.2) in Eq. (2.3), we can deduce

$$U_1^{1+2} = \frac{\alpha_{11}\beta_{11}}{\alpha_{11} + \beta_{11}} F_1 \tag{2.4}$$

and then the receptance of the rod 1+2 as a function of α_{11} and β_{11} is inferred

$$\mu_{11} = \frac{\alpha_{11}\beta_{11}}{\alpha_{11} + \beta_{11}} \tag{2.5}$$

Now, let us consider the decoupling problem as illustrated in figure 15. It consists in estimating the receptance α_{11} of the rod 1 from the ones of the rod 1+2, μ_{11}, and of the rod 2, β_{11}. In what follows, rod 1 will be referred to as "target rod", whereas rods 2 and 1+2 will be referred to as "subtracted rod" and "master rod", respectively, as in figure 13. For our basic system, α_{11} is obtained straightforwardly by inverting Eq. (2.5)

$$\alpha_{11} = \frac{\beta_{11}\mu_{11}}{\beta_{11} - \mu_{11}} \tag{2.6}$$

With this operation, has been established the principle of the local decoupling where only two quantities are needed for the calculation of α_{11}: the receptance at the point 1 of the master rod and the receptance at the point 1 of the subtracted rod. Under the considered assumptions, the proposed calculation with Eq. (2.6) is exact. However, in practice, the receptances μ_{11} and β_{11} are not necessarily estimated with the same calculation process. Some differences

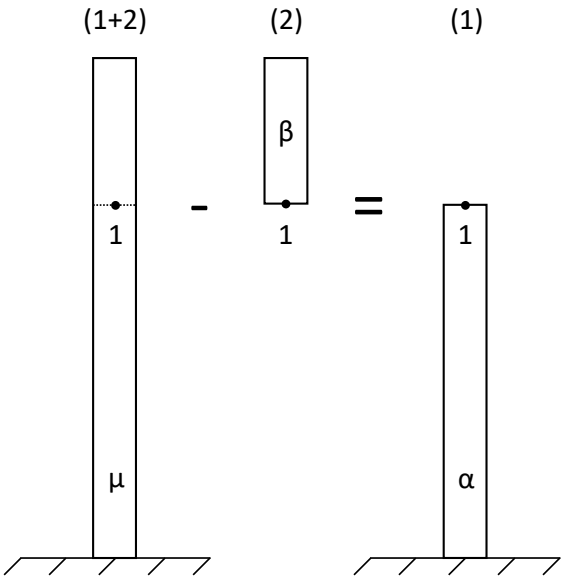

Figure 15: Decoupling of rods.

between the two models considered for these calculations can be introduced. The goal of the following investigations is to estimate the impact of these model errors on the decoupling accuracy and to highlight the parameters allowing to reduce the sensitivity to these errors.

2.1.2 Test case parameters and calculation of the receptances

The mechanical characteristics and dimensions of the nominal rods for the numerical applications are given in the table 1. The structural damping is introduced in the modelling through a complex Young's modulus: $E^* = E(1 + j\eta)$.

Parameter	**Notation**	**Value**	**Unit**
Young modulus	E	210	GPa
Poisson coefficient	ν_s	0.3	-
Density	ρ_s	7800	kg/m^3
Structural damping coeff.	η_s	0.02	-
Celerity of long. waves	c_s	6020	m/s
Length of the target rod 1	L_1	3	m
Length of the subtracted rod 2	L_2	0.8	m
Length of the master rod 1+2	L_{1+2}	3.8	m
Section of the rods	S	0.05^2	m^2

Table 1: Mechanical characteristics and rod dimensions.

By comparing the results of the decoupling approach in Eq. (2.6) with an analytical calculation of the receptance of the target rod, we will be able to estimate the accuracy of the technique. Two processes for estimating the receptances of the master rod and the subtracted rod used in the decoupling technique will be considered in the following:

- the first one consists of an analytical calculation based on the forced wave decomposition approach as described in [194]. This approach is exact in the sense that the equations of motion of the rod as well as the boundary conditions are strictly verified if the assumptions of the theory are verified.

- the second is based on a FEM simulation. The rod is decomposed in a certain amount of 1-dimensional rod elements and the forced response corresponding to the receptance is obtained by a direct analysis in the FEM Structural Dynamic toolbox implemented in MATLAB® [195]. The accuracy of the response depends on the element size. This approach can be qualified as approximate in opposition to the exact analytical calculation.

Several combinations of these processes for evaluating β_{11} and μ_{11} are possible:

- the first one consists in considering an analytical calculation for both receptances. The good agreement between this calculation and the reference one that was observed allowed us to numerically validate Eq. (2.6) and the analytical calculations of the different receptances (results not shown here). The expressions of these receptances for the three rods are given in Appendix B.

- the second one consists of considering a FEM simulation for both receptances. The good accuracy of this solution compared to the reference results validated the numerical process for estimating the receptances (results not shown here). They were calculated in the frequency band [100, 10000] Hz, with 2000 values logarithmically spread over the domain in order to describe properly the resonances and anti-resonances of the rods. The size of the finite elements was 0.1 m in order to satisfy the criterion of at least 6 elements per longitudinal wavelength at 10000 Hz, and the mesh was applied regularly along the rods. In the following, these calculation characteristics will still be considered.

- the last one that will be of interest for our study consists of considering the analytical model for the receptance of the master rod while the FEM model is used to estimate the receptance of the subtracted rod. These results will be analyzed in the next section.

2.1.3 Results

In the following, we show and discuss different results concerning the decoupling of the analytical model of the master rod with the FEM model of the subtracted rod. Let us start by comparing the receptance α_{11} obtained by decoupling with the reference analytical calculation as shown in figure 16a. The relative error made on α_{11}, calculated using the analytical reference result, is also shown in figure 16b.

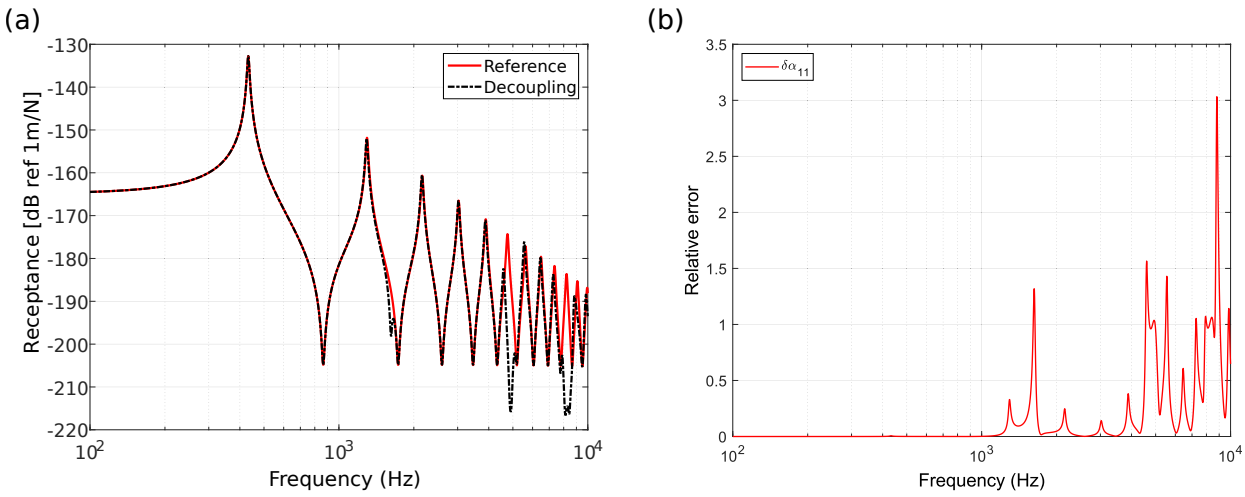

Figure 16: (a) Receptance α_{11} obtained by decoupling. (b) Relative error on α_{11}.

The results show a good fit between the two curves in the main part of the frequency range. Some discrepancies can however be observed around 1600 Hz, 4800 Hz and 8200 Hz, and they appear clearly when looking at the relative error in figure 16b. These discrepancies were not obtained when the receptances of the subtracted rod were calculated analytically. The cause of these errors will be investigated in the next section in order to assess the method's sensitivity to model errors.

2.1.3.1 Analysis of errors

As the analytical calculation serves as a reference and the receptance of the master rod has been calculated analytically, there are no model errors on μ_{11}. The model errors hence rely only on the subtracted rod. From the expression of α_{11} given in Eq. (2.6), we can derive the small variations of α_{11} due to the small variations of β_{11}

$$\delta\alpha_{11} = -\frac{\mu_{11}^2}{(\beta_{11}-\mu_{11})^2}\delta\beta_{11} \tag{2.7}$$

From Eq. (2.7), we can deduce that there are two critical conditions that induced significant errors on α_{11}:

- as could be expected, the first condition is when the errors on β_{11}, namely $\delta\beta_{11}$, are high.

- the second condition is when β_{11} is close to μ_{11}, and μ_{11} is non-zero.

As it was observed in figure 16 that the errors on α_{11} are the highest around the three mentioned frequencies (i.e. 1600 Hz, 4800 Hz and 8200 Hz), one could expect that at least one of the two conditions previously evoked are satisfied at these frequencies. The relative error on β_{11} is shown in figure 17a, while the receptances β_{11} and μ_{11} are plotted in the figure

17b, both in terms of amplitude and phase. As a comparison, the receptance β_{11} is presented for the two calculations (analytical and FEM modelling), while only the analytical value is presented for the receptance μ_{11}.

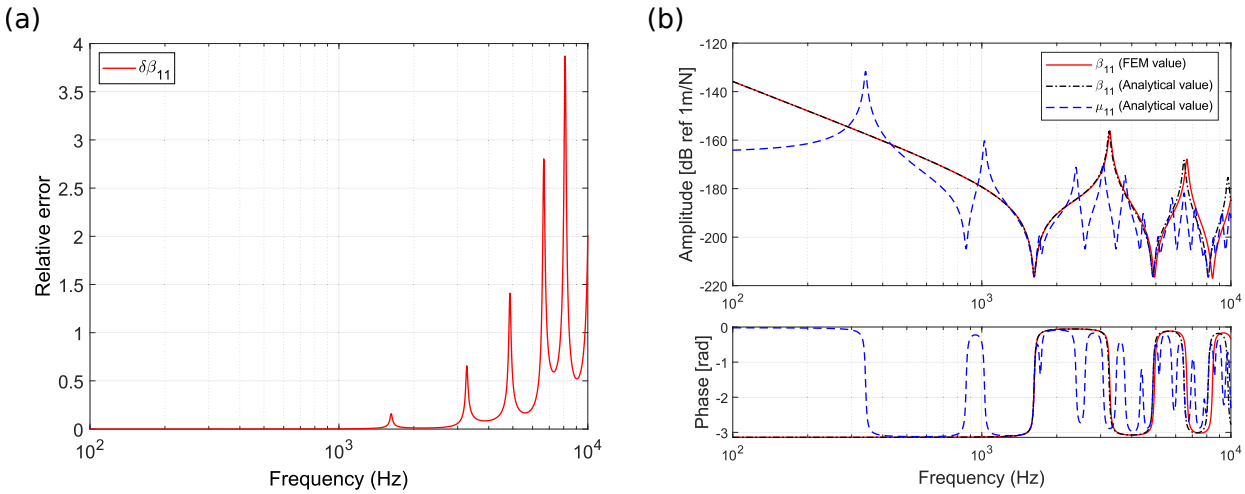

Figure 17: (a) Relative error on β_{11}. (b) Comparison between β_{11} and μ_{11}.

From figure 17, we can deduce that the two critical conditions are indeed satisfied at the three incriminated frequencies, which explains the errors observed in figure 16. In figure 17a, we notice that the model errors on β_{11} are significant for the resonant frequencies and the anti-resonant frequencies (due to a slight shift of the frequencies between the analytical and FEM calculations). Furthermore, the figure 17b shows that all the anti-resonant frequencies of β_{11} are also anti-resonant frequencies for μ_{11}, which means that the receptances of the two beams are equal or close in the relatively small frequency ranges surrounding these anti-resonant frequencies. On the contrary, at the resonant frequencies of β_{11}, even if the error on β_{11} is significant, the receptances β_{11} and μ_{11} are very different, which explains why there is no apparent error made on α_{11}. Besides, there are some frequencies for which the curves of β_{11} and μ_{11} cross each other (i.e. 960 Hz and 3870 Hz), but for which there are no signficant errors made on α_{11}. This can be explained by the fact that the errors on β_{11} are relatively small for these frequencies as they do not correspond to resonant or anti-resonant frequencies.

In conclusion, the errors on α_{11} are significant when the two critical conditions described above are fulfilled, and this corresponds to the anti-resonant frequencies of the subtracted rod. It should be emphasized that regarding the figure 17a, the relative error on β_{11} can be quite high, meaning that the hypothesis of small variations of β_{11} is not always verified. Nevertheless, the analysis carried out in this section gives a good insight on the sources of errors of the decoupling method.

One solution for reducing the errors on α_{11} consists in limiting the numerical errors on β_{11} by considering a finer mesh for the FEM model. As the subtracted rod is relatively small

and the original FEM model is not too large in terms of degrees of freedom, refining the mesh would not affect significantly the calculation time. However, this solution would not be well adapted for more complex cases. Alternatively, the errors on α_{11} will be small if β_{11} and μ_{11} are significantly different. In the following two sections, we are going to investigate the influence of both the length of the subtracted rod and the structural damping.

2.1.3.2 Influence of the length of the subtracted rod

From the previous observations, it can be expected that the length of the subtracted rod plays a key role on the errors made on the receptances of the target rod when the decoupling is done because the anti-resonances of the subtracted rod are incriminated.

The receptances β_{11} (computed with FEM modelling) and μ_{11} (computed using the analytical solution) are compared in figure 18 for two new lengths of the subtracted rod: $L_2 = 0.3$ m and $L_2 = 1.3$ m, while L_1, the length of the target rod, is kept unchanged. It can be observed that when the subtracted rod is 1.3 m long, its receptance β_{11} has 5 anti-resonances in common with μ_{11} whereas the receptance of the 0.3 m long subtracted rod has only 1 anti-resonance in common with μ_{11}.

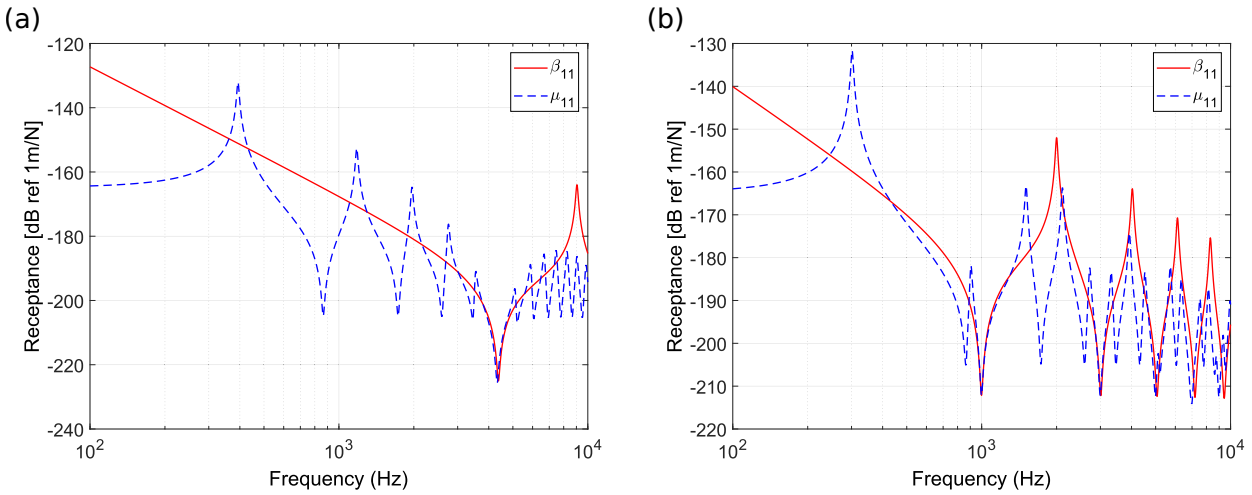

Figure 18: Comparison of β_{11} and μ_{11} for two different lengths of the subtracted rod. (a) L_2=0.3 m. (b) L_2=1.3 m.

As a result, the decoupling with the 1.3 m long subtracted rod exhibits more critical frequency domains than the one with the 0.3 m long subtracted rod as it can be observed in figure 19, where the relative errors on α_{11} have been plotted as a function of frequency. The subtracted rod studied in section 2.1.3 was also added to this figure ($L_2 = 0.8$ m). These critical frequency domains correspond to the mutual anti-resonances of the master and subtracted rods as already observed for the initial case in figure 16. We can emphasize that for these new calculations, the length of the master rod has been adapted such that the length of the target rod remains unchanged.

To have an overview on the errors on α_{11}, the mean value of the relative errors over the whole frequency range were calculated for the three subtracted rod lengths (0.3 m, 0.8 m and 1.3 m). We obtain 9.6%, 14.7% and 18.1%, respectively, which means that there is a clear trend showing that the errors on α_{11} are higher when the subtracted rod is longer.

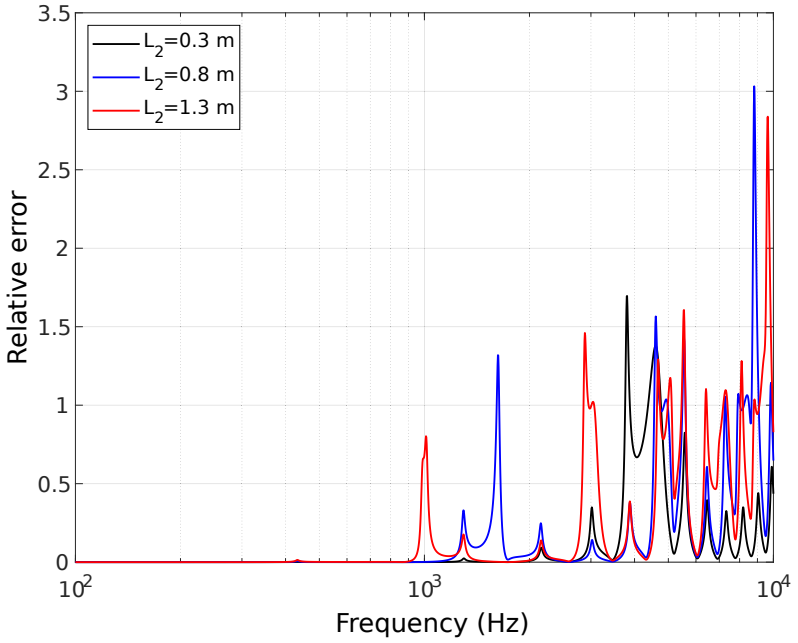

Figure 19: Relative error on α_{11} for several lengths of the subtracted rod.

2.1.3.3 Influence of structural damping

Another alternative to avoid errors on α_{11} is to modify the amplitude of the anti-resonances such that the influence of the common anti-resonances between the two rods will be reduced. A way of achieving this aim is to increase the structural damping of the rods. Hence, the calculations made previously were reiterated with a structural damping coefficient of 20% (i.e. $\eta_s = 0.2$) against 2% (i.e. $\eta_s = 0.02$) previously. The geometrical parameters of the rods are the ones of the nominal case defined in table 1.

The receptance α_{11} obtained with the 20% structural damping coefficient is displayed in figure 20a and shows that the reference and decoupling curves fit much better than in figure 16. There are still errors around the anti-resonant frequencies of β_{11}, but these errors are much smaller than the ones with the 2% structural damping coefficient. Figure 20b shows the relative error made on α_{11} with the two different values of the structural damping coefficient. It can be seen that the maximum error is 10 times smaller. Also, the mean relative error in the whole frequency range of interest, which is of 4.9%, has been divided by 3 when the structural damping coefficient is increased by a factor 10.

With the same geometrical and mechanical parameters (except the structural damping

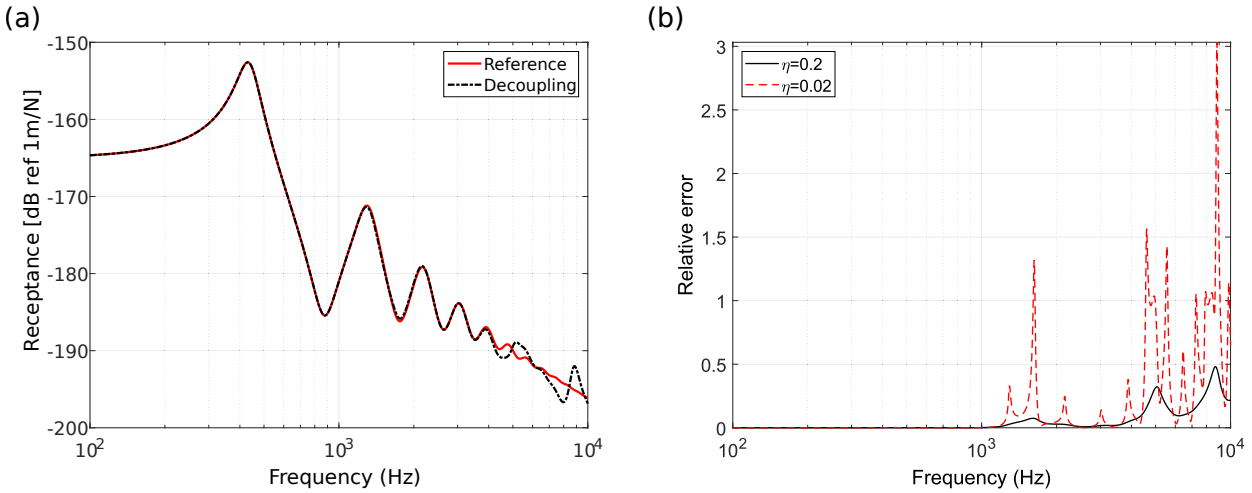

Figure 20: (a) Receptance α_{11} obtained by decoupling. (b) Relative error on α_{11} with two different values of the structural damping coefficient.

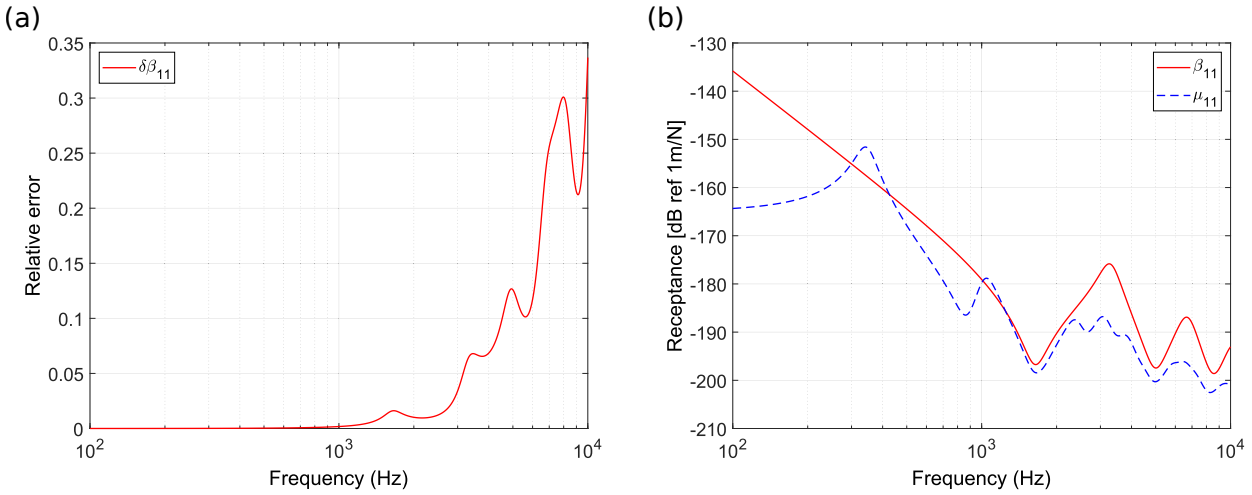

Figure 21: Sources of errors with a higher structural damping coefficient. (a) Absolute error on β_{11}. (b) Comparison between β_{11} and μ_{11}.

coefficient) and the same mesh size, it is interesting to note that in figure 21a, the model errors on β_{11} have been reduced by a factor 10. Also, in figure 21b, around the anti-resonant frequencies, the values of the receptances are not as close to each other as they are in figure 17b. This means that even when the two critical conditions are satisfied, the error made on α_{11} is limited, as can be seen in figure 20b. The amplitude of the relative error is also much lower, even at frequencies where the two critical conditions are not necessarily satisfied.

To conclude this section, we can emphasize that the results obtained with this local decoupling approach have shown that the sensitivity of the method to model errors is influenced by the length of the subtracted rod and the structural damping of the different rods. However, for the practical applications of the subtractive modelling, the geometrical and mechanical properties of the master and target structures will be fully defined. It will hence not be possible to change the dimensions nor the structural damping coefficient of

the subtracted structure to reduce the sensitivity to model errors, considering this local decoupling approach. To circumvent this issue, in the next section, we focus on another reverse formulation of the receptance approach.

2.2 Second approach: global decoupling

2.2.1 Principle

Let us now consider the new decoupling problem presented in figure 22a. Instead of decoupling the master rod at one of its ends, it is disassembled at an intermediary position by the subtracted rod. As a result, the decoupling process will exhibit two different rods. The part below the coupling point 1 corresponds to the target rod as in section 2.1 whereas the part above the coupling point 2 will not be of interest in the following. With such a decoupling process, we will be able to modify the length of the subtracted rod without modifying the length of the part of interest. Indeed, if the position of the point 1 is considered as fixed, only the length of the part which is not of interest will change when the subtracted rod's length changes.

The coupling problem associated to the new decoupling process is shown in figure 22b. The equations associated to this coupling problem will be presented before being reversed to exhibit the decoupling problem.

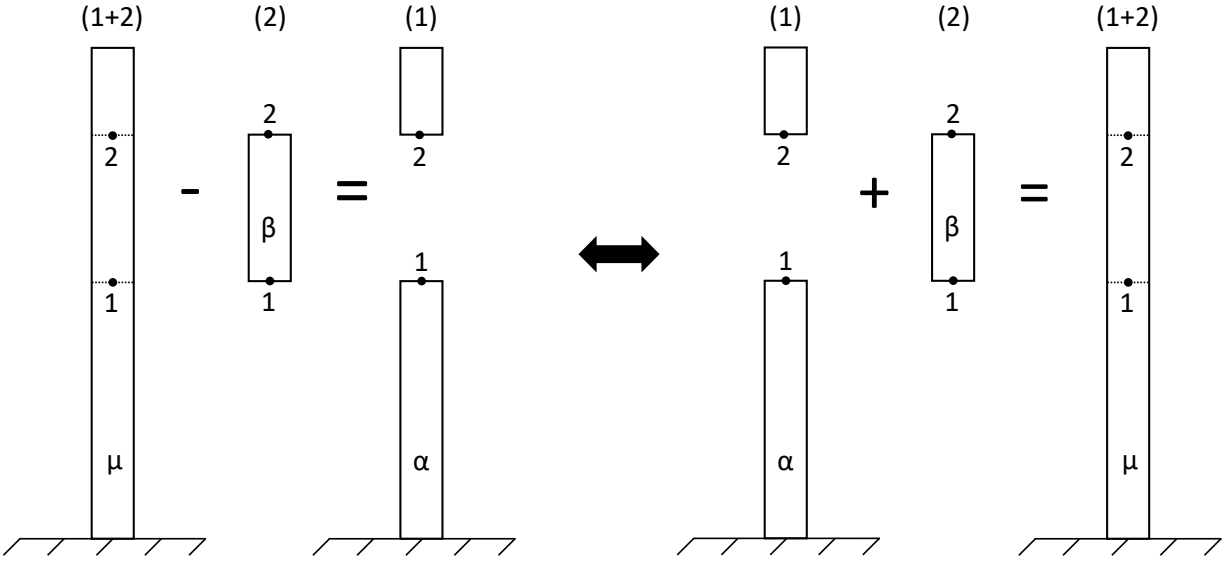

Figure 22: (a) Decoupling at an intermediary position of the master rod by a subtracted rod. (b) Coupling problem associated to the decoupling one.

As the problem exhibits two coupling points, each rod is characterized by receptance matrices to account for the direct receptances at points 1 and 2, and for the cross receptance be-

tween point 1 and point 2. The receptance matrices for the rods 1, 2, and 1+2, are respectively defined by

$$\mathbf{A} = \begin{bmatrix} \alpha_{11} & \alpha_{12} \\ \alpha_{12} & \alpha_{22} \end{bmatrix}, \qquad \mathbf{B} = \begin{bmatrix} \beta_{11} & \beta_{12} \\ \beta_{12} & \beta_{22} \end{bmatrix}, \qquad \mathbf{M} = \begin{bmatrix} \mu_{11} & \mu_{12} \\ \mu_{12} & \mu_{22} \end{bmatrix}, \tag{2.8}$$

Their expressions for the analytical model are given in Appendix B whereas the same process as the one described in section 2.1 is used to extract them from the FEM model.

In order to derive the receptance matrix of the master rod as a function of those of the target and subtracted rods, a unitary harmonic longitudinal force is prescribed successively at the coupling points 1 and 2. At first, let us suppose that the unit force is applied at point 1. The force vector is then defined by

$$\mathbf{F} = \begin{bmatrix} 1 \\ 0 \end{bmatrix} \tag{2.9}$$

The displacement vectors (containing the displacements at the point junctions) associated to the two rods can be written as a function of the receptance matrix and the force vector (considering the superposition principle for linear passive systems). On another hand, the displacement continuity and force equilibrium at the junction can be written with the displacement and force vector quantities. It yields

$$\begin{cases} \mathbf{U_1} = \mathbf{A}\mathbf{F_1} \\ \mathbf{U_2} = \mathbf{B}\mathbf{F_2} \\ \mathbf{U_{1+2}} = \mathbf{U_1} = \mathbf{U_2} \\ \mathbf{F} = \mathbf{F_1} + \mathbf{F_2} \end{cases} \tag{2.10}$$

where $\mathbf{U_\zeta}$ represents the displacement vector of rod ζ, and $\mathbf{F_\zeta}$ corresponds to the applied force vector on rod ζ (ζ stands for 1, 2 or 1+2). The resolution of this system of equations gives

$$\mathbf{U_{1+2}} = \mathbf{A}(\mathbf{A}+\mathbf{B})^{-1}\mathbf{B}\mathbf{F} \tag{2.11}$$

$\mathbf{U_{1+2}}$ contains the displacements at the coupling points for the master rod when excited by a unit point force at point 1. It corresponds then to the first column of the receptance matrix $\mathbf{M}$ of the master rod. Repeating the process for a force applied at point 2, we deduce the expression of the receptance matrix $\mathbf{M}$

$$\mathbf{M} = \mathbf{A}(\mathbf{A}+\mathbf{B})^{-1}\mathbf{B} \tag{2.12}$$

As in the section 2.1, the decoupling problem is derived from the coupling problem by inverting Eq. (2.12). The receptance matrix $\mathbf{A}$ of the targeted rod is then written

$$\mathbf{A} = \mathbf{B}(\mathbf{B}-\mathbf{M})^{-1}\mathbf{M} \tag{2.13}$$

We can notice that this expression has the same form than the one derived in Eq. (2.6), but with matrices instead of single values. In the following sections, the general decoupling formula of Eq. (2.13) is going to be used to obtain the receptances α of the target rod, but ultimately only the receptance α_{11} will be of interest for us, as it was the initial quantity of interest of the study. In theory, α_{12} and α_{21} will be null as there is no physical coupling between the two points on the target rod. It must hence be checked that the values given by the decoupling technique concerning these quantities are negligible compared to the direct receptances, α_{11} and α_{22}. The material characteristics are the same than those of table 1, and the dimensions of the rods are given in table 2. One has to be aware that, now that the rod 1 is composed of two parts, L_{11} refers to the lower part of the rod (which is of interest, and remains the target rod), while L_{12} refers to the upper part of the rod, and will be refered to as "residual rod".

Length of the target rod	L_{11}	3	m
Length of the residual rod	L_{12}	0.3	m
Length of the subtracted rod 2	L_2	0.5	m
Length of the master rod 1+2	L_{1+2}	3.8	m
Section of the rods	S	0.05^2	m^2

Table 2: Dimensions of the rods.

It should be noted that the size of the master rod as well as the position of the coupling point 1 have been chosen to be the same than in section 2.1, so that the comparison between the two studies remains relevant.

2.2.2 Results

The decoupling process was achieved using Eq. (2.13) and the receptance matrix of the master rod **M** calculated analytically (see B.2.1), whereas those of the subtracted rod **B** were computed by FEM simulation as in section 2.1. The results in terms of α_{11} are shown in figure 23a, while the amplitudes of the receptances β_{11} (computed analytically and with FEM modelling) and μ_{11} are presented in figure 23b.

Figure 23a shows discrepancies around 5500 Hz for α_{11}, and contrary to the observations made in the section 2, these discrepancies do not appear around the anti-resonant frequency of the subtracted rod. According to figure 23b, it can be stated that the discrepancies tend to appear around the resonant frequency of the subtracted rod which is 5271 Hz. We can also observe, as it could be expected, that the receptances β_{11} and μ_{11} do not present common anti-resonances as it was the case in section 2.1, because the subtracted rod is no longer located at the extremity of the master rod. On the other hand, the cross receptances α_{12} and α_{21} obtained by the decoupling technique present values significantly lower than those of α_{11}

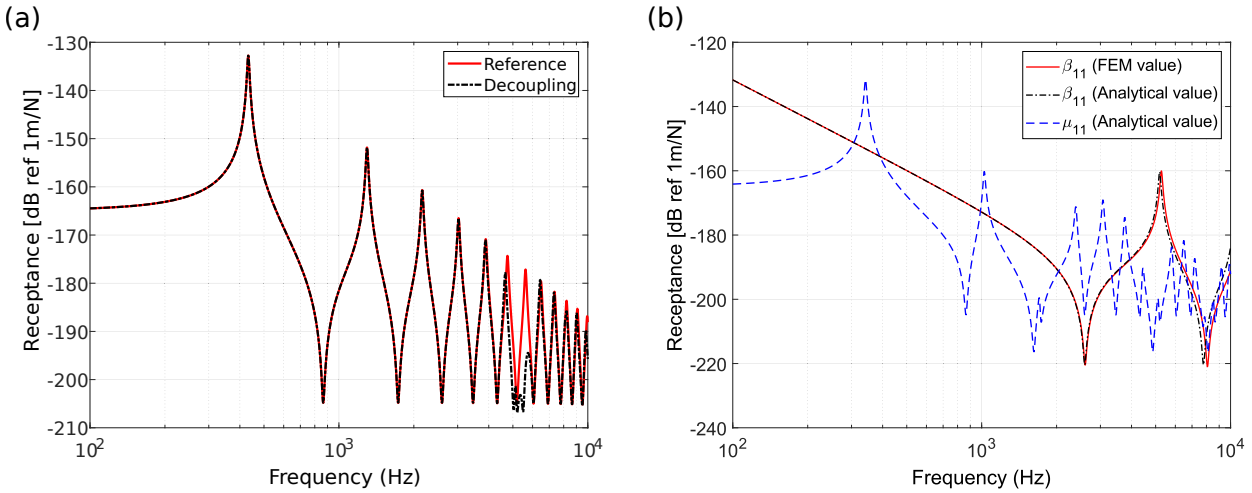

Figure 23: (a) Comparison of α_{11} between Eq. 2.13 and the reference analytical calculation. (b) Amplitude of the receptances β_{11} and μ_{11}.

(i.e. between -280 dB and -220 dB, except for few frequencies corresponding to maxima of the relative error). These non-null cross receptances are the results of numerical errors, but they express well that the points 1 and 2 are not physically coupled in the subsystem 1.

The decoupling formula of Eq. (2.13) involves the inversion of the matrix $\mathbf{B} - \mathbf{M}$. This inversion can amplify the numerical discrepancies related to the model errors and lead to the errors observed in figure 23a. The sensitivity of this matrix inversion to numerical errors can be characterized by the condition number, which corresponds to the ratio between the highest of the two eigenvalues of the matrix over the lowest one. The condition number of the receptance matrices $\mathbf{B}$, $\mathbf{M}$, and $\mathbf{B} - \mathbf{M}$, are shown in figure 24a. The relative error on α_{11} is also presented in figure 24b, in order to investigate the relation between a potentially high condition number of the inverted matrix $\mathbf{B} - \mathbf{M}$ and a significant relative error on α_{11}. As there are no apparent errors below 1000 Hz in figure 23a, the curves in figure 24 are plotted only above 1000 Hz for a better clarity.

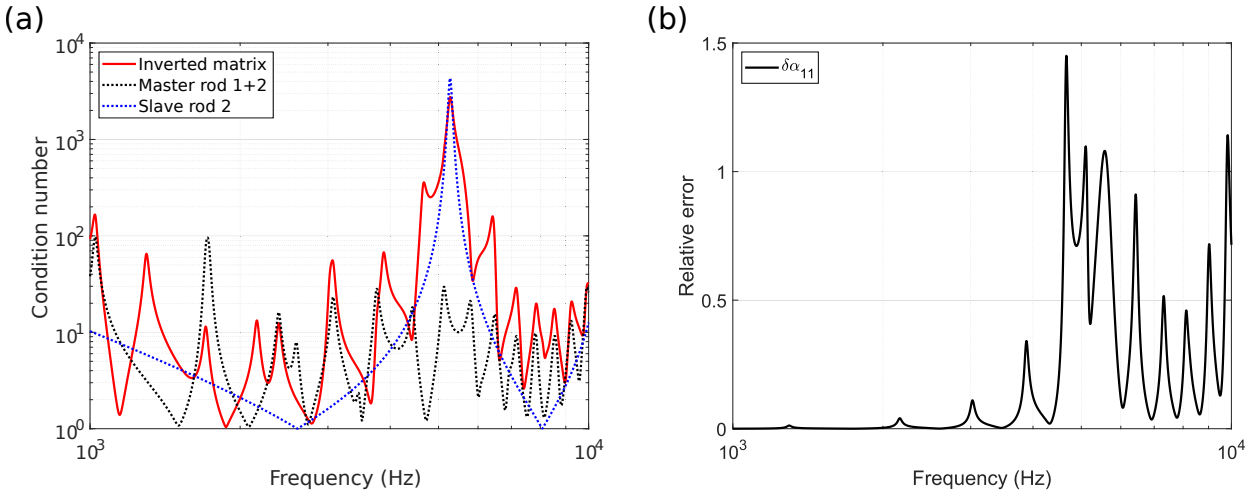

Figure 24: (a) Condition number of the receptance matrices. (b) Relative error on α_{11}.

The red curve displayed in figure 24a, corresponding to the inverted matrix, shows that there is a frequency domain between 4600 Hz and 6500 Hz where the condition number is relatively high (i.e. greater than 100). This high condition number can be associated to the ill-conditoning of the matrix **B** for frequencies close to the resonant frequency, 5271 Hz (see the blue curve). In addition, as previously shown in section 2.1.3.1, model errors on the receptances of the subtracted rod are the most significant at the resonant and anti-resonant frequencies of the rod. As a result, the ill-conditioning of the inverted matrix amplifies the model errors committed on the receptances of the subtracted rod at frequencies close to its resonances. This may explain the important relative errors on α_{11} in figure 24b in the frequency band [4600 - 6500] Hz. For frequencies higher than 6500 Hz, the relative errors observed in figure 24b remain significant. However, these errors can be associated to slight frequency shifts in the prediction of α_{11} as it can be observed in figure 23a.

It has been observed here that the global decoupling technique leads to significant discrepancies compared to the reference for frequencies close to the resonant frequency of the subtracted rod. This contrasts with the local decoupling technique studied in section 2.1 which exhibited significant discrepancies for frequencies close to the anti-resonant frequencies of the subtracted rod. In order to investigate in further details this difference, we are going to study in the next section the results of the global decoupling technique when the length of the residual rod tends towards zero (i.e. when the subtracted rod moves to the extremity of the master rod). We can wonder if the results of the local decoupling technique, which supposes a decoupling at one end of the master rod, can be found to be an asymptotic case of the global decoupling technique.

2.2.3 Influence of the length of the residual rod

In the following, the length of the subtracted rod has been set to L_2=0.8 m as in section 2.1. This choice is motivated by the fact that this length allows the presence of several resonant (i.e. 3264 Hz and 6651 Hz) and anti-resonant frequencies (i.e. 1624 Hz, 4941 Hz and 8433 Hz) in the frequency range of interest (see figure 17b), thus allowing a better potential of analysis than with a shorter rod.

In figure 25, the condition number and the relative error on α_{11} as a function of frequency and of the length L_{12} are shown. The length L_{12} is varying between 1 cm and 1.5 m (with a logarithm scale), and since the position of the coupling point 1 has not changed, it means that the size of the master rod also varies in this study. The red dashed lines correspond to the resonant frequencies of the subtracted rod, while the white dashed lines correspond to the resonant frequencies of the residual rod. In figure 25b, the scale of the plot was reduced to a maximum relative error of 5. Even if larger errors can appear, the interest of the present

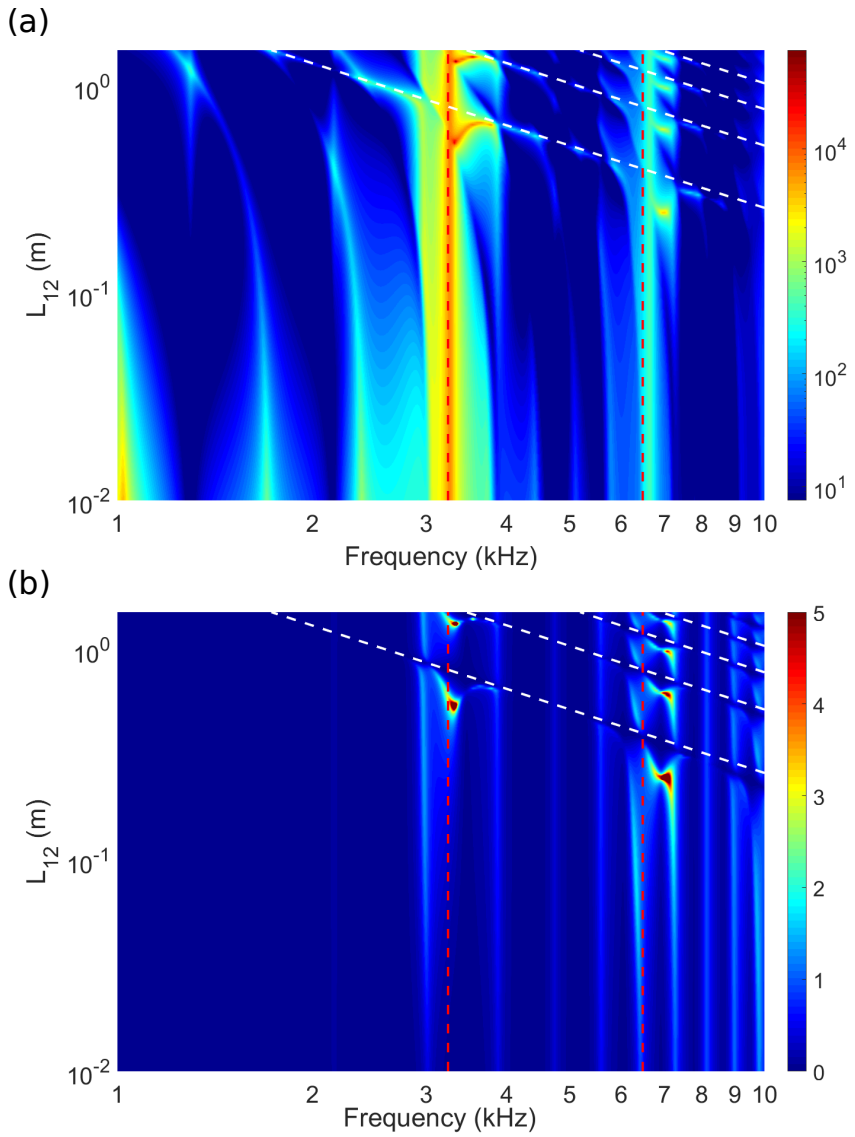

Figure 25: Asymptotic study - (a) Condition number of the inverted matrix. (b) Relative error on α_{11}.

study relies on the frequency localization of the maximum errors rather than their values (when they are large). The tendencies observed on these two figures seem to remain the same, regardless of the position of the subtracted rod. The condition number of the inverted matrix keeps maximum values at the resonances of the subtracted rod which are 3264 Hz and 6651 Hz. Equivalently, the main errors on α_{11} are located around these resonances of the subtracted rod. This phenomenon tends to stay the same when L_{12} gets closer to zero, even if a decrease of the errors may be observed. Also, it is interesting to notice that the diagonal patterns that tend to appear following the maxima of relative errors are parallel to the resonances of the residual rod (see the white dashed lines). This means that there is a correlation between the errors of the global decoupling technique and the presence of resonances of the residual rod. This phenomenon explains the fact that when the residual rod is too short to have any resonance in this frequency domain, the errors are much lower. We

can also underline that the other frequencies at which moderate errors are observed when L_{12} is small correspond to resonances of the master rod. However, no particular error seems to appear at the anti-resonant frequencies of the subtracted rod when L_{12} tends towards zero. This is particularly highlighted in figure 26 showing the amplitude of α_{11} and the associated relative error as a function of frequency when L_{12}=0. The discrepancies that were observed in figure 16 with the local decoupling technique are not recovered. Although this situation corresponds to a decoupling at the extremity of the master rod with the global decoupling technique, we do not find back the same results as with the local decoupling technique.

The difference between the two techniques can be highlighted with the analytical expression of α_{11}, when resolving Eq. (2.13)

$$\alpha_{11} = \frac{\left((\beta_{22} - \mu_{22})\mu_{11} + \mu_{12}^2\right)\beta_{11} - \beta_{12}^2\mu_{11}}{(\beta_{22} - \mu_{22})\left(\beta_{11} - \mu_{11}\right) - \left(\beta_{12} - \mu_{12}\right)^2} \tag{2.14}$$

This expression differs from Eq. (2.6). It does not depend only on the receptances at point 1 that characterized the local decoupling technique, but it depends also on the receptances at point 2 as well as the cross receptances betweeen the two points. This is a characteristic of the global decoupling technique which is less sensitive to model errors but needs more parameters to be computed. As a result, it can be seen in figure 26 that the remaining errors correspond to slight frequency shifts in the prediction of α_{11}, due to the frequency shifts resulting from the FEM calculations on β_{11} that can be seen in figure 17b. One must note that the scale of the vertical axis in figure 17b is smaller than in figure 16b.

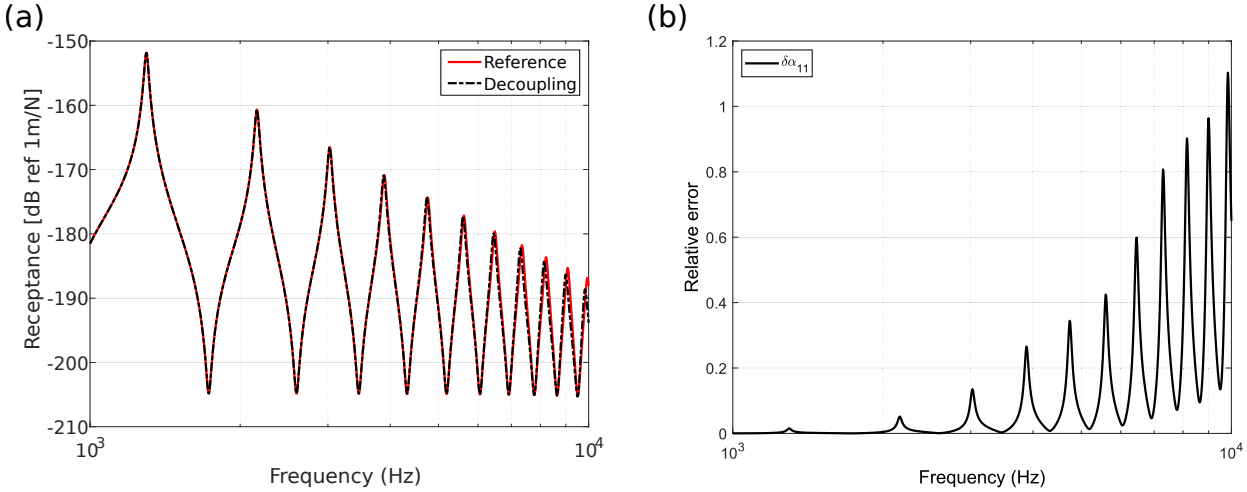

Figure 26: (a) Amplitude of the receptance α_{11} when the global decoupling technique is applied at the extremity of the master rod. (b) Associated relative error.

2.2.4 Optimization of the decoupling process

Before concluding this study, one can be interested in finding the optimal configuration allowing to minimize the errors on α_{11}. Indeed, when applying a subtractive modelling

technique, we generally start from a model of the master structure whereas the characteristics of the target model are already defined. Hence, the only parameters that are not fixed are related to the model of the subtracted structure. In our rod problem, the length of the master rod and the position of the coupling point 1 (that defined the length of the target rod) are fixed. Hence the only parameter that can be adjusted is the length of the subtracted rod. Moreover, it has previously been highlighted that the main errors induced by the global decoupling technique appear at the resonances of the subtracted rod. By reducing the size of this rod, it can be expected that the first resonance would be shifted outside the frequency band of interest, leading to a better accuracy of the method.

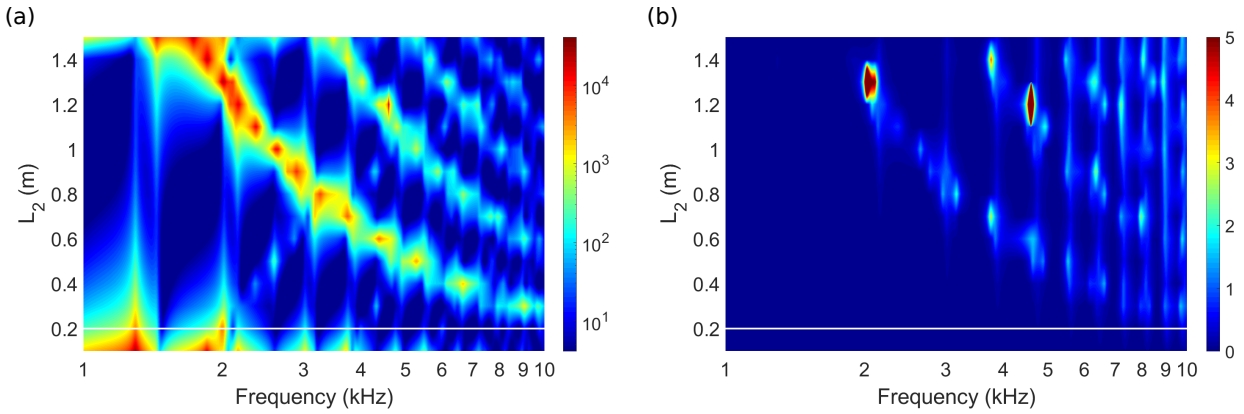

Figure 27: Optimization - (a) Condition number of the inverted matrix. (b) Relative error on α_{11}.

In figure 27, the condition number and relative error are then plotted for several lengths of the subtracted rod as a function of frequency. The length of the subtracted rod varies from 0.1 m to 1.5 m with 0.1 m increments. As the length of the master rod is fixed (i.e. 4.5 m), as well as the position of the coupling point 1 (hence the length of the target rod), the length of the residual rod is varied in reverse, from 1.4 m to 0 m. The length of the target rod L_{11} remains 3.0 m (as in the previous calculations). We can clearly see in this figure that the maxima of the condition number, corresponding to the resonances of the subtracted rod, are shifted towards the high frequencies as L_2 decreases, until reaching 0.2 m (delimited by the white line on the figure). For L_2 between 0.1 m and 0.2 m, the subtracted rod does not exhibit resonances in the frequency band anymore. The condition number tends however to increase in the low frequency domain. The global trend of the relative error on α_{11} that can be observed in figure 27b is in agreement with the one of the condition number: the relative error decreases when L_2 decreases, until becoming negligible when L_2 is lower than 0.2 m. Besides, the high condition numbers in the low frequencies for the small lengths of the subtracted rod that was observed in figure 27a do not impact the relative error. This can be explained by the small errors induced by the FEM calculation of the receptances of the subtracted rod in the low frequency range (compared to those in the higher part of the

frequency range).

The figure 28 shows the global decoupling process as well as the associated relative error on α_{11} when the subtracted rod is 0.1 m long. The maximum relative error is 12% (see the black curve), which is much lower than the relative error observed in the figure 24b for which the length of the subtracted rod was 0.5 m. Moreover, taking into account of the small size of the subtracted rod, the FEM mesh can be refined without greatly affecting the computational cost. For instance, for a subtracted rod of 0.1 m, the calculation of its receptances with a mesh size of dx=0.1 m took 5.6 s, while the same calculation with a mesh size of dx=0.01 m required 6.6 s. The comparison of the results of the decoupling process and relative errors for these two calculations is presented in figure 28a (blue curve) for the results and figure 28b (red curve) for the relative error. For a difference of computing time of only 1 s, the errors were reduced by a factor that goes up to 73. Hence, the balance between the increase of the computing time and the decrease of the errors is largely in favour of the latter, by the use of a finer mesh.

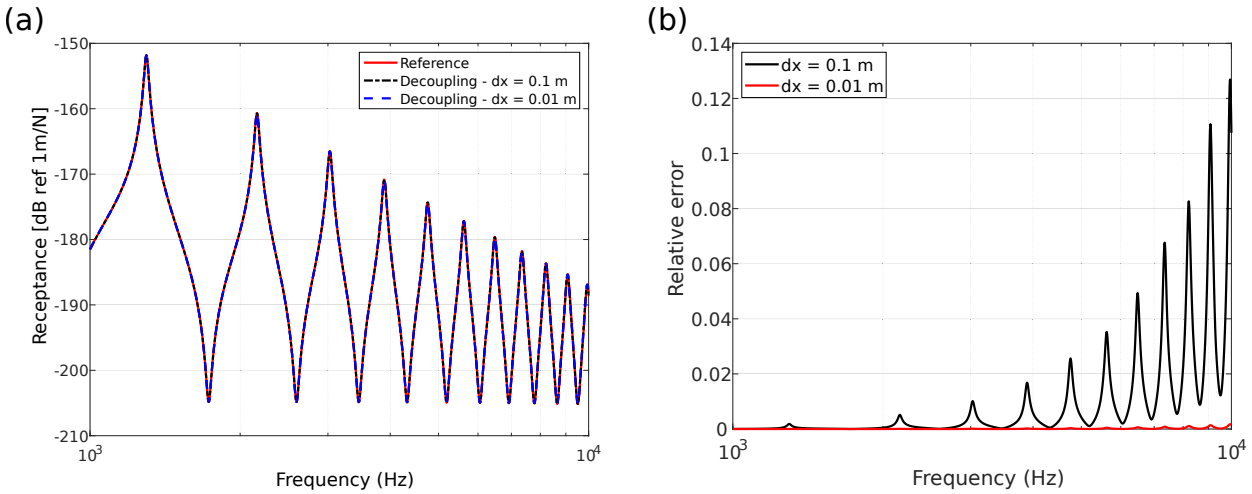

Figure 28: (a) Amplitude of the receptance α_{11} when the global decoupling technique is optimized, for two different mesh sizes. (b) Associated relative errors.

2.3 Conclusion

The concept of subtractive modelling that consists in predicting the behavior of a target structure by decoupling a subtracted structure from the master one has been investigated for the case of rods decoupling. The use of this academic structure allowed studying the sensitivity of the decoupling to model errors. These model errors correspond to the difference that can appear between the numerical models of the master structure and the subtracted structure, and their real value. In the numerical applications that were presented, the master

rods were represented by analytical models whereas the subtracted rods were simulated by FEM models. Two reverse formulations of the receptance approach have been studied:

- The first one, the local approach, is only based on the receptances at the coupling junction of interest. In this case, the decoupling was performed by removing the subtracted rod located at one extremity of the master rod. Significant errors were observed at the anti-resonant frequencies of the subtracted rods. They are due to the conjunction of two phenomena. On the one hand, the errors induced by the FEM model of the subtracted rod compared to an analytical model are significant at the resonances and anti-resonances of the rod. On the other hand, the sensitivity analysis for small variations carried out on the analytical formula of the reverse formulation showed that an amplification of the errors appears when the receptances of the subtracted and master rods are close to each other. This situation appears at the anti-resonance frequencies of the subtracted rods;

- The second one, the global approach, is based on a matrix formulation considering the receptances between different points. The decoupling was performed with a subtracted rod located at any position of the master rod. With this approach, the errors appear at the resonant frequencies of the subtracted rod due to the ill-conditioning of the matrix to be inverted. The process can however be improved by considering a short subtracted rod for which the first resonance is outside the frequency range of interest. In this situation, the decoupling technique exhibits a good accuracy even if the subtracted rod is modelled by the FEM with a relatively coarser mesh. The accuracy can still be increased by considering a finer mesh that would not affect greatly the computing time as the size of the subtracted rod is small.

These results obtained on a simple case give some important insights for the extension of the decoupling technique for subtractive modelling on more complex cases. In the next chapter, an acoustical 3-D problem will be considered, exhibiting a more complex and global formulation.

Chapter 3

Subtractive modelling on a complex vibroacoustic system: principle of the reverse Condensed Transfer Function method

The subtractive modelling principle explored in the previous chapter is extended here for complex vibroacoustic problems. This generalization is made by reversing the formalism of the Condensed Transfer Function method [172], recently developed to couple mechanical and acoustical subsystems. For the sake of conciseness and clarity, the reverse formulation will be developed and applied in this chapter for a 3-D acoustical system, although it could also be developed and applied for vibroacoustic problems as it will be shown in chapter 5. In addition to this extension, particular attention is paid in this chapter on the estimation of the response at any point of the target subsystem (and not only on the estimation of the transfer functions at the decoupling interface). To this end, a dedicated formulation is proposed and numerically validated in this chapter.

The formalism of the Condensed Transfer Function method, introduced in [172], is proposed for an acoustical system in section 3.1. The equations of the CTF method are then reversed to obtain the reverse Condensed Transfer Function (rCTF) method in section 3.2. Subsequently, the rCTF method is applied on an academic test case consisting in the scattering of an acoustic plane wave by a rigid sphere in an infinite water domain in section 3.3. The possibility of local and a global decoupling formulations will be investigated as an analogy with the developments in chapter 2. This application serves as an numerical validation of the rCTF method, with the Condensed Transfer Functions (CTFs) necessary to apply the method being calculated analytically.

Part of this chapter is based on the article "Vibroacoustic subtractive modeling using a reverse condensed transfer function approach", published in the *Journal of Sound and Vibration* [196].

3.1 Principle of the direct CTF method for acoustic problems

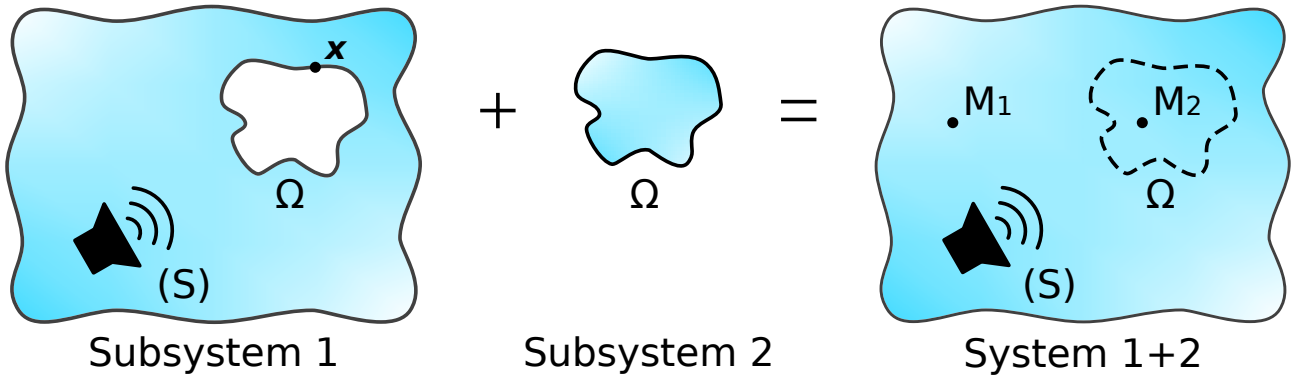

Figure 29: Principle of the direct CTF method.

In this section, the principles of the CTF approach for an acoustic problem are recalled (see the references of Meyer [172] and Hu [175] for details and for vibroacoustic and mechanical problems). Let us consider two acoustical domains coupled along a surface Ω, where $\mathbf{x}$ is a point on Ω, and excited by an acoustic source (S) applied on subsystem 1, as shown in figure 29. The responses are calculated in harmonic regime. A set of N orthonormal functions defined on Ω, called the condensation functions (CFs), is considered: $\{\varphi^i\}_{1\leqslant i\leqslant N}$. It is assumed that for each subsystem α, the pressures p_α and the normal velocities u_α (where the outer-pointing normal is defined as positive) at the junction can be approximated as a linear combination of the CFs

$$p_\alpha(\mathbf{x}) \simeq \sum_{i=1}^{N} P_\alpha^i \varphi^i(\mathbf{x}) \quad \text{and} \quad u_\alpha(\mathbf{x}) \simeq \sum_{i=1}^{N} U_\alpha^i \varphi^i(\mathbf{x}) \quad \forall \mathbf{x} \in \Omega \tag{3.1}$$

where P_α^i and U_α^i are the unknowns. To estimate them, it is necessary to define for each uncoupled subsystem $\alpha \in \{1,2\}$, the condensed transfer function between φ^i and φ^j by applying a prescribed velocity $u_\alpha = \varphi^j$ on Ω

$$Z_\alpha^{ij} = \frac{\langle \bar{p}_\alpha, \varphi^i \rangle}{\langle u_\alpha, \varphi^j \rangle} = \langle \bar{p}_\alpha, \varphi^i \rangle \tag{3.2}$$

with $\bar{p}_\alpha$ the resulting pressure at the junction Ω when the subsystem is excited by $u_\alpha = \varphi^j$ and $\langle \bullet, \bullet \rangle$ the scalar product defined on the surface Ω by

$$\langle f, g \rangle = \iint_\Omega f(\mathbf{x}) g^*(\mathbf{x}) \, \mathrm{d}\mathbf{x} \tag{3.3}$$

where * denotes the complex conjugate. Moreover, the condensed blocked pressure of each uncoupled subsystem α is defined by

$$\tilde{P}_\alpha^i = \langle \tilde{\tilde{p}}_\alpha, \varphi^i \rangle \tag{3.4}$$

where $\tilde{\tilde{p}}_\alpha$ is the pressure at the junction of the uncoupled subsystem α when only external loading is applied. Assuming there is no external load applied on subsystem 2, $\tilde{P}_2^i = 0, \forall i \in [\![0, N]\!]$.

In the following, the condensed impedance matrix of subsystem α will be referred to as $\mathbf{Z}_\alpha$, where the coefficient of the i^{th} row and j^{th} column corresponds to Z_α^{ij}. Similarly, $\mathbf{U}_\alpha$, $\mathbf{P}_\alpha$ and $\tilde{\mathbf{P}}_\alpha$ will denote the condensed velocity vector, the condensed pressure vector, and the condensed blocked pressure vector associated with subsystem α, respectively.

An external load (S) is applied on subsystem 1, while the junction Ω exhibits a normal velocity u_1 on subsystem 1 and u_2 on subsystem 2. In response to these normal velocities and the external load, the superposition principle for linear passive systems [173] gives us expressions relating to the condensed velocities and pressure vectors

$$\begin{cases} \mathbf{P_1} = \tilde{\mathbf{P}}_\mathbf{1} + \mathbf{Z_1 U_1} \\ \mathbf{P_2} = \mathbf{Z_2 U_2} \end{cases} \tag{3.5}$$

The pressure continuity and normal velocities equilibrium at the junction yields (taking into account the definition of the normals)

$$\begin{cases} p_1(\mathbf{x}) = p_2(\mathbf{x}) \\ u_1(\mathbf{x}) + u_2(\mathbf{x}) = 0 \end{cases}, \quad \forall \mathbf{x} \in \Omega \tag{3.6}$$

By injecting Eq. (3.1) in Eq. (3.6) and projecting the results on the CFs, one obtains

$$\begin{cases} \mathbf{P_1} = \mathbf{P_2} \\ \mathbf{U_1} + \mathbf{U_2} = 0 \end{cases} \tag{3.7}$$

In the following, when the two subsystems are coupled, $\mathbf{P_{1+2}}$ denotes the condensed pressure vector whereas $\mathbf{U_{1+2}}$ denotes the condensed velocity vector on Ω. By convention, $\mathbf{U_{1+2}} = \mathbf{U_1} = -\mathbf{U_2}$ and $\mathbf{P_{1+2}} = \mathbf{P_1} = \mathbf{P_2}$. By combining Eq. (3.5) and Eq. (3.7), the coupling velocities $\mathbf{U_{1+2}}$ between the two subsystems can be deduced

$$(\mathbf{Z_1} + \mathbf{Z_2})\, \mathbf{U_{1+2}} = -\tilde{\mathbf{P}}_\mathbf{1} \tag{3.8}$$

Once the coupling velocities have been calculated by inverting Eq. (3.8), the response at given points M_1 (in subsystem 1) and M_2 (in subsystem 2) can be deduced

$$\begin{cases} p_{1+2}(M_1) = \tilde{p}_1(M_1) + \mathbf{Z_1}(M_1)\mathbf{U_{1+2}} & \text{(3.9a)} \\ p_{1+2}(M_2) = -\mathbf{Z_2}(M_2)\mathbf{U_{1+2}} & \text{(3.9b)} \end{cases}$$

$\mathbf{Z}_\alpha(M_\alpha)$ is the vector of the point condensed impedance and should be distinguished from the condensed impedance matrix $\mathbf{Z}_\alpha$. The i^{th} component of this vector, $Z_\alpha^i(M_\alpha)$, is defined as

the pressure at point M_α when a normal velocity corresponding to the condensation function φ^i is prescribed on Ω.

3.2 Reverse CTF method

3.2.1 Principle

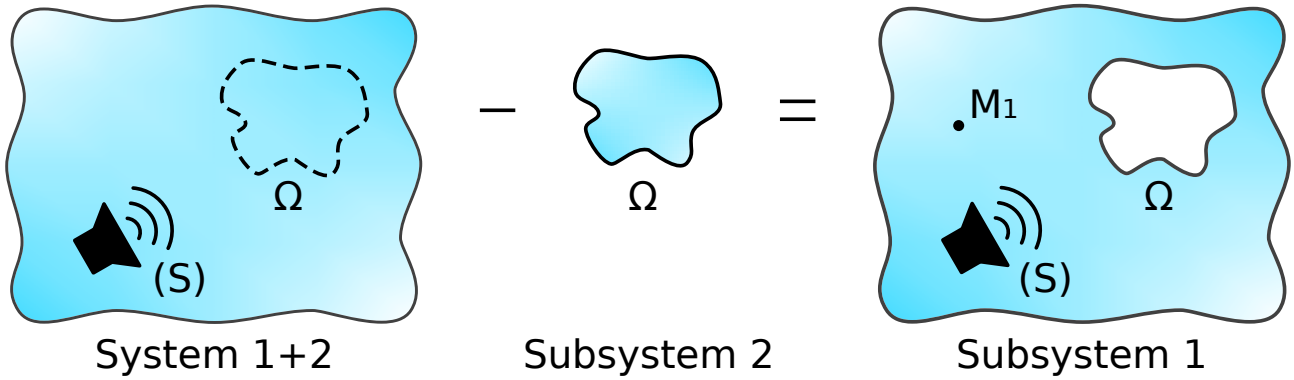

Figure 30: Principle of the rCTF method.

In this section, we develop the subtractive approach consisting in reversing the CTF approach. The behavior of the complete system 1+2 as well as that of subsystem 2 are assumed as known, and the aim of this development is to deduce the behavior of subsystem 1, as shown in figure 30. In Eq. (3.9a), $\tilde{p}_1(M_1)$ represents the pressure at point M_1 when subsystem 1 is uncoupled from subsystem 2. It is thus the quantity of interest for the present study. We can write

$$\tilde{p}_1(M_1) = p_{1+2}(M_1) - \mathbf{Z_1}(M_1)\mathbf{U_{1+2}} \tag{3.10}$$

The coupling velocities $\mathbf{U_{1+2}}$ at the junction can be retrieved using Eq. (3.5) combined with the pressure continuity and velocity equilibrium of Eq. (3.7)

$$\mathbf{U_{1+2}} = -\mathbf{Z_2}^{-1}\mathbf{P_{1+2}} \tag{3.11}$$

Finally, the pressure at a given point M_1 of uncoupled subsystem 1 can be rewritten as

$$\tilde{p}_1(M_1) = p_{1+2}(M_1) + \mathbf{Z_1}(M_1)\mathbf{Z_2}^{-1}\mathbf{P_{1+2}} \tag{3.12}$$

As the behavior of subsystem 2 and of the global system 1+2 are assumed as known, $p_{1+2}(M_1)$, $\mathbf{Z_2}$ and $\mathbf{P_{1+2}}$ are therefore known quantities. In order to evaluate $\tilde{p}_1(M_1)$, the next subsections are focused on determining $\mathbf{Z_1}(M_1)$ as well as $\mathbf{Z_1}$, the condensed impedance matrix of subsystem 1.

3.2.2 Calculation of the point condensed impedance using a reciprocity principle

We now focus on the calculation of the impedance $\mathbf{Z_1}(M)$, with M being a given point located in the acoustic domain associated with subsystem 1. We recall that the i^{th} component of this vector, $Z_1^i(M)$, corresponds to the pressure at point M when a prescribed velocity corresponding to the condensation function φ^i is imposed on the coupling surface. It can be expressed as

$$Z_1^i(M) = \iint_\Omega H_{p/Q}\left(M, M'\right) \varphi^i\left(M'\right) \mathrm{d}M' \tag{3.13}$$

where $H_{p/Q}\left(M, M'\right) = \frac{p(M)}{Q(M')}$ is the transfer function corresponding to the ratio between the pressure at point M and the volume velocity flow of the monopole source at point M'. In Eq. (3.13), $\varphi^i\left(M'\right) \mathrm{d}M'$ is the product between normal velocity $\varphi^i\left(M'\right)$ and elementary surface $\mathrm{d}M'$, and corresponds to a volume velocity flow. Hence, $H_{p/Q}\left(M, M'\right) \varphi^i\left(M'\right) \mathrm{d}M'$ represents the pressure at point M induced by a monopole source of volume velocity $\varphi^i\left(M'\right) \mathrm{d}M'$ and of elementary surface $\mathrm{d}M'$. The sum of these contributions over the surface Ω corresponds to the quantity $Z_1^i(M)$.

On the other hand, the reciprocity principle states that the response of a linear system to a time-harmonic disturbance that is applied at some point by an external agent is invariant with respect to the exchange of the input and observed reponse points [193, 197]. In this case, it means that the pressure radiated at point M when it is excited by a monopole source of unit volume velocity at point M' equals the pressure radiated at point M' when it is excited by a monopole source of unit volume velocity at point M

$$H_{p/Q}\left(M, M'\right) = H_{p/Q}\left(M', M\right) \tag{3.14}$$

Hence, Eq. (3.13) can be rewritten

$$Z_1^i(M) = \iint_\Omega H_{p/Q}\left(M', M\right) \varphi^i\left(M'\right) \mathrm{d}M' \tag{3.15}$$

A new interpretation of $Z_1^i(M)$ can be given from Eq. (3.15). It corresponds to the pressure on the coupling surface projected on the condensation function φ^i, induced by a monopole source of unit volume velocity situated on point M. From this interpretation, $\mathbf{Z_1}(M)$ is therefore the vector of the blocked pressure on the coupling surface when the excitation is a monopole source of unit volume velocity: $\mathbf{Z_1}(M) = \tilde{\mathbf{P}}_\mathbf{1}^\mathbf{M}$. The exponent M is introduced in the notation to specify that the considered excitation is a unitary monopole located at point M.

This quantity, $\tilde{\mathbf{P}}_{\mathbf{1}}^{\mathbf{M}}$, can be estimated from the knowledge of the pressure induced by the monopole source on the global system 1+2. Let us assume that we know $\mathbf{P}_{\mathbf{1+2}}^{\mathbf{M}}$, the vector of the condensed pressure induced by the monopole source of unit volume velocity and located at the point M in the global system 1+2.

Eq. (3.5) and Eq. (3.7) related to the CTF approach can still be applied for the present case. From these equations, $\tilde{\mathbf{P}}_{\mathbf{1}}^{\mathbf{M}}$ can be expressed as

$$\tilde{\mathbf{P}}_{\mathbf{1}}^{\mathbf{M}} = \left(\mathbf{I} + \mathbf{Z_1}\mathbf{Z_2}^{-1}\right) \mathbf{P}_{\mathbf{1+2}}^{\mathbf{M}} \tag{3.16}$$

where $\mathbf{I}$ is the identity matrix.

At this stage, $\mathbf{Z_1}$ is still unknown. We will see in the next subsection how to estimate it from the condensed impedance matrix of subsystem 2, $\mathbf{Z_2}$, and of the global system, $\mathbf{Z_{1+2}}$.

3.2.3 Calculation of the condensed impedances of subsystem 1

Our aim in this subsection is to derive the condensed impedance matrix of subsystem 1, $\mathbf{Z_1}$, from those of subsystem 2 and the global system 1+2, respectively $\mathbf{Z_2}$ and $\mathbf{Z_{1+2}}$.

The condensed impedances of subsystems 1 and 2 were previously defined by Eq. (3.2). Let us now define the condensed transfer function of the global system 1+2 between φ^i and φ^j by applying a prescribed velocity jump at the junction Ω corresponding to the condensation function φ^j

$$Z_{1+2}^{ij} = \frac{P_{1+2}^{i}}{\delta U_{1+2}^{j}} = \frac{\left\langle \bar{p}_{1+2}, \varphi^i \right\rangle}{\left\langle \varphi^j, \varphi^j \right\rangle} = \left\langle \bar{p}_{1+2}, \varphi^i \right\rangle \tag{3.17}$$

where $\bar{p}_{1+2}$ corresponds to the pressure at junction Ω resulting from the prescribed velocity jump, $\delta U_{1+2}^{j} = \varphi^j$.

The condensed velocity jump vector at the junction associated with the prescribed velocity jump corresponding to the condensation function φ^j is given by

$$\delta \mathbf{U_{1+2}} = \begin{bmatrix} 0 \\ \vdots \\ 0 \\ 1 \\ 0 \\ \vdots \\ 0 \end{bmatrix}, \tag{3.18}$$

where the position of 1 corresponds to the j^{th} component. Eq. (3.5) and Eq. (3.7) related to the CTF approach can still be applied for this case, but as there is no external excitation in subsystem 1, and the prescribed velocity jump is applied at the junction, they are slightly modified

$$\begin{cases} \mathbf{P}_{\mathbf{1}}^{\delta} = \mathbf{Z_1}\mathbf{U}_{\mathbf{1}}^{\delta} \\ \mathbf{P}_{\mathbf{2}}^{\delta} = \mathbf{Z_2}\mathbf{U}_{\mathbf{2}}^{\delta} \\ \mathbf{P}_{\mathbf{1+2}}^{\delta} = \mathbf{P}_{\mathbf{1}}^{\delta} = \mathbf{P}_{\mathbf{2}}^{\delta} \\ \delta\mathbf{U_{1+2}} = \mathbf{U}_{\mathbf{1}}^{\delta} + \mathbf{U}_{\mathbf{2}}^{\delta} \end{cases} \tag{3.19}$$

One has to keep in mind that the outer-pointing normal is defined as positive, thus explaining the last equation in the system of Eq. (3.19). The exponent δ is introduced to signify that the vectors of the condensed pressure and normal velocity result from the prescribed velocity jump defined by Eq. (3.18). From Eq. (3.19), we can deduce

$$\mathbf{P}_{\mathbf{1+2}}^{\delta} = \mathbf{Z_1}\left(\mathbf{Z_1} + \mathbf{Z_2}\right)^{-1}\mathbf{Z_2}\delta\mathbf{U_{1+2}} \tag{3.20}$$

Since a velocity jump at the junction Ω corresponding to the condensation function φ^j is prescribed at the junction, this condensed pressure vector gives us the j^{th} column of the condensed impedance of the global system, $\mathbf{Z_{1+2}}$. By replacing $\delta\mathbf{U_{1+2}}$ by the identity matrix, in order to sweep all the cases of excitation by the CFs, we can then deduce the following relation

$$\mathbf{Z_{1+2}} = \mathbf{Z_1}\left(\mathbf{Z_1} + \mathbf{Z_2}\right)^{-1}\mathbf{Z_2} \tag{3.21}$$

By inverting the previous equation, we finally obtain

$$\mathbf{Z_1} = \mathbf{Z_2}\left(\mathbf{Z_2} - \mathbf{Z_{1+2}}\right)^{-1}\mathbf{Z_{1+2}} \tag{3.22}$$

This result is the same than the one in Eq. (2.13) and shows the analogy which can be drawn between the different methods of decoupling.

3.2.4 Synthesis of the reverse CTF principle

In the previous sections, all the quantities needed for the application of the rCTF method were obtained from information concerning subsystem 2 and the global system 1+2. Finally, putting all this information together will allow us to estimate the pressure at a given point of the uncoupled subsystem 1.

The expression of the vector of the point condensed impedance, corresponding to the blocked pressure induced by a unitary monopole can be obtained by injecting the result of Eq. (3.22) into Eq. (3.16)

$$\mathbf{Z_1}(M_1) = \tilde{\mathbf{P}}_{\mathbf{1}}^{\mathbf{M_1}} = \left(\mathbf{I} + \mathbf{Z_2}\left(\mathbf{Z_2} - \mathbf{Z_{1+2}}\right)^{-1}\mathbf{Z_{1+2}}{\mathbf{Z_2}}^{-1}\right)\mathbf{P}_{\mathbf{1+2}}^{\mathbf{M_1}} \tag{3.23}$$

Ultimately, the pressure at point M_1 of the uncoupled subsystem 1 given by Eq. (3.12) can be rewritten as

$$\tilde{p}_1(M_1) = p_{1+2}(M_1) + \left(\mathbf{I} + \mathbf{Z_2}\left(\mathbf{Z_2} - \mathbf{Z_{1+2}}\right)^{-1}\mathbf{Z_{1+2}}\mathbf{Z_2}^{-1}\right)\mathbf{P}_{\mathbf{1+2}}^{\mathbf{M_1}}\mathbf{Z_2}^{-1}\mathbf{P_{1+2}} \tag{3.24}$$

This final expression constitutes the main theoretical result of reverse Condensed Transfer Function (rCTF) method. It permits estimating the response at any point of subsystem 1 from the knowledge of quantities related to subsystem 2 and to the global system 1+2.

3.3 Analytical validation of the proposed rCTF approach

3.3.1 Test case definition

To validate and evaluate the accuracy of the rCTF method proposed in the previous section and based on Eqs. (3.22) and (3.24), we are going to compare the results obtained with the rCTF method to the reference results for an academic test case. The latter consists in the scattering problem of a rigid sphere in an infinite water domain, impacted by an acoustic plane wave. The choice of this test case was motivated by the fact that it constitutes a common reference case in the literature to study the acoustic scattering by an immersed object and that the principle of the proposed approach is general and can be applied to various cases. Furthermore, the reference calculation, developed in [8] and based on the expansion of a plane wave in spherical harmonics, is an analytical solution easy to implement and gives accurate results with reasonable calculation costs. Consistently with the developments in chapter 2, this problem will be investigated under a local and a global form, and the results obtained from these two formulations will be compared in order to see if the conclusion from the rod case study can be extended to a 3-D problem.

3.3.1.1 Local form of the problem

In chapter 2, the local formulation of the decoupling problem was defined by taking into account only one coupling point. The analogy with the 3-D case of interest here is to take into account one coupling surface between the two subsystems. As illustrated in figure 31, the rCTF approach will deal with this problem by removing a water sphere (i.e. the subsystem 2) from an infinite water domain (i.e. the global system 1+2). An infinite water domain with a rigid sphere will then be obtained (i.e. subsystem 1). The characteristics of the infinite domain and the sphere are given in table 3. The origin of the coordinates is taken at the center of the sphere, and the calculations will be conducted in the spherical coordinate system shown in figure 31.

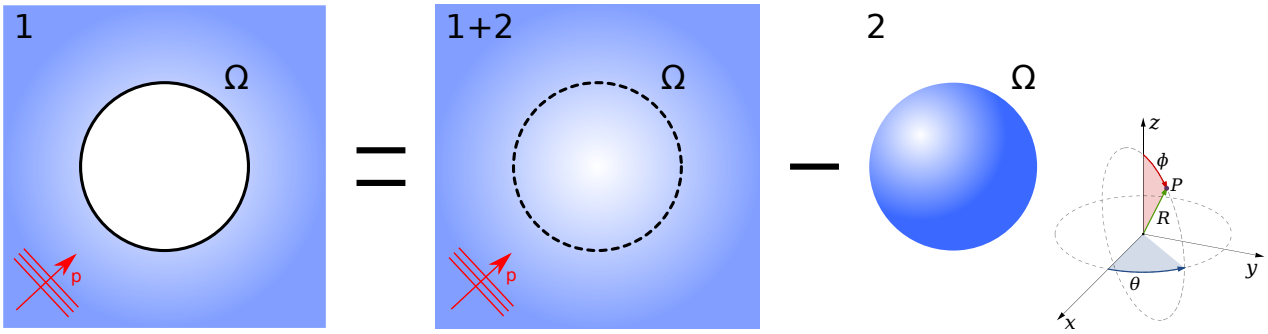

Figure 31: Illustration of the rCTF method principle applied to the scattering of a rigid sphere - local approach.

Parameter	Notation	Value	Unit
Radius	a	1	m
Density	ρ_f	1000	$kg.m^{-3}$
Sound speed	c_f	1500	$m.s^{-1}$

Table 3: Fluid characteristics and dimensions of the local problem.

3.3.1.2 Global form of the problem

Concerning the global formulation of the problem, two coupling surfaces will be considered, as illustrated in figure 32. Hence the rCTF approach will deal with this problem by removing a hollow water sphere (i.e. the subsystem 2) from an infinite water domain (i.e. the global system 1+2). An infinite water domain with a rigid sphere and a residual water sphere will then be obtained (i.e. subsystem 1), and the pressure field scattered by the rigid sphere should be the same than in the local form and the reference calculation. In order to distinguish these two parts of the decoupled subsystem, in the following, the part corresponding to the infinite water domain with a rigid sphere will be referred to as the target subsystem, while the part corresponding to the residual water sphere will be referred to as the residual subsystem, as a reference to the denominations in section 2.2. Consistently with the conclusion of subsection 2.2.4 concerning the optimization process of the rod case study, the interior radius of the hollow sphere should be chosen to be close from the exterior radius of the sphere. This will reduce the thickness of the hollow sphere, hence limiting the standing waves in the radial direction in order to minimize the number of resonances and anti-resonances of the subsystem in the frequency range of interest (as it was observed in chapter 2 that model errors can be amplified at these frequencies). The characteristics of the infinite domain and of the hollow sphere are given in table 4. One must emphasize that for this global decoupling process, only the response in the infinite medium with the rigid sphere at its center will be of interest, as we are not interested in the response in the residual water sphere.

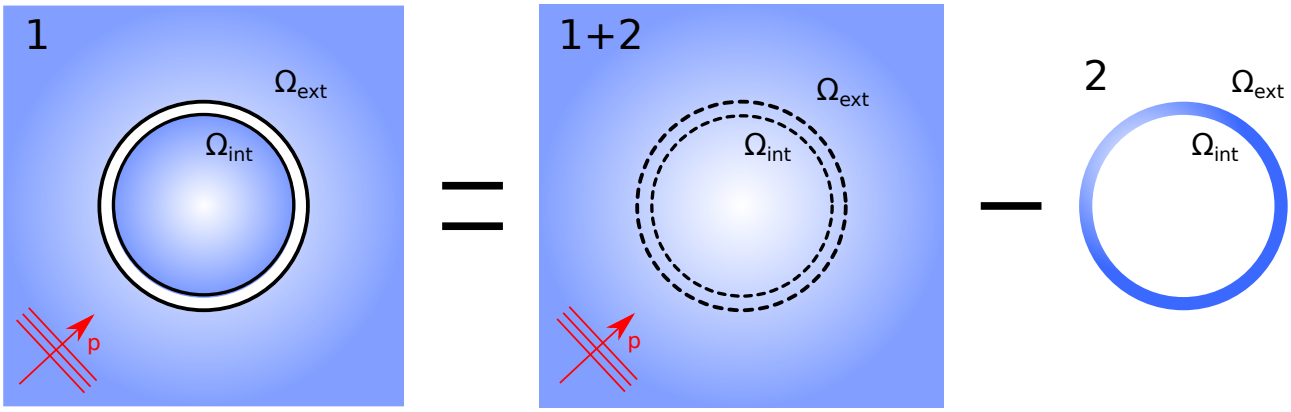

Figure 32: Illustration of the rCTF method principle applied to the scattering of a rigid sphere - global approach.

Parameter	Notation	Value	Unit
Exterior radius	a_{ext}	1	m
Interior radius	a_{int}	0.9	m
Density	ρ_f	1000	$kg.m^{-3}$
Sound speed	c_f	1500	$m.s^{-1}$

Table 4: Fluid characteristics and dimensions of the global problem.

3.3.1.3 Definition of the reference calculation and of the calculation parameters

For the purposes of comparison, a theoretical reference calculation is performed by developing the incident plane wave and the scattered pressure field in spherical harmonics, and by writing that the normal velocity at the surface of the sphere is null [8]. Harmonic responses are calculated from frequencies between 100 Hz and 1000 Hz, with a step of 1 Hz. This frequency range was considered to obtain the first two resonant frequencies of the water sphere (i.e. 497 Hz and 798 Hz) and its first anti-resonant frequency (i.e. 750 Hz).

It is reminded here that the objective of this test study is to validate from a practical point of view the subtractive modelling approach developed in section 3.2, and to study the influence of several parameters, as the type and the number of CFs. At this stage of the development of the proposed approach, it is then more relevant to focus on the validity and convergence of the approach rather than its computational performances compared to alternative ones. This is why the reference calculation of this application test is a theoretical one and that there is no emphasis on the computational time of the proposed approach in this chapter.

Finally, it must be emphasized that, for the direct CTF approach, the coupling between the model of a water sphere and the model of a rigid sphere immersed in water can be qualified as strong coupling. Indeed, the behavior of these subsystems when they are coupled together (corresponding to the model of an infinite water medium) is significantly different from those

when they are uncoupled. Considering this case allows to evaluate the ability of the rCTF approach to decouple subsystems that are strongly coupled.

To apply the rCTF approach, in accordance with the theoretical backgrounds of section 3.2, the condensed impedances defined by Eq. (3.2) for subsystem 2 and Eq. (3.17) for system 1+2 should be calculated. These quantities are related to the set of CFs, $\{\varphi^i\}_{1\leqslant i\leqslant N}$. Two types of CFs are considered and presented in the next section before analyzing the results of the rCTF approach.

3.3.2 Definition of the condensation functions

Two types of CFs will be considered in the following, in order to study their influence on the performance of the rCTF method:

- the weighted spherical harmonics;
- the 2D gate functions.

3.3.2.1 Weighted spherical harmonics

As developed in Appendix C, the pressure field in the infinite domain and in the sphere can be described as an infinite sum of so called spherical harmonics. Hence, for the condensed impedances, using spherical harmonics as CFs will result in a greatly simplified expression. The spherical harmonics are defined in spherical coordinates as

$$\psi_{n,m}(\theta,\phi) = \sqrt{\frac{2n+1}{4\pi}\frac{(n-m)!}{(n+m)!}}P_n^m(\cos\theta)\mathrm{e}^{\mathrm{j}m\phi}, \quad n\in[\![0,N_L]\!], \quad m\in[\![-n,n]\!] \tag{3.25}$$

where P_n^m is the associated Legendre polynomial and N_L is the maximal degree of the associated Legendre polynomial. The condensation function φ^i associated with the spherical harmonic $\psi_{n,m}$ and called the weighted spherical harmonic is then defined at the surface of the sphere of radius a by

$$\varphi^i = \frac{1}{a}\psi_{n,m}, \quad i\in[\![1,N]\!], \quad n\in[\![0,N_L]\!], \quad m\in[\![-n,n]\!] \tag{3.26}$$

The number of CFs N is directly linked to the maximal degree of the associated Legendre polynomial N_L by the following relation

$$N = (N_L+1)^2 \tag{3.27}$$

As an illustration, examples of spherical harmonics on the surface of the sphere are presented in figure 33. The condensation functions associated with the spherical harmonics

form an orthonormal set for the scalar product in spherical coordinates at the surface of the sphere

$$\left\langle \varphi^i, \varphi^j \right\rangle = \int_0^{2\pi} \int_{-\pi/2}^{\pi/2} \varphi^i \varphi^{j*} a^2 \sin\theta \, \mathrm{d}\theta \, \mathrm{d}\phi = \delta_{ij}, \tag{3.28}$$

with δ_{ij} being the Kronecker symbol, and * denoting the complex conjugate.

Applying the rCTF approach using weighted spherical harmonics as CFs will result in considering condensed impedance matrices that are diagonal, as a result of the orthonormal properties of the spherical harmonics. This means that the contributions of the different CFs (i.e. the spherical harmonics) will be independent from one another. This consitutes a particular case that can be compared to the decoupling of rods in chapter 2, but it can be useful for analyzing the results.

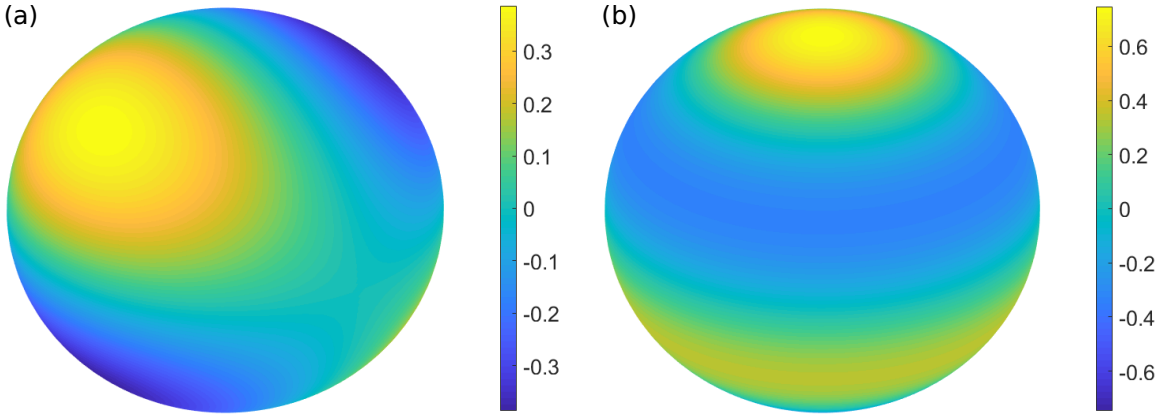

Figure 33: Examples of spherical harmonic functions. (a) $\psi_{2,1}$ (b) $\psi_{3,0}$

3.3.2.2 2D gate functions

The second type of CFs investigated are the 2D gate functions $\varphi^i, i \in [\![1, N]\!]$. They are defined depending on their area Ω_s as follows

$$\varphi^i(\theta_s, \phi_s) = \begin{cases} \frac{1}{\sqrt{\Omega_s}} & \text{if} \quad \begin{cases} \theta_{i-1} \leqslant \theta_s < \theta_i \\ \phi_{i-1} \leqslant \phi_s < \phi_i \end{cases} \\ 0 \quad \text{elsewhere} \end{cases} \tag{3.29}$$

It can be easily verified that the CFs defined by Eq. (3.29) are orthonormal with the scalar product defined in Eq. (3.28). The four angles θ_{i-1}, θ_i, ϕ_{i-1}, ϕ_i that appear in this expression are defined in figure 34a. They parametrize the corners of the patch i that can be linked to the i^{th} 2D gate function. The coupling surface Ω is then divided into N patches defining the N gate functions as CFs (see figure 34b). The condensed impedance between CF i and CF j corresponds to the mean pressure on the patch i when a unit prescribed normal velocity is imposed on patch j. Contrary to the spherical harmonics as CFs, the 2D gate functions as CFs lead to non-diagonal condensed impedance matrices. In terms of matrix resolution, the latter

case is more general than the former one, as it can be applied on non-canonical geometries. It is also emphasized that the CTF approach considering this type of CFs corresponds to the PTF approach described in the literature. Applying the rCTF approach in this case can therefore be considered as applying the reverse PTF approach.

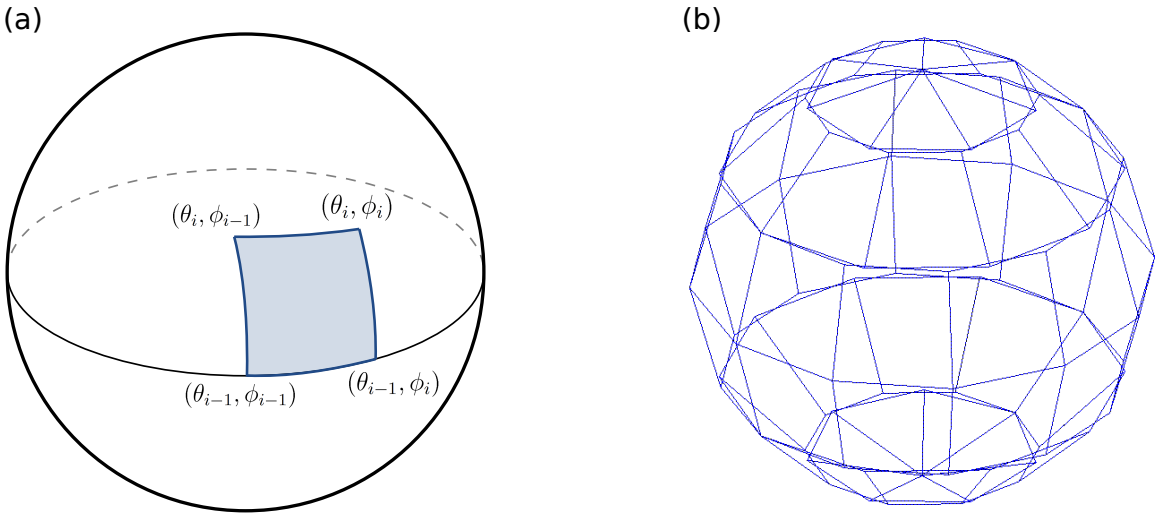

Figure 34: (a) Definition of a patch related to a 2D gate functions. (b) Definition of the patches over the sphere surface.

3.3.2.3 Calculation of the condensed transfer functions and convergence criteria

To apply the rCTF approach, the condensed impedances of the water sphere $\mathbf{Z_2}$ and the infinite water medium $\mathbf{Z_{1+2}}$ must be calculated. Moreover, to assess the accuracy of the method for evaluating the condensed impedances of the water sphere $\mathbf{Z_1}$ using Eq. (3.22), it is necessary to calculate $\mathbf{Z_1}$ directly to obtain a comparison point. The analytical calculations of these condensed impedances for both subsystems and for the global system are developed in Appendix C for the two types of CFs. These calculations are based on a spherical harmonics decomposition of the pressure field in the water medium.

The number of CFs considered and thus of condensed impedances, plays a key role in the convergence of the CTF method [172, 175, 176]. According to the previous studies on the CTF method, a criterion equivalent to the Nyquist-Shannon sampling theorem assuming at least two points per wavelength to sample a signal should be applied. As the problem considered is purely acoustical, the acoustic wavelength at the highest frequency of interest (i.e. 1000 Hz), $\lambda_{\text{min}} = 1.5$ m, should be considered for the criterion. For the weighted spherical harmonics as CFs, the maximal degree of the Legendre polynomial N_L related to Eq. (3.26) should respect the criterion [172]

$$N_L \geqslant \frac{2\pi a}{\lambda_{\text{min}}} \tag{3.30}$$

In the present case, this criterion yields $N_L = 5$, giving a number of CFs equal to $N = 36$ (following Eq. (3.27)). For the 2D gate functions as CFs, the size d of the patches should be smaller than half the smallest wavelength

$$d < \frac{\lambda_{\min}}{2} \tag{3.31}$$

In order to be compliant with this criterion, the sphere is divided into 58 patches, with 12 patches on the principal circumference. The patches considered in the following calculations are those displayed in figure 34b). It can be seen that the patches on the top and the bottom of the sphere take the shape of triangles instead of trapezoids for the other patches, and that the nodes between two consecutive patches are not necessarily coincident. However, these geometrical particularities concerning the patches do not have any influence on the results of the PTF method (see [171]). It can be noticed that the number of CFs considered with the weighted spherical harmonics is lower than that considered with the 2D gate functions. This is due to the fact that the size of some patches is well below the criterion in [171], because of geometrical constraints.

According to the calculation of the condensed impedances for the 2D gate functions as CFs in Appendix C, their expressions (see Eq. (C.14), Eq. (C.23) and Eq. (C.34)) depend on an infinite sum of spherical harmonics. In practice, these series must be truncated to a finite value N_L^{2D}, corresponding to the maximal degree of the associated Legendre polynomials of the spherical harmonics decomposition of the pressure fields. The value of N_L^{2D} influences the convergence and the cost of the calculation of the condensed impedances. After trial and error tests, it was found that using N_L^{2D}=50 is a good compromise in order to converge correctly without being too numerically costly. We underline here that this parameter is related to the method of evaluating the condensed impedances and does not directly concern the convergence of the CTF or rCTF approaches, which is characterized by the criteria in Eqs. (3.30) and (3.31).

3.3.3 Decoupling of the condensed impedances with the local rCTF approach

3.3.3.1 Results

As a first validation of the local decoupling approach (figure 31), the condensed impedances of subsystem 1, $\mathbf{Z_1}$, obtained from $\mathbf{Z_2}$, $\mathbf{Z_{1+2}}$ and the decoupling formula of Eq. (3.22), are compared to the results of the analytical expression of $\mathbf{Z_1}$ given in Eq. (C.33) for the weighted spherical harmonics, and Eq. (C.34) for the 2D gate functions.

The comparison is proposed in figure 35. The comparison for 3 weighted spherical harmonics as CFs (respectively the couples $(n,m) = (0,0), (n,m) = (1,0), (n,m) = (2,0)$)

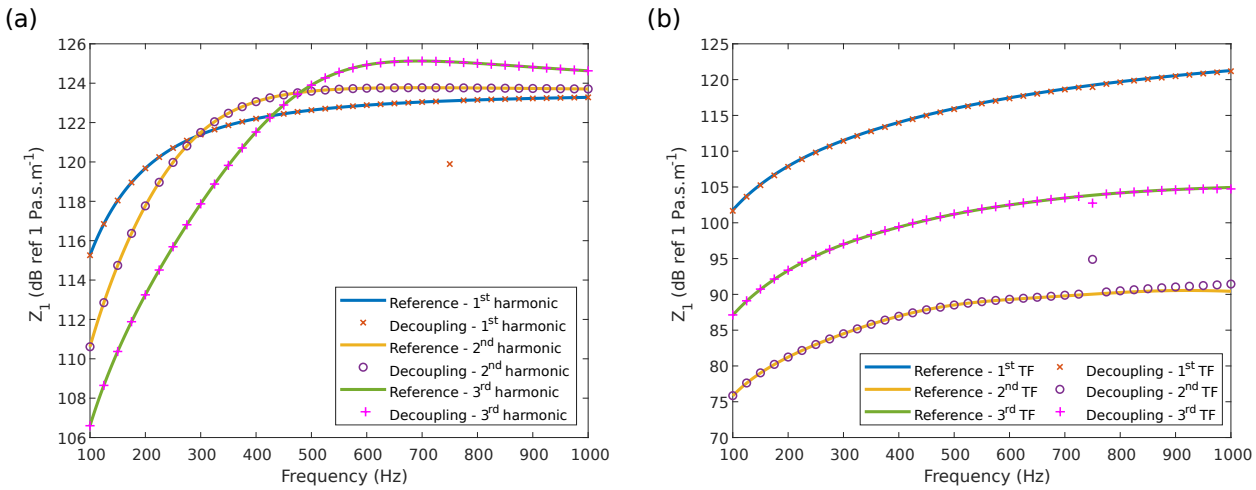

Figure 35: Comparison between the condensed impedances computed analytically and with the local rCTF approach. (a) Weighted spherical harmonics. (b) 2D gate functions.

are plotted in figure 35a. A perfect match can be seen between the rCTF approach and the reference calculation, except for a single frequency at 750 Hz for the first spherical harmonic. The reasons for this discrepancy at this particular frequency will be studied in the next subsection.

Concerning the comparison for 2D gate functions as CFs, figure 35b shows the results for 3 different condensed transfer functions (TFs) in order to sweep different possibilities (the coordinates given correspond to the $(\theta_{i-1}, \phi_{i-1})$ bottom left angle in figure 34a, with the origin of coordinates taken on the top of the sphere):

- the first TF is a direct impedance on a trapezoid patch ($\theta_{i-1} = \pi/2, \phi_{i-1} = 0$): the excitation patch and the observation patch are the same.

- the second TF is a crossed impedance between two trapezoid patches that are widely separated one from another ($\theta_{i-1} = \pi/3, \phi_{i-1} = 9\pi/5, \theta_{j-1} = 5\pi/6, \phi_{j-1} = 9\pi/5$).

- the third TF is a crossed impedance between a trapezoid patch and a triangular patch that are close to each other ($\theta_{i-1} = \pi/3, \phi_{i-1} = 8\pi/5, \theta_{j-1} = \pi/6, \phi_{j-1} = 12\pi/7$).

As with the weighted spherical harmonics, the comparison between the reference curves and the rCTF curves show a quasi-perfect match, except for the second and third transfer functions for which an error appears at 750 Hz (as in figure 35a for the weighted spherical harmonics as CFs).

In the following subsection, the numerical sensitivity of the method will be investigated to identify the possible sources of this error at 750 Hz.

3.3.3.2 Analysis of numerical sensitivity

The application of Eq. (3.22) related to the rCTF method involves the inversion of the subtraction of the impedance matrices, $\mathbf{Z_2} - \mathbf{Z_{1+2}}$. This inversion can imply numerical instabilities. As it has already been explained in subsection 2.2.2, the sensitivity of the matrix inversion to the numerical errors can be characterized by the condition number. Particularly high values indicate that the problem is ill-conditioned and sensitive to numerical errors.

In figure 36, the condition numbers of the impedance matrix of subsystem 2 and system 1+2, as well as the condition number of the inverted matrix, are plotted as a function of frequency for the weighted spherical harmonics. As the condensed impedance matrices are diagonal in this case, the condition number corresponds to the ratio between the largest value on the diagonal and the smallest one. It appears that for each of the matrices investigated, the problem is particularly ill-conditioned at 750 Hz, which was the critical frequency identified in the previous subsection. It can also be noted that for $\mathbf{Z_2}$ and $\mathbf{Z_2} - \mathbf{Z_{1+2}}$, two other frequencies show high condition numbers, at 497 Hz and 798 Hz. These two particular frequencies correspond to the resonance frequencies of the water sphere. As these frequencies are clearly identified and no significant error can be observed at these frequencies in the figure, they will not be investigated.

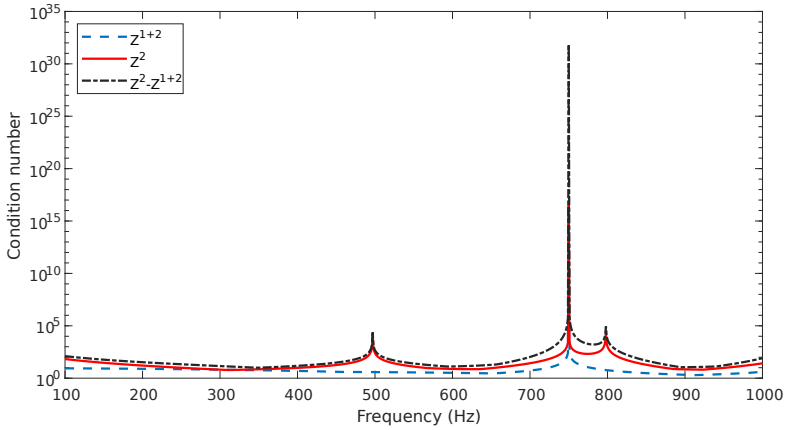

Figure 36: Condition number of the condensed impedances: case of the weighted spherical harmonics as CFs.

As the problem encountered in figure 35a appears only on the condensed impedance associated with the first spherical harmonic, the first condensed impedances of subsystems 2 and 1+2 are shown in figure 37. It can be seen that for both systems, an anti-resonant phenomenon appears at 750 Hz (i.e. the impedances tend toward zero). Looking at Eq. (C.22) and Eq. (C.13) reveals that this anti-resonant phenomenon is due to the first spherical Bessel function of the first kind that cancels at this frequency. In addition, since the two condensed impedances have the same value at this frequency, the subtraction of the two matrices that appear in Eq. (3.22) is also null. This explains the particularly high value of the condition

number and the numerical errors observed previously.

The same analysis was carried out with the 2D gate functions as CFs. The condition number also presents significant values for the two resonance frequencies of the water sphere and a very high value at 750 Hz, the anti-resonant frequency of the water sphere. Since the analysis leads to the same conclusions as for the weighted spherical harmonics, the results are not plotted here. These observations are consistent with the obervation made when evaluating the local decoupling of rods in subsection 2.1. This stresses out an intrinsic property of local decoupling procedures: they are particularly sensitive around the anti-resonant frequencies of the known subsystems, regardless of the considered problem (this conclusion was already evoked in previous works, see [180, 181]).

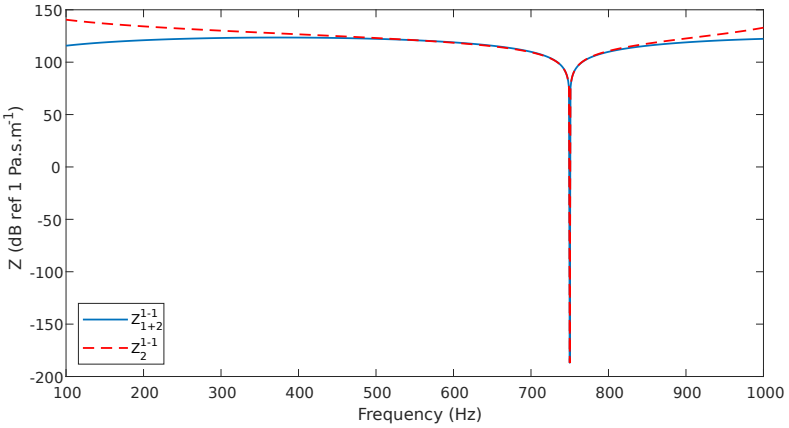

Figure 37: Comparison of the 1st condensed impedance of subsystems 2 and 1+2 (weighted spherical harmonics as CFs).

It must be noted that the previous calculations were performed considering a null damping loss factor for the fluid domain that constitutes the theoretical case. We observed that the absence of damping in the model leads to the high numerical instabilities encountered, especially around the anti-resonant frequency. This is also consistent with the observation made for the local decoupling of rods in subsection 2.1, when an increased damping coefficient led to mitigated errors in the decoupling process.

In practice, acoustic waves are slightly attenuated during their propagation due to dissipative effects (viscosity and thermal conductivity). In order to consider this physical phenomenon and to evaluate the impact of the damping on the numerical sensitivity of the method, slight damping is introduced in the model through a complex acoustic wavenumber

$$k_f^* = k_f(1 - \mathrm{j}\eta) \tag{3.32}$$

where j is the complex number $\mathrm{j}^2 = -1$.

In the following part of the study, the damping loss factor of the water is set to $\eta = 0.001$. The condition numbers related to the impedance matrices were recalculated by considering

this slight damping and are shown in figure 38. It is noteworthy that the values were greatly reduced in general and for the critical frequencies in particular, compared to the case without damping. The inverted matrix $\mathbf{Z_2} - \mathbf{Z_{1+2}}$ is still ill-conditioned at the anti-resonant frequency, but to a much smaller extent.

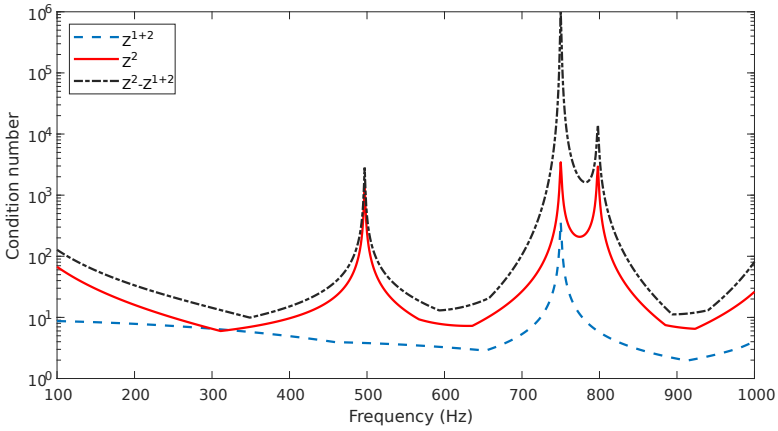

Figure 38: Condition number of the condensed impedances with a slight damping (weighted spherical harmonics as CFs).

As the condition number was significantly reduced by adding damping in the model, we can expect to obtain accurate results with the rCTF approach over the whole frequency range of interest. This is verified in figure 39. The errors observed in figure 35 for the case without damping are not observed for the case with slight damping. This result is valid for the two types of CFs considered in this paper.

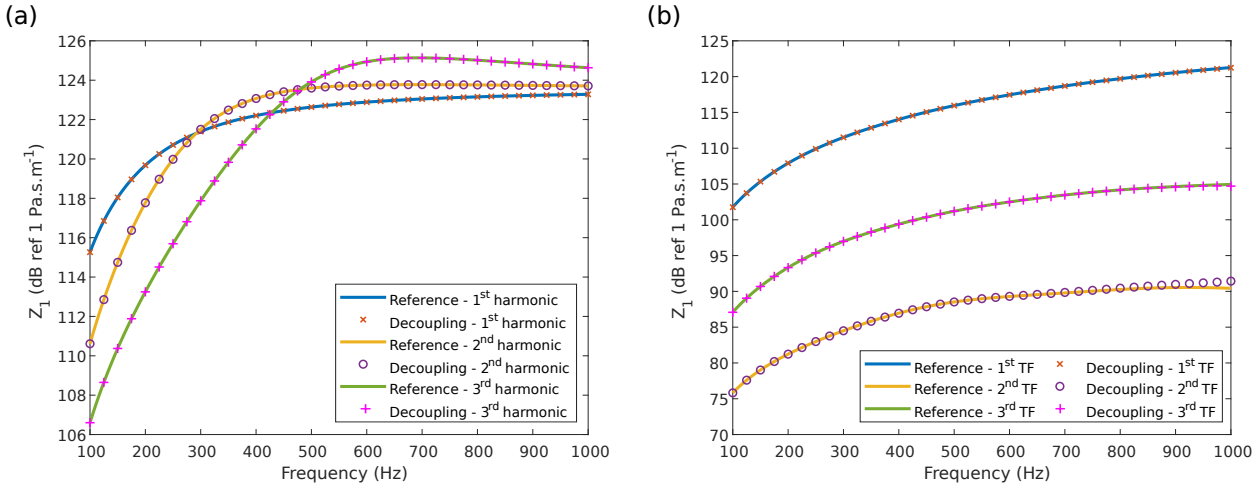

Figure 39: Comparison between the condensed impedances computed analytically and with the local rCTF approach. Case with a slight damping in the model. (a) Weighted spherical harmonics. (b) 2D gate functions.

It can be concluded from this study that the decoupling formula in Eq. (3.22) is validated numerically for the practical case including a slight damping in the water medium (i.e. for the non-conservative system). The dissipative effect allows to avoid the numerical errors

at the anti-resonant frequency of the water sphere that were observed for the case without damping (i.e. the conservative system).

3.3.4 Decoupling of the condensed impedances with the global rCTF approach

3.3.4.1 Results

If the decoupling formula of Eq. (3.22) has been validated for the local decoupling technique, it will now be investigated for the global decoupling approach presented in figure 32. The results of the decoupling will be compared to the results of the analytical expression of $\mathbf{Z_1}$ (given in Appendix C). Even if we are only interested in the response of the target subsystem, it can also be interesting to study the capacity of the global decoupling approach to correctly describe the condensed impedances of the residual subsystem, and to account for the decoupling between the target and residual subsystems. Also, if in subsection 3.3.3, the results were shown for the two different kinds of CFs, the investigations here will be carried out using the 2D gate functions only as CFs. This choice is motivated by the fact that the weighted spherical harmonics were useful to analyze the results of the decoupling but they will be hardly transposable to other systems. In addition, it can be observed in figure 39 that the decoupling with the weighted spherical harmonics produces perfect results in the entire frequency range, while the decoupling with the 2D gate functions exhibits slight shifts in the high frequencies. It will hence be interesting to see if these discrepancies subsist with the global decoupling approach.

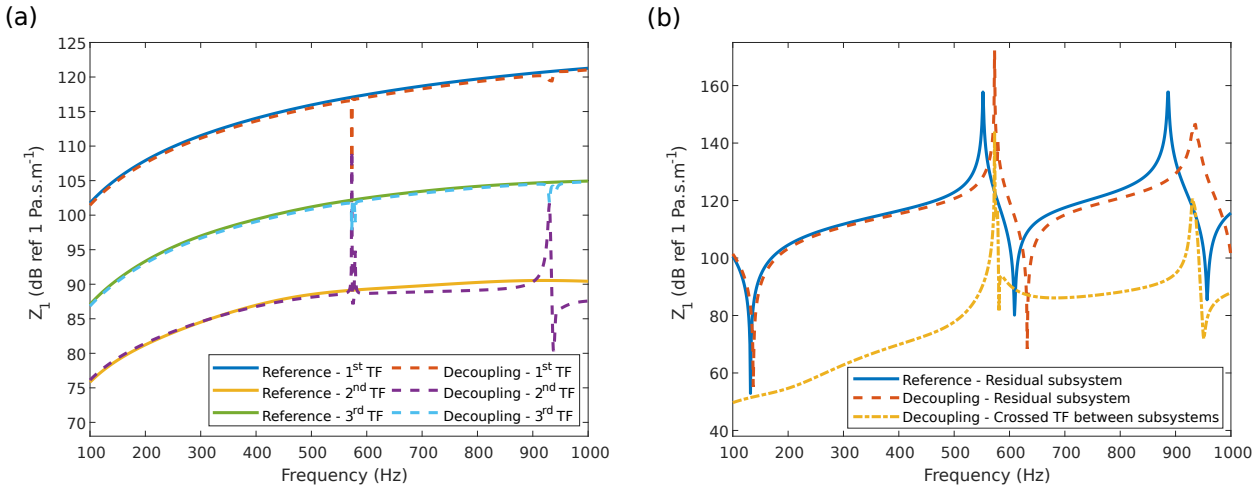

Figure 40: Comparison between the condensed impedances computed analytically and with the global rCTF approach. (a) Condensed impedances of the target subsystem. (b) Condensed impedances of the residual subsystem and crossed condensed impedance between a patch on the exterior surface and a patch on the interior surface.

The results of the global decoupling technique are shown in figure 40. The condensed impedances of the target subsystem are presented in figure 40a for the same TFs as in figure

39b. We can see that this global decoupling process induces huge errors around 575 Hz and 935 Hz, errors that have not been observed for the local decoupling case. Also, the behavior of the residual subsystem (corresponding to a water sphere with a radius of 0.9 m) in figure 40b is not correctly described, as the predicted resonance frequencies (573 Hz and 935 Hz) are higher than the real ones (552 Hz and 887 Hz). It is interesting to notice that the resonance frequencies of the residual subsystem obtained with the rCTF method correspond to the frequencies for which large errors were observed on the prediction of the condensed impedances of the target subsystem in figure 40a (i.e. 575 Hz and 935 Hz). Finally, when looking at the yellow curve in figure 40b, the decoupling between the target and residual subsystems is not taken into account. Indeed, we should only see residual values as the two parts are not physically coupled (as it has been observed in section 2.2) whereas the values here are not negligible. In particular, peaks of resonance appear and seem to be located at the same frequencies than the errors observed for the target and residual subsystems.

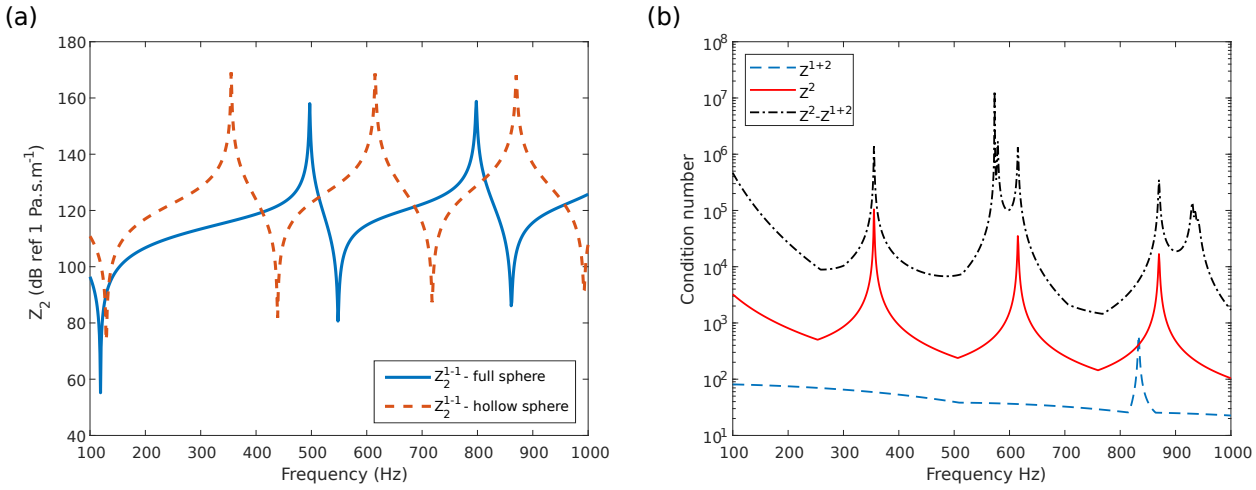

Figure 41: (a) Comparison of the condensed impedances of the full and hollow water spheres. (b) Condition number of the condensed impedance matrices of the global rCTF approach.

The direct condensed impedance on a trapezoidal patch of the hollow water sphere (subsystem 2) is shown in figure 41a, and a comparison is made with the same condensed impedance for the full water sphere used in the local decoupling approach in subsection 3.3.3. The first observation that can be made is that there is a supplementary resonance in the frequency range of interest for the hollow sphere than for the full sphere. This result was not expected at first sight as the goal of considering a hollow sphere was to reduce the standing waves in the radial direction and then the number of resonances of the subtracted subsystem. The resonances that are observed for the hollow sphere are resonances in the circumference of the system and were not anticipated. Furthermore, when looking at the condition number of the inverted matrix $\mathbf{Z_2} - \mathbf{Z_{1+2}}$, we can see two peaks appearing around the two previously identified frequencies (i.e. 575 Hz and 935 Hz). However, these peaks in

the condition number curves are not related to any resonance or anti-resonance of the hollow water sphere nor the infinite domain. This means that, contrary to what was observed in section 2.2, the resonant frequencies of the removed subsystem are not necessarily the most ill-conditioned in the global approach of decoupling. Hence, the promising results of the global decoupling technique observed in section 2.2 for the rod case study are not recovered here.

An explanation of the discrepancies observed could be found from the proximity of the two coupling surfaces. Indeed, it has already been observed for the case of strong coupling between an elastic plate and an acoustic cavity filled with water in [170, 171] that substructuring in the near-field of the plate could induce problems of convergence of the CTF approach. In the next subsection, a new test case will be considered in order to study this hypothesis on a different case.

3.3.4.2 Coupling and decoupling of a full water sphere and a hollow water sphere

The supplementary coupling and decoupling test case is presented in figure 42. The coupling problem in figure 42a consists in adding a hollow sphere to a full sphere. The interior radius of the hollow sphere corresponds to the radius of the full sphere, such that the coupling between these two subsystems is a sphere having the same radius as the exterior radius of the hollow sphere. It results that the decoupling problem in figure 42b consists in subtracting a hollow sphere from a full sphere in order to obtain a sphere of smaller radius than the initial one. The radii in this study are the same than the ones defined in table 4.

The formulation of the problem is slightly different than for the case illustrated in figure 32, as the subsystem 1 (the small sphere) has one coupling surface Ω_{int} to account for, whereas the subsystem 2 (the hollow sphere) has two coupling surfaces Ω_{ext} and Ω_{int}. Hence, the condensed impedance matrix of subsystem 2 will be separated into 4 submatrices as follows

$$\mathbf{Z_2} = \begin{bmatrix} \mathbf{Z_2^{11}} & \mathbf{Z_2^{12}} \\ \mathbf{Z_2^{21}} & \mathbf{Z_2^{22}} \end{bmatrix} \tag{3.33}$$

where the superscript 1 corresponds to the exterior coupling surface Ω_{ext} while the superscript 2 corresponds to the interior coupling surface Ω_{int}. The analytical values of these condensed impedances are given in Appendix C.3. We can underline that, as Ω_{ext} is at the boundary of the fluid domain, the excitation used to define the condensed impedances of the system 1+2 related to the patches belonging to this surface is a prescribed normal velocity (corresponding to the condensation function). As for the interior surface Ω_{int}, a prescribed normal velocity jump is used to define the condensed impedances as for the previous problem, because for the system 1+2 this inner surface is a fictitious one. Applying the superposition principle for linear passive systems along with the pressure continuity and velocities equilibrium as in

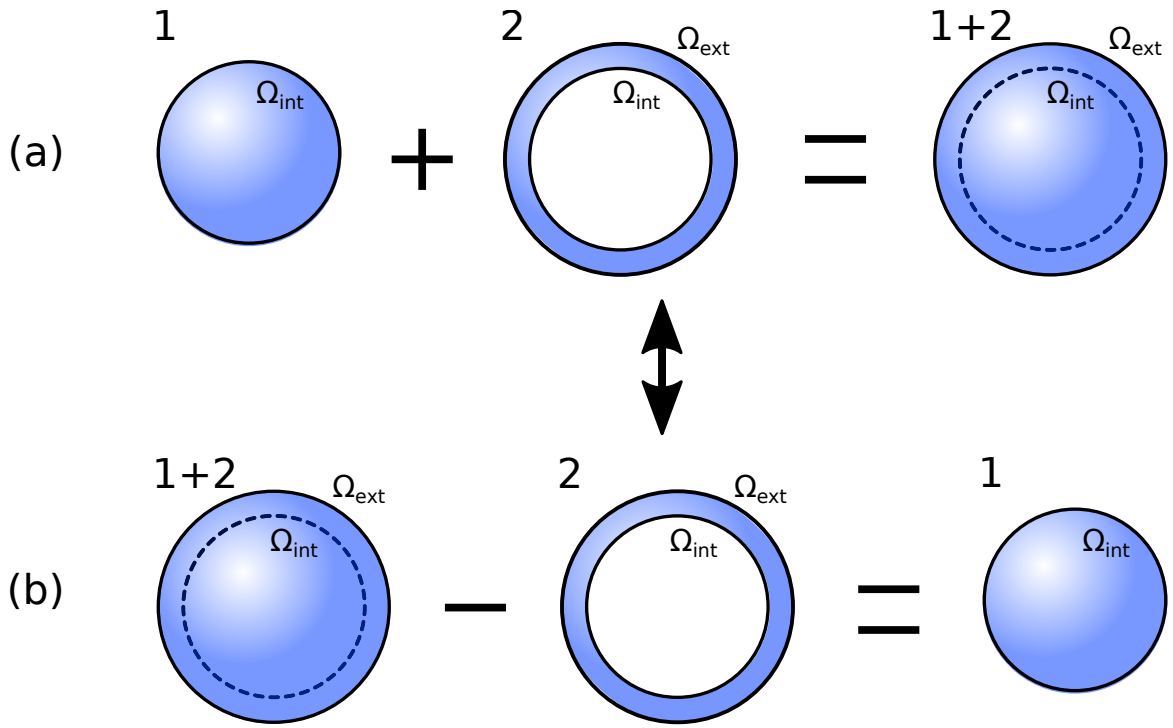

Figure 42: Supplementary coupling and decoupling test case. (a) Coupling problem. (b) Decoupling problem.

section 3.1 yields, after some development, the following expression for $\mathbf{Z_{1+2}}$

$$\mathbf{Z_{1+2}} = -\mathbf{Z_2^{12}} \left(\mathbf{Z_1} + \mathbf{Z_2^{22}}\right)^{-1} \mathbf{Z_2^{21}} + \mathbf{Z_2^{11}} \tag{3.34}$$

The decoupling problem can then be solved by inverting Eq. (3.34) in order to express the condensed impedances of the subsystem 1 from the condensed impedances of the subsystems 1+2 and 2

$$\mathbf{Z_1} = -\mathbf{Z_2^{21}} \left(\mathbf{Z_2^{11}} - \mathbf{Z_{1+2}}\right)^{-1} \mathbf{Z_2^{12}} + \mathbf{Z_2^{22}} \tag{3.35}$$

The result obtained with Eq. (3.35) is compared to an analytical calculation of the condensed impedances of a water sphere of radius 0.9 m in figure 43 for the same TFs as in figure 40. We can see that, for the same removed subsystem and the same distance between the two coupling surfaces as in the global decoupling approach (figure 32), the decoupling process of the condensed impedances works well better here than in subsection 3.3.4.1 with the infinite fluid domain 1+2. This means that the poor convergence of the decoupling process in the previous subsection does not come from the proximity between the two coupling surfaces. Hence, the origin of the two particularly ill-conditioned frequencies observed in figure 41b has not been clearly identified.

Alternatively, it was observed in subsection 2.2.3 that when the residual subsystem does not have any resonance in the frequency range of interest, the errors from the global decoupling approach are mitigated. This will be investigated in the next subsection.

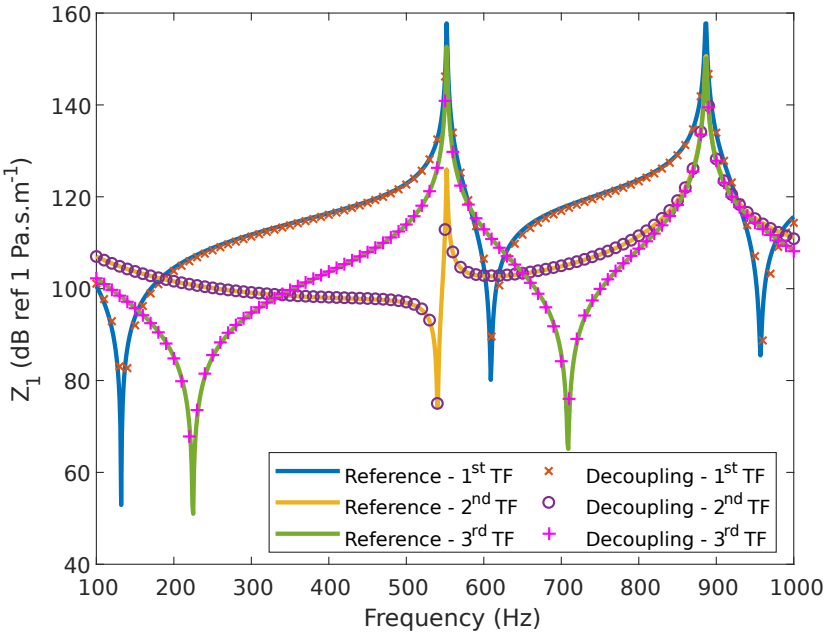

Figure 43: Comparison between the condensed impedances computed analytically and with the rCTF approach for the near-field test case.

3.3.4.3 Global decoupling with a small residual subsystem

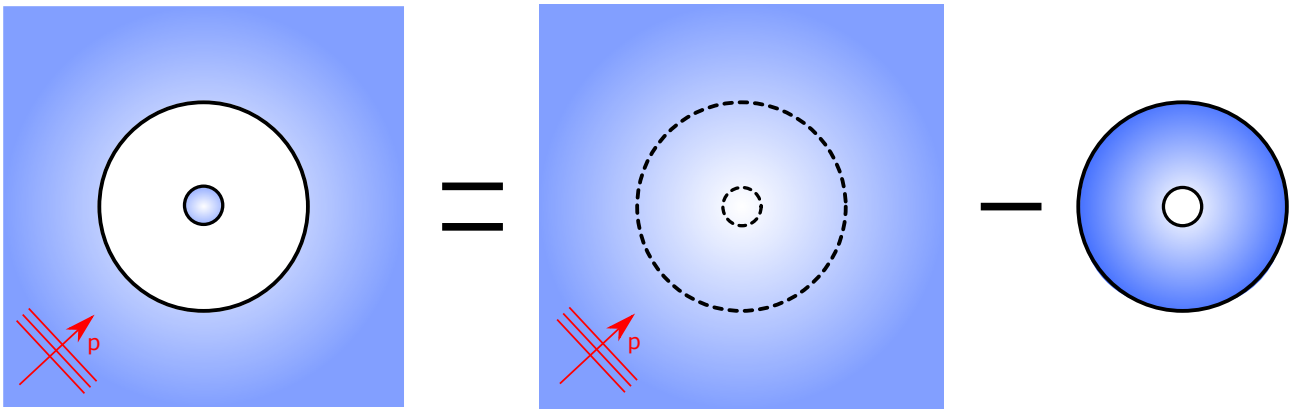

Figure 44: Global decoupling approach with an interior radius of 0.1 m.

In subsection 2.2.3, it was observed that for the exact same case of rod decoupling at the extremity of the master rod, the global decoupling approach was much more accurate than the local one. More generally, the global decoupling approach has shown that, for a given size of the subtracted subsystem, the results were better in the absence of resonances of the residual subsystem. Following this statement, the global decoupling approach will be investigated here for the case of a hollow sphere with an interior radius of 0.1 m as illustrated in figure 44.

If we compare the condensed impedances of the full sphere with the condensed impedances of the hollow sphere of interior radius 0.1 m in figure 45a, we can see that the two subsystems

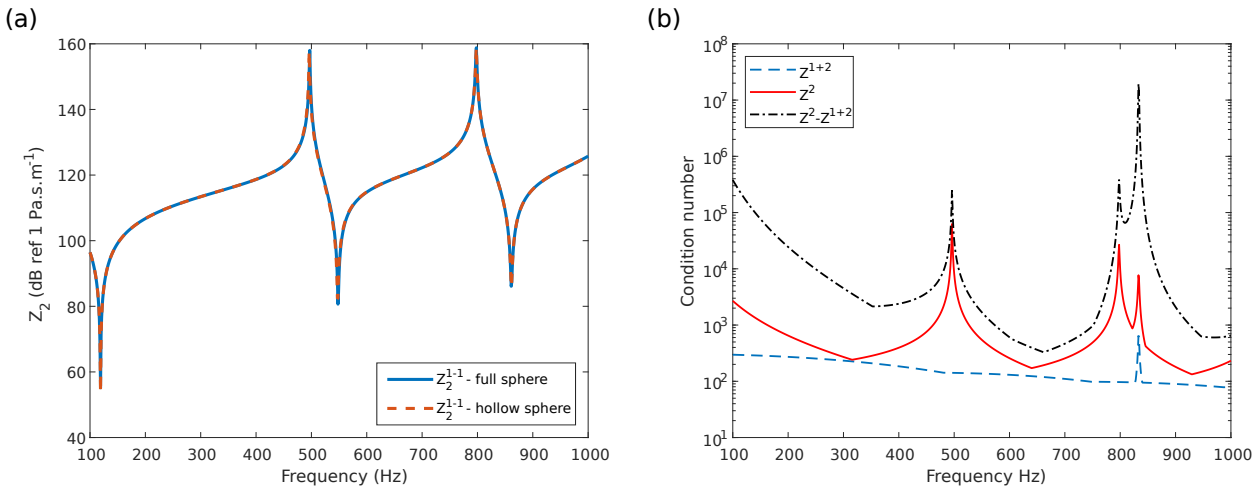

Figure 45: (a) Comparison of the condensed impedances of the full water sphere and the hollow water sphere of interior radius 0.1 m. (b) Condition number of the condensed impedance matrices of the global rCTF approach with the hollow water sphere of interior radius 0.1 m.

have an almost identical behavior, as there is only a 1 Hz shift in the first resonance of the subsystem, while the second resonance appears at the same frequency. This means that the comparison between this global decoupling appraoch and the local decoupling one of figure 31 can be considered as a 3D analogy of the asymptotic approach in subsection 2.2.3.

Also, looking at the condition number of the inverted matrix in figure 45b shows that that there isn't any ill-conditioned frequency that is not associated with a resonant or anti-resonant phenomenon. Indeed, the most ill-conditioned (i.e. 833 Hz) frequency corresponds to the common anti-resonant frequency of the hollow sphere and of the infinite water medium. For the latter, it is different than for the local decoupling case even if the subsystem is the same, because the condensed impedance matrix does not have the same size nor values (see Appendix C.1).

Following this, the comparison between the analytical and global rCTF calculations of $\mathbf{Z_1}$ is shown in figure 46a for the target subsystem and figure 46b for the residual subsystem. The same TFs as in figure 40 are presented. We can observe that the results in figure 46a are very close to the ones of figure 39b related to the local decoupling approach. Furthermore, the residual system is correctly described in figure 46b, which can be explained by the fact that there is no resonant nor anti-resonant phenomenon in the frequency range of interest for the residual system. Finally, the absence of coupling between the two surface Ω_{int} and Ω_{ext} is correctly taken into account as the values displayed by the yellow curve are negligible compared to the other curves.

The results obtained for this study show that the global approach of the rCTF study for 3D cases can only by valid in the absence of resonant and anti-resonant phenomena of the residual subsystem in the frequency range of the study. This limits the applicability of

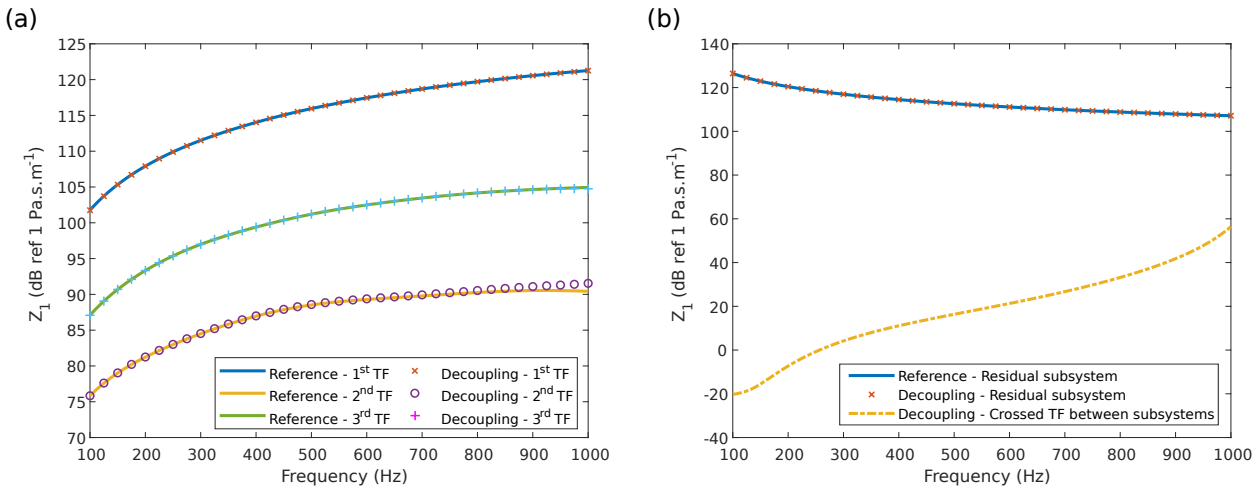

Figure 46: Comparison between the condensed impedances computed analytically and with the global rCTF approach with the hollow water sphere of interior radius 0.1 m. (a) Condensed impedances of the target subsystem. (b) Condensed impedances of the residual subsystem and crossed condensed impedance between a patch on the exterior surface and a patch on the interior surface.

the method, but there could still be an interest of using this approach when evaluating the response at any point of the decoupled subsystem. This will be investigated in the next section.

3.3.5 Prediction inside the fluid domain with the rCTF method: pressure scattered by the rigid sphere

Now, let us focus on assessing the rCTF approach to predict the pressure at a given point inside the target subsystem using the formula in Eq. (3.24). To do that, we consider the scattering problem of a plane wave impacting a rigid sphere, as this case was intensively studied in literature [8] (see figure 47). In the following section, the principle of this calculation used as reference will be recalled before comparing its results with the rCTF approach.

3.3.5.1 Reference calculation

In spherical coordinates, the pressure field of a plane wave of angular frequency ω travelling in the direction $(\theta = \pi, \phi = 0)$ can be defined by

$$p_i(R,\theta) = P_i \mathrm{e}^{\mathrm{j}k_f R\cos\theta} \tag{3.36}$$

with P_i being the amplitude of the plane wave, and k_f the acoustic wavenumber in the fluid domain. The expression in Eq. (3.36) can be expanded in spherical harmonics using Legendre polynomials

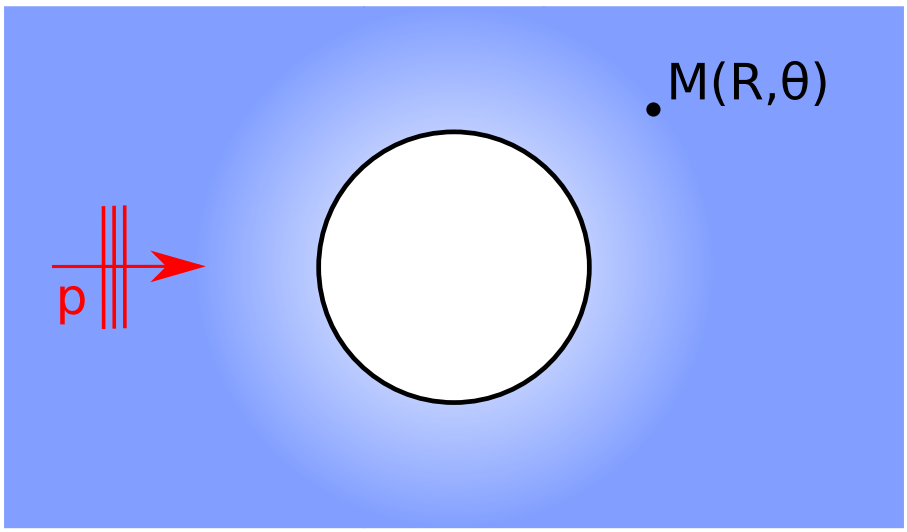

Figure 47: Reference case: plane wave travelling towards a rigid sphere.

$$p_i(R,\theta) = P_i \sum_{n=0}^{+\infty} (2n+1)\,\mathrm{j}^n P_n(\cos\theta)\, j_n(k_0 R) \tag{3.37}$$

with $P_n(\cos\theta)$ the Legendre polynomial, and j_n the spherical Bessel function of the first kind.

Considering the solutions in the spherical coordinates of the homogeneous Helmholtz equation and the homogeneous Euler equation at the surface of the sphere, we can calculate the pressure scattered by the rigid sphere of radius a [8]

$$p_{s\infty}(R,\theta) = -P_i \sum_{n=0}^{+\infty} (2n+1)\,\mathrm{j}^n P_n(\cos\theta)\, \frac{j_n'(k_0 a)}{h_n'(k_0 a)} h_n(k_0 R) \tag{3.38}$$

where h_n is the spherical Hankel function of the first kind, and j_n' and h_n' are the derivatives of the spherical Bessel function of the first kind and the spherical Hankel function of the first kind with respect to their argument, respectively. The total pressure field in the medium is thus the addition of the incident and the scattered pressures $p_{\text{tot}} = p_i + p_{s\infty}$. In practice, the infinite sums in Eqs. (3.37) and (3.38) must be truncated to a finite value. After trial and errors testing, the calculation converged for $N = 40$ spherical harmonics. This yields

$$p_{\text{tot}}(R,\theta) = P_i \sum_{n=0}^{40} (2n+1)\,\mathrm{j}^n P_n(\cos\theta) \left[j_n(k_0 R) - \frac{j_n'(k_0 a) h_n(k_0 R)}{h_n'(k_0 a)} \right] \tag{3.39}$$

3.3.5.2 Comparison for the local decoupling approach

To apply the decoupling formula in Eq. (3.24) to predict the total pressure at any point M_1 in the fluid domain, we must still evaluate $\mathbf{P_{1+2}}$, the condensed pressure vector induced by the acoustic plane wave and $\mathbf{P_{1+2}^{M_1}}$, the condensed pressure vector induced by a monopole source located at point M_1 and of unit volume velocity. The details of the calculations are

given in Appendix C.5. The results of the rCTF calculations can be observed in two different ways. The first possibility is to evaluate the pressure at a given point of the domain over the whole frequency range, and the second one is to plot a cartography of the pressure in the domain, at a given frequency. For the sake of clarity and in order to avoid having too many figures, the first solution will be presented for the calculation using the weighted spherical harmonics as CFs, while the second solution will be presented for the calculation using the 2D gate functions as CFs (this is related to the local rCTF form, as only the 2D gate functions were used as CFs for the global rCTF form).

At first, the decoupling formula in Eq. (3.24) is tested using the weighted spherical harmonics as CFs for the local decoupling approach, by evaluating the pressure at a given point of the domain over the frequency range of interest. This calculation is also a means of evaluating the criterion proposed in Eq. (3.30), related to the maximal degree of the associated Legendre polynomial N_L. The results are presented in figure 48 for 4 different points, to account for different possibilities regarding the angle and the distance to the surface of the sphere. The quantity plotted here is the sound pressure level (SPL), in dB, the reference sound pressure being $p_0 = 1\ \mu Pa$

$$L_p = 20 \log \left(\frac{p}{p_0} \right) \tag{3.40}$$

For each point, the rCTF method is applied with 3 different values of N_L to evaluate the convergence of the method regarding the criterion defined. In section 3.3.2.3, the criterion in Eq. (3.30) yielded $N_L = 5$, corresponding to $N = 36$ CFs. The results are also presented for $N_L = 3$ and $N_L = 7$, corresponding to $N = 16$ and $N = 64$ CFs, respectively. Both calculations were carried out considering a damping loss factor, $\eta = 0.001$.

The results displayed in figure 48 show that the convergence criterion proposed in Eq. (3.30) is verified, because the evolution of the pressure for each evaluated point is described correctly, with errors that never exceed 1 dB. The results with $N_L = 3$ clearly show that taking fewer CFs than the criterion defined leads to large errors, while the results with $N_L = 7$ are very accurate, but required an increase in computation time. Finally, we can conclude that the results obtained with $N_L = 5$ are very satisfactory, both in terms of accuracy and computation time, and the criterion in Eq. (3.30) is validated from a practical point of view.

In the following, the calculation of the total pressure in the domain (corresponding to the sum of the incident pressure and the pressure scattered by the rigid sphere) is carried out using the 2D gate functions as CFs, using the definition of the patches at the surface of the sphere presented in figure 34b. The results obtained with the proposed method (i.e. Eq. (3.24)) can be compared to the theoretical results given by Eq. (3.39). The map of the sound pressure

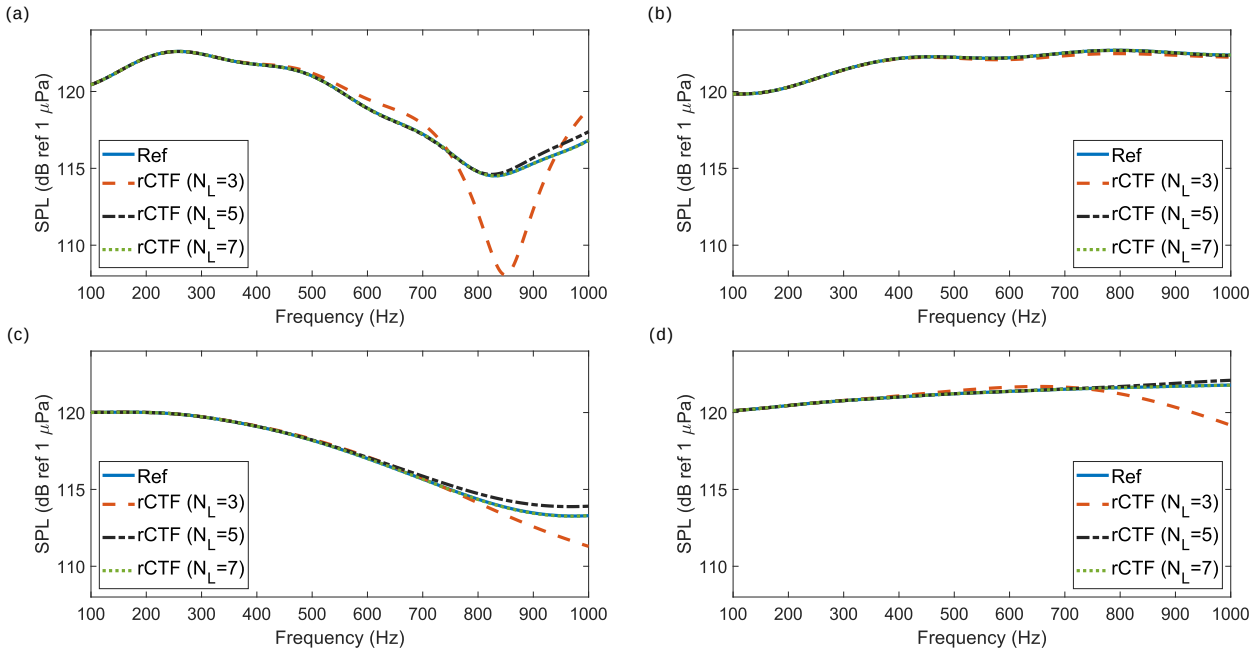

Figure 48: Total pressure in the medium - Comparison between the theoretical results and the local rCTF results for 4 different points with the weighted spherical harmonics as CFs. Point 1 - $r = 1.5$ m, $\theta = \pi$; Point 2 - $r = 1.3$ m, $\theta = 4\pi/7$; Point 3 - $r = 1$ m, $\theta = \pi/3$; Point 4 - $r = 1.5$ m, $\theta = 0$.

level (in dB ref 1 μPa according to equation 3.40) around the sphere is presented in figure 49 for the 2 calculations and for 3 different frequencies:

- f_1=497 Hz corresponds to the first resonant frequency of the water sphere.
- f_2=750 Hz corresponds to the anti-resonant frequency of the water sphere.
- f_3=1000 Hz corresponds to the highest calculated frequency.

The latter allows us to verify if the method converges correctly when the criterion is applied whereas the first two correspond to the critical frequencies already evoked in the previous section.

For all the graphs, the plane wave is travelling towards the positive x direction and reaches the sphere at $x = -1$. The graphs on the left hand side show the results of the theoretical calculation (i.e. Eq. (3.39)), while the figures on the right hand side show the results of the decoupling calculation (i.e. Eq. (3.24)). As for the weighted spherical harmonics, both calculations were carried out considering a damping loss factor $\eta = 0.001$.

All the graphs display a similar global behavior, with a maximum pressure around the point of impact of the plane wave with the sphere (i.e. $(x, y) = (-1, 0)$) while the minimum pressures are located in the shadow zone of the sphere (around $\theta = \pi/6$) and in a zone before the point of impact (between $x = -1.2$ and $x = -2$) where destructive interferences appear.

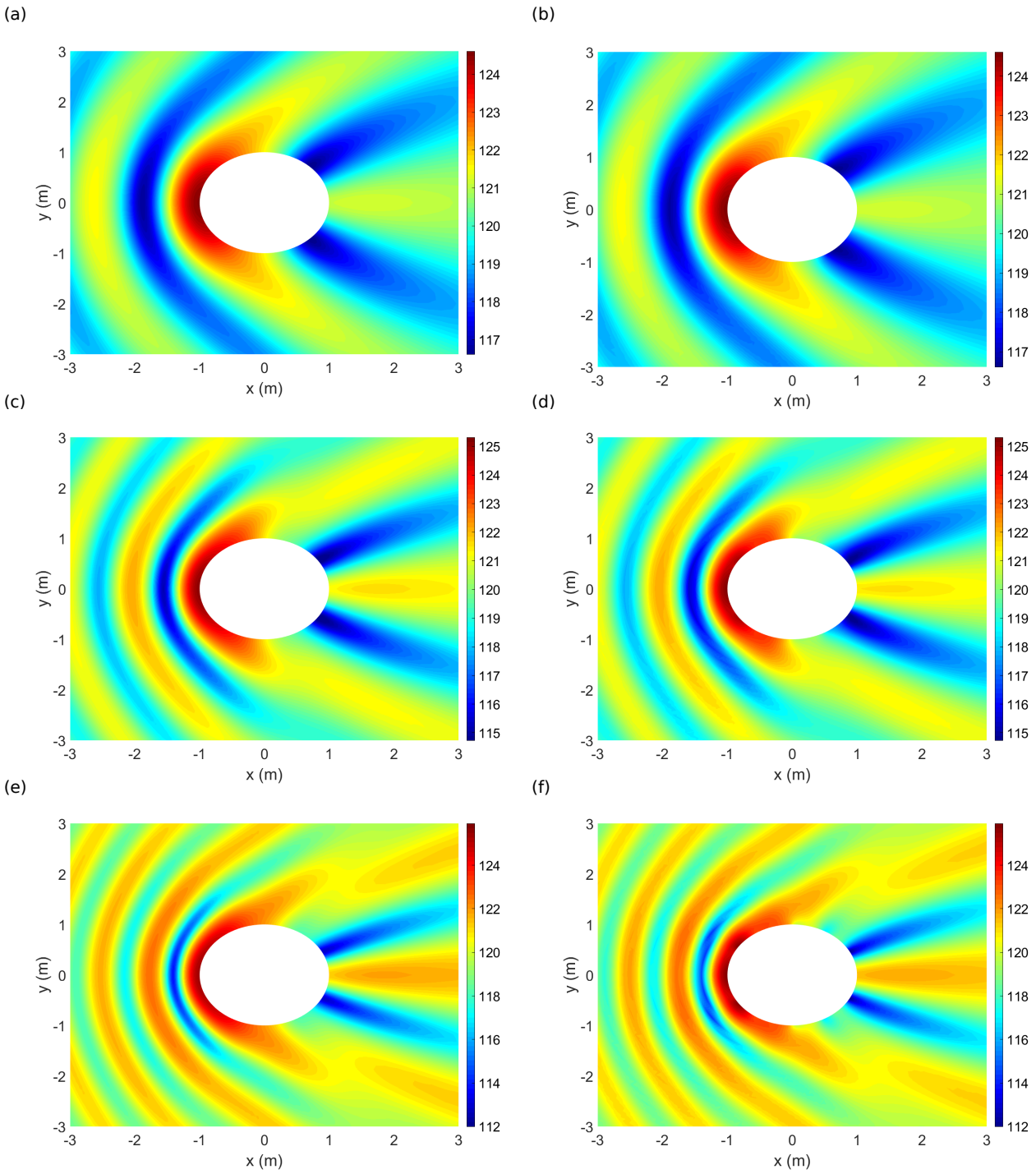

Figure 49: Total pressure in the medium - Comparison between the theoretical results (a,c,e) and the local rCTF results using 2D gate functions as CFs (b,d,f) for 3 frequencies: (a,b), 497 Hz; (c,d), 750 Hz; (e,f), 1000 Hz.

The comparison shows a very good agreement between the two calculations. Minor errors occur in the shadow zone of the sphere, and several numerical discontinuities occur at the maximum frequency, but the errors never exceed 1 dB. One has to be aware that the different fields of interest in this study (acoustic pressure, acoustic velocity) exhibit continuous properties. However, as described in Eq. (3.1), these fields are approximated on the basis of the CFs which, in the present case, are discontinuous (following the definition

of the patches in Eq. (3.29)). Hence, the decomposition of continuous fields on the basis of discontinuous functions leads to slightly rougher approximations than the decomposition on the weighted spherical harmonics displayed on figure 48, thus explaining the numerical discontinuities occuring at the maximum frequency. These discontinuities are thus not related to the number of CFs nor to the convergence criterion proposed in Eq. (3.31). Finally, we can affirm that these results are very satisfactory and thus we can conclude on the validity of the proposed developments for the local decoupling approach.

3.3.5.3 Comparison for the global decoupling approach

Concerning the global decoupling approach, the results will be presented for the case described in subsection 3.3.4.3 (i.e. with an interior radius of 0.1 m for the hollow sphere), still with the 2D gate functions as CFs. Once again, the calculations are carried out with a damping loss factor of $\eta = 0.001$. At first, the evolution of the scattered pressure as a function of frequency at the 4 same points as in figure 48 is shown in figure 50. Even if a comparison with figure 48 would not be relevant as the CFs are not the same, plotting these curves for the global decoupling approach allows verifying that there isn't any problematic frequency that has not been identified in subsection 3.3.4.3. The results of the global decoupling process in figure 50 are consistent with the observations made for the decoupling of the condensed impedances. The method is accurate from an analytical point of view, even if some slight disturbances can be observed in the high frequencies.

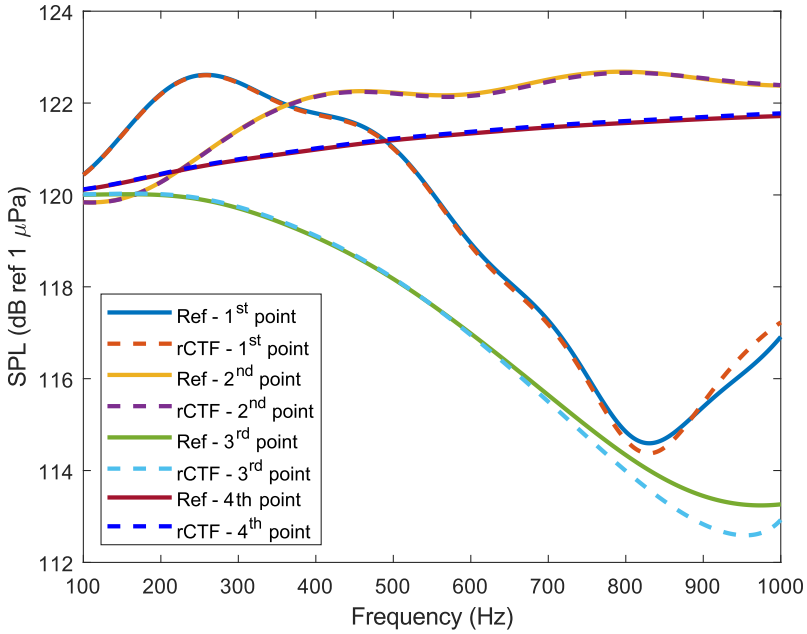

Figure 50: Total pressure in the medium - Comparison between the theoretical results and the global rCTF results for 4 different points. Point 1 - $r = 1.5$ m, $\theta = \pi$; Point 2 - $r = 1.3$ m, $\theta = 4\pi/7$; Point 3 - $r = 1$ m, $\theta = \pi/3$; Point 4 - $r = 1.5$ m, $\theta = 0$.

Similarly as for the local decoupling approach, a cartography of the pressure can be plotted for several frequencies in order to verify that the scattered field is correctly described. This is done in figure 51, where the scattered field is presented at 833 Hz (as it is the ill-conditioned frequency identified in figure 45b) and 1000 Hz. The results from this global approach at 1000 Hz are almost identical to the results from the local approach in figure 49, while at 833 Hz the calculation is very accurate. The global approach is thus also validated from an analytical point of view. Following this statement, the potential interest of the global approach compared to the local approach will have to be investigated when model errors are introduced in the calculations. This will be done in the next chapter.

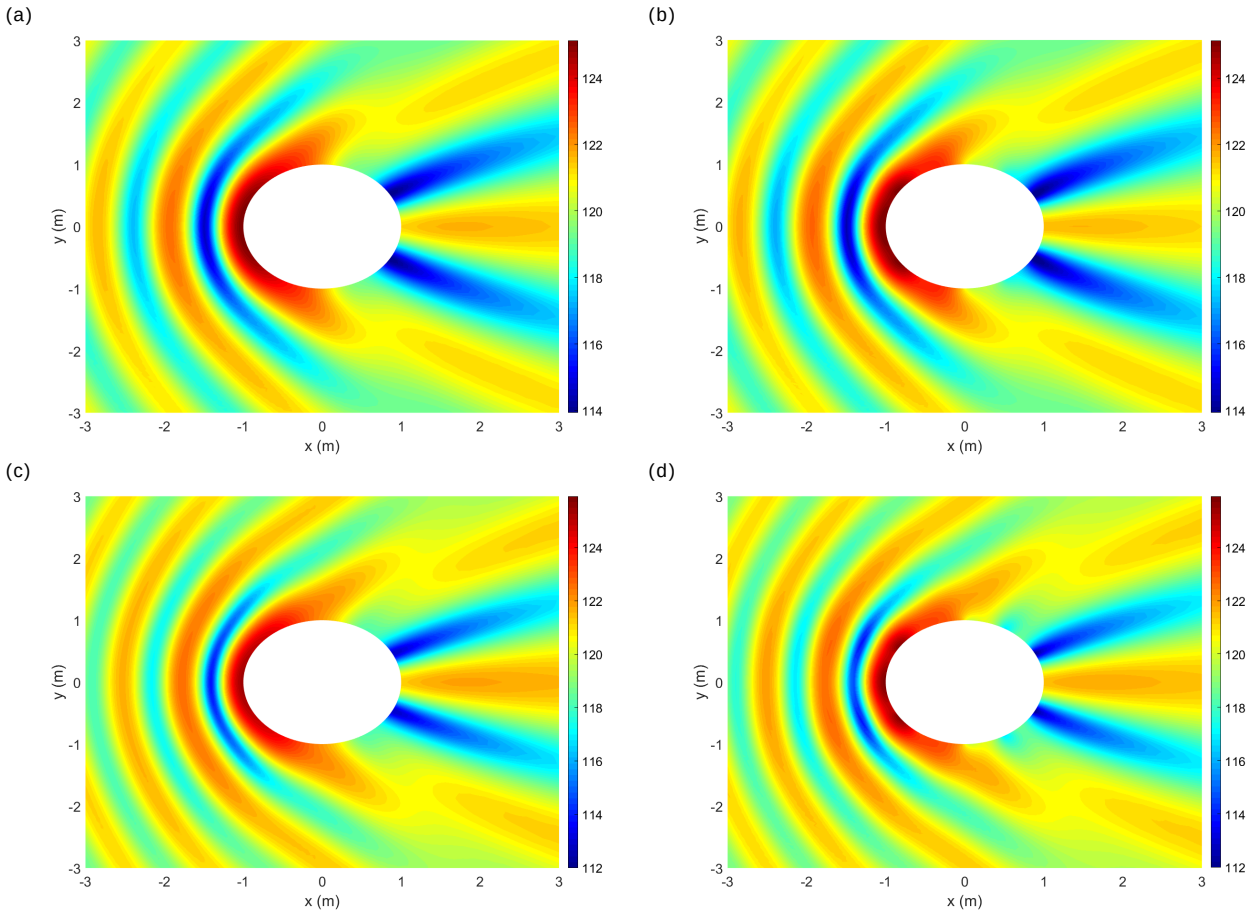

Figure 51: Total pressure in the medium - Comparison between the theoretical results (a,c) and the global rCTF results (b,d) for 2 frequencies: (a,b), 833 Hz; (c,d), 1000 Hz.

3.4 Conclusion

In this chapter, the theoretical framework of the reverse Condensed Transfer Function method has been established in order to estimate both the condensed impedances and the response at any point of the target subsystem. The principle has been presented for the case of acoustic problems. However, as the formalism of the CTF approach was developed for mechanical,

acoustic or vibroacoustic problems, the reverse formulation can be easily derived for these different types of problems.

The formulation was studied numerically in the case of a rigid sphere immersed in water and impacted by a plane wave. Investigations were carried out to derive a local and a global decoupling approach and the accuracy of both methods has been studied. In the local approach, using analytical models of the infinite water medium and of the water filled sphere, the proposed approach allowed predicting by subtraction the behavior of the rigid sphere immersed in water. Comparisons of the results with theoretical calculations led to validate the approach for two types of condensation functions, namely weighted spherical harmonics and 2D gate functions. The case with the weighted spherical harmonics as condensation functions is a particular case where the impedances of the different condensation functions are uncoupled. Consistently with the observations made in the local decoupling technique of chapter 2, the introduction of damping in the model (as it occurs in real situation due to viscosity and thermal conductivity) mitigates the numerical instabilities around the anti-resonance of the water sphere in the local approach.

For the global decoupling approach, the behavior of the rigid sphere immersed in water was obtained from a model of the infinite water medium and of the hollow water sphere. It was found that the method works only when the residual subsystem (a water sphere of smaller radius in this case) does not exhibit any resonant or anti-resonant behavior in the frequency range of interest. The damping introduced in the local approach was directly taken into account for the investigations of the global approach, but it must be noted that it doesn't reduce all the observed discrepancies.

In the next chapter, numerical investigations will be carried out on the same test case by introducing model errors in the calculation of the condensed impedances. The investigations will be carried out with the local and global decoupling approaches in order to compare their robustness when model errors are introduced.

Chapter 4

Numerical sensitivity of the reverse Condensed Transfer Function method

In chapter 3, the principle of the reverse Condensed Transfer Function method has been presented, and the method was validated on a test case considering a local and a global formulation. For practical applications, the CTFs of the global system or of the subtracted subsystem would be generally evaluated using numerical methods. The use of such methods will introduce numerical errors in the evaluation of the CTFs and condensed pressures. In this chapter, the effect of these numerical errors on the prediction of the subtractive modelling approach is investigated. By doing so, the sensitivity of the method to numerical errors will be investigated for the two formulations. The principle of computing the condensed impedances from numerical models of bounded and unbounded domains will be presented in section 4.1, while an application on the same test case as in the previous chapter will be carried out in section 4.2. The robustness of the local and global rCTF approaches will be compared in order to select which of these two approaches will be used in the next chapter.

4.1 Computing the condensed impedances and pressures from numerical acoustic models

In this chapter, all the developments are carried by considering the 2D gate functions as CFs (i.e. the patches). Indeed, the weighted spherical harmonics presented in section 3.3.3 were interesting in order to understand the principle of the method as the components of each spherical harmonics are uncoupled one from each other, but they constitute a particular case which cannot be applied on other non-spherical systems.

When considering acoustic or vibroacoustic systems, it is important to draw a distinction between bounded and unbounded domains in order to apply the most appropriate numerical method to describe the system. Indeed, as presented in subsection 1.3.1, while the FEM can be very accurate for multiple problems, it is not adapted for infinite domains, for which the BEM is generally used. The calculation of the CTFs from numerical models will hence

be presented here for these two cases. The developments will be carried out for acoustical systems, which means that the condensed transfer functions will be condensed impedances, but the reasoning can be transposed to other systems.

4.1.1 Condensed impedances of bounded systems

The Finite Element Method has proven itself to be a powerful tool to study bounded acoustic systems of moderate size. The principle for calculating the condensed impedances of a bounded subsystem α (for instance, the sphere of the subtracted subsystem in the previous chapter) from its FEM model will be developed here. For an acoustical system, the FEM formulation that is solved yields

$$\Big([\mathbf{K}] - \omega^2[\mathbf{M}](1 - 2\mathrm{j}\eta)\Big)\{\mathbf{P}\} = \{\mathbf{Q}\} \tag{4.1}$$

where $[\mathbf{K}]$ and $[\mathbf{M}]$ are the acoustic stiffness and mass matrices, respectively, η is the damping loss factor, $\{\mathbf{P}\}$ is the output pressure vector, and $\{\mathbf{Q}\}$ is the input volume velocity vector.

In order to compute the condensed impedance matrix of this system, the nodes of the FEM model on the coupling surface Ω (or coupling surfaces Ω_{int} and Ω_{ext} for the particular case of global decoupling) of the system must be associated with the different patches. For an incident patch j, all the nodes that have been identified to be belonging to this patch are excited by a unit volume velocity flow rate weighted by the area of the patch (consistently with the definition of the CFs in Eq. (3.29)). Following this, the input volume velocity vector $\{\mathbf{Q^j}\}$ associated to the incident patch j will have N_j components Q_n^j, with N_j being the number of nodes belonging to the patch j

$$Q_n^j = \frac{\delta S_n}{\sqrt{\Omega_j}}, \quad n \in [\![1, N_j]\!] \tag{4.2}$$

where δS_n is the area around the node n, and Ω_j the area of the patch j. The resulting pressure vector $\mathbf{P^j}$ of the FEM model is then obtained by inverting the dynamic matrix of Eq. (4.1)

$$\mathbf{P^j} = \Big([\mathbf{K}] - \omega^2[\mathbf{M}](1 - 2\mathrm{j}\eta)\Big)^{-1}\{\mathbf{Q^j}\} \tag{4.3}$$

In order to compute the condensed impedance between the incident patch j and the receiving patch i, all the M_i nodes belonging to the receiving patch must be identified, and the resulting pressures at these nodes are summed

$$Z_\alpha^{ij} = \frac{1}{\sqrt{\Omega_i}} \sum_{m=1}^{M_i} P_m^j \delta S_m \tag{4.4}$$

where P_m^j is the pressure at node m (belonging to the patch i) when the system is excited on the patch j, δS_m is the area around the node m, and Ω_i the area of the patch i.

4.1.2 Condensed impedances of unbounded systems

To compute the condensed impedances at the coupling surface Ω of an unbounded system γ (for instance, the infinite fluid domain of system 1+2 in the previous chapter), a formulation derived from the indirect BEM formulation will be considered. As evoked in Eq. (1.35), the pressure field from a radiating surface can be expressed using a linear combination of single and double layer potentials [98]

$$p(M) = \alpha p_s(M) + \beta p_d(M) \tag{4.5}$$

In the following, as we are only interested in emulating a velocity jump at the crossing of the fictitious surface, only the single layer potential will be of interest. Hence, β is set to 0 while α is set to 1. The pressure field can then be written [96]

$$p(M) = \int\int_{\Omega} \nu(P) G(M,P)\, \mathrm{d}\Omega(P), \quad M \in \Omega, \quad P \in \Omega \tag{4.6}$$

where $\nu(P)$ is the single layer potential due to a layer of monopole sources and represents a velocity jump at the crossing of the fictitious surface Ω. $G(M,P)$ is the free-field Green function and corresponds to the pressure field at point M due to a monopole source located at point P. Its value is recalled

$$G(M,P) = -\frac{\mathrm{e}^{\mathrm{j}k_f(1-\mathrm{j}\eta)|M-P|}}{4\pi|M-P|} \tag{4.7}$$

with k_f being the acoustic wavenumber, η the damping loss factor and $|M-P|$ the Euclidian distance between points M and P. In order to evaluate numerically the integral in Eq. (4.6), the surface Ω is discretized into a finite number of points. The size of this discretization will be discussed later. To include this formulation into the rCTF problem to calculate the condensed impedances of an unbounded subsystem, the velocity jump in Eq. (4.6) must correspond to a condensation function φ^j (i.e. a patch), and each point of the discretization belonging to the incident patch j must be identified. Let us place the problem in an arbitrary system of coordinates, where the patches are distributed along the ξ and ζ dimensions. If the patch j is discretized into R_j points between ξ_{j-1} and ξ_j in the ξ dimension and into S_j points between ζ_{j-1} and ζ_j in the ζ dimension, the integral in Eq. (4.6) is approximated using a rectangular rule

$$p(M) = \sum_{r_j=1}^{R_j}\sum_{s_j=1}^{S_j} \frac{G(\xi_{r_j}-\xi_M, \zeta_{s_j}-\zeta_M)}{\sqrt{\Omega_j}} \delta\xi_j \delta\zeta_j, \quad \begin{cases} \xi_{r_j} \in [\xi_{j-1}, \xi_j] \\ \zeta_{r_j} \in [\zeta_{j-1}, \zeta_j] \end{cases} \tag{4.8}$$

where Ω_j is the surface of the patch j, and $\delta\xi_j$ and $\delta\zeta_j$ are the discretization step in the ξ dimension and ζ dimension of patch j, respectively.

In order to compute the condensed impedance between the incident patch j and the receiving patch i, all the points of the discretization belonging to the receiving patch must be identified, and the resulting pressures at these points are summed. If the patch i is discretized into R_i points between ξ_{i-1} and ξ_i in the ξ dimension and into S_i points between ζ_{i-1} and ζ_i in the ζ dimension, it yields

$$Z_\alpha^{ij} = \sum_{r_i=1}^{R_i} \sum_{s_i=1}^{S_i} \sum_{r_j=1}^{R_j} \sum_{s_j=1}^{S_j} \frac{G(\xi_{r_j} - \xi_{r_i}, \zeta_{s_j} - \zeta_{s_i})}{\sqrt{\Omega_j \Omega_i}} \delta\xi_j \delta\zeta_j \delta\xi_i \delta\zeta_i, \quad \begin{cases} \xi_{r_i} \in [\xi_{i-1}, \xi_i] \\ \zeta_{r_i} \in [\zeta_{i-1}, \zeta_i] \end{cases} \tag{4.9}$$

where Ω_i is the surface of the patch i, and $\delta\xi_i$ and $\delta\zeta_i$ are the discretization step in the ξ dimension and ζ dimension of patch i, respectively.

4.2 Application on the academic test case: scattering of a plane wave by a rigid sphere

Now that the framework to numerically compute the condensed impedances of acoustic bounded and unbounded subsystems has been developed, it will be applied to a test case. The same case as in section 3.3 will be considered (see figure 31 for the local approach and figure 32 for the global approach), as the analytical developments have already been carried out and can constitute a basis to compare the results of the analytical and numerical calculations.

4.2.1 Numerical calculations of the condensed impedances and pressures

4.2.1.1 Condensed impedances of the water sphere for the local approach

For the case of the water sphere, as the domain is bounded, a FEM formulation will be used as described in subsection 4.1.1. The FEM model of the sphere is generated using the Altair Hypermesh® software [198] and the mass and stiffness matrices are extracted from the model generated by the Structural Dynamic Toolbox implemented in MATLAB® [195]. The size of the mesh is a key element for the method to correctly converge. In acoustic problems, the retained criterion is generally 6 elements per acoustic wavelength at the highest considered frequency, f_{max}

$$d_e < \frac{c_f}{6 f_{max}} \tag{4.10}$$

with c_f=1500 m/s. As the computation is carried out between 100 and 1000 Hz, the maximum size of the elements should be lower than 0.25 m. The model obtained with this criterion is showed in figure 52a, and exhibits 1613 nodes and 7686 elements. It must be stressed that a damping loss factor of η=0.001 has been introduced in the FEM model as in chapter 3. In order to compute the condensed impedances of this subsystem, the surface of this sphere

is partitioned into patches as shown in figure 34b, following the criterion for the size of the patches defined in Eq. (3.31). According to the developments described in subsection 4.1.1, the nodes belonging to the incident patch j and the receiving patch i must be identified in the FEM model. An example of this identification is shown in figure 52b. The black dots correspond to the limits of each patch, while the green and red dots are the nodes of the FEM model belonging to the incident and receiving patches, respectively.

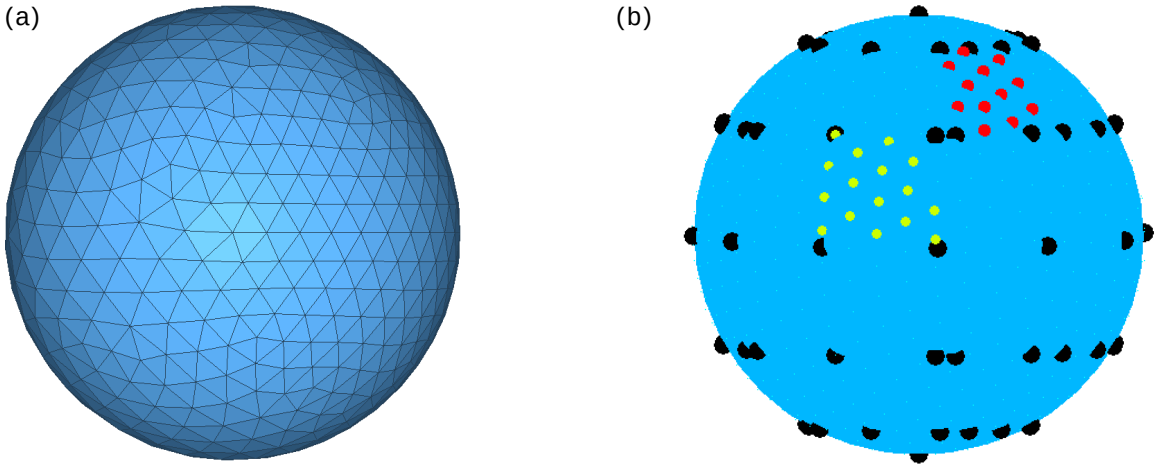

Figure 52: a) FEM model of the water sphere with a criterion of 6 elements per wavelength at the highest considered frequency. b) Localization of the nodes belonging to the incident and receiving patches.

Following the procedure 4.1.1, the matrix of the condensed impedances is computed, and the results can be compared to the analytical calculation described in Appendix C.2. In figure 53, the results obtained with the analytical and FEM calculation are compared for 2 different condensed impedances, a direct condensed impedance (1^{st} TF) and a crossed condensed impedance (2^{nd} TF).

We can observe that the results of the FEM calculation are globally correct, but the resonances of the water sphere are not accuratly predicted. Indeed, it was identified in subsection 3.3.1.3 that the water sphere exhibits two resonances in this frequency range, the first one at 497 Hz and the second one at 798 Hz. These are slightly shifted in the FEM calculation, as the first resonance of the FEM calculation is at 500 Hz while the seconde one is at 807 Hz. As is has been highlighted in subsection 3.3.3.2, the ill-conditioning of the inverted matrix in Eq. (3.22) at the resonant frequencies could lead to significant amplifications of the errors induced by these frequency shifts. For this reason, the retained criterion of 6 elements per acoustic wavelength at the highest considered frequency may not be enough for applying the rCTF. These calculations were hence reiterated on a finer model of the water sphere, with a criterion of 15 elements per acoustic wavelength at the highest considered frequency. This model is shown in figure 54a, and we can see in 54b that there are much more nodes belonging to each patch that there were for the criterion of 6 elements per acoustic

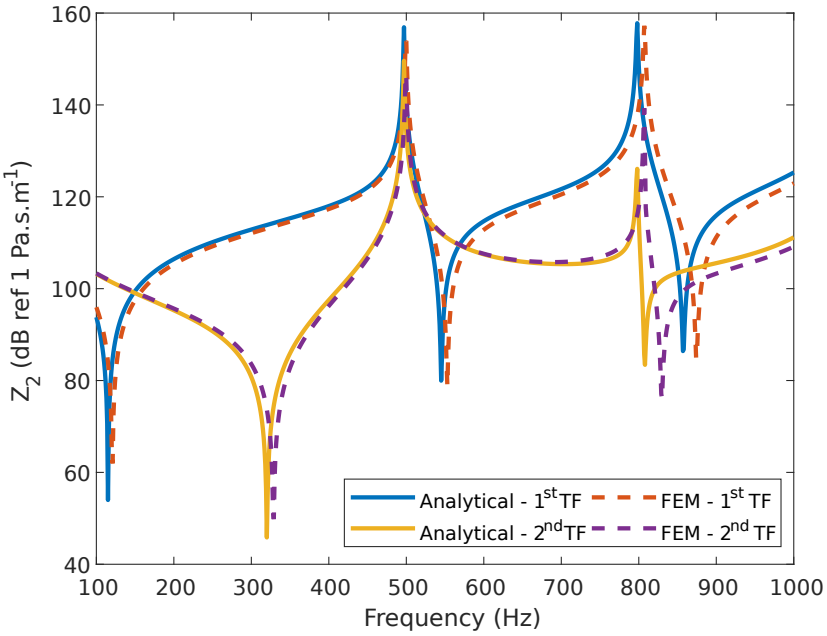

Figure 53: Comparison of the condensed impedances of the water sphere obtained with an analytical calculation and a FEM model.

wavelength. Indeed, the model exhibits 31302 nodes and 176996 elements.

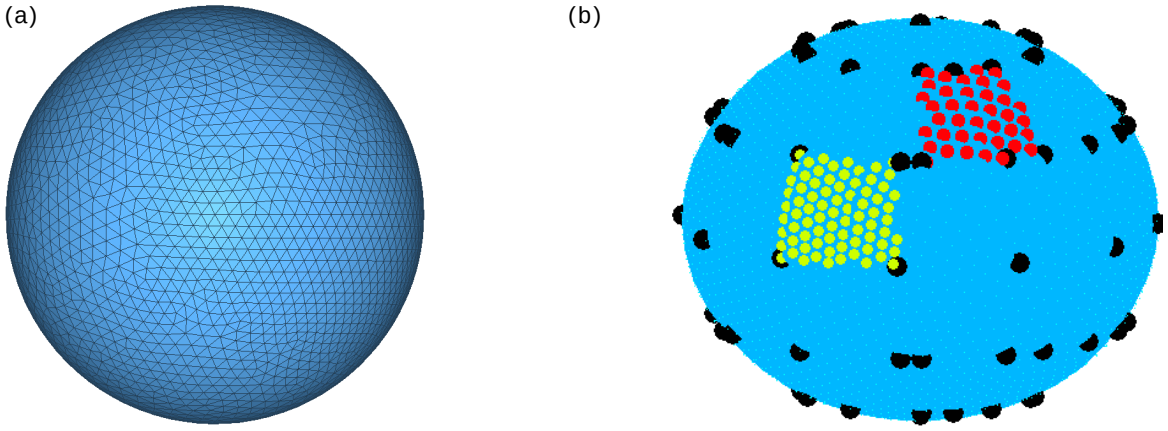

Figure 54: a) FEM model of the water sphere with a criterion of 15 elements per wavelength at the highest considered frequency. b) Localization of the nodes belonging to the incident and receiving patches.

When comparing the analytical and FEM calculations in figure 55, we can see that the new FEM calculation is more accurate. The first resonance appears at 497 Hz as for the analytical computation, while the second resonance appears at 799 Hz, which is a 1 Hz shift compared to the analytical computation. This means that, even if slight errors are remaining, better results can be expected when performing the decoupling calculations using the rCTF method than with the previous criterion.

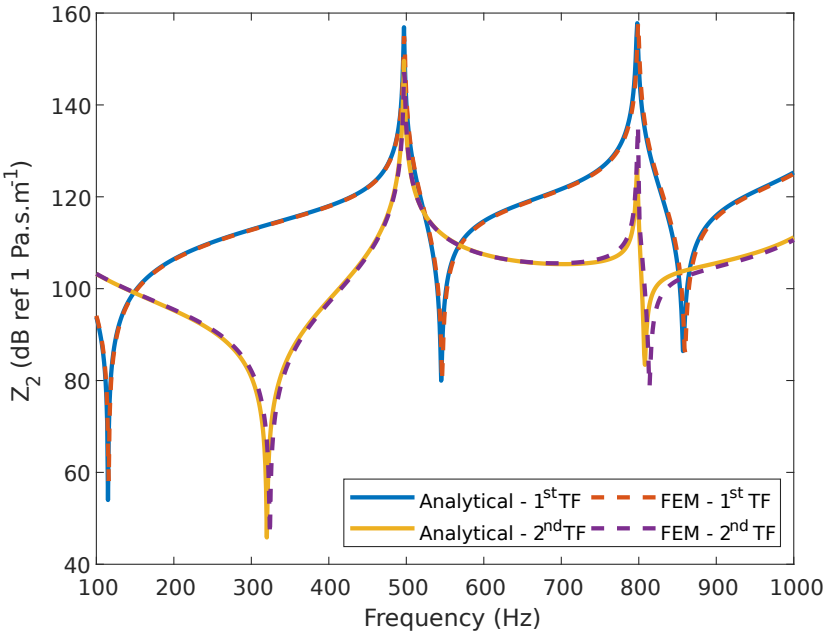

Figure 55: Comparison of the condensed impedances of the water sphere obtained with an analytical calculation and a finer FEM model.

4.2.1.2 Condensed impedances of the hollow water sphere for the global approach

For the case of the hollow water sphere necessary for the global decoupling procedure, as it is also a bounded system, a FEM formulation is used as well. The FEM model of the subsystem studied in subsection 3.3.4.3 is shown in figure 56, with a sectional view in figure 56b in order to see the interior radius of the hollow sphere. The criterion of 15 elements per acoustic wavelength at the highest considered frequency is once again retained, and the procedure for calculating the condensed impedances of the subsystem is the same as in subsection 4.2.1.1 for the water sphere.

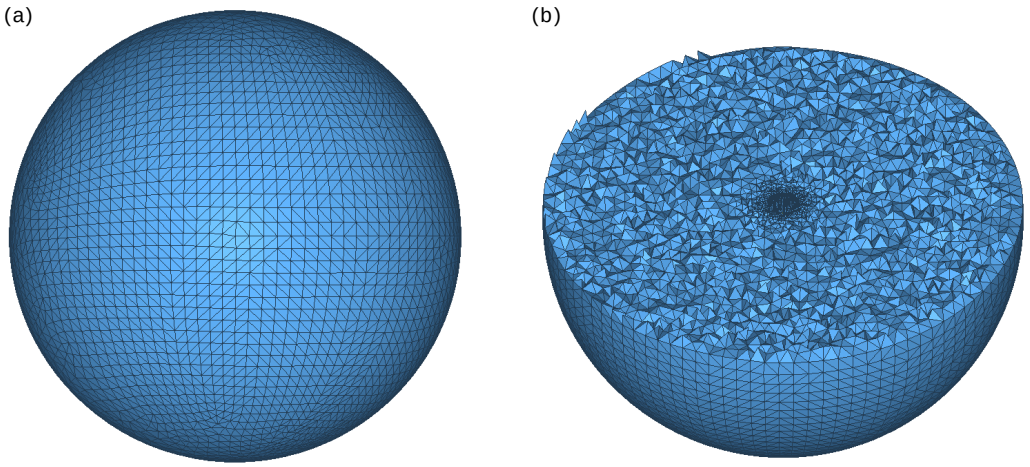

Figure 56: FEM model of the hollow water sphere. (a) Exterior view. (b) Sectional view.

The comparison between the analytical calculation (given in Appendix C.3) and FEM

calculations for the condensed impedances of the hollow sphere are shown in figure 57 for three different TFs:

- 1st TF: direct condensed impedance at the exterior surface of the hollow sphere.
- 2nd TF: crossed condensed impedance between two patches located at the interior surface of the hollow sphere.
- 3rd TF: crossed condensed impedance between a patch located at the exterior surface of the hollow sphere and a patch located at the interior surface of the hollow sphere.

As it was observed for the water sphere, the FEM calculation of the hollow sphere is very accurate, as there is at most a 1 Hz shift between the resonances calculated analytically and the ones calculated with the FE formulation.

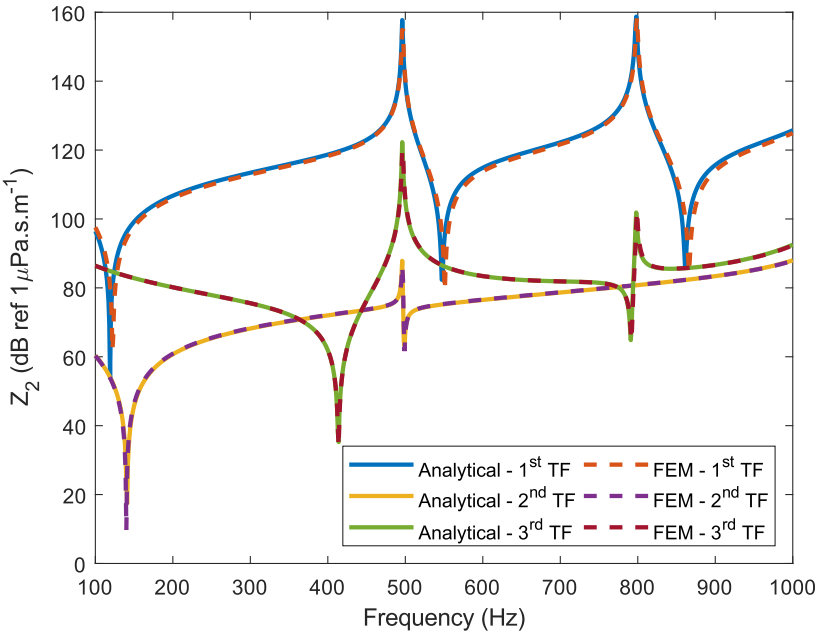

Figure 57: Comparison of the condensed impedances of the hollow water sphere obtained with an analytical calculation and a FEM calculation.

4.2.1.3 Condensed impedances of the infinite water medium

Concerning the infinite water medium, the condensed impedances will be computed using the procedure described in subsection 4.1.2 as it is an unbounded domain. As developed in Appendix C.1, the approach is the same whether the local or global formulations are considered. In the following, the reasoning will be carried out considering the local rCTF formulation, exhibiting only one fictitious surface Ω in the infinite medium. Similarly to the case of the FEM model of the water sphere, the size of the discretization of the fictitious surface

Ω of the sphere in the infinite medium plays a key role in the accuracy of the computation. However, there isn't any common criterion as for the FEM method, so an initial size of the discretization will be chosen arbitrarily and a trial and error test has been carried out to determine the appropriate size of discretization in order to have a good balance between accurate results and reasonable computational costs.

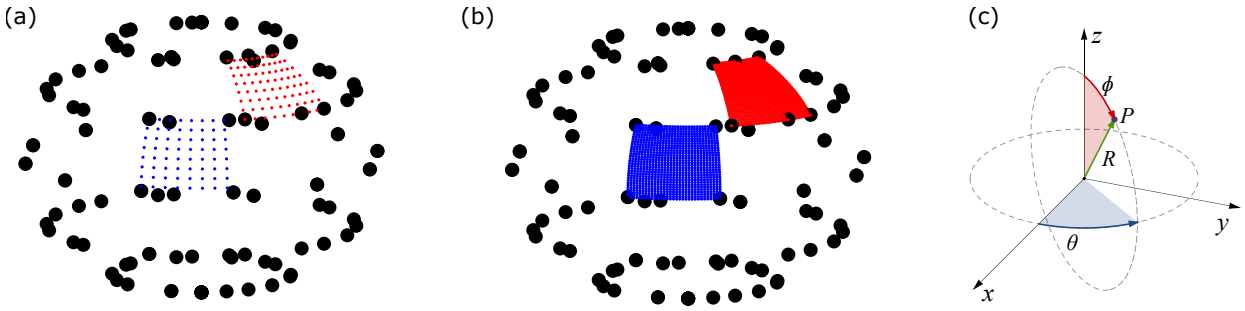

Figure 58: Example of two discretizations of the incident and receiving patches. (a) $\delta\theta = \delta\phi = 4°$. (b) $\delta\theta = \delta\phi = 1°$. (c) Associated spherical coordinate system.

In figure 58, two examples of discretizations of the incident and receiving patches are presented. In figure 58a, the discretization step is 4° in the θ and ϕ dimensions, while in figure 58b, the discretization step is 1° in the θ and ϕ dimensions (see figure 58c for the spherical coordinate system). The results for these two discretization sizes will be compared to the analytical calculations of the condensed impedances of the infinite water medium developed in Appendix C.1.

A particular attention must be paid to the case of the "input" condensed impedances (i.e. when the excited and receiving patches are the same). Indeed, looking at Eq. (4.7), the Green function exhibits a singularity when the source and receiving points are the same. A first possibility to circumvent this issue is to define a criterion of minimal distance ε between two points. Hence, if the source and receiving points are the same or if the distance between them is smaller than ε, one of the points is slightly shifted so that the distance between the two points will be ε.

A second possibility to circumvent this issue is to approximate this condensed impedance using an analogy with the radiation impedance of a baffled circular piston having the same surface as the patch. This quantity, corresponding to the pressure at the surface of the piston when a uniform vibrating velocity is prescribed, is defined as [199]

$$Z_R = Z_0 \left(1 - \frac{J_1(2k_f a_p)}{k_f a_p} - \mathrm{j}\frac{S_1(2k_f a_p)}{k_f a_p} \right) \tag{4.11}$$

where Z_0 is the acoustic impedance, a_p is the radius of the circular piston, J_1 is the Bessel function of the first kind and S_1 is the Struve function. By analogy, the impedance of a

uniform velocity jump on a circular surface is given by the same expression. The radius a_p of the baffled circular piston is obtained from the area Ω_i of the patch i:

$$a_p = \sqrt{\frac{\Omega_i}{\pi}} \tag{4.12}$$

One must note that this solution is independent of the discretization size, as the input condensed impedance of the patch is associated to the impedance calculated in Eq. (4.11). These two solutions are compared in figure 59 for two cases of direct condensed impedances corresponding to the two different geometries of patches (trapezoid patches and triangular patches). For each figure, a zoom is presented in the high frequency range in order to have clearer vision of the differences with the analytical calculation.

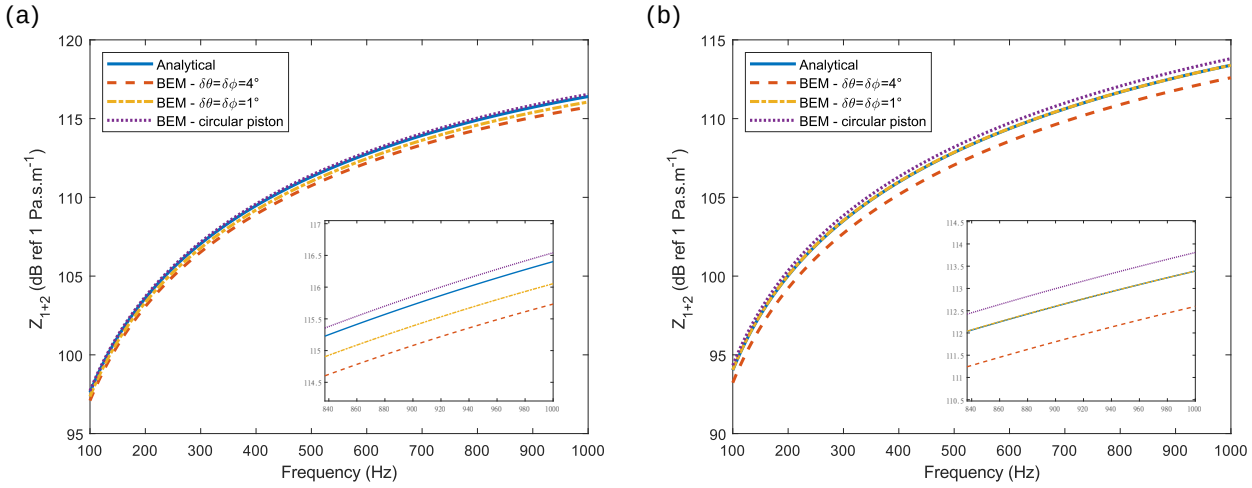

Figure 59: Accuracy of the calculation of direct impedances. a) Trapezoid patch. b) Triangular patch.

It is interesting to observe that for the trapezoid patch in figure 59a, the analogy of the circular piston is more accurate than the criterion of minimal distance for both discretization sizes. For the triangular patch however (figure 59b), the criterion of minimal distance is more accurate for a discretization size of 1°. This could be explained by two facts. Firstly, the equivalence between the triangular shape of the patch and the circular surface associated to Eq. (4.11) is certainly less accurate than for a trapezoidal shape. And secondly, the points of the discretization are closer to one another near the "top" of the sphere, meaning that there are more points in the triangular patches than there are in the trapezoid patches. Finally, it is relevant to compare the calculation times for the 3 solutions (for one condensed impedance), as it is necessary, in an industrial context, to mitigate the calculation costs. For a calculation from 100 Hz and 1000 Hz with a frequency resolution of 1 Hz, they yield:

- Criterion of minimal distance with a discretization size of 4°: 0.91 s and 0.97 s for the trapezoid and triangular patches, respectively.

- Criterion of minimal distance with a discretization size of 1°: 15 s and 44 s for the trapezoid and triangular patches, respectively.

- Analogy with the circular piston: 0.09 s and 0.12 s for the trapezoid and triangular patches, respectively.

From this observation, it can be concluded that the analogy with the circular piston is the best choice in order to have the best balance between accuracy and reasonable computational cost.

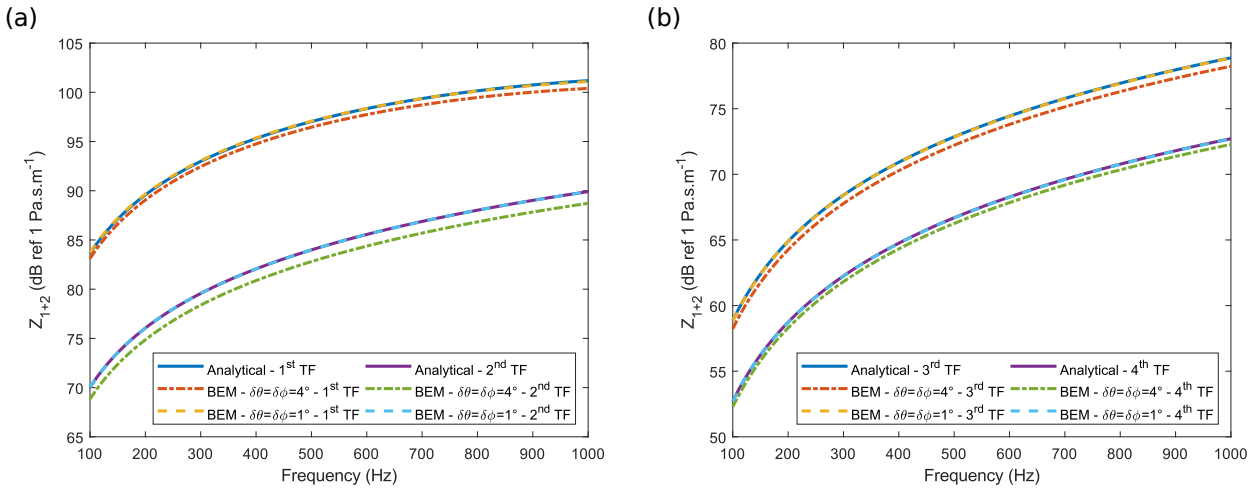

Figure 60: Comparison between the analytical and numerical calculations for the crossed impedances of the infinite water medium. a) Crossed impedances at the surface Ω for the local approach and Ω_{ext} for the global approach. b) Crossed impedances involving Ω_{int} for the global approach.

For the case of the crossed condensed impedances, a comparison between the analytical calculation (developed in Appendix C.1) and the numerical calculation is proposed in figure 60a for two different condensed impedances (involving trapezoid and triangular patches) at the fictitious surface Ω. Results are also shown for the global rCTF approach in figure 60b in order to verify that the results are correct regardless of the considered fictitious surface. Hence, the 3$^{\text{rd}}$ TF corresponds to a crossed impedance where the two patches are located on the two different fictitious surfaces Ω_{ext} and Ω_{int}, while the 4$^{\text{th}}$ TF corresponds to a crossed impedance for which the two patches are located on the interior fictitious surface Ω_{int}. For the numerical calculation, the results are presented for the two discretization sizes of 4° and 1°. It can be observed that the calculation with the finer discretization is more accurate, but more time consuming. The impact of these differences will have to be studied when performing the decoupling calculations in order to obtain the best balance between computation costs and accurate results.

4.2.1.4 Condensed pressures of the infinite water medium

Finally, in order to apply the rCTF method to predict the pressure at any point of the decoupled subsystem (Eq. (3.24)), it is necessary to compute the condensed pressures from the exterior and monopole excitations, $\mathbf{P_{1+2}}$ and $\mathbf{P_{1+2}^{M_1}}$, respectively, in the infinite water medium. To do so, the same discretization as in subsection 4.2.1.3 is used at the fictitious surface Ω of the sphere for the local approach, or fictitious surfaces Ω_{ext} and Ω_{int} for the global approach.

In order to compute the condensed pressure induced by the acoustic plane wave excitation, $\mathbf{P_{1+2}}$, the expression of the incident pressure from the plane wave is considered

$$P_{inc} = P_i \mathrm{e}^{\mathrm{j}k_f r\cos\theta} \tag{4.13}$$

where P_i is the amplitude of the incident plane wave. The condensed pressure on the receiving patch i is then obtained by evaluating this expression at each point of the discretization of the patch i, and by summing these responses using a rectangular rule. If the patch i is discretized into R_i points between θ_{i-1} and θ_i in the θ dimension and into S_i points between ϕ_{i-1} and ϕ_i in the ϕ dimension, it yields

$$\mathbf{P_{1+2}}(i) = \frac{P_i}{\sqrt{\Omega_i}} \sum_{r_i=1}^{R_i} \sum_{s_i=1}^{S_i} \mathrm{e}^{\mathrm{j}k_f a\cos\theta_{r_i}} r\sin\theta_{r_i}\delta\theta_i\delta\phi_i, \quad \begin{cases} \theta_{r_i} \in [\theta_{i-1}, \theta_i] \\ \phi_{s_i} \in [\phi_{i-1}, \phi_i] \end{cases} \tag{4.14}$$

where r can either be the radius of the exterior surface of the sphere or the radius of the interior surface of the hollow sphere, depending on the considered approach.

The procedure for calculating $\mathbf{P_{1+2}^{M_1}}$ is similar, with the incident pressure from the monopole located at the point M_1 replacing the incident pressure from the plane wave. The incident pressure at a given point M belonging to the fictitious surface Ω induced by a monopole source located at the point M_1 is given by

$$P_{inc}^{M_1} = -Q_i \mathrm{j}\omega\rho_f \frac{\mathrm{e}^{\mathrm{j}k_f|M_1-M|}}{4\pi|M_1-M|} \tag{4.15}$$

where Q_i is the amplitude of the monopole and $|M_1 - M|$ is the cartesian distance between the source and receiving points. The condensed pressure is obtained by evaluating this expression at each point of the discretization of the receiving patch i, and by summing these responses using a rectangular rule. If the patch i is discretized into R_i points between θ_{i-1} and θ_i in the θ dimension and into S_i points between ϕ_{i-1} and ϕ_i in the ϕ dimension, it yields

$$\mathbf{P_{1+2}^{M_1}}(i) = \frac{-Q_i \mathrm{j}\omega\rho_f}{\sqrt{\Omega_i}} \sum_{r_i=1}^{R_i} \sum_{s_i=1}^{S_i} \frac{\mathrm{e}^{\mathrm{j}k_f|M_1-M(\theta_{r_i},\phi_{s_i})|}}{4\pi|M_1-M_{r_i}|} r\sin\theta_{r_i}\delta\theta_i\delta\phi_i, \quad \begin{cases} \theta_{r_i} \in [\theta_{i-1}, \theta_i] \\ \phi_{s_i} \in [\phi_{i-1}, \phi_i] \end{cases} \tag{4.16}$$

The expressions in Eqs. 4.14 and 4.16 are compared to the analytical calculation (for which the expressions are given in Appendix C.5) in figure 61. The condensed pressure from the plane wave excitation is shown in figure 61a for a trapezoidal patch (1st CP) and a triangular patch (2nd CP), while it is shown for the monopole excitation in figure 61b for a trapezoidal patch (1st CP) and a triangular patch (2nd CP). Concerning the monopole excitation, the incident point was located at a point M_1 of spherical coordinates $(2, 0, 0)$. Once again, the results from the numerical calculation are presented for the two discretization steps of 4° and 1°. The results presented in figure 61 only correspond to patches at the exterior surface Ω_{ext} of the fictitious sphere (or hollow sphere for the global approach). Results at the interior fictitious surface Ω_{int} for the global rCTF approach are very similar, the only difference being the amplitude of the pressures. As the conclusions will be the same as for the exterior surface Ω_{ext}, they are not shown here.

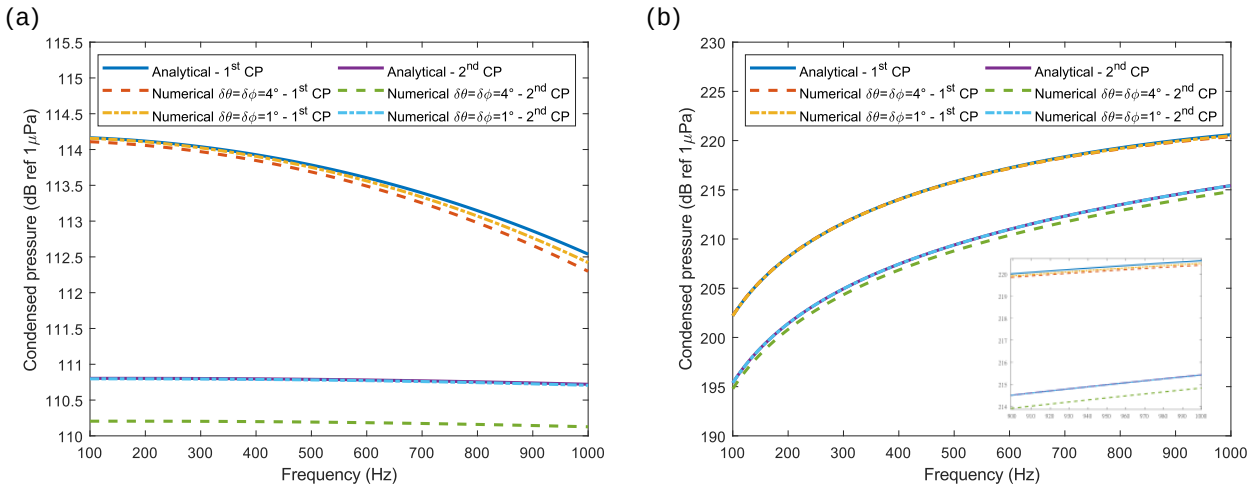

Figure 61: Comparison between the analytical and numerical calculations for the condensed pressures. a) Plane wave excitation. b) Monopole excitation.

Similarly as for the condensed impedances in subsection 4.2.1.3, the calculation with the finer discretization is more accurate and very close to the analytical calculation, but it is more time consuming. For the plane wave excitation, this does not cause any problem as the calculation has to be carried out once, but for the monopole excitation, it must be computed for all the points of the medium in order to draw a cartography of the scattered pressure as in figures 49 or 51. The choice of the discretization for this calculation will then be driven by the accuracy of the decoupling calculation. It is important to mention that, contrary to the calculation of the condensed impedances, the calculation of the condensed pressures will be less sensitive to model errors as it does not involve an inversion of matrix that amplifies errors. If this accuracy is judged to be sufficient for the coarser discretization size, this solution will be retained.

4.2.2 Decoupling calculations with the numerical models

4.2.2.1 Decoupling of the condensed impedances

As a first step of evaluating the sensitivity of the rCTF method to model errors, the calculation of the condensed impedances of the decoupled subsystem 1, $\mathbf{Z_1}$, are computed using $\mathbf{Z_{1+2}}$, $\mathbf{Z_2}$, and the decoupling formula of Eq. (3.22). The computations are carried out for the local and global rCTF approaches, and the results are compared to the analytical calculation of $\mathbf{Z_1}$ presented in Appendix C.4. In order to sweep different possibilities of transfer functions (TFs), the comparison is shown for:

- a direct condensed impedance on a trapezoid patch (the excitation and observation patch are the same) - 1$^{\text{st}}$ TF.
- a direct condensed impedance on a triangular patch - 2$^{\text{nd}}$ TF.
- a crossed condensed impedance between two trapezoid patches that are close to each other - 3$^{\text{rd}}$ TF.
- a crossed condensed impedance between a trapezoid patch and a triangular patch that are widely separated one from another - 4$^{\text{th}}$ TF.

Also, for the global rCTF approach, the condensed impedances of the residual subsystem (i.e. the water sphere of radius 0.1 m) and between the two surfaces Ω_{ext} and Ω_{int} are evaluated. For the latter, the absence of coupling between the subsystems must result in negligible values of the condensed impedances when performing the decoupling. This will be investigated in the next paragraphs.

The comparison between the analytical calculation and the numerical decoupling calculation is shown in figure 62. Figures 62a and b concern the local rCTF approach, while the results of the global rCTF approach are presented in figures 62c and d. Also, figures 62 a and c present the results for the coarse discretization in the infinite water medium (i.e. $\delta\theta = \delta\phi = 4°$), while figures 62 b and d present the results for the fine discretization in the infinite water medium (i.e. $\delta\theta = \delta\phi = 1°$). Comparing the results for the coarse and the fine discretizations allows having a perspective on the necessary level of accuracy of the numerical models to apply the rCTF method. We can see that for the local rCTF approach, the results are globally correct except around the anti-resonant frequency of the water sphere. For the global rCTF approach however, the errors are globally more constant along the frequency range, even if some slight disturbances can be observed for the 3$^{\text{rd}}$ and 4$^{\text{th}}$ TFs around 830 Hz. For both approaches, there is no substantial difference between the calculations with the two different discretization sizes.

What was observed in chapter 3 is found back in this numerical calculation, and is amplified due to the presence of numerical errors. Indeed, when looking at the condition

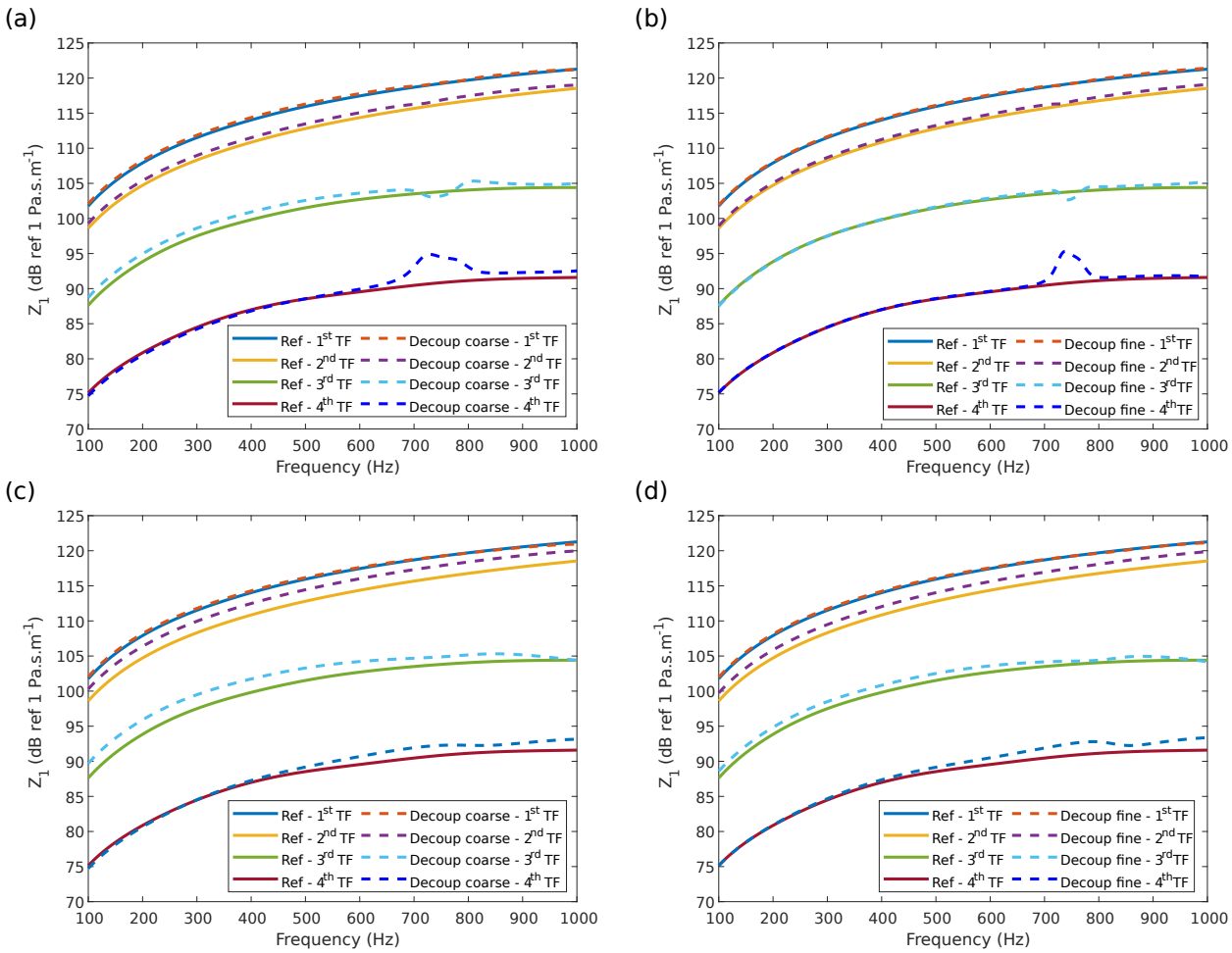

Figure 62: Comparison between the condensed impedances computed analytically and with the numerical rCTF approach. (a) Coarse discretization in the infinite water medium - local rCTF approach. (b) Fine discretization in the infinite water medium - local rCTF approach.(c) Coarse discretization in the infinite water medium - global rCTF approach. (d) Fine discretization in the infinite water medium - global rCTF approach.

number of the condensed impedance matrices of subsystems 1+2 and 2 and of the inverted matrix in figure 63, the maxima of the condition number for both the local and global approaches are located at the same frequencies shown in figures 38 and 45b, respectively. If the amplitudes of these maxima are lower than for the analytical case, this observation is due to the fact that contrary to the analytical calculation, for the numerical ones, the condensed impedance matrices of the global system 1+2 and of the subtracted subsystem 2 are not computed using the same approach. However, the presence of maxima in the condition numbers, especially around the anti-resonant frequencies of the subsystems, result in increased errors when performing the rCTF calculation with numerical errors in the condensed impedances of the subsystems. Also, we can see in figure 63 that the condition number is generally higher for the global approach, meaning that the errors can be more amplified. This explains that, except for the anti-resonant frequency, the errors are generally higher in the frequency range for the global approach than for the local approach in figure 62.

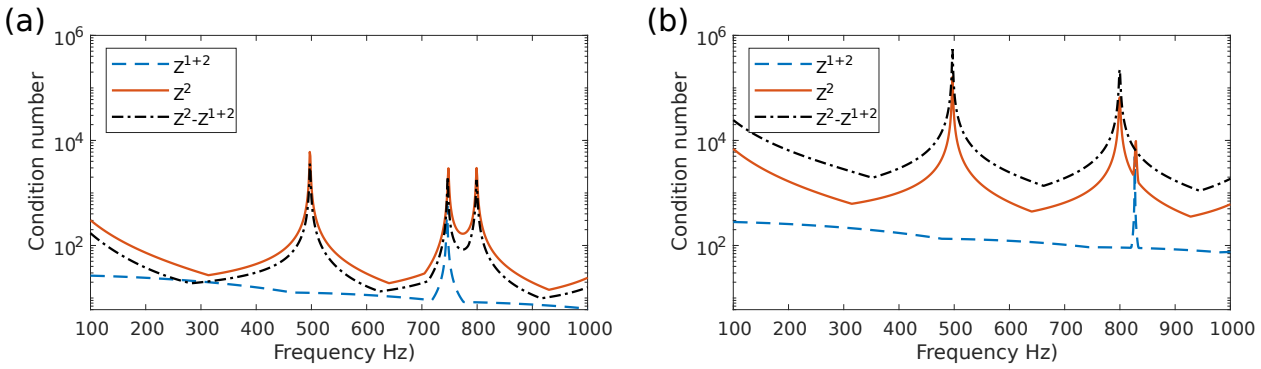

Figure 63: Condition number of the condensed impedance matrices and of the inverted matrix. (a) Local rCTF approach. (b) Global rCTF approach.

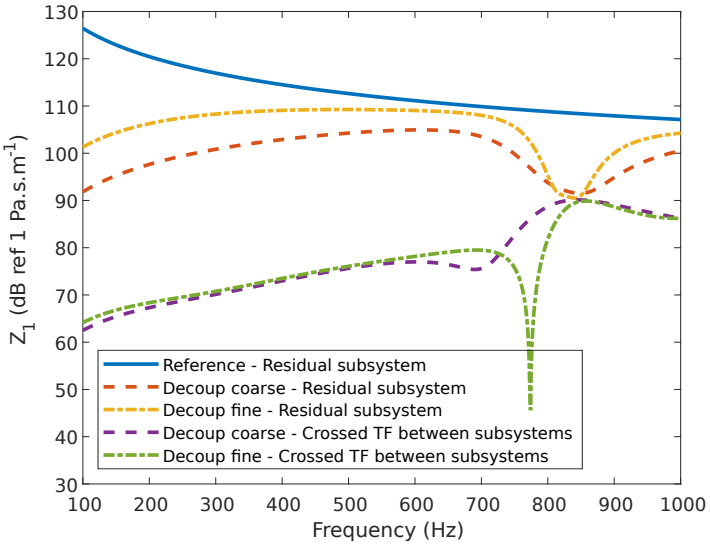

Figure 64: Condensed impedances of the residual subsystem and crossed condensed impedance between the two subsystems.

Concerning the condensed impedances involving the residual subsystem for the global rCTF approach, the results are shown in figure 64. Compared to the analytical case in subsection 3.3.4.3, the introduction of numerical errors induces important errors in the whole frequency range. The behavior of the residual subsystem is not correctly decribed and the errors are even amplified around 830 Hz which is the anti-resonant frequency of the hollow sphere and a frequency at which the condensed impedance matrix of the infinite water medium is ill-conditioned. The calculation with a finer discretization size is slightly better, but the errors remain high compared to the reference case. Concerning the crossed impedance between the subsystems, as also shown in figure 64, the absence of coupling is not correctly accounted for, as the amplitude of these condensed impedances cannot be considered as negligible, especially in the high frequencies of the calculation. The influence of these results on the computation of the scattered pressure using the global rCTF method will be investigated in the next section.

4.2.2.2 Total pressure in the medium

Finally, the sensitivity of the method to model errors will be investigated when evaluating the total pressure in the medium (it is reminded that this quantity corresponds to the sum of the incident pressure and the pressure scattered by the rigid sphere) using Eq. (3.24). At first, the evolution of the pressure is presented as a function of the frequency for 3 different points of the domain, chosen at different distances and orientations from the surface of the sphere. The comparison is made with the theoretical calculation described by Eq. (3.39). As for the decoupling of the condensed impedances in subsection 4.2.2.1, the results are shown for the two different discretization sizes in the infinite water medium in figure 65, for both the local and global rCTF approaches. The scales have been set to be the same for all figures in order to observe more clearly the differences between the calculations.

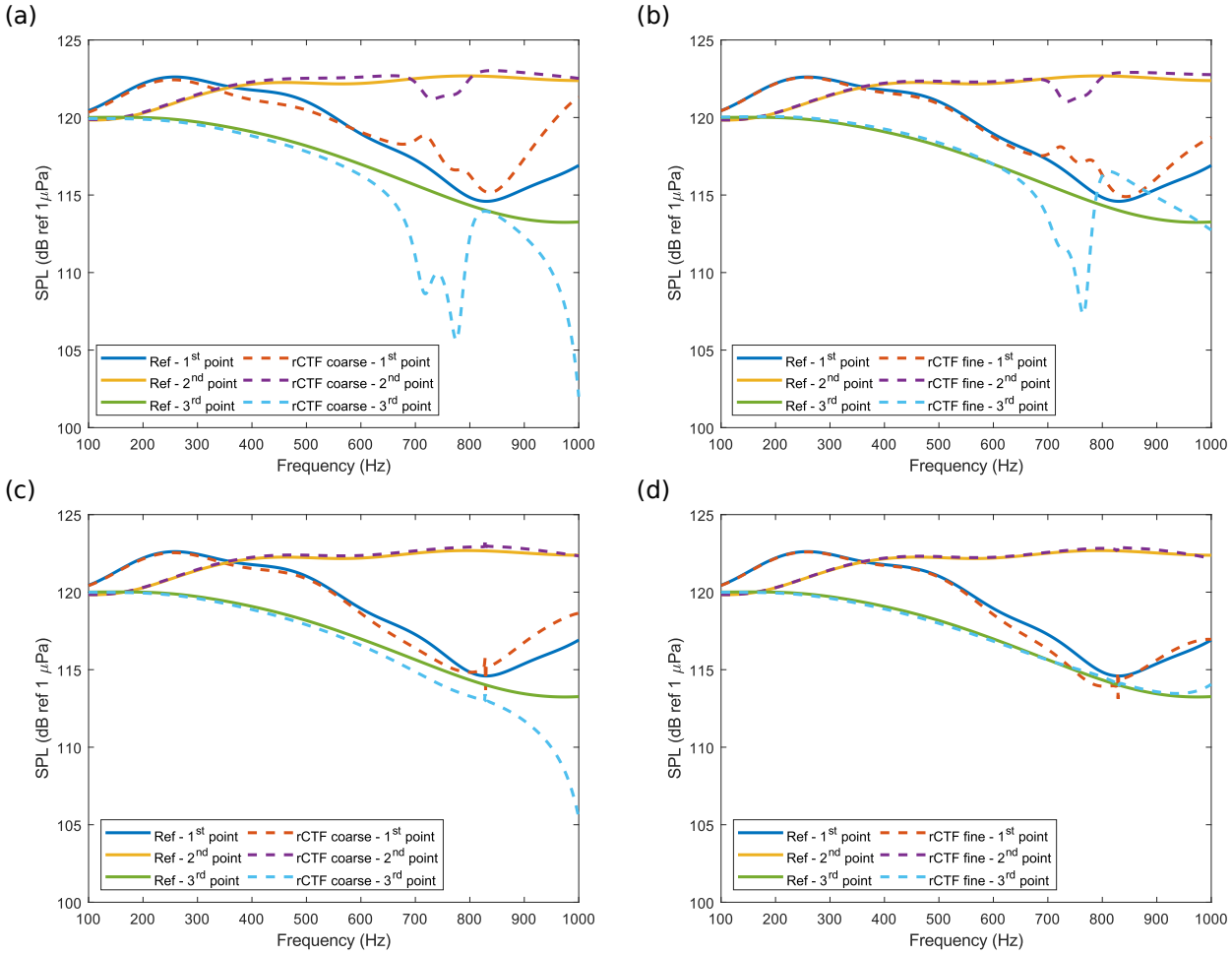

Figure 65: Total pressure in the medium - evaluation of the rCTF approach for 3 points in the fluid domain. Point 1 - $r = 1.5$ m, $\theta = \pi$; Point 2 - $r = 1.3$ m, $\theta = 4\pi/7$; Point 3 - $r = 1$ m, $\theta = \pi/3$. (a) Coarse discretization in the infinite water medium - local rCTF approach. (b) Fine discretization in the infinite water medium - local rCTF approach. (c) Coarse discretization in the infinite water medium - global rCTF approach. (d) Fine discretization in the infinite water medium - global rCTF approach.

For the local approach (figures 65a and b), the behavior that was observed for the decou-

pling of the impedances, namely exhibiting errors situated around the anti-resonance of the water sphere, are found back here, and the errors have been slightly amplified. One can also notice that these errors seem to be higher when the pressure is observed at the surface of the sphere (i.e.point 3). Even if a criterion was established to circumvent the singularities that can happen when the monopole is situated at the surface of the sphere, the high values exhibited by monopoles at such short distances may be prohibitive. Also, the calculations with the two different discretization sizes exhibit similar results. As it was observed for the decoupling of the condensed impedances, we can consider that the gain in accuracy provided by the finer discretization is not sufficient compared to the substantial increase of computation time. Finally, we can emphasize that in most parts of the frequency range of the calculation, the local decoupling technique can be considered as very accurate.

Concerning the global approach (figures 65c and d), the results are globally better than for the local approach, as the results are correct over the whole frequency range. Slight errors appear around 830 Hz as this was the ill-conditioned frequency identified before, but these errors remain low. Errors also appear at higher frequencies, especially for the point located on the surface of the sphere, as it was already observed for the local rCTF approach. However, it is interesting to notice that, for this calculation, there is a non-negligible difference when considering the two different discretization sizes. The finer discretization exhibits much better results, especially in the high frequencies. As this behavior was not observed when decoupling the condensed impedances using Eq. (3.22), this means that the improvement given by the finer discretization is related to the computation of the condensed pressures. However, one has to keep in mind that the computation times are substantially increased when considering this solution.

In order to verify the accuracy of the rCTF method even at the frequencies where errors appear in figure 65, a cartography of the total pressure field around the rigid sphere can be plotted for these frequencies. For the local rCTF approach, these cartographies are shown in figure 66 and compared to the theoretical calculation of Eq. (3.39). They are plotted at 750 Hz and 1000 Hz for the coarser discretization size, as the difference between the two discretization sizes is not substantial, contrary to their difference in computation time. The results can be considered as very satisfactory, as even for the most critical frequency (figure 66b), the global behavior is well described in the medium despite some discrepancies located mainly at the vincinity of the sphere. It is important to mention that the maxima and minima of pressure are correctly located.

Concerning the global approach, these cartographies are shown at 828 Hz (where the discrepancies happen due to the ill-conditioning issue) and 1000 Hz, for the coarser discretization size as well. Even if for this approach, the finer discretization size seems more

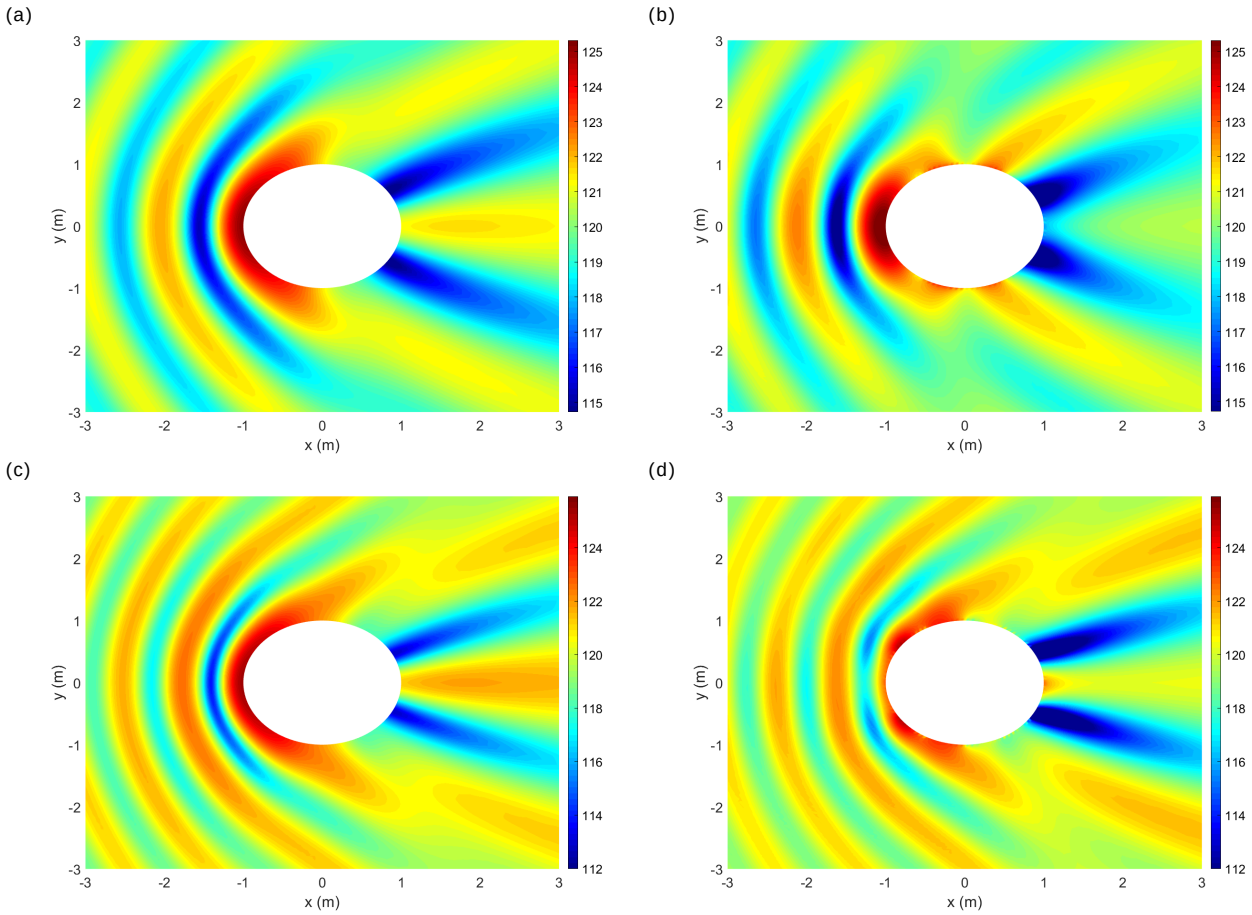

Figure 66: Total pressure in the medium - Comparison between the theoretical results (a,c) and the numerical local rCTF results (b,d) for 2 frequencies: (a,b), 750 Hz; (c,d), 1000 Hz.

accurate, it is important to verify the results when the coarser discretization is chosen in order to have reasonable computation costs. As was observed for the local approach, the results are accurate as the behavior of the system is correctly described despite some discrepancies. One can also observe, for this case more than for the local rCTF approach, that the result of the calculation is not symmetric with respect to the incident angle of the plane wave, whereas the system is symmetric (as it can be observed for the theoretical result). This phenomenon is due to the fact that the FEM model of the hollow sphere (see figure 56) is not perfectly symmetric. However, this does not change the conclusions of this study as the maxima and minima of pressure are correctly located, even if the amplitudes can show some discrepancies.

Finally, it can be concluded from this study that introducing numerical errors in the calculation of the condensed impedances and pressures does not lead to prohibitive errors when performing the rCTF method. For the local rCTF method, the discretization size of the infinite water medium does not play a significant role in the accuracy of the results. For the global rCTF method however, the results are more accurate with a finer discretization size in the infinite water medium, but this solution comes with a substantial increase of computation time. In order to quantify this increase, the computation times for all the

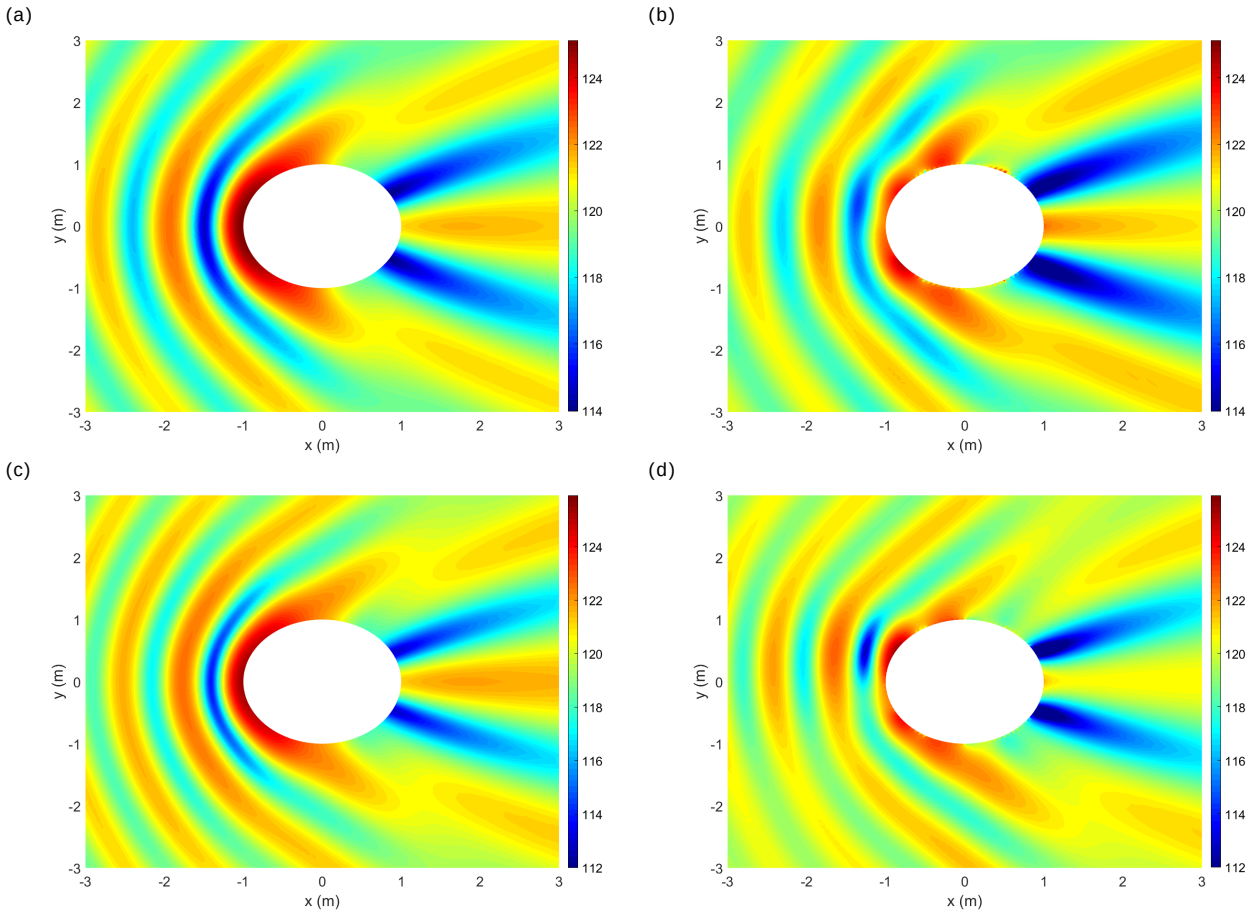

Figure 67: Total pressure in the medium - Comparison between the theoretical results (a,c) and the numerical global rCTF results (b,d) for 2 frequencies: (a,b), 828 Hz; (c,d), 1000 Hz.

considered approaches are summed up in table 5 for the calculation of:

- the scattered pressure field around the rigid sphere at a single frequency; this calculation includes the calculation of the condensed pressures.
- the condensed impedance matrix of the system 1+2 (the infinite water medium).
- the condensed impedance matrix of the subsystem 2 (the water sphere for the local rCTF approach and the hollow water sphere for the global rCTF approach).

Looking at this table, we can see that when the discretization size in the infinite water medium is relatively coarse, most of the computing time is taken by the calculation of the condensed impedances of the subsystem 2. As these calculations do not exhibit substantial differences in their result, it can be preferable to choose the local rCTF approach as it is slightly less computationally intensive and easier to derive. For the local approach, improving the discretization size does not change considerably the results while being much more computationally intensive, which means that this solution is less optimal for industrial applications. Finally, the global rCTF approach with a finer discretization size is the most

accurate one, but also far more computationally intensive. This means that, for an industrial application of the method as the one that will be studied in the next chapter, this increase in computation time may limit the advantages of the rCTF method compared to existing methods such as FEM. In the following chapter, the local rCTF method will hence be retained as it shows accurate results with reasonable computing times.

rCTF approach	**Discretization size**	**Calculation time**		
		Cartography	$\mathbf{Z_{1+2}}$	$\mathbf{Z_2}$
Local	Coarse ($\delta\theta = \delta\phi = 4°$)	1 min 54 s	1 min 56 s	7 h 48 min
	Fine ($\delta\theta = \delta\phi = 1°$)	30 min 2 s	8 h 35 min	
Global	Coarse ($\delta\theta = \delta\phi = 4°$)	3 min 27 s	6 min 7 s	8 h 55 min
	Fine ($\delta\theta = \delta\phi = 1°$)	1 h 7 min	27 h 31 min	

Table 5: Computation times

4.3 Conclusion

In this chapter, the sensitivity of the rCTF method to model errors was investigated for the local and global approaches described in chapter 3. The principles for calculating the condensed impedances and pressures from numerical models of the subsystems were established and applied on the same test case than in chapter 3. For bounded systems, the FEM method is used to calculate the condensed impedances, while for unbounded systems, a Green formulation derived from the integral formulation is used to estimate the condensed impedances and pressures.

For the local rCTF approach, the introduction of numerical errors led to discrepancies around the anti-resonance of the water sphere and of the infinite water medium, and in the high frequencies at the vicinity of the rigid sphere. The mesh size of the FEM model and the discretization size of the Green formulation played a key role in the convergence of the method. However, it is not necessary to choose a very fine discretization size for the Green formulation as the substantial increase of computing time is not balanced with an increase in the accuracy of the results.

Concerning the global rCTF approach, some slight discrepancies were observed around the resonance of the hollow sphere, and also in the high frequencies at the vicinity of the rigid sphere. However, contrary to the local rCTF approach, refining the discretization size of the Green formulation for the infinite water medium leads to more accurate results, especially in the high frequency range. However, this solution comes with a substantial increase of computing time. Also, it is important to mention that this solution is valid only in the case where the residual subsystem does not exhibit any resonant or anti-resonant phenomenon in the frequency range of interest, as it was observed in the previous chapter.

The rCTF method based on numerical models has thus shown its ability to correctly predict the behavior of the target subsystem. The local approach appeared more appropriate in an industrial context by being less computationally intensive compared to the global approach. The global approach has however shown some interesting insights in the potential of the method that should be further investigated in the future. In the following chapter, the local rCTF method will be applied on a case closer to the industrial application, consisting in studying the acoustic radiation from a partially coated cylindrical shell.

Chapter 5

Acoustic radiation from a partially coated cylindrical shell using the rCTF method

In the previous chapters, the principle of the reverse Condensed Transfer function method has been established, and the Condensed Transfer Functions necessary to apply the method have been calculated using analytical formulations in chapter 3, and numerical formulations in chapter 4. In this chapter, the local rCTF method will be used to study the radiation from a partially coated cylindrical shell (subsystem 1 in figure 68). To do so, a part of the coating (subsystem 2 in figure 68), represented by a FEM-type numerical model, will be removed from a semi-analytical model of the fully coated cylindrical shell (system 1+2 in figure 68).

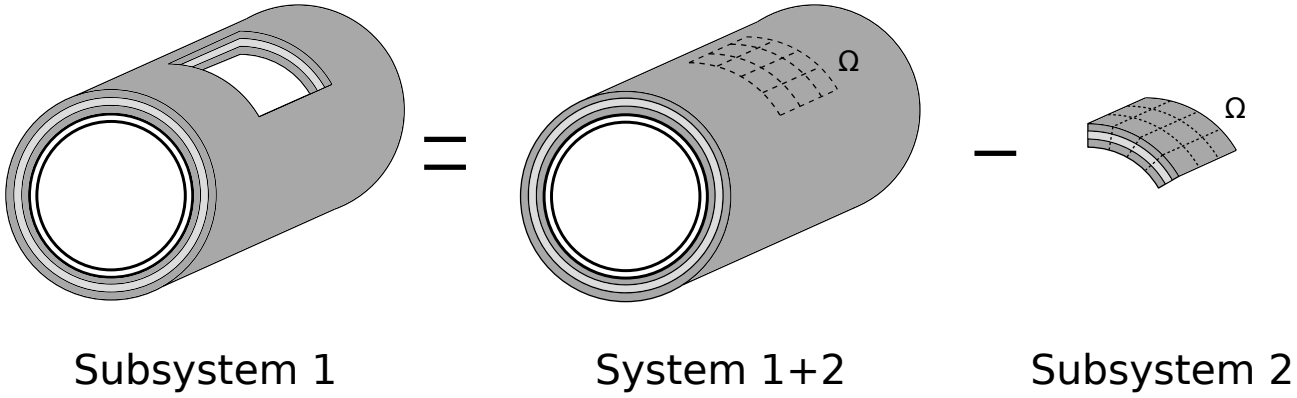

Figure 68: Principle of studying a partially coated cylindrical shell using the rCTF method.

The calculation of the CTFs and condensed pressures of the global system 1+2 and of the CTFs of the decoupled subsystem 2 will be developed in section 5.1. Then, the decoupling procedures of the rCTF method will be performed in section 5.2, while the possibility of recoupling this model to a numerical model of the water occupying the removed part of the coating will be investigated in section 5.3. Finally, a parametric study will be carried out in section 5.4 in order to evaluate the influence of the size of the removed part of the coating and the location of the external mechanical force on the vibroacoustic behavior of the partially coated cylindrical shell. It is worth mentioning that, although the theoretical developments are proposed for a 3-D model, the calculations developed in this chapter are carried out from

2-D models, in order to be able to compare the results to a reference calculation. This will be explained in more details in section 5.1.

5.1 Calculation of the Condensed Transfer Functions and condensed pressures

As in chapter 4, the CFs are 2D gate functions, meaning that the decoupling interface Ω is divided into a given number of patches for system 1+2 and subsystem 2, as shown in figure 68. Following this definition of the CFs, the CTFs of the system 1+2 and the subsystem 2 can be calculated.

The calculation of the CTFs of the system 1+2 will be developed in subsection 5.1.1, by considering two different decoupling boundaries. The condensed pressures and condensed radial velocities of the system 1+2 will be calculated in subsection 5.1.2, while the Condensed Transfer Functions of the subsystem 2 will be investigated in subsection 5.1.3.

5.1.1 Calculation of the Condensed Transfer Functions of the system 1+2

5.1.1.1 Presentation of the system

In order to compute the CTFs of the system 1+2, which is the fluid loaded fully coated cylindrical shell, the integral formulation presented in section 4.1.2 is used as the system is unbounded. In the following, we consider a fluid loaded infinite cylindrical shell with a single layer of coating, excited by a radial point force located at the inner surface of the shell, as shown as a sectional view in figure 69. The developments that will be carried out in the next paragraphs can nevertheless be extended to the case of multilayered coatings. As a matter of simplicity for this first application of the rCTF method to a partially coated cylindrical shell, the considered coating will be soft rubber (reference to such materials can be found in [81] and [82]), which implies that it will be modelled as an equivalent fluid in which the shear waves are neglected. However, it is important to indicate that the extension of this formulation to layers of solid material to model the coating is possible, but more complex in practice. Indeed, in order to take into account both the compressional and shear waves in the material, the displacements in the three directions in the material must be considered (see [55] for the reference to such materials). As this extension is not the primary aim of this thesis, it will not be considered here.

The shell has radius R, thickness h, Young's modulus E , density ρ_s and Poisson's ratio ν_s, while U, V and W denote the axial, tangential and radial displacements of the shell, respectively. Its behavior will be described using the Flügge's equations introduced in section 1.1. The coating is a rubber of thickness h_p, density ρ_p, and is modelled as an equivalent fluid, meaning that the transverse waves travelling in the coating are not taken into account. The

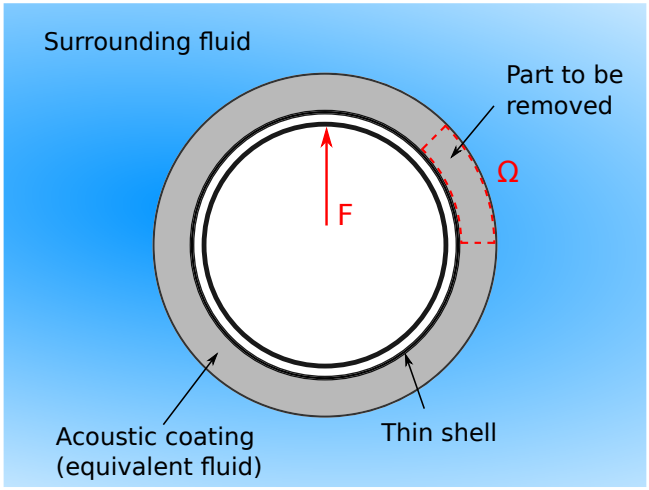

Figure 69: System 1+2: fully coated cylindrical shell immersed in an infinite fluid medium.

celerity of longitudinal waves in the coating is denoted by c_p, and the damping loss factor is denoted by η_p. The shell is surrounded by an infinite fluid domain of density ρ_f and speed of sound c_f, in which a damping loss factor η is accounted for as in chapters 3 and 4. Both fluid domains are modelled using the Helmholtz equations, the Sommerfeld radiation condition is verified at infinity (see Eq. (1.11)) for the exterior fluid, and the continuity of normal velocities and pressures at the shell-soft rubber and soft rubber-exterior fluid are considered.

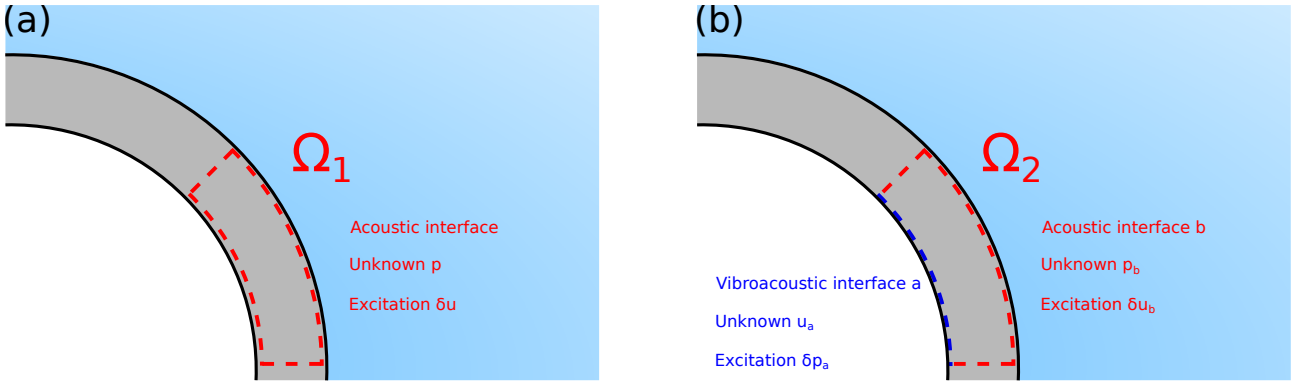

Figure 70: (a) Definition of the decoupling boundary Ω_1. (b) Definition of the decoupling boundary Ω_2.

To compute the CTFs of the system 1+2, two different decoupling boundaries will be considered:

- The decoupling boundary Ω_1 is shown in figure 70a and exhibits a single acoustic interface, with a residual coating layer.
- The decoupling boundary Ω_2 is shown in figure 70b and exhibits one acoustic interface (for the patches located at the acoustic coating-surrounding fluid interface and the patches located in the thickness of the acoustic coating) and one vibroacoustic interface (for the patches located at the shell-acoustic coating interface).

Following this, two different kinds of excitations must be considered, leading to two different ways of computing the CTFs:

- an acoustical excitation (i.e. array of monopole sources representing a velocity jump at the crossing of the surface) for the acoustic interface;
- a mechanical excitation (i.e. array of point forces representing a pressure jump at the crossing of the surface) for the vibroacoustic interface.

The calculation of the CTFs of the system 1+2 is performed by a semi-analytical spectral procedure which is fully developed in Appendix D. The equations of the problem are transposed in the wavenumber domain by a Fourier transform along the coordinate x and a Fourier series decomposition along the coordinate θ. These equations are then solved for the coordinate r to deduce the impedance of the fluid and the coating, and the response of the system to the different excitations. These quantities are then transposed back to the physical domain by the means of a 2-D inverse Fourier Transform, and the CTFs can then be computed. In the following, this procedure will be referred to as the "spectral approach".

When the decoupling boundary Ω_1 is considered, all the CTFs will be condensed impedances, and they are computed following the procedure described in chapter 3. The CTF matrix will hence be noted $\mathbf{Z_{1+2}}$, and the developments to compute these condensed impedances are presented in Appendix D.5.1.

However, when the decoupling boundary Ω_2 is considered, the CTF matrix of the system 1+2 exhibits 4 different kinds of CTFs:

- Condensed impedances (i.e. acoustic pressure over acoustic velocity) when both incident and receiving patches are located on an acoustic interface.
- Condensed mobilities (i.e. radial shell velocity over radial pressure applied on the shell) when both incident and receiving patches are located on a vibroacoustic interface.
- Condensed velocity transmissibilities (i.e. radial shell velocity over acoustic velocity) when the incident patch is located on an acoustic interface while the receiving patch is located on a vibroacoustic interface.
- Condensed pressure transmissibilities (i.e. acoustic pressure over radial pressure applied on the shell) when the incident patch is located on a vibroacoustic interface while the receiving patch is located on an acoustic interface.

The CTF matrix will hence be noted $\mathbf{H_{1+2}}$ (the notation "H" is used to signify that the CTFs are not necessarily condensed impedances), and will be separated into 4 submatrices which are each computed separately,

$$\mathbf{H_{1+2}} = \begin{bmatrix} \mathbf{H_{1+2}^{u_a \delta p_a}} & \mathbf{H_{1+2}^{u_a \delta u_b}} \\ \mathbf{H_{1+2}^{p_b \delta p_a}} & \mathbf{H_{1+2}^{p_b \delta u_b}} \end{bmatrix} \tag{5.1}$$

where

$$\mathbf{H_{1+2}^{u_a \delta p_a}} = \begin{bmatrix} \frac{u_a^{1+2}}{\delta p_a^{1+2}} \end{bmatrix}, \quad \mathbf{H_{1+2}^{u_a \delta u_b}} = \begin{bmatrix} \frac{u_a^{1+2}}{\delta u_b^{1+2}} \end{bmatrix}, \quad \mathbf{H_{1+2}^{p_b \delta p_a}} = \begin{bmatrix} \frac{p_b^{1+2}}{\delta p_a^{1+2}} \end{bmatrix}, \quad \mathbf{H_{1+2}^{p_b \delta u_b}} = \begin{bmatrix} \frac{p_b^{1+2}}{\delta u_b^{1+2}} \end{bmatrix} \tag{5.2}$$

Following this notation, the CTF matrix $\mathbf{H_{1+2}}$ links the excitation vector $\mathbf{\Delta_{1+2}}$ and the unknown vector $\boldsymbol{\xi}_{\mathbf{1+2}}$ via the following relation

$$\boldsymbol{\xi}_{\mathbf{1+2}} = \mathbf{H_{1+2}} \mathbf{\Delta_{1+2}} \tag{5.3}$$

with

$$\mathbf{\Delta_{1+2}} = \begin{bmatrix} \delta p_a^{1+2} \\ \delta u_b^{1+2} \end{bmatrix}, \quad \boldsymbol{\xi}_{\mathbf{1+2}} = \begin{bmatrix} u_a^{1+2} \\ p_b^{1+2} \end{bmatrix} \tag{5.4}$$

All the developments to compute the CTFs of the system 1+2 when the decoupling boundary Ω_2 is considered are presented in Appendix D.5.2.

5.1.1.2 Results and comparison with a reference calculation

In order to verify the formulations developed in the previous subsections, the results can be compared to a reference calculation obtained from a FEM model of the system 1+2. In the following sections, the calculations will be carried out with 2-D models of the systems of interest. Indeed, studying the radiation from the partially coated cylindrical shell with 2-D models in a first place presents some advantages. As the rCTF formulation is rather complex, using 2-D models removes a layer of complexity, hence increasing the possibility of testing different configurations. Furthermore, considering 2-D models allows performing FEM calculations to serve as reference for comparing with the results of the rCTF method. This would not have been possible with 3-D models as the FEM method is not indicated for solving problems involving infinite cylindrical shells. Finally, one can stress out that considering 2-D models for the partially coated cylindrical shell is sufficient to obtain a first overview on the effects of partial coating in the vibroacoustic behavior of the shell. If the results obtained from this 2-D study are considered satisfactory, a 3-D study will be taken into consideration for a further work.

(a) Presentation of the calculation parameters and of the reference calculation

The calculation is carried out with a cylindrical shell coated with a rubber-like material having characteristics close to decoupling coatings. The coated shell is surrounded by water. The characteristics of the shell, the coating and the water are presented in table 6. The calculations are performed in a frequency range between 5 Hz and 1500 Hz, with a frequency step of 5 Hz. It is important to mention that for this application, the material properties were considered constant in the frequency range of interest. This is generally not the case when decoupling coatings are considered in industrial applications.

Parameter	**Notation**	**Value**	**Unit**
Shell radius	R	1	m
Shell thickness	h_s	0.01	m
Shell Young's modulus	E	210	GPa
Shell Poisson's ratio	ν_s	0.3	-
Shell density	ρ_s	7800	$kg.m^{-3}$
Shell damping loss factor	η_s	0.01	-
Rubber thickness	h_p	0.1	m
Rubber density	ρ_p	1000	$kg.m^{-3}$
Rubber speed of sound	c_p	290	$m.s^{-1}$
Rubber loss factor	η_p	0.1	-
Exterior fluid density	ρ_f	1000	$kg.m^{-3}$
Exterior fluid speed of sound	c_f	1500	$m.s^{-1}$
Exterior fluid loss factor	η	0.001	$m.s^{-1}$

Table 6: Material and fluid characteristics of the problem.

We are interested in removing a part of the coating ranging from 0 to $\pi/4$ rad (as illustrated with Ω in figure 69). As the problem is now in 2-D, the CFs will be gate functions, meaning that the interface Ω must be divided into a finite number of segments. The size of these segments will be determined from the smallest wavelength at the highest considered frequency (i.e. 1500 Hz) between:

- the minimal acoustic wavelength in the surrounding fluid, λ_f^{min};
- the minimal acoustic wavelength in the rubber, λ_p^{min};
- the minimal flexural wavelength of the shell, λ_s^{min}. It must be emphasized that this value will be approximated using the flexural wavelength of a plate of similar thickness. As the curvature increases the stiffness of the plate, the wavelength at a given frequency increases as well, meaning that the criterion for the plate will be more restrictive than the criterion for the shell.

As we saw in chapter 3, the segments must be smaller than half the minimal wavelength at the highest considered frequency in order for the calculation to converge, which means

$$d_{segm} \leqslant \min\left(\frac{\lambda_f^{min}}{2}, \frac{\lambda_p^{min}}{2}, \frac{\lambda_s^{min}}{2}\right) \tag{5.5}$$

At 1500 Hz, they yield

$$\lambda_f^{min} = 1 \text{ m}\,, \quad \lambda_p^{min} = 0.19 \text{ m}\,, \quad \lambda_s^{min} = 0.26 \text{ m} \tag{5.6}$$

We must hence take the acoustic wavelength in the rubber as the most critical criterion, hence leading to the following minimal size for the segments

$$d_{segm} \leqslant 0.095 \text{ m} \tag{5.7}$$

Following this criterion, the interface Ω is divided into 9 segments along the θ coordinate and 2 segments along the r coordinate. The accuracy of this division (and of the selected criterion) will be discussed in section 5.2 when the decoupling calculations will be performed. In order to compute the CTFs of the system 1+2, the segments must be discretized into a finite number of points to apply the integral formulation described in section 4.1.2. As a first step, the segments are discretized into 7 points. The accuracy of the calculations with this discretization size will be evaluated in subsection 5.2.2, and if needed, the discretization will be refined. The obtained discretized interface Ω is displayed in figure 71. It can be noticed that some discretization points belong simultaneously to two segments, but this particular configuration does not have any impact on the calculations.

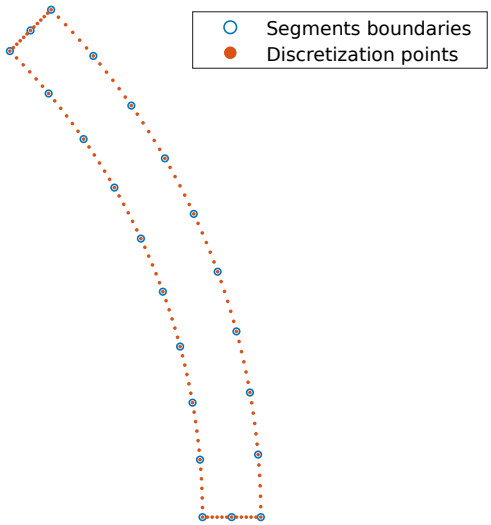

Figure 71: Division of Ω into segments and discretization of the segments.

To serve as a reference, a FEM calculation is performed using the software COMSOL Multiphysics® 5.6 [101] with the Acoustics module. However, it is important to mention that

there is no possibility to define directly in COMSOL Multiphysics® an excitation corresponding to a velocity jump at the crossing of a surface in an acoustic medium. This is problematic in the aim of computing the condensed impedances Z_{1+2}^{ij} for the acoustic formulation and the CTFs $H_{1+2}^{p_b \delta u_b, ij}$ and $H_{1+2}^{u_a \delta u_b, ij}$ for the vibroacoustic formulation. To circumvent this issue, an array of 7 monopole sources is placed along the incident segments to simulate the velocity jump as for the rCTF calculation. Concerning the calculations of $H_{1+2}^{u_a \delta p_a, ij}$ and $H_{1+2}^{p_b \delta p_a, ij}$ for the excited segments on the vibroacoustic interface, a pressure load can be directly applied in COMSOL Multiphysics®. The CTFs are then obtained by integrating the pressure (or the shell radial velocity depending on the considered CTF) along the receiving segment using the *intop* command (which allows evaluating the integral of the chosen quantity over a defined volume, area or line) and dividing this value by the square root of the length of the receiving segment according to the definition of the CFs. For a receiving segment located at the interface between the coating and the surrounding fluid, it yields

$$Z_{1+2}^{ij} = \frac{1}{\sqrt{d_i}} \int_{\theta_{i-1}}^{\theta_i} p^j (R + h_p) \, \mathrm{d}\theta \tag{5.8}$$

where p^j is the pressure induced by the excitation on the incident segment j, and d_i is the length of the receiving segment i for which θ_{i-1} and θ_i are the angular boundaries.

Finally, it is important to stress that, as the calculations are carried out using 2-D models, the formulation developed in the previous subsections is simplified. The 2-D assumptions transform the k_x vector into a single value which will be 0 in the computations. Thus, to go back to the physical space for a spectral quantity $\tilde{\tilde{p}}$, a 1-D inverse Fourier transform (which takes here the form of a discrete sum of the components of a Fourier series) is necessary

$$p = \frac{1}{2\pi} \sum_{n=-\infty}^{n=+\infty} \tilde{\tilde{p}} \mathrm{e}^{\mathrm{j}n\theta} \tag{5.9}$$

As for the n vector, an infinite sum appears in Eq. (5.9), which must in practice be truncated to a finite value. This value, N_{max}, is derived from the maximal value of the different wavenumbers of the problem,

$$N_{max} = \mathrm{int}\left[\kappa_n R \max(k_f, k_p, k_s)\right] + 1 \tag{5.10}$$

where κ_n is a margin coefficient (typically $\kappa_n = 1.5$), k_f is the acoustic wavenumber in the surrounding fluid, k_p is the acoustic wavenumber in the rubber, and k_s is the flexural wavenumber of a plate with the same thickness and material properties as the cylindrical shell.

(b) Results for the decoupling boundary Ω_1

At first, the condensed impedances of the system 1+2 are shown when the decoupling boundary Ω_1 is considered, exhibiting acoustic interfaces only. The results diplayed in figure 72a correspond to the comparison between the semi-analytical model (for which the developments are presented in Appendix D) and the FEM calculation. Three different condensed impedances are displayed in figure 72a: one direct condensed impedance (1st TF), one crossed condensed impedance with two segments far away from each other (2nd TF), and one crossed condensed impedance with two segment close to each other (3rd TF). The excited and receiving segments corresponding to those condensed impedances are shown in figure 72b. The blue point corresponds to the excited segment for the three TFs (and hence the receiving segment also for the 1st TF), the yellow point corresponds to the receiving segment for the 2nd TF and the green point corresponds to the receiving segment for the 3rd TF.

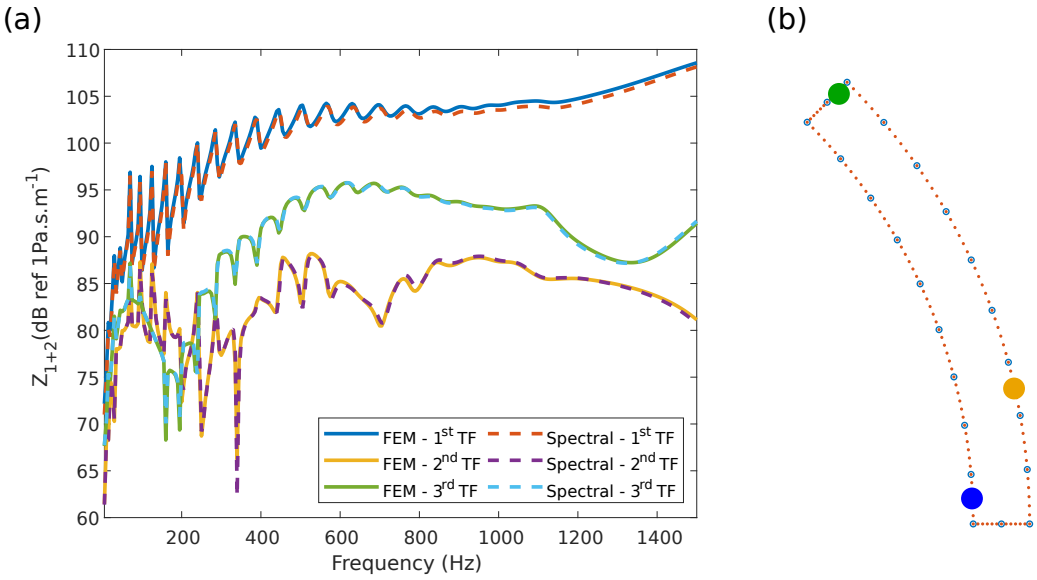

Figure 72: (a) Condensed impedances of the system 1+2 for the decoupling boundary Ω_1 (including the acoustic interface). (b) Position of the excited and receiving segments.

Some minor discrepancies can be observed, for example in the high-frequency range for the direct condensed impedance. These discrepancies do not necessarily mean that the errors come from the spectral calculations, but rather from the difference between the spectral formulation and the reference calculations (which can come from the differences of modelling of the shell, which was described using the Flügge theory for the spectral formulation, while solid elements were used for the FEM calculation). However, the aim of this comparison is to validate the proposed formulation and to make sure that we model correctly the behavior of the fully coated cylindrical shell, and we can safely affirm that this aim has been met from the observation of figure 72.

(c) Results for the decoupling boundary Ω_2

We are now interested in evaluating the CTFs of the system 1+2 when considering the decoupling boundary Ω_2, exhibiting acoustic and vibroacoustic interfaces. The comparison between the spectral approach and the FEM calculation are shown in figure 73 for the 4 different kinds of CTFs regarding the position of the incident and receiving segments. For the condensed mobilities (figure 73a) and condensed impedances (figure 73d), the first TF corresponds to a direct TF (i.e. the excited and receiving segments are the same), while the second TF corresponds to a crossed TF (i.e. the excited and receiving segments are different). As for the condensed velocity transmissibilities (figure 73b) and condensed pressure transmissibilities (figure 73c), the first TF corresponds to a crossed TF where the excited and receiving segments are close to each other, while the second TF corresponds to a crossed TF where the excited and receiving segments are far away from each other. For each CTFs displayed in figure 73, the excited and receiving segments are shown next to the corresponding figure (the blue point always corresponds to the excited segment).

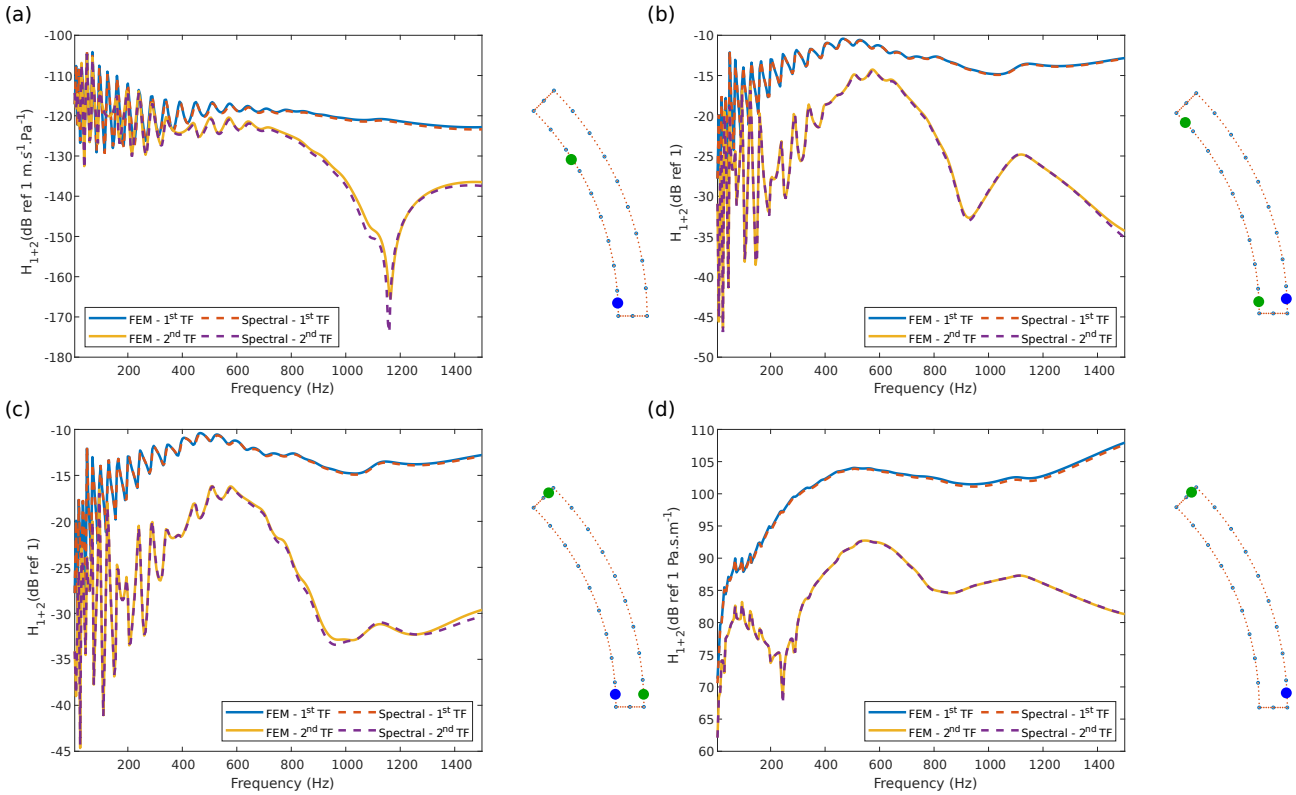

Figure 73: CTFs of the system 1+2 for the decoupling boundary Ω_2 (including the vibroacoustic interface). (a) $H_{1+2}^{u_a \delta p_a, ij}$. (b) $H_{1+2}^{u_a \delta u_b, ij}$. (c) $H_{1+2}^{p_b \delta p_a, ij}$. (d) $H_{1+2}^{p_b \delta u_b, ij}$.

As it was already observed for the decoupling boundary Ω_1, we can see some minor discrepancies between the reference calculation and the semi-analytical formulation, but there is globally a very good correlation between the two calculations. We can also notice

that, depending on the nature of the CTFs, the amplitudes are very different, but this is only due to the nature of the excitation and of the measured quantity.

5.1.2 Condensed pressures and condensed radial velocities of system 1+2

In order to apply the equations of the rCTF method, we have seen in chapter 3 that condensed pressures must be computed for the global system 1+2. For the case of interest here, this is also true when the decoupling boundary Ω_1 is considered. The two kinds of condensed pressures that must be computed are:

- $\mathbf{P_{1+2}}$: the condensed pressures from the external excitation, which is a mechanical point force on the inner surface of the shell;
- $\mathbf{P^M_{1+2}}$: the condensed pressures induced by a monopole excitation located point M in the exterior fluid. It is reminded that this condensed pressure allows evaluating the pressure at point M in the target subsystem using a reciprocity principle (see subsection 3.2.2).

When the decoupling boundary Ω_2 is considered, condensed radial velocities must be computed for the patches located on a vibroacoustic interface, in addition to the condensed pressures for the patches located on an acoustic interface. The two kinds of condensed radial velocities are:

- $\mathbf{U_{1+2}}$: the condensed radial velocities from the external excitation;
- $\mathbf{U^M_{1+2}}$: the condensed radial velocities induced by a monopole excitation located point M in the exterior fluid.

Hence, when the decoupling boundary Ω_2 is considered, we can separate the vector of the condensed pressures and radial velocities into two different vectors

$$\mathbf{\Lambda_{1+2}} = \begin{bmatrix} \mathbf{U_{1+2,a}} \\ \mathbf{P_{1+2,b}} \end{bmatrix}, \quad \mathbf{\Lambda^M_{1+2}} = \begin{bmatrix} \mathbf{U^M_{1+2,a}} \\ \mathbf{P^M_{1+2,b}} \end{bmatrix} \tag{5.11}$$

The procedure to compute the condensed pressures and condensed radial velocities of the system 1+2 is developed in Appendix D.6.

As in subsection 5.1.1.2, the calculation is carried out with a 2-D model of the fully coated cylindrical shell, and the results are compared with a FEM calculation performed with COMSOL Multiphysics® 5.6. The comparison between the two calculations when the excitation is the mechanical point force is shown in figure 74 for two condensed radial velocities (figure 74a) and two condensed pressures (figure 74b). We can see that there are a few minor discrepancies, especially around some anti-resonant frequencies, but globally the

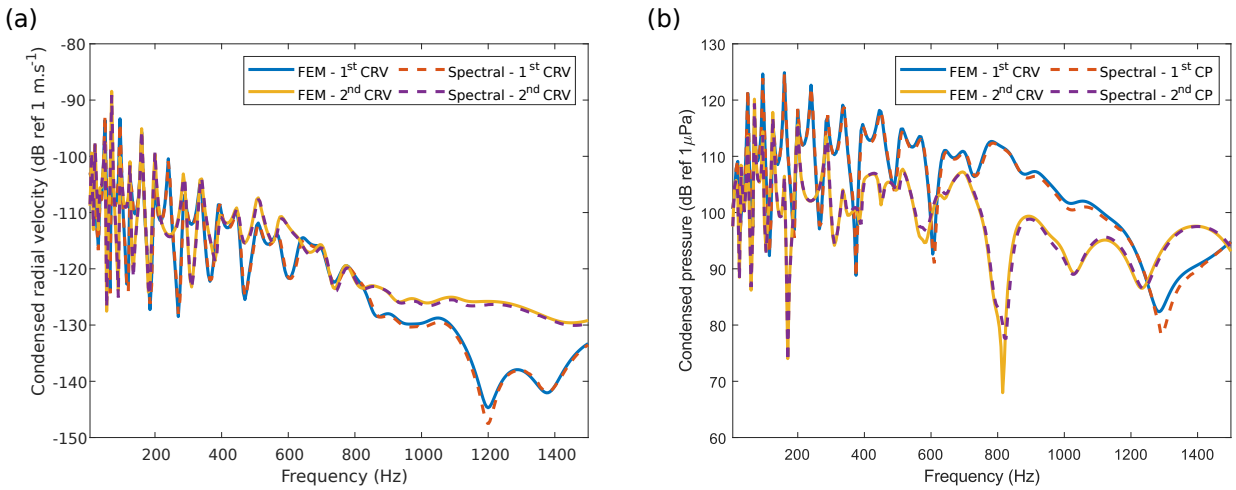

Figure 74: (a) Condensed radial velocities due to a mechanical point force. (b) Condensed pressures due to a mechanical point force.

concordance between the FEM calculation and the spectral formulation is very good. This observation thus validates these calculations.

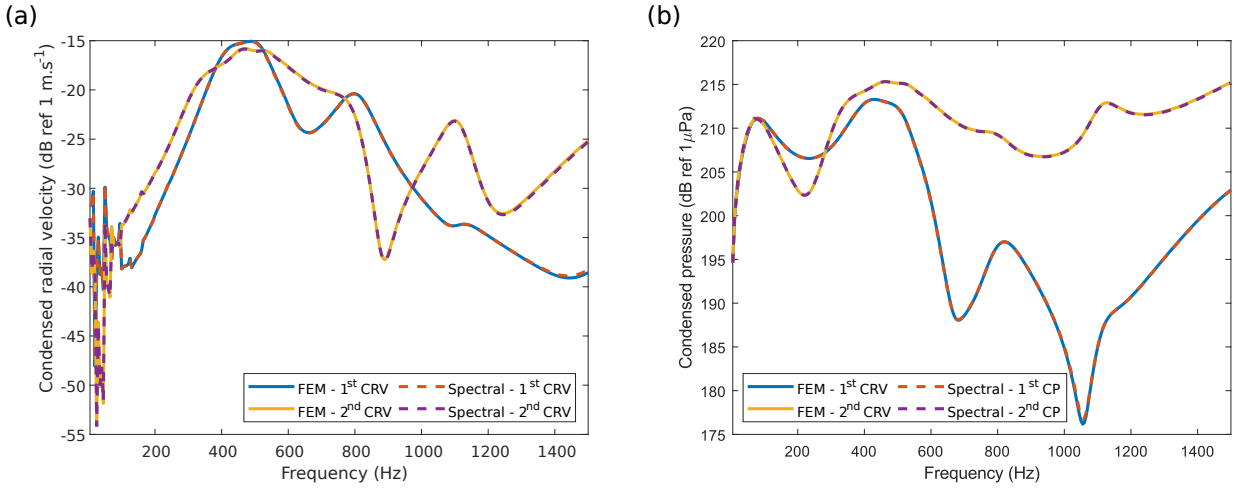

Figure 75: (a) Condensed radial velocities due to a unitary monopole. (b) Condensed pressures due to a unitary monopole.

As for the monopole excitation in the surrounding fluid, the comparison between the two calculations is shown in figure 75 for two condensed radial velocities (figure 75a) and two condensed pressures (figure 75b). The results are very accurate as the comparison between both calculations shows a quasi-perfect match, hence also validating these calculations. Following this, we can focus on computing the CTFs of the subtracted subsystem.

5.1.3 Condensed Transfer Functions of subsystem 2

We are now interested in computing the CTFs of the subsystem 2, which is the missing part of the coating in the target subsystem and will be referred to as the removed patch in the following (this must not be confused with the patches used as condensation functions in the

previous chapters). As this is a bounded subsystem, the procedure to compute these CTFs is the one described in section 4.1.1. A FEM model of the removed patch is generated using the Acoustics module of the software COMSOL Multiphysics® 5.6 [101], and the acoustic mass and stiffness matrices of the model are extracted using LiveLink™ for MATLAB® [200]. The FEM model is shown in figure 76, with a size of elements that has been obtained using the common criterion of 6 elements per acoustic wavelength at the highest considered frequency.

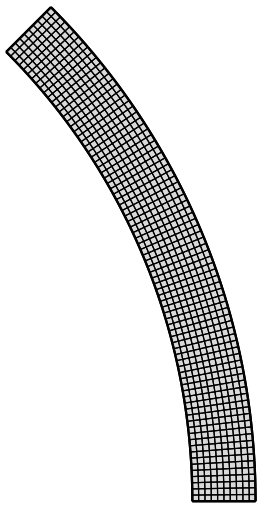

Figure 76: FEM model of the removed patch.

As this subsystem is entirely acoustical, the CTFs will be condensed impedances. For this subsystem, there is no reference calculation, but the condensed impedances have been double checked by considering a second way of carrying out the calculation to obtain these CTFs. This second calculation is performed entirely in the COMSOL Multiphysics® software. The segments are defined at the exterior boundaries of the model, and all the segments are successively excited by an acoustic normal velocity, while the others remain rigid. The pressure in the receiving segments is then evaluated by performing an integration over the segments (using the command *intop* as evoked in subsection 5.1.1) to obtain the CTFs as in Eq. (5.8). Besides, the FEM model is rather small, with few nodes and elements, hence the sources of errors when computing the CTFs are limited. Three condensed impedances of the subsystem 2 are shown in figure 77a: one direct condensed impedance (1st TF), one crossed condensed impedance with two segments far away from each other (2nd TF), and one crossed condensed impedance with two segment close to each other (3rd TF). The position of the excited and receiving segments are displayed in figure 77b, with the color of the points matching the color of the curves (it is worth mentioning that there is no necessity to precise which segment is the excited one and which segment is the receiving one as the condensed impedances are symmetric). This figure allows identifying the resonant and anti-resonant frequencies of the subtracted subsystem, which are the most likely to cause

errors when performing the decoupling calculations. As a way a validating these calculations, an eigenvalue study has been carried out on the FEM model to derive the eigenfrequencies of the model. It turns out that the first five eigenfrequencies of the subsystem are: 175 Hz, 350 Hz, 525 Hz, 700 Hz and 874 Hz, which is consistent with the resonances observed in figure 77.

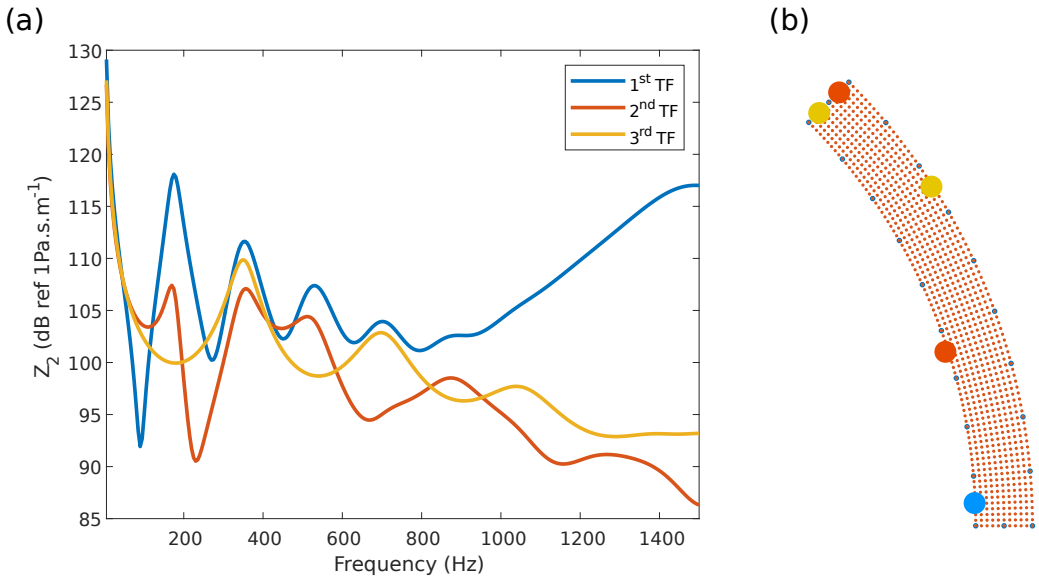

Figure 77: (a) Condensed impedances of subsystem 2. (b) Position of the excited and receving segments.

In subsection 5.1.1, the boundary Ω_2 has been defined in order to consider the vibroacoustic interface. In view of applying the decoupling calculation of the rCTF method with the boundary Ω_2, some adjustments are necessary when considering the CTFs of the subsystem 2. Indeed, as already stated, this subsystem is entirely acoustical. However, it must be stressed that the rCTF formulation derived in section 3.2 was designed for acoustical (sub)systems, and one cannot replace condensed impedances with CTFs of different nature without modifying the rCTF formulation. To this end, the condensed impedances of the subsystem 2 will be converted into a vibroacoustic form to match with the formulation accounting for the decoupling boundary Ω_2 in subsection 5.1.1 , and a vibroacoustic formulation of the rCTF method will be derived in a following section.

In order to convert $\mathbf{Z_2}$ into its vibroacoustic form $\mathbf{H_2}$, the matrix is separated into 4 submatrices, as it was done for $\mathbf{H_{1+2}}$. To be consistent with the notations used in section 5.1.1, in the following, the subscript a will denote segments located at a solid-fluid interface, while the subscript b will denote segments located at a fluid-fluid interface. We can hence note

$$\mathbf{Z_2} = \begin{bmatrix} \mathbf{Z_2^{p_a u_a}} & \mathbf{Z_2^{p_a u_b}} \\ \mathbf{Z_2^{p_b u_a}} & \mathbf{Z_2^{p_b u_b}} \end{bmatrix} \tag{5.12}$$

where

$$\mathbf{Z_2^{p_a u_a}} = \begin{bmatrix} \frac{p_a^2}{u_a^2} \end{bmatrix}, \quad \mathbf{Z_2^{p_a u_b}} = \begin{bmatrix} \frac{p_a^2}{u_b^2} \end{bmatrix}, \quad \mathbf{Z_2^{p_b u_a}} = \begin{bmatrix} \frac{p_b^2}{u_a^2} \end{bmatrix}, \quad \mathbf{Z_2^{p_b u_b}} = \begin{bmatrix} \frac{p_b^2}{u_b^2} \end{bmatrix} \tag{5.13}$$

Let us define the excitation vector $\mathbf{\Phi_2}$ and the unknown vector $\mathbf{\Psi_2}$ as

$$\mathbf{\Phi_2} = \begin{bmatrix} u_a^2 \\ u_b^2 \end{bmatrix}, \quad \mathbf{\Psi_2} = \begin{bmatrix} p_a^2 \\ p_b^2 \end{bmatrix} \tag{5.14}$$

The excitation and unknown vectors are linked by the condensed impedance matrix of the subsystem

$$\mathbf{\Psi_2} = \mathbf{Z_2 \Phi_2} \tag{5.15}$$

The aim is hence to convert this last equation into a vibroacoustic equation similar to Eq. (5.3)

$$\mathbf{\xi_2} = \mathbf{H_2 \zeta_2} \tag{5.16}$$

with

$$\mathbf{\zeta_2} = \begin{bmatrix} p_a^2 \\ u_b^2 \end{bmatrix}, \quad \mathbf{\xi_2} = \begin{bmatrix} u_a^2 \\ p_b^2 \end{bmatrix}, \quad \mathbf{H_2} = \begin{bmatrix} \mathbf{H_2^{u_a p_a}} & \mathbf{H_2^{u_a u_b}} \\ \mathbf{H_2^{p_b p_a}} & \mathbf{H_2^{p_b u_b}} \end{bmatrix} \tag{5.17}$$

After some developments, it is possible to go from Eq. (5.15) to Eq. (5.16) by expressing $\mathbf{H_2}$ using the submatrices of $\mathbf{Z_2}$

$$\mathbf{H_2} = \begin{bmatrix} (\mathbf{Z_2^{p_a u_a}})^{-1} & -(\mathbf{Z_2^{p_a u_a}})^{-1}\mathbf{Z_2^{p_a u_b}} \\ \mathbf{Z_2^{p_b u_a}}(\mathbf{Z_2^{p_a u_a}})^{-1} & \mathbf{Z_2^{p_b u_b}} - \mathbf{Z_2^{p_b u_a}}(\mathbf{Z_2^{p_a u_a}})^{-1}\mathbf{Z_2^{p_a u_b}} \end{bmatrix} \tag{5.18}$$

The behavior of these CTFs is shown in figure 78 for the 4 different submatrices. For each submatrix, a sketch is proposed with the blue point corresponding to the incident segment, and the green points corresponding to the receiving segments. For the condensed admittances (figure 78a) and condensed impedances (figure 78d), the blue curve corresponds to a direct CTF (i.e. the incident and receiving segments are the same), which explains that there is only one green point in these figures.

The behaviors exhibited in figure 78 are very different from the ones observed in figure 77 for the acoustic interface Ω_1. The resonances have been shifted towards higher frequencies, as the first resonance appears above 700 Hz. This is due to the change in the boundary conditions of the problem. Indeed, for the acoustic interface Ω_1, the condensed impedances were computed considering a null velocity on all the segments except the incident one. For the vibroacoustic interface Ω_2 however, the segments located at a solid-fluid interface have a zero-pressure boundary condition. This also explains for example the behavior of the 2$^{\text{nd}}$ TF in figure 78d, as the receiving segment is located in the thickness of the coating, hence

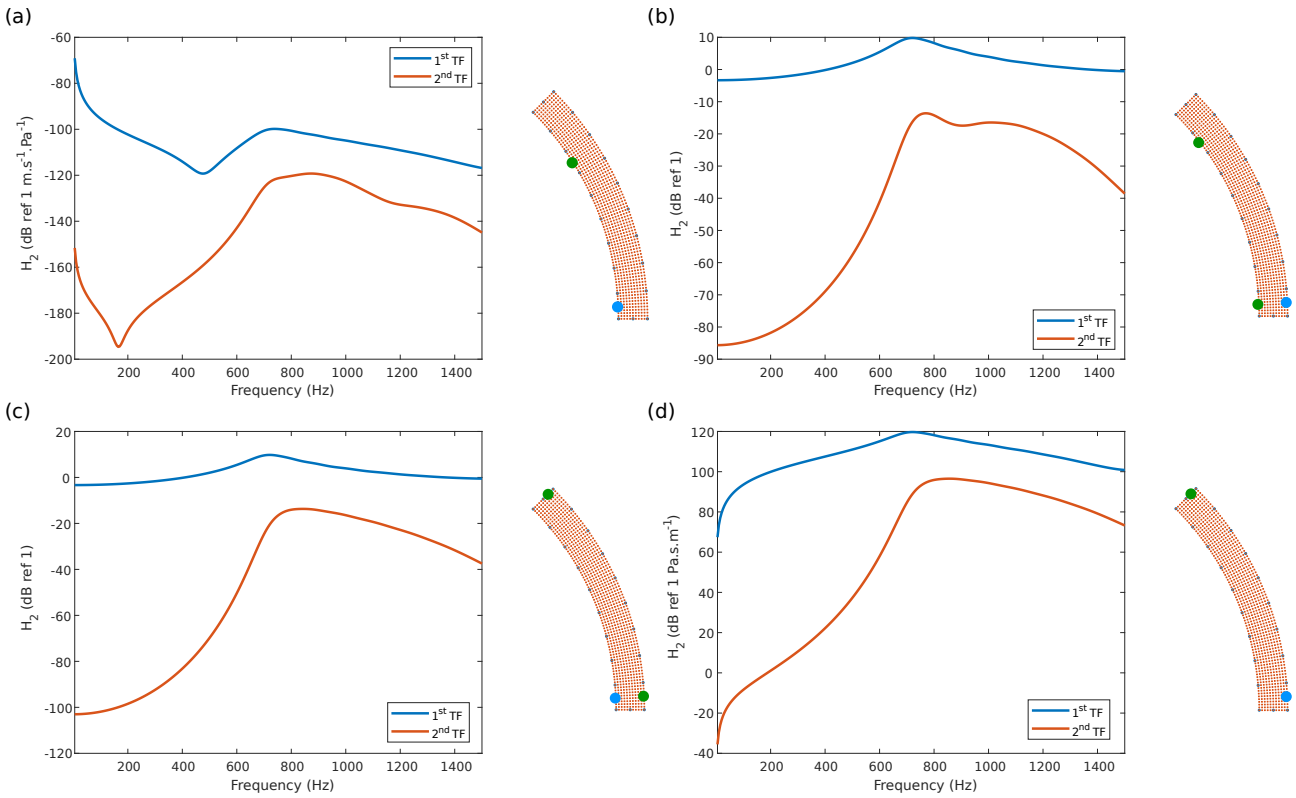

Figure 78: CTFs of subsystem 2 converted in vibroacoustic form. (a) $H_2^{u_a p_a,ij}$. (b) $H_2^{u_a u_b,ij}$. (c) $H_2^{p_b p_a,ij}$. (d) $H_2^{p_b u_b,ij}$.

being close to the zero-pressure boundary condition. A FEM verification has also been carried out with this change in boundary conditions in order to compute the eigenfrequencies of the subsystem with the vibroacoustic interface Ω_2. The first five eigenfrequencies are: 711 Hz, 732 Hz, 790 Hz, 878 Hz and 989 Hz. This is also consistent with the resonances observed in figure 78, even if they are slightly blurred, due to the proximity of the different resonances and to the high damping of the subsystem. Besides, we can observe that, for a single submatrix, the amplitudes of the CTFs can cover a wide range of values, a behavior that was not observed for the system 1+2. This could induce a difference in the conditioning of the CTF matrix compared to the condensed impedance matrix and have an implication on the accuracy of the rCTF calculations. This will be investigated when performing the decoupling calculations in the next section, as all the quantities necessary to apply the rCTF method have been obtained.

5.2 Decoupling calculations using the rCTF method

In this section, the decoupling calculations of the local rCTF method will be carried out to remove the coating tile from the fully coated cylindrical shell. However, before performing these calculations, the procedure to derive the CTFs of the target subsystem 1 from the CTFs of the global system and the subtracted subsystem when the decoupling boundary Ω_2 is

considered must be explicited. This will allow predicting the pressure inside the target subsystem for the vibroacoustic formulation. It must be mentioned that the intermediary results corresponding to the decoupling of the CTFs (i.e. Eq. (3.22)), which were investigated in details in chapters 3 and 4, will not be addressed in this section. Indeed, in the previous chapters, this investigation constituted a first insight in evaluating the accuracy of the rCTF method (in chapter 3) and its sensitivity to model errors (in chapter 4). However, these results do not constitute the main objective of this application, which is to study the response at any point of the decoupled subsystem. This will hence be the main focus in this section.

5.2.1 Vibroacoustic formulation of the rCTF method

In order to compute the CTFs of the target subsystem for the decoupling boundary Ω_2 exhibiting the vibroacoustic interface, the procedure developed in section 3.2.3 must be reiterated for the problem at hand here. If the CTFs of the global system (Eqs. 5.1 and 5.2) and of the subtracted subsystem (Eqs. 5.18 and 5.13) have already been defined, one must explicit the CTFs of the target subsystem in consistency with the vibroacoustic interface

$$\mathbf{H_1} = \begin{bmatrix} \mathbf{H_1^{u_a p_a}} & \mathbf{H_1^{u_a u_b}} \\ \mathbf{H_1^{p_b p_a}} & \mathbf{H_1^{p_b u_b}} \end{bmatrix} \tag{5.19}$$

where

$$\mathbf{H_1^{u_a p_a}} = \begin{bmatrix} \frac{u_a^1}{p_a^1} \end{bmatrix}, \quad \mathbf{H_1^{u_a u_b}} = \begin{bmatrix} \frac{u_a^1}{u_b^1} \end{bmatrix}, \quad \mathbf{H_1^{p_b p_a}} = \begin{bmatrix} \frac{p_b^1}{p_a^1} \end{bmatrix}, \quad \mathbf{H_1^{p_b u_b}} = \begin{bmatrix} \frac{p_b^1}{u_b^1} \end{bmatrix} \tag{5.20}$$

Following this notation, the CTF matrix $\mathbf{H_1}$ links the excitation vector $\boldsymbol{\zeta_1}$ and the unknown vector $\boldsymbol{\xi_1}$ via the following relation

$$\boldsymbol{\xi_1} = \mathbf{H_1}\boldsymbol{\zeta_1} \tag{5.21}$$

with

$$\boldsymbol{\zeta_1} = \begin{bmatrix} p_a^1 \\ u_b^1 \end{bmatrix}, \quad \boldsymbol{\xi_1} = \begin{bmatrix} u_a^1 \\ p_b^1 \end{bmatrix} \tag{5.22}$$

To express $\mathbf{H_1}$ as a function of $\mathbf{H_{1+2}}$ and $\mathbf{H_2}$, we consider at first the coupling problem to express $\mathbf{H_{1+2}}$ from $\mathbf{H_1}$ and $\mathbf{H_2}$. The velocity equilibrium at the solid-fluid interface and pressure continuity at the fluid-fluid interface yield

$$\begin{cases} u_a^1 + u_a^2 = 0 \\ p_b^1 - p_b^2 = 0 \end{cases} \tag{5.23}$$

From these conditions, it is not possible to obtain a direct relation between $\boldsymbol{\xi_1}$ and $\boldsymbol{\xi_2}$. To circumvent this issue, a change in the normal orientation is considered for u_a^2, leading to the following: $\bar{u}_a^2 = -u_a^2$. The subtracted subsystem hence reads

$$\bar{\xi}_2 = \bar{\mathbf{H}}_2 \zeta_2 \tag{5.24}$$

with

$$\bar{\xi}_2 = \begin{bmatrix} \bar{u}_a^2 \\ p_b^2 \end{bmatrix}, \quad \bar{\mathbf{H}}_2 = \begin{bmatrix} -(\mathbf{Z}_2^{\mathbf{p_a u_a}})^{-1} & (\mathbf{Z}_2^{\mathbf{p_a u_a}})^{-1} \mathbf{Z}_2^{\mathbf{p_a u_b}} \\ \mathbf{Z}_2^{\mathbf{p_b u_a}} (\mathbf{Z}_2^{\mathbf{p_a u_a}})^{-1} & \mathbf{Z}_2^{\mathbf{p_b u_b}} - \mathbf{Z}_2^{\mathbf{p_b u_a}} (\mathbf{Z}_2^{\mathbf{p_a u_a}})^{-1} \mathbf{Z}_2^{\mathbf{p_a u_b}} \end{bmatrix} \tag{5.25}$$

Using these notations, a system similar than the one in Eq. (3.19) can be obtained

$$\begin{cases} \xi_1 = \mathbf{H}_1 \zeta_1 \\ \bar{\xi}_2 = \bar{\mathbf{H}}_2 \zeta_2 \\ \xi_1 = \bar{\xi}_2 = \xi_{1+2} \\ \Delta_{1+2} = \zeta_1 + \zeta_2 \end{cases} \tag{5.26}$$

All calculations done, the CTFs of the global system can then be expressed using the CTFs of the target and subtracted subsystems

$$\mathbf{H}_{1+2} = \mathbf{H}_1 \left(\mathbf{H}_1 + \bar{\mathbf{H}}_2 \right)^{-1} \bar{\mathbf{H}}_2 \tag{5.27}$$

Subsequently, the CTFs of the target subsystem can obtained by inverting the expression in Eq. (5.27)

$$\mathbf{H}_1 = \bar{\mathbf{H}}_2 \left(\bar{\mathbf{H}}_2 - \mathbf{H}_{1+2} \right)^{-1} \mathbf{H}_{1+2} \tag{5.28}$$

And finally, the pressure at any point of the target subsystem can be obtained after some developments using the vibroacoustic form of the CTFs

$$\tilde{p}_1(M) = p_{1+2}(M) + \left(\mathbf{I} + \bar{\mathbf{H}}_2 \left(\bar{\mathbf{H}}_2 - \mathbf{H}_{1+2} \right)^{-1} \mathbf{H}_{1+2} \bar{\mathbf{H}}_2^{-1} \right) \mathbf{\Lambda}_{1+2}^{\mathbf{M}} \bar{\mathbf{H}}_2^{-1} \mathbf{\Lambda}_{1+2} \tag{5.29}$$

5.2.2 Pressure radiated in the surrounding medium using the rCTF method

The rCTF method is used here to predict the pressure at any point of the surrounding medium in the target subsystem. One has to be aware that this does not exactly correspond to the partially coated cylindrical shell, as removing the coating patch will result in a rigid screen in place of the coating patch (illustrated in figure 79). To study the radiation from the partially coated cylindrical shell, the target subsystem obtained here must be coupled to a model of a water patch in a subsequent step. This will be investigated in section 5.3.

The pressure radiated by the shell in the surrounding fluid of the target subsystem is calculated at first at 2 different points (see figure 79, in which the distances between the points and the rubber-surrounding fluid interface have not been scaled): the first point is 1 m away from the shell and at the same angle as the mechanical force (i.e. $\theta = \pi/2$ rad), while the second point is 50 cm away from the shell, and at an angle corresponding to a boundary of

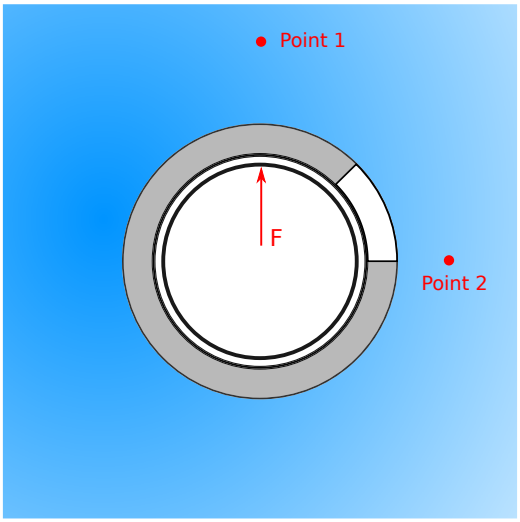

Figure 79: Target subsystem: localization of the measurement points.

the removed patch (i.e. $\theta = 0$ rad). The results of the rCTF method are shown in figure 80 for both formulations (corresponding to Eq. (3.24) for the acoustic formulation and Eq. (5.29) for the vibroacoustic formulation), and are compared to a FEM calculation serving as a reference. We can see that, for the first point, the results are globally good above 600 Hz, but the errors are higher in the low frequencies, especially for the vibroacoustic formulation. As for the second point, which is more impacted by the presence of the rigid screen, both formulations exhibit considerable errors.

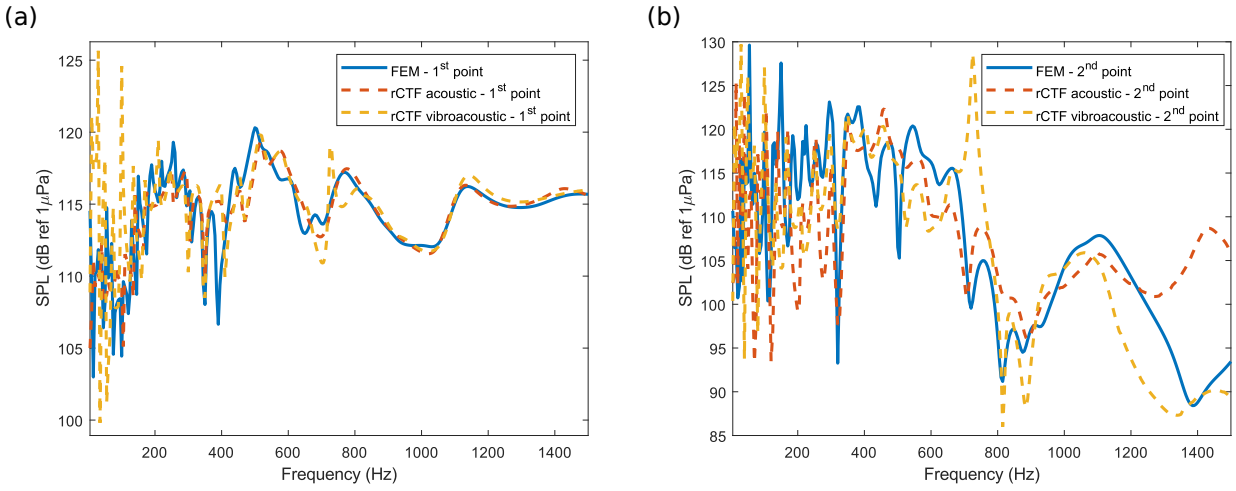

Figure 80: Radiated pressure in the target subsystem using the rCTF method. (a) 1st point. (b) 2nd point.

A first way to mitigate those errors would be to refine the discretization for the computation of the CTFs of the global system 1+2, and for the condensed pressures and radial velocities. In figure 80, 7 points were used to discretize the segments, as evoked in subsection 5.1.1.2. A new calculation is hence carried out by discretizing the segments into 25 points, and the results are shown in figure 81. We can see that, for both points, the results are slightly

better than before, but subsequent errors persist in the low frequencies, and for the second point in the whole frequency range.

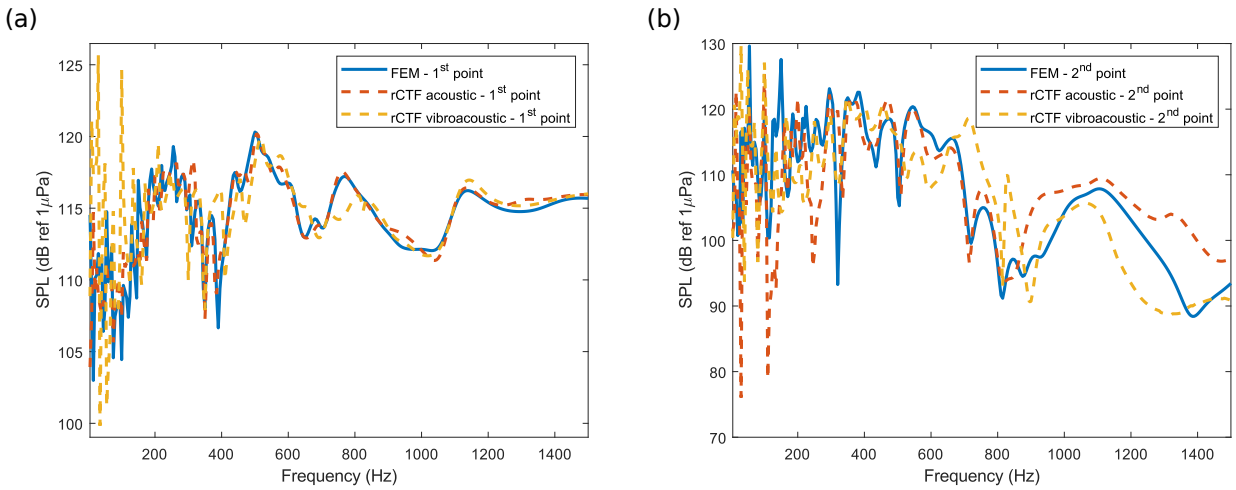

Figure 81: Radiated pressure in the target subsystem using the rCTF method - computation with a finer discretization. (a) 1st point. (b) 2nd point.

The difference of results for the two decoupling boundaries is particularly glaring in the low-frequency range, especially for the first point where the errors are much higher for the decoupling boundary Ω_2. To explain this fact, one can have a look at the condition number of the different CTFs matrices of interest in both formulations. We can see in figure 82 that the CTFs matrices when the decoupling boundary Ω_2 is considered are much more ill-conditioned than those in the acoustic formulation. As it has already been evoked in subsection 5.1.3, the CTFs matrices in the vibroacoustic formulation exhibit a very wide range of amplitudes for both the global system and the subtracted subsystem. This behavior can potentially lead to important disparities in the eigenvalues of the matrices, and hence high values of the condition numbers. This probably explains why the vibroacoustic formulation is much more sensitive to model errors.

A second possibility to mitigate those errors could be to use a finer mesh for the FEM model of the subsystem 2. However, this solution has been tested and does not really have an influence on the results, as the model is sufficiently described using the criterion of 6 elements per acoustic wavelength at the highest considered frequency. The results are thus not shown here. We can thus conclude that the decoupling does not work really well here. One explanation could come, as it has already been evoked in section 3.3.4, from the fact that substructuring in the near-field of a structure (a plate in references [170, 171]) can induce problems of convergence of the CTF approach (or PTF in the references). To explore this lead, in the next subsection, the decoupling will be carried out by considering removing only a fraction of the patch along the thickness.

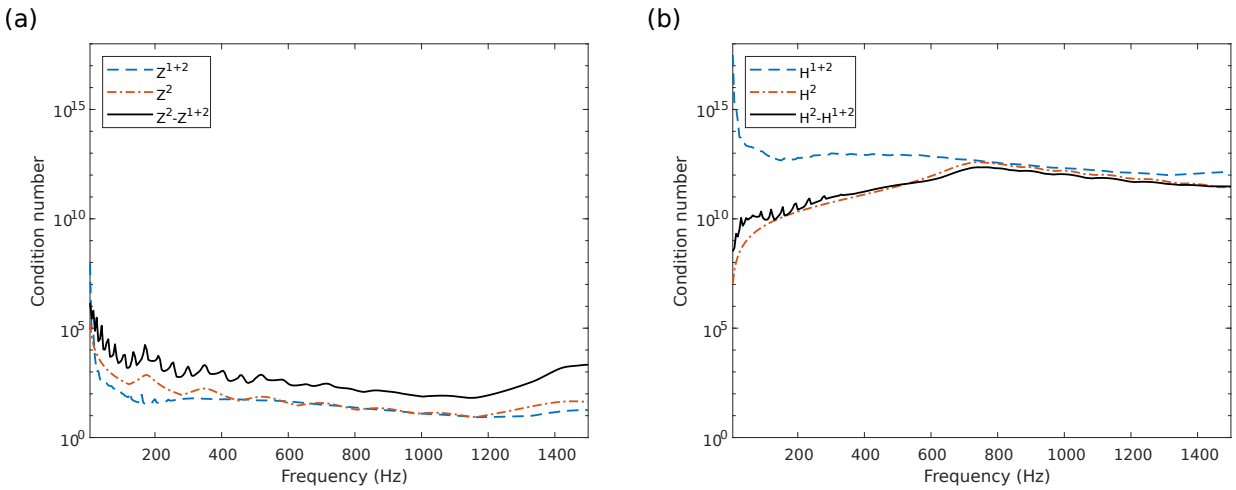

Figure 82: Condition number of the CTFs matrices. (a) Acoustic rCTF formulation. (b) Vibroacoustic rCTF formulation.

5.2.3 Removing a fraction of the patch

5.2.3.1 Test case with a half-patch

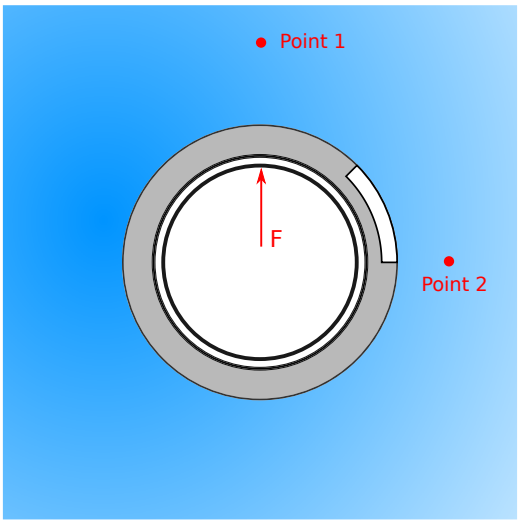

Figure 83: Target subsystem obtained by removing a half-patch.

To verify if the hypothesis proposed in the previous paragraph is correct, we are interested here in removing only a half-thickness of the initial subtracted subsytem: the part that is not directly bonded to the shell. This allows partioning at a given distance of the vibrating structure, as it was proposed in [171], and in order to avoid the description, with the rCTF method, of the complex interaction between the vibrating structure and the surrounding fluid. The target subsytem is hence a coated cylindrical shell, with an angular domain where only half of the coating thickness is coated, the other half being a rigid screen, as shown in figure 83. Given that there is no more vibroacoustic decoupling interface, only the acoustic formulation of the rCTF method will be explored here.

The results of the decoupling calculation using the rCTF method are presented in figure 84

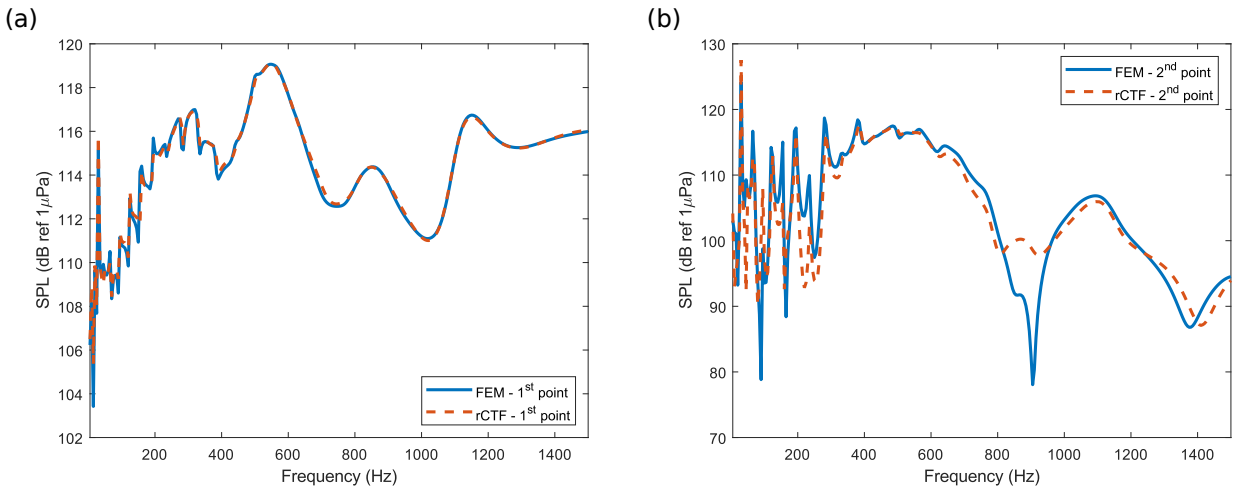

Figure 84: Radiated pressure in the target subsystem when removing a half-patch using the rCTF method. (a) 1st point. (b) 2nd point.

for the same points, and with 7 points used to discretize the segments for the global system. We can see that the results are much better for this case study, as the comparison with the reference FEM calculation shows a quasi-perfect match for the first point. The results for the second points show more discrepancies, but it is important to mention that, unlike the previous calculation, the resonances and anti-resonances are located at the correct frequencies, especially in the low-frequency range.

To verify the validity of this calculation in another way, cartographies can be plotted at a single frequency to observe the radiated pressure field in the surrounding fluid medium. At first, a cartography is proposed at 500 Hz is figure 85, a frequency at which the results of the rCTF calculation is very close to the reference calculation for both points. In addition, a cartography at the same frequency is shown in figure 85c for the global system 1+2, which is the fully coated cylindrical shell, and for the same mechanical excitation. There is an excellent correlation between the reference (figure 85a) and rCTF (figure 85b) calculations, with minor discrepancies in the shadow area of the shell where the pressure is at its minima values. It is also very interesting to notice that there is a clear difference between the pressure field in the target subsystem and the pressure field in the global system. The loss of axisymmetry is well observed, and the presence of the rigid screen in the target subsystem in place of a part of the coating is correctly taken into account when performing the rCTF calculation. This statement is very important, as it shows that even if some errors can appear when performing the decoupling calculations, the impact of the default (here, the missing part of the coating) is correctly modelled.

In a second step, cartographies are proposed in figure 86 at 2 frequencies: at 195 Hz, which is a resonant frequency of the target subsystem in the low frequency range (see figure 84), and at 905 Hz, which is the anti-resonant frequency at which the error is the highest in

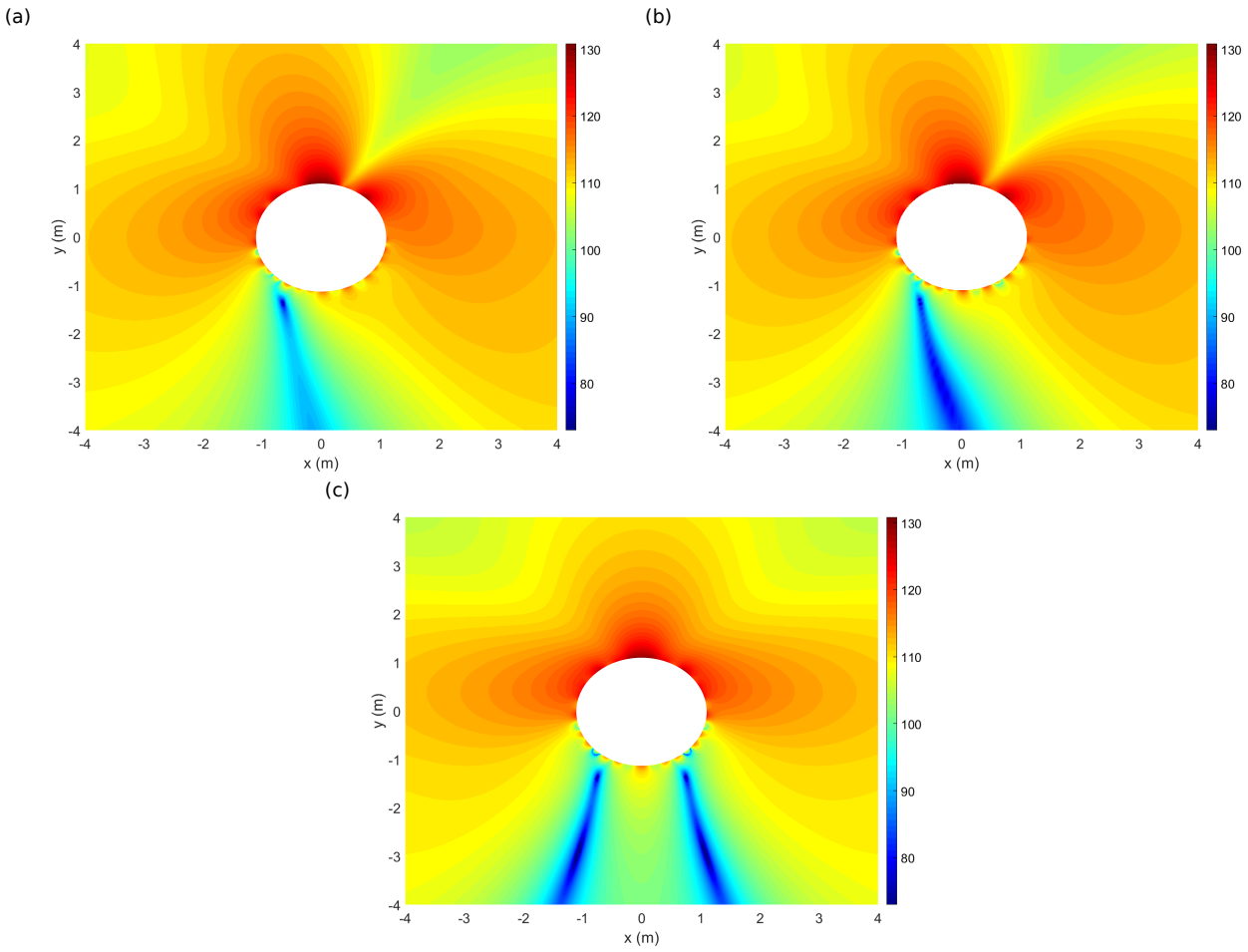

Figure 85: Cartography of the radiated pressure in the surrounding fluid using the rCTF method. (a) FEM calculation at 500 Hz. (b) rCTF calculation at 500 Hz. (c) FEM calculation 500 Hz for the global system 1+2.

figure 84b. From the observation of these cartographies, we can see that the radiated pressure field is correctly described in all the surrounding fluid medium, as the patterns of maxima and minima of pressure are precisely localized. Some discrepancies in the amplitudes can sometimes be observed, particularly in the vicinity of the subtracted subsystem, but these errors do not change the global behavior of the pressure field in this area. Furthermore, as already evoked when analyzing figure 85, the pressure field is not axisymmetric, highlighting the presence of the rigid screen for both FEM and rCTF calculations.

5.2.3.2 Parametric study on the thickness of the removed coating patch

Following this observation, it could be interesting to carry out a parametric study regarding the fraction of the thickness of the coating patch that is removed. Starting from the case studied in subsection 5.2.3.1 (i.e. 50%), we can go towards cases where the inner coupling interface gets closer to the exterior surface of the shell. Ultimately, it will also be interesting to compare the differences between the several target subsystems that are going to be studied here, and also with the target subsystem of interest described in figure 79.

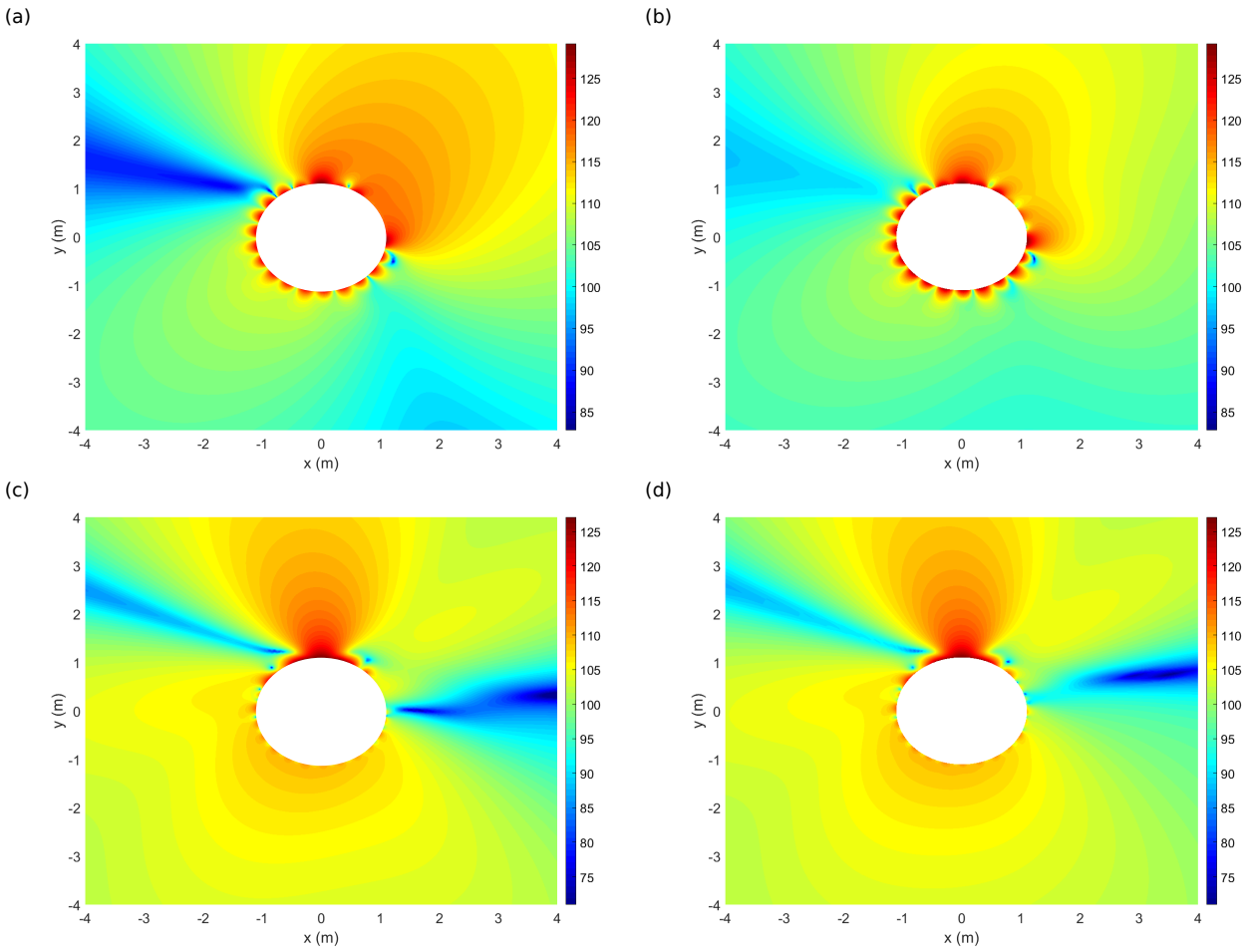

Figure 86: Cartography of the radiated pressure in the surrounding fluid using the rCTF method. (a) FEM calculation at 195 Hz. (b) rCTF calculation at 195 Hz. (c) FEM calculation at 905 Hz. (d) rCTF calculation at 905 Hz.

In figure 87, the pressure radiated at the two previously studied points are displayed for the FEM and rCTF calculations, for four different fractions of removed coating patch: 75% (figure 87a), 80% (figure 87b), 85% (figure 87c) and 90% (figure 87d). It is reminded that the results for the 100% case are presented in figure 80 while the results for the 50 % case are shown in figure 84. The observation of the results, especially for the second point, shows a clear tendancy for the results to deteriorate when the inner coupling interface gets closer to the shell's surface. Above the fact that the size of the subtracted subsystem increases (which can result in higher errors as it has been highlighted in chapter 2), the explanation of these errors comes from the proximity of the shell's surface. Hence, it can be interesting to compare the evolution of the radiated pressure at the points of interest for the different configurations. This will permit estimating the accuracy of the calculation if only a fraction of the coating thickness is removed, instead of the whole coating thickness.

The comparison between the different configurations is displayed in figure 88 for the second point only as it is the one more impacted by the changes in configurations (the configurations have been split into two figures in order to keep a clear view of the different

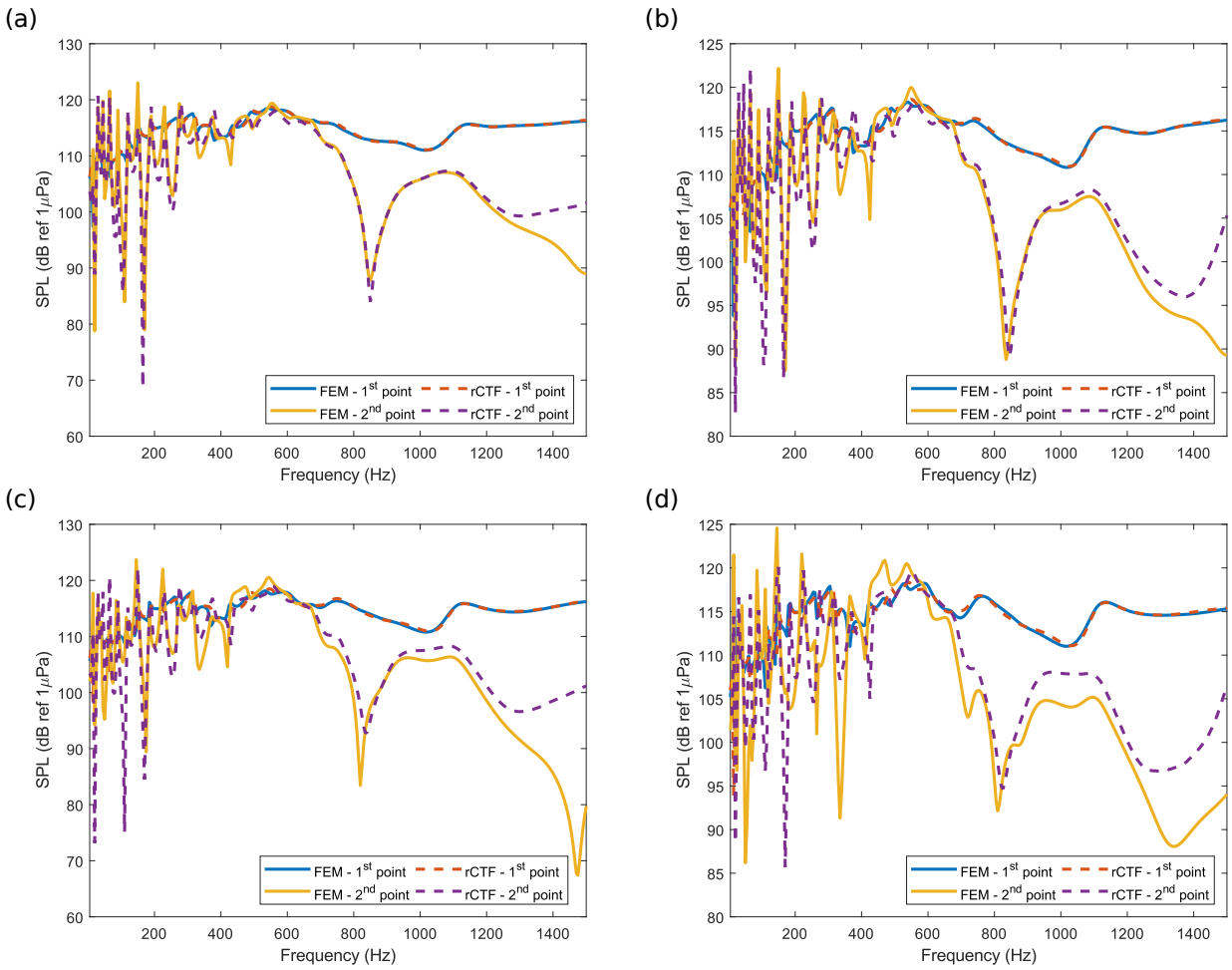

Figure 87: Parametric study for several fractions of thickness of the coating. (a) 75%. (b) 80%. (c) 85%. (d) 90%

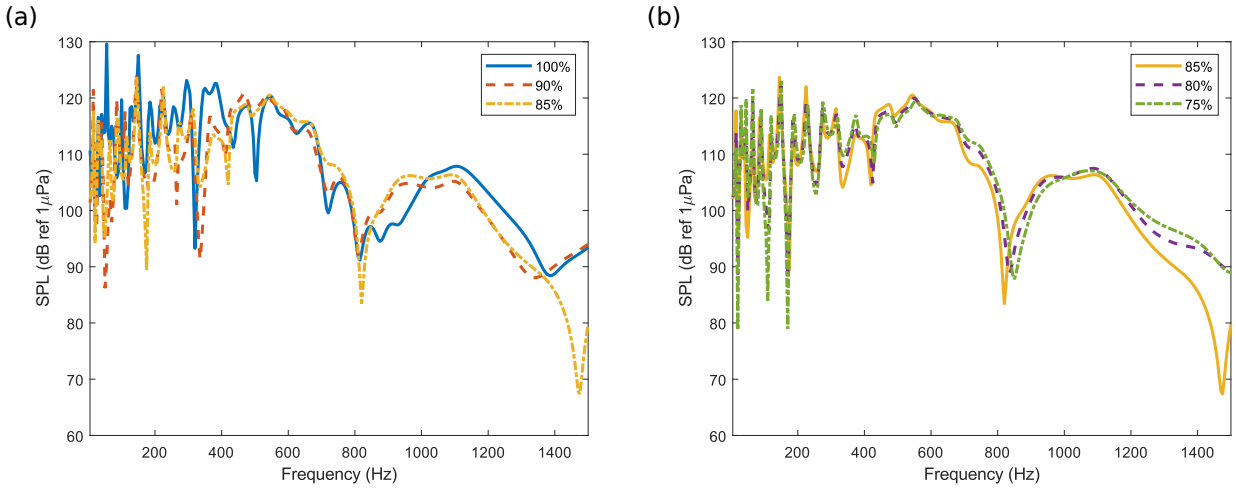

Figure 88: Comparison of the FEM reference calculation for several fractions of thickness of the coating. (a) 100%, 90% and 85%. (b) 85%, 80% and 75%.

curves). It is interesting to notice that in figure 88b, the behavior of the three configurations is very close, especially in the low frequency range. However, the 90% and 100% configurations in figure 88a exhibit different behaviors, especially in the low frequency range. This means

that for points close to the coupling interface in the surrounding fluid of the target subsystem, it is not possible to use a less sensitive configuration in order to get an approximated value of the radiated pressure. Hence, in order to correctly predict the radiated pressure in this area, another way must be explored to improve the results of the rCTF for the 90% and, as much as possible, 100% configurations.

5.2.4 Influence of the size of the segments

When the interface between two subsystems is situated in the near-field of a structure, it has been observed in [170] that the criterion of Eq. (3.31) used for the size of the patches to apply the PTF method may not be sufficient. The investigations in [170] show that for this situation, corresponding to substructuring in the near field zone of the vibrating structure, refining the criterion regarding the minimum wavelength (considering the acoustic and structural subsystems) at the highest considered frequency can significantly improve the results (the criterion $\lambda/6$ was retained in [170]). On another hand, in her PhD thesis, Berton [201] observed that, to predict the fluid added mass effect on the modes of a vibrating structure immersed in water, a criterion $\lambda_n/15$ was necessary, where λ_n corresponds to the modal wavelength of the considered mode n. We can hence verify the influence of the size of the segments on the results of the rCTF calculation here.

5.2.4.1 Calculations with the 90% patch

At first, this study is carried out by removing 90% of the thickness of the coating patch. As a preliminary observation, we can notice that a zoom in the low-frequency range of figure 87d shows that the calculation for the 90% patch seems to converge until 30 Hz with the criterion $\lambda/2$, at least regarding the correct placement of the resonances and anti-resonances. At this frequency, the different wavelengths of interest read

$$\lambda_f = 50 \text{ m}\,, \quad \lambda_p = 9.76 \text{ m}\,, \quad \lambda_s = 1.81 \text{ m} \tag{5.30}$$

Hence, at this frequency, the most restraining criterion is linked to the flexural wavelength of the shell. Regarding the initial size of the segments, this limit of convergence is reached for a criterion equivalent to $\lambda/18$. This means that it may be necessary to apply this criterion at 1500 Hz in order for the calculation to converge completly. Before verifying this assumption, it can be interesting to see if a less restraining criterion could be sufficient. Indeed, reducing the size of the segments considerably increases the computing time, hence a good balance must be found between satisfactory results and computational cost. To this end, the evolution of the radiated pressure in the target subsystem is evaluated in figure 89 for three different criteria regarding the size of the segments: $\lambda/2$, $\lambda/4$ and $\lambda/6$ (the criterion used in [170]). A zoom in

the low-frequency range is proposed in figure 89b in order to have a better appreciation of the convergence of the calculations in this range.

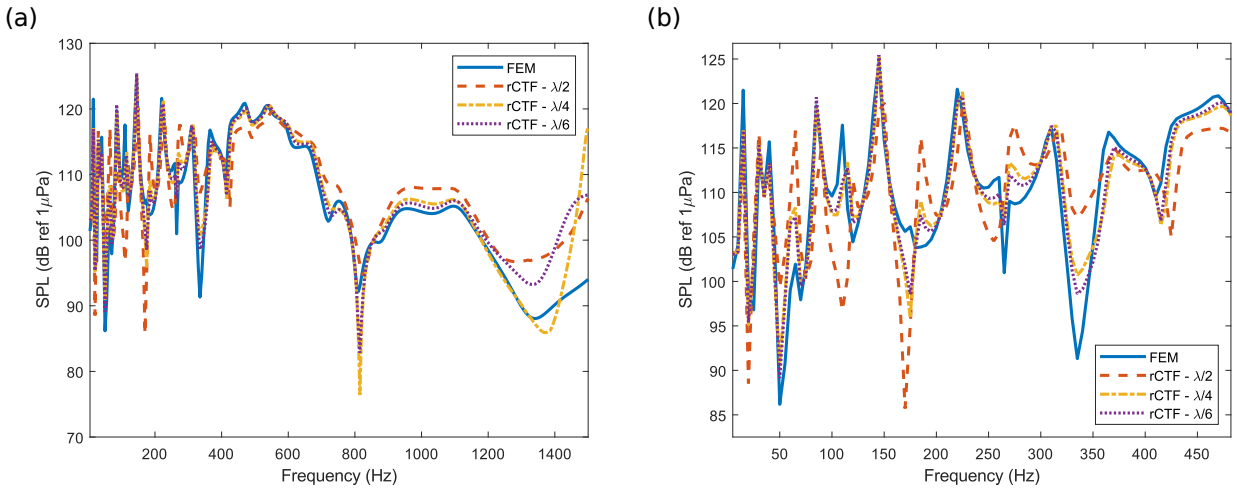

Figure 89: Evaluation of the influence of the criterion for the size of the segments. (a) Results in the whole frequency range. (b) Zoom in the low frequency range.

We can see a huge difference between the $\lambda/2$ calculation, and the $\lambda/4$ and the $\lambda/6$ calculations. However, between the $\lambda/4$ and the $\lambda/6$ calculations, the difference is not substantial. Some discrepancies can be observed, but there is no clear difference in the frequency at which the convergence is reached (between 1200 Hz and 1300 Hz for both calculations, with some minor discrepancies appearing at the resonances and anti-resonances). The $\lambda/4$ calculation even seems to present a better convergence, but the discrepancies are slightly higher at the resonances and anti-resonances than for the $\lambda/6$ calculation.

In order to verify these observations, a cartography of the radiated pressure can be plotted for these three criteria at 540 Hz, frequency at which the criterion $\lambda/2$ should not converge, contrary to the other 2 criteria. It could also be interesting to verify if there is a notable difference between the $\lambda/4$ and $\lambda/6$ calculations.

The cartographies presented in figure 90 confirm the previous observations. The rCTF calculation has not converged in figure 90b for the criterion $\lambda/2$, but it has converged for the criteria $\lambda/4$ (90c) and $\lambda/6$ (90d). Also, the calculations for the $\lambda/4$ and $\lambda/6$ criteria are almost entirely identical, which supports the observations drawn from figure 89. Thus, we can imagine that a more restraining criterion won't necessary improve the results. To verify this statement, the rCTF calculation is carried out for 3 other criteria in figure 91: $\lambda/8$, $\lambda/12$ and $\lambda/18$ (which was previously identified as the possible criterion for the rCTF calculation to correctly converge).

From the results presented in figure 91, we can confirm the previous assumption. Indeed, there isn't any substantial benefit in applying more restrictive criteria, as the limit of convergence is globally the same for all the studied criteria from $\lambda/4$ to $\lambda/18$. As the point at which

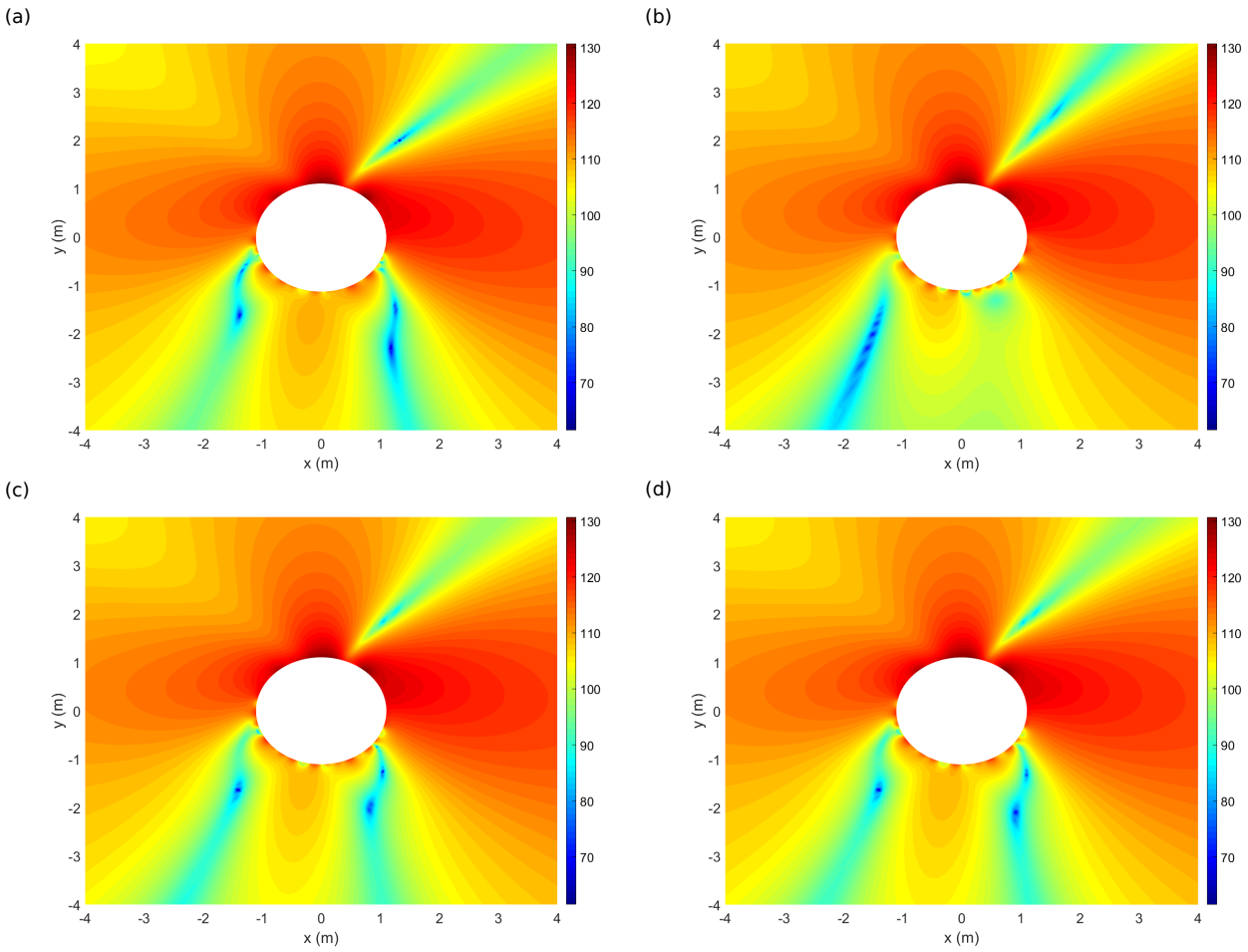

Figure 90: Cartography of the radiated pressure at 540 Hz for several criteria regarding the size of the segments, when removing 90% of the coating patch. (a) FEM calculation. (b) rCTF calculation with $\lambda/2$ criterion. (c) rCTF calculation with $\lambda/4$ criterion. (d) rCTF calculation with $\lambda/6$ criterion.

the results are presented is located in the most critical area where errors can appear, we can safely assume that this conclusion will not change when considering other points, further away from the rigid screen. Besides, the discrepancies observed above 1300 Hz remain for all the studied criteria, meaning that the rCTF method fails to converge in this frequency domain. Possibilities to improve this convergence will be discussed in the perspectives of this work. We can now try to carry out the same investigations for the initial rCTF calculation consisting in removing the whole coating patch, in order to obtain more satisfactory results.

5.2.4.2 Calculations with the whole patch considering the acoustic formulation

When the whole patch is removed, as it has been investigated in subsection 5.2.2, it is difficult to identify a limit on convergence for the second investigated point (see figure 81b), as the calculation does not seem to converge at all. Hence, a first calculation is carried out for the criteria $\lambda/4$ and $\lambda/6$ in figure 92 (with a zoom in the low frequency range in figure 92b). If the results are slightly better than for the $\lambda/2$ criterion, it is still difficult to identify clearly

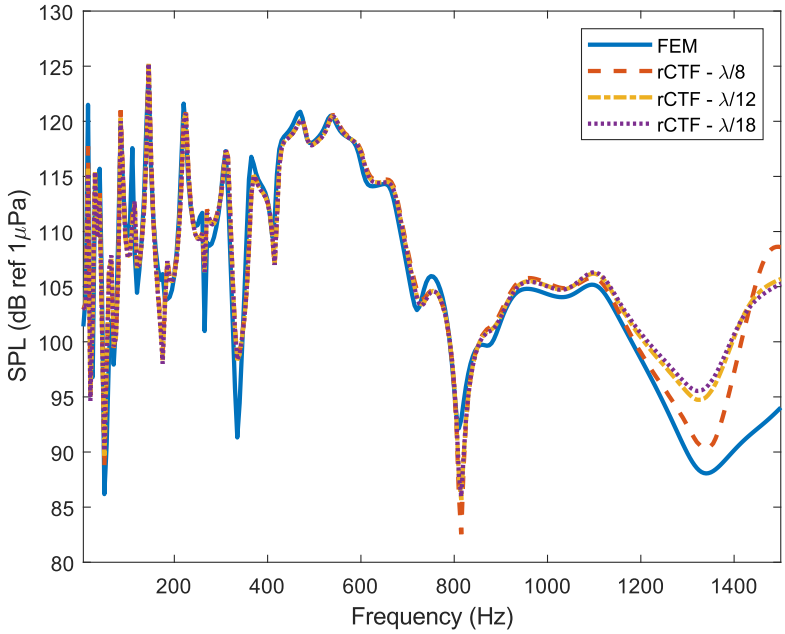

Figure 91: Radiated pressure from rCTF calculations with restrictive criteria regarding the size of the segments.

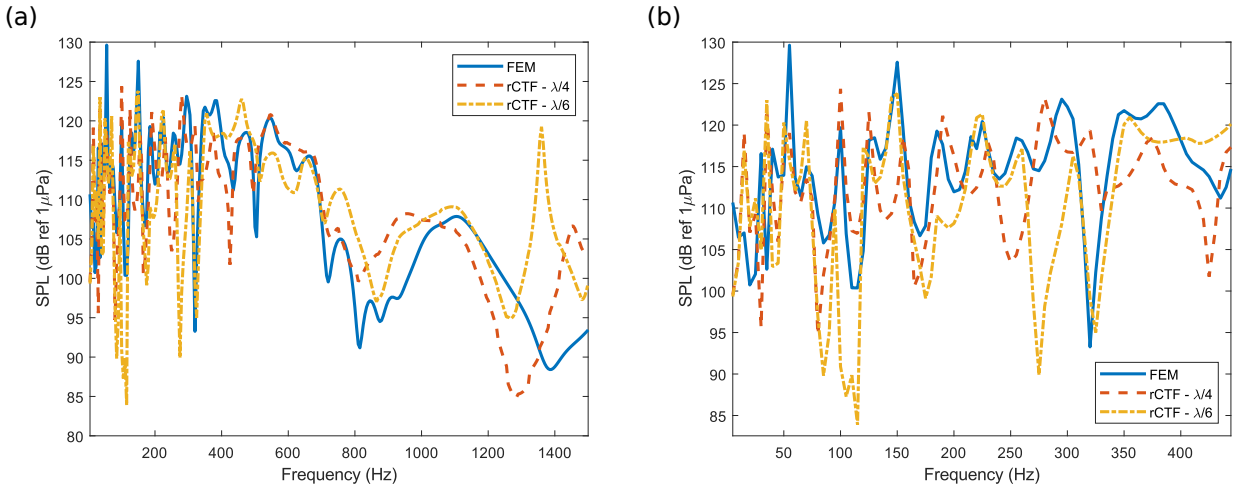

Figure 92: Evaluation of the influence of the criterion for the size of the segments when removing the full patch. (a) Results in the whole frequency range. (b) Zoom in the low frequency range.

a convergence frequency as it was done when removing the 90% patch. However, for this case, the inner coupling interface is bonded to the shell's surface, which means that a more restrictive criterion could be necessary, contrary to the 90% patch. The calculations where hence carried out for criteria ranging from $\lambda/8$ to $\lambda/25$, but the results did not improve and are thus not shown here. This assumption can be confirmed when a cartography of the pressure field is plotted at 1000 Hz for the $\lambda/4$ and $\lambda/6$ criteria in figure 93. We can see a slight benefit in using the $\lambda/6$ criterion instead of the $\lambda/4$ criterion, especially in the area where the pressure is lower on the left-hand side of the shell. Some discrepancies can be

observed between the FEM and rCTF calculations in the vicinity of the coupling interface, but in the majority of the domain, there is a very good agreement between both calculations.

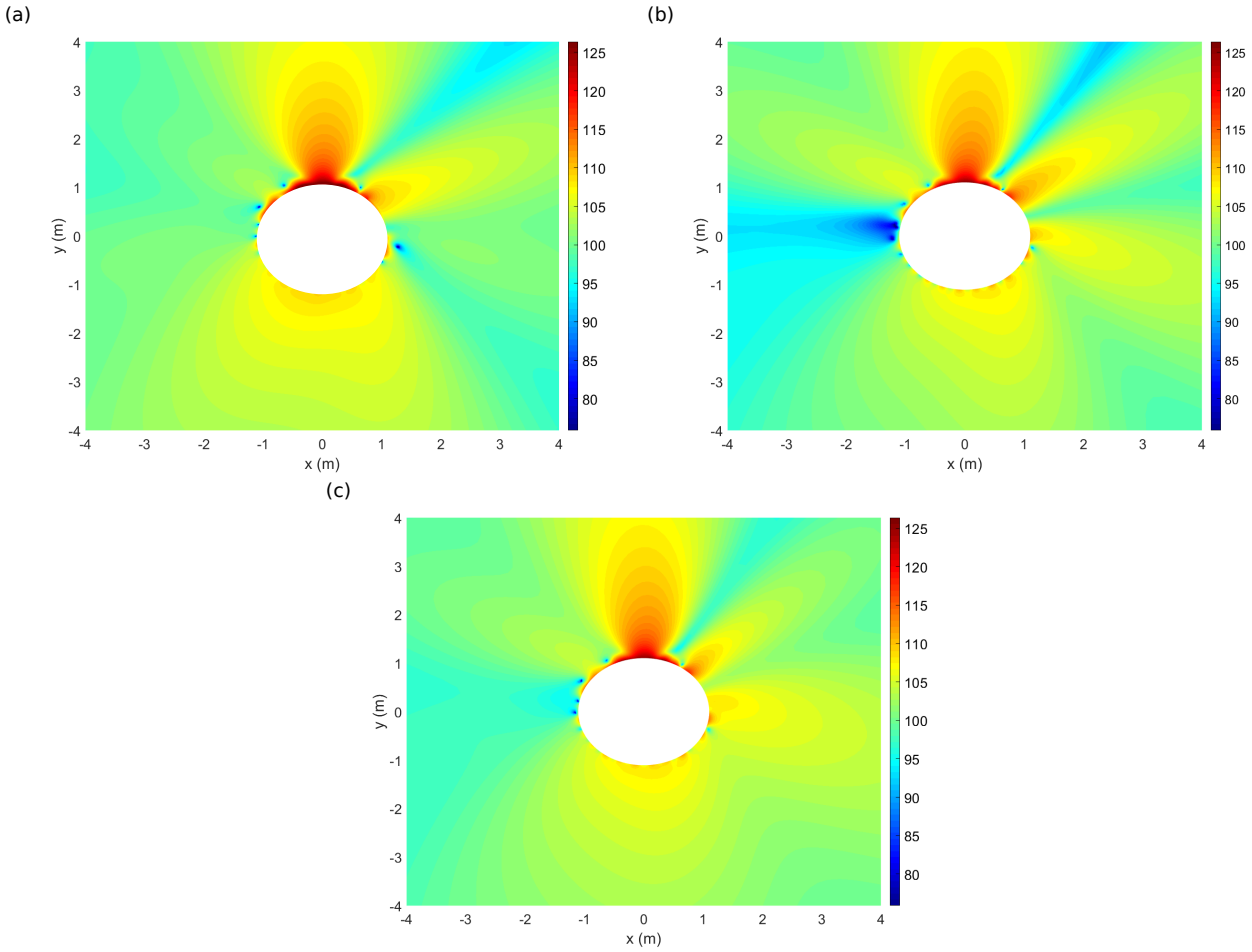

Figure 93: Cartography of the radiated pressure at 1000 Hz for several criteria regarding the size of the segments, when removing 100% of the coating patch. (a) FEM calculation. (b) rCTF calculation with $\lambda/4$ criterion. (c) rCTF calculation with $\lambda/6$ criterion.

5.2.4.3 Calculations with the whole patch considering the vibroacoustic formulation

Besides, if this study has been carried out for the acoustic formulation, it could also be interesting to perform rCTF calculations considering the vibroacoustic formulation with smaller segments to see if the results from this formulation can be improved.

The results of these investigations for the vibroacoustic rCTF formulation are presented in figure 94 for the criteria $\lambda/4$ and $\lambda/6$ (with a zoom in the low frequency range in figure 94b). They show no significant improvement compared to the $\lambda/2$ calculation in figure 81b, and we can also notice that there is almost no difference between those two calculations. We can hence conclude that the size of the segments has an influence on the results of the rCTF method only when the acoustic formulation is considered.

The investigations carried out in this section gave significant insights on the validity of the rCTF method for the present case of interest. Of the two proposed formulations, the acoustic

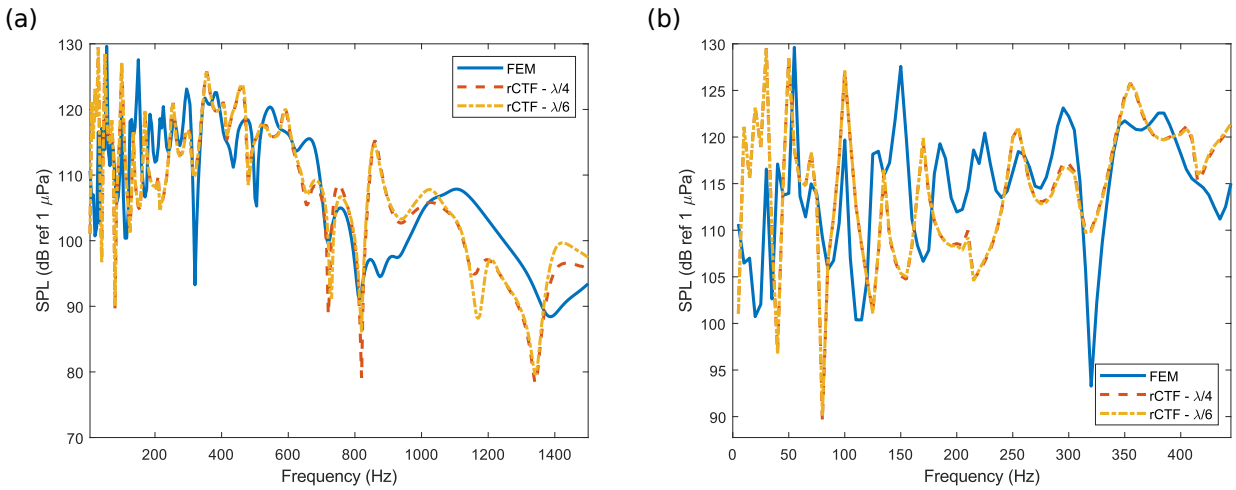

Figure 94: Evaluation of the influence of the criterion for the size of the segments when removing the full patch considering the vibroacoustic formulation. (a) Results in the whole frequency range. (b) Zoom in the low frequency range.

one presented the best results and a better potential for improvement when considering the size of the segments and the fraction of the patch to be removed. It will hence be the one retained. It is important to stress that the mitigated results discussed here concern the particular case of the pressure field in the area close to the coupling interface. The pressure field in the remaining parts of the target subsystem obtained using the rCTF method is very close to the reference calculation. However, the target subsystem obtained here corresponds to a partially coated cylindrical shell where a rigid screen has taken the place of the missing part of the coating. In order to study the radiation from a partially coated cylindrical shell in water, this target subsystem must be coupled to a water patch to fill the rigid screen. This is investigated in the next section.

5.3 Recoupling with a water tile

Now that a coating patch has been removed from the fully coated cylindrical shell, we are interested in coupling this model to a FEM model of the water to fill the missing part of the coating, as shown in figure 95. Here after, this operation will be referred to as "recoupling". The formulation to perform this recoupling calculation, based on the direct CTF approach, is developed before being applied to the radiation of the partially coated cylindrical shell.

5.3.1 Formulation for the recoupling

The necessary equations to couple two subsystems along an interface Ω have been presented in section 3.1. The two equations of interest here are reminded

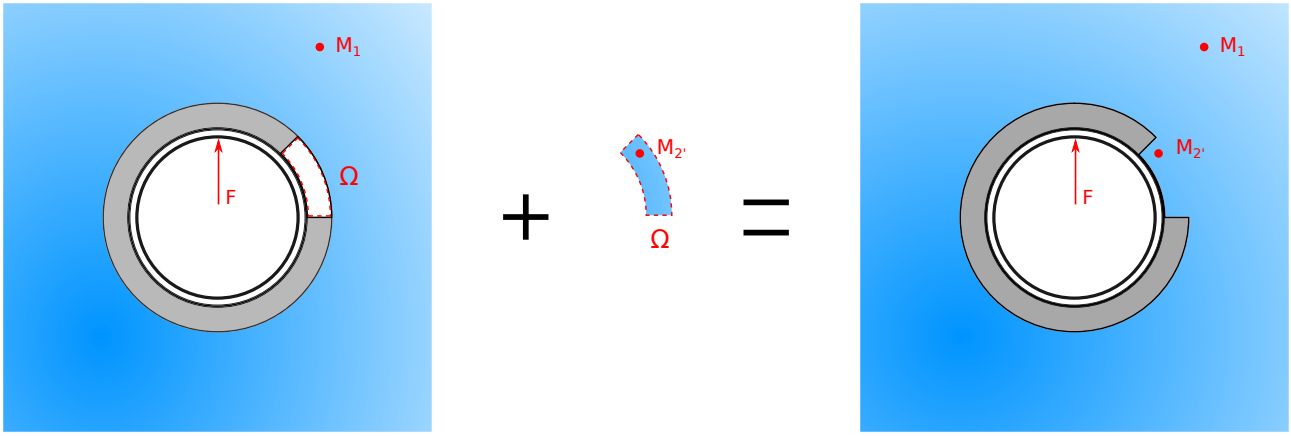

Figure 95: Recoupling with a water tile.

$$\begin{cases} p_{1+2'}(M_1) = \tilde{p}_1(M_1) + \mathbf{Z_1}(M_1)\mathbf{U_{1+2'}} & (5.31a) \\ p_{1+2'}(M_{2'}) = -\mathbf{Z_{2'}}(M_{2'})\mathbf{U_{1+2'}} & (5.31b) \end{cases}$$

where the point M_1 initially belongs to subsystem 1, while the point $M_{2'}$ initially belongs to subsystem 2'. These equations correspond to the pressure at any point of the final recoupled subsystem, and the subscript 2' denotes the recoupled water patch. Let us, at first, focus on Eq. (5.31a), in order to obtain the radiated pressure in the exterior acoustic domain. $\tilde{p}_1(M_1)$ is the blocked pressure when the subsystem 1 is uncoupled from subsystem 2' and corresponds to the quantity computed in section 5.2. We must hence calculate $\mathbf{Z_1}(M_1)$ and $\mathbf{U_{1+2'}}$.

$\mathbf{Z_1}(M_1)$ is the vector of the point condensed impedances of subsystem 1, and its components are defined as the pressure at point M_1 when normal velocities corresponding to each condensation function are prescribed on Ω. Using a reciprocity principle as in section 3.2.2, this quantity is equal to the condensed pressure at the surface Ω when a monopole of unit volume velocity is located at the point M_1 of the uncoupled subsystem 1. It is hence noted $\tilde{\mathbf{P}}_{\mathbf{1}}^{\mathbf{M_1}}$, and has been calculated in Eq. (3.23)

$$\tilde{\mathbf{P}}_{\mathbf{1}}^{\mathbf{M_1}} = \left(\mathbf{I} + \mathbf{Z_2}\left(\mathbf{Z_2} - \mathbf{Z_{1+2}}\right)^{-1}\mathbf{Z_{1+2}}\mathbf{Z_2}^{-1}\right)\mathbf{P}_{\mathbf{1+2}}^{\mathbf{M_1}} \tag{5.32}$$

Concerning $\mathbf{U_{1+2'}}$, it is given directly by Eq. (3.8)

$$\mathbf{U_{1+2'}} = -\left(\mathbf{Z_1} + \mathbf{Z_{2'}}\right)^{-1}\tilde{\mathbf{P}}_{\mathbf{1}} \tag{5.33}$$

As $\mathbf{Z_1}$ has already been computed, the necessary quantities here are $\mathbf{Z_{2'}}$ (which can be obtained in the same way as $\mathbf{Z_2}$, through a FEM calculation), and $\tilde{\mathbf{P}}_{\mathbf{1}}$. The latter corresponds to the condensed pressure at the surface Ω of the uncoupled subsystem 1 when the excitation is the external mechanical force and can then be noted $\tilde{\mathbf{P}}_{\mathbf{1}}$. It is calculated in a similar way as $\tilde{\mathbf{P}}_{\mathbf{1}}^{\mathbf{M_1}}$ in Eq. (5.32)

$$\tilde{\mathbf{P}}_{\mathbf{1}} = \left(\mathbf{I} + \mathbf{Z_2}\left(\mathbf{Z_2} - \mathbf{Z_{1+2}}\right)^{-1}\mathbf{Z_{1+2}}\mathbf{Z_2}^{-1}\right)\mathbf{P_{1+2}} \tag{5.34}$$

From these information, Eq. (5.31a) can be rewritten

$$\begin{aligned} p_{1+2'}(M_1) = p_{1+2}(M_1) &+ \left(\mathbf{I} + \mathbf{Z_2}\left(\mathbf{Z_2} - \mathbf{Z_{1+2}}\right)^{-1}\mathbf{Z_{1+2}}\mathbf{Z_2}^{-1}\right)\mathbf{P}_{\mathbf{1+2}}^{\mathbf{M_1}}\mathbf{Z_2}^{-1}\mathbf{P_{1+2}} \\ &- \tilde{\mathbf{P}}_{\mathbf{1}}^{\mathbf{M_1}}\left(\mathbf{Z_2}\left(\mathbf{Z_2} - \mathbf{Z_{1+2}}\right)^{-1}\mathbf{Z_{1+2}} + \mathbf{Z_{2'}}\right)^{-1}\tilde{\mathbf{P}}_{\mathbf{1}} \end{aligned} \tag{5.35}$$

Concerning the pressure at the point $M_{2'}$, initially belonging to the subsystem 2' (i.e. the water patch), it is described in Eq. (5.31b). The quantity $\mathbf{Z_{2'}}(M_{2'})$ can be obtained by placing a unitary monopole at point $M_{2'}$ in subsystem 2' and computing the condensed pressure at the surface Ω. This calculation can be done directly in the FEM model of the water patch. All the necessary quantities to compute the pressure in the recoupled system have then already been calculated. The computations will hence be carried out in the next sections.

5.3.2 Recoupling with the 90% patch

In section 5.2, we have seen that the decoupling calculations of the rCTF exhibit non negligible errors in the vicinity of the coupling interface. A way to mitigate those errors was to reduce the size of the segments, and to consider removing only a fraction of the coating patch instead of its entirety. These two combined solutions gave interesting results, which lead us to consider, at first, this configuration for the recoupling calculations. In the following, the calculations will be carried out considering the $\lambda/6$ criterion to define the size of the segments.

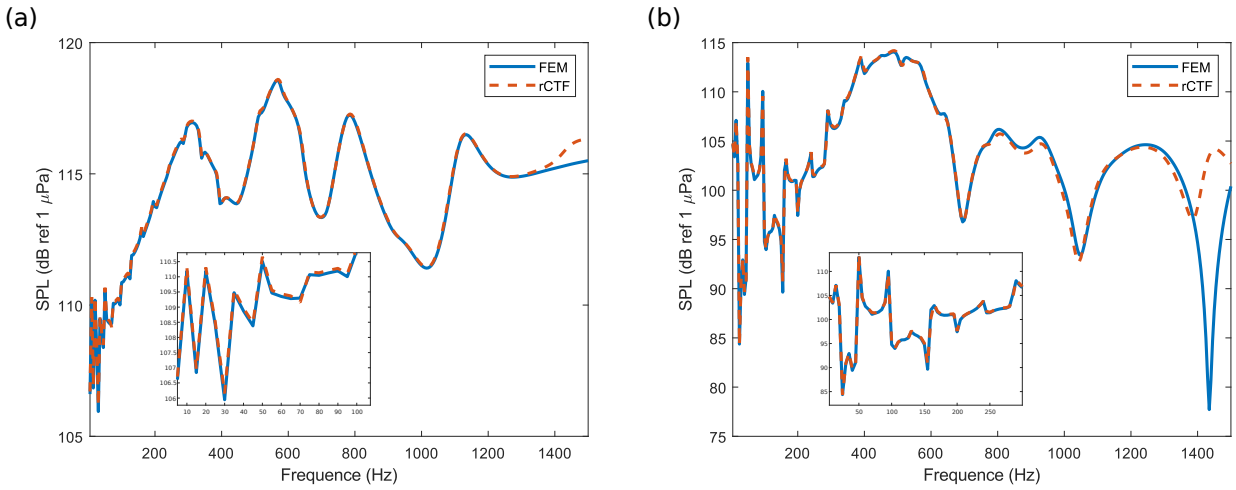

Figure 96: Pressure radiated by the partially coated shell after recoupling with the 90% patch. (a) 1st point. (b) 2nd point.

The pressure radiated by the partially coated cylindrical shell when 90% of the coating patch is removed (and replaced by water) is shown in figure 96 for the two points previously

investigated (see figure 79). At first sight, we can notice that the recoupling seems to work fine until 1300 Hz. Above this frequency, some discrepancies appear, especially for the point located close to the coupling interface. The zoom in the low-frequency range allows verifying that the resonances and anti-resonances in this range are perfectly described, both in terms of frequency and amplitude.

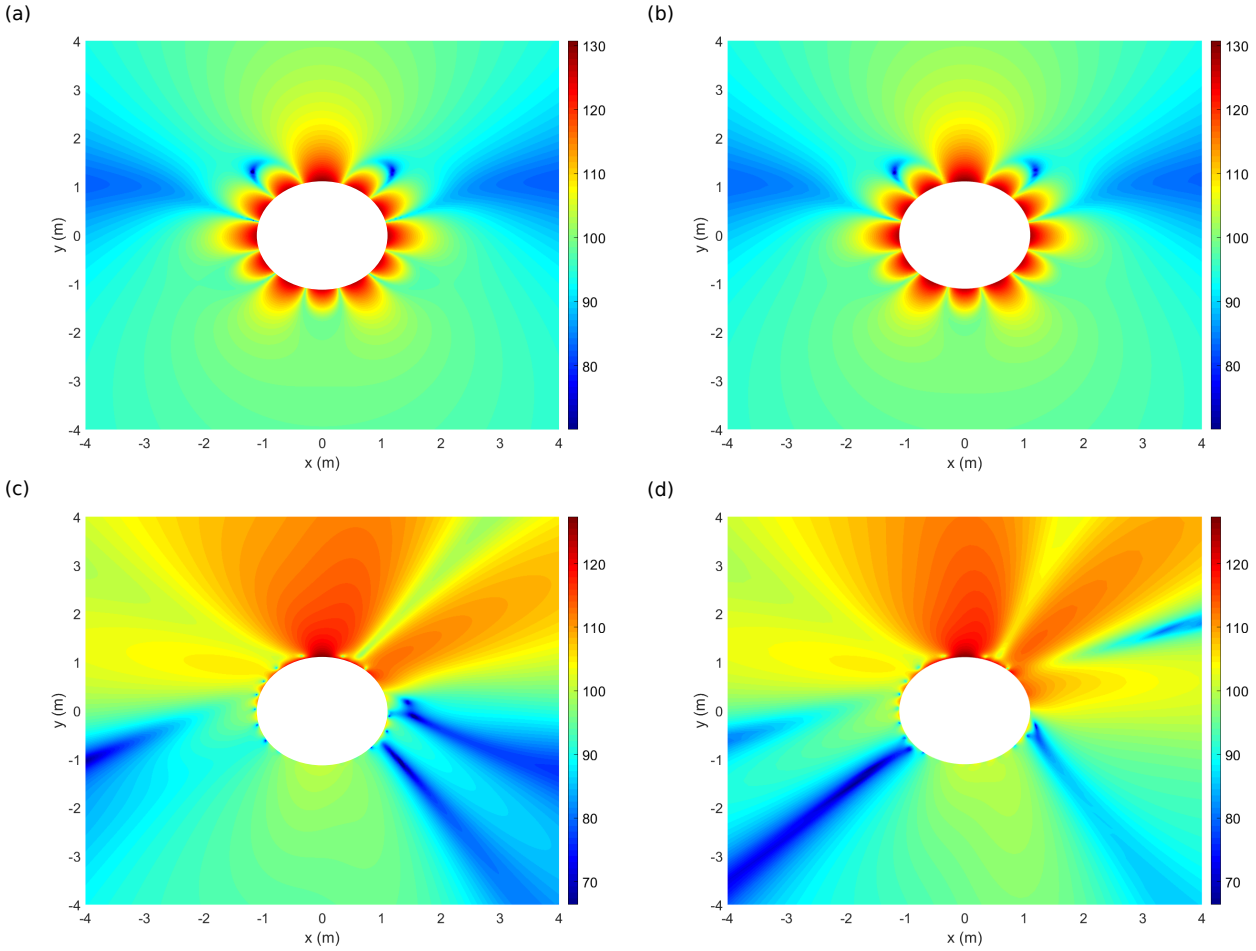

Figure 97: Pressure radiated by the partially coated shell after recoupling with the 90% patch - cartographies. (a) FEM calculation at 50 Hz. (b) rCTF calculation at 50 Hz. (c) FEM calculation at 1435 Hz. (d) rCTF calculation at 1435 Hz.

These results can be completed with cartographies plotted at several frequencies. In figure 97, cartographies are shown at 50 Hz (which is a resonant frequency of the system in the low-frequency range) and 1435 Hz, as it is the frequency at which the error is maximal in figure 96b. The first cartography, at 50 Hz shows a perfect match, but we can observe that the pressure field is symmetric with respect to the direction of application of the force (i.e. $\theta = \pi/2$ rad). This highlights that the effect of the removed patch is negligible at this frequency, which means that, if at least the rCTF calculation does not introduce errors for this configuration, this result is not sufficient to conclude that the rCTF calculation is accurate. Besides, the cartography at 1435 Hz shows discrepancies between the FEM calculation and the rCTF calculation, even if global trends are similar on the two figures. Contrary to the

calculation at 50 Hz, it is possible to observe the effect of the missing patch, as the pressure field is not symmetric anymore. To draw a stronger conclusion on the result of this study, a cartography is hence plotted at 800 Hz in figure 98. At this frequency, the influence of the removed patch is highlighted by the asymmetry of the pressure field, and the match between the two calculations is almost perfect, with very minor discrepancies located at points where the pressure is minimal. The comparison with the radiated pressure field when the shell is fully coated will be carried out in subsection 5.3.3 when the recoupling of the whole patch will be investigated.

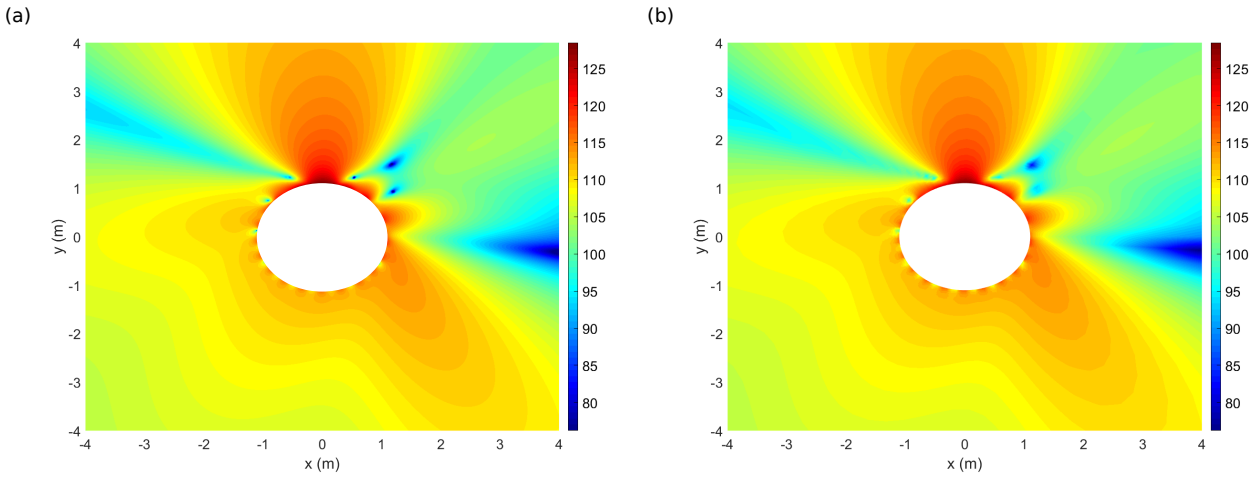

Figure 98: Pressure radiated by the partially coated shell after recoupling with the 90% patch - cartographies. (a) FEM calculation at 800 Hz. (b) rCTF calculation at 800 Hz.

5.3.3 Recoupling with the whole patch

The results in subsection 5.3.2 show that recoupling the target subsystem of section 5.2 with a water patch tends to mitigate the errors of the decoupling. This can be explained, notably, by the fact that the recoupled system (i.e. the partially coated cylindrical shell) exhibits less resonances and anti-resonances than the target subsystem of section 5.2, when the missing part of the coating was replaced by a rigid screen. These promising results will hence be applied to the practical case of interest: the partially coated cylindrical shell where the whole coating patch has been removed and replaced by a water patch. The results of this recoupling are shown in figure 99 for the same two points. A supplementary curve has been added to show the behavior of the fully coated cylindrical shell. This comparison allows highlighting the influence of the partial coating.

If the comparison between the reference calculation and the rCTF one shows that the recoupling with the whole patch is slightly less accurate than for the 90% patch (due to the higher errors resulting from the decoupling process), the results remain very satisfactory. In the low-frequency range, the resonances and anti-resonances are still correctly described

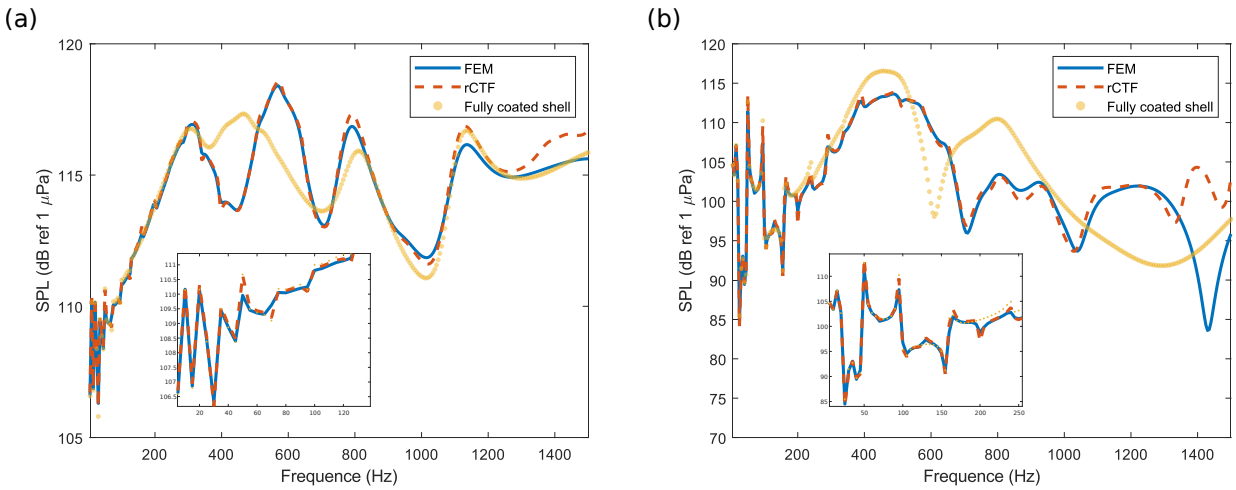

Figure 99: Pressure radiated by the partially coated shell after recoupling with the whole patch. (a) 1st point. (b) 2nd point.

both in terms of frequency and amplitude. Some slight discrepancies can be observed at higher frequencies, but the errors remain low, except above 1300 Hz as it has already been highlighted in subsection 5.3.2. Besides, the comparison with the curves corresponding to the fully coated cylindrical shell show that the influence of the partial coating is correctly taken into account with the rCTF calculations. The difference of behavior between the fully coated and partially coated shell is particularly highlighted in figure 99b corresponding to the second investigated point, which was predictable as this point is located close to the missing part of the coating. It is also interesting to notice that, for both points, the zoom in the low-frequency range shows that the fully coated and partially coated shells exhibit a very similar behavior, with the same resonances and anti-resonances. Once again, these results can be validated with cartographies to observe the radiated pressure field in the recoupled system.

A first cartography is proposed at 800 Hz in figure 100, with the reference FEM calculation in figure 100a, the rCTF calculation in figure 100b, and a FEM calculation of the pressure radiated by the fully coated shell in figure 100c. This frequency was chosen as, in subsection 5.3.2, this frequency was estimated to be more meaningful than the calculation at 50 Hz, as it highlights the influence of the removed patch (contrary to the low-frequency range, as it has been observed in figure 99). Besides, the comparison between figures 96 and 99 shows that in the low-frequency range, the behavior of the recoupled system whether the removed patch in the 90% one or the 100% one is almost identical. Hence, for the calculation at 50 Hz, the cartography looks very much like the one in figure 97a or b. We can observe that the results of the rCTF calculation at 800 Hz are excellent compared to the reference one, and the difference between the partially coated shell and the fully coated shell is well highlighted. Besides, it is interesting to notice that the pressure fields for the partially coated shell in figure

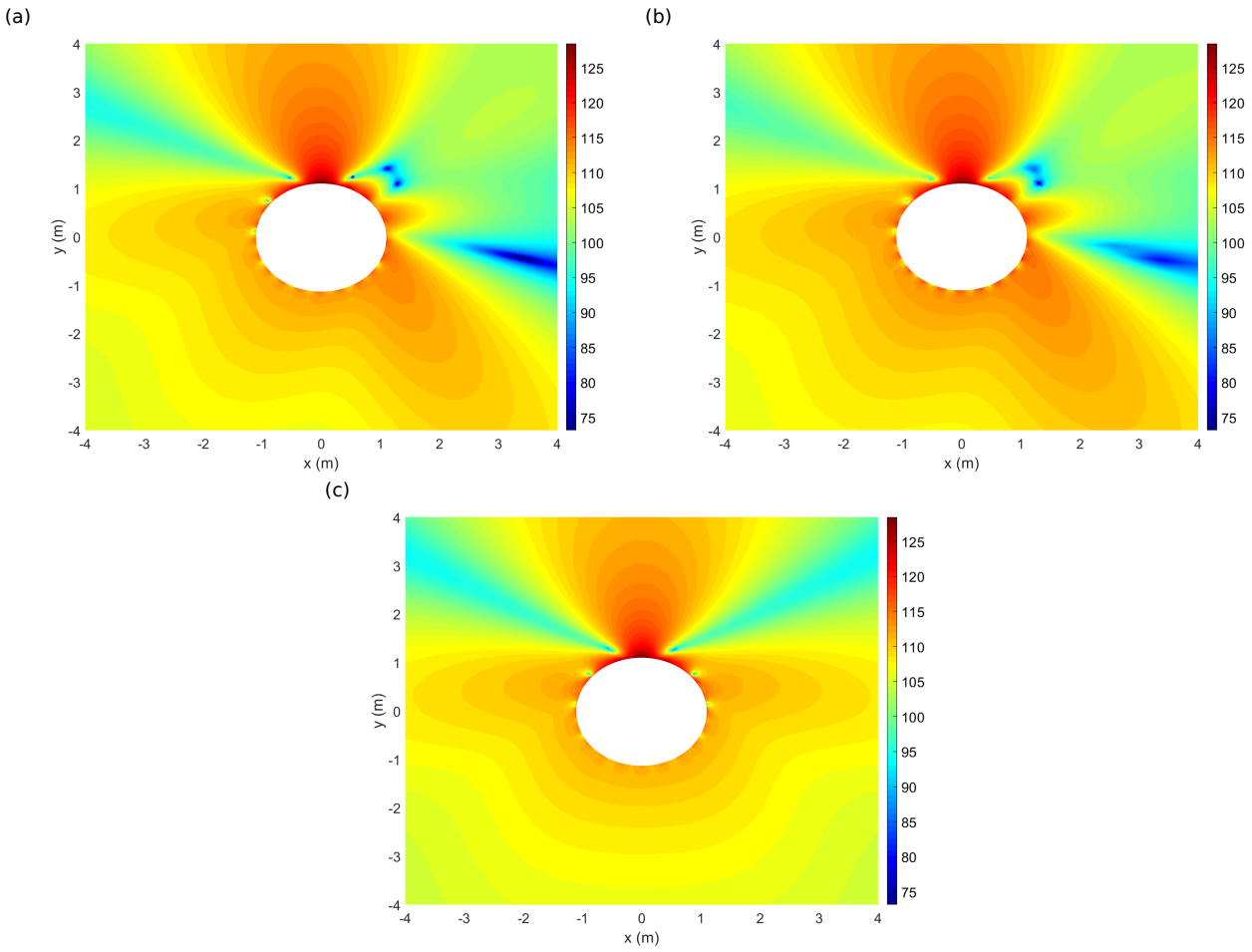

Figure 100: Pressure radiated by the partially coated shell after recoupling with the 100% patch - cartographies at 800 Hz. (a) FEM calculation. (b) rCTF calculation. (c) Pressure radiated by the fully coated shell.

100 stays very similar to the ones in figure 98 related to the 90% patch. This means that the results obtained with the latter, which are slightly better than for the 100% patch, remain a satisfactory approximation of the behavior of the partially coated shell when it is studied using the rCTF method.

At 1435 Hz, as we can see in figure 101, there is also a significant difference between the radiated pressure fields of the partially coated and fully coated cases. If some discrepancies can be observed between the rCTF and FEM calculations, the global behavior of the pressure field is correctly described and the difference with the fully coated configuration is well accounted for. Furthermore, it is important to keep in mind that the cartographies proposed here correspond to the frequency at which the errors are higher, meaning that in all the remaining of the frequency range, the results will be very accurate as in figure 100. This leads us to the conclusion that the rCTF method gives meaningful results when evaluating the radiation properties of the partially coated cylindrical shell.

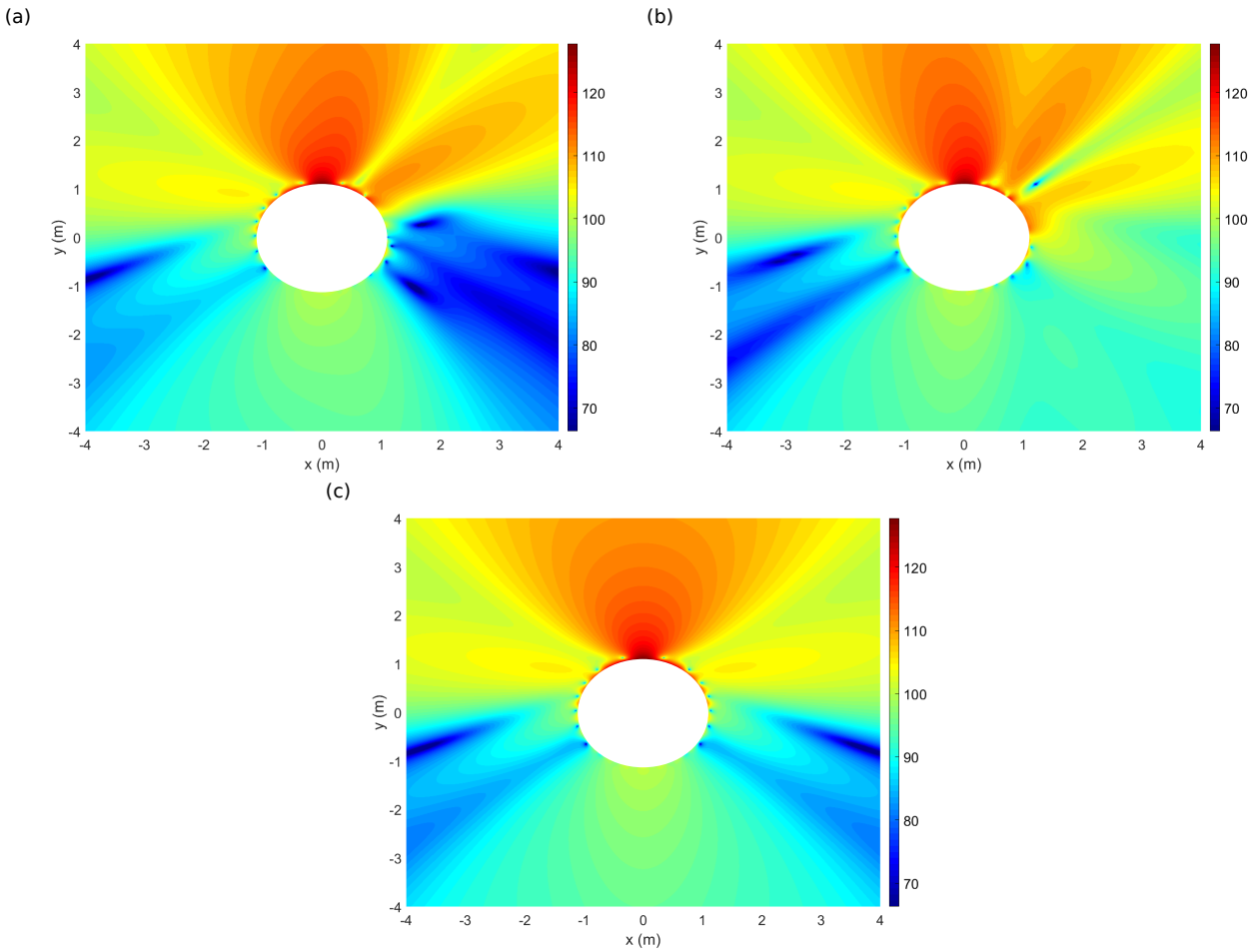

Figure 101: Pressure radiated by the partially coated shell after recoupling with the 100% patch - cartographies at 1435 Hz. (a) FEM calculation. (b) rCTF calculation. (c) Pressure radiated by the fully coated shell.

5.4 Influence of the size of the removed tile and of the location of the external force

In the previous section, we have seen that the rCTF method, applied to the radiation of a partially coated cylindrical shell, provides meaningful results. Given this observation, the influence of several parameters, such as the size of the patch (in terms of angular spreading of the removed patch), or the location of application of the external force relative to the location of the removed patch, is studied. As we have seen in section 5.3 that the rCTF method with the recoupling of the water patch converges almost perfectly up to 1300 Hz, the results in this section will be limited to this frequency range. The possibilities of improvement of the method to higher frequencies will be discussed in the conclusion of this work.

5.4.1 Influence of the size of the removed patch

As a first study, we are interested in evaluating the influence of the size of the removed patch. Indeed, it is important to know to what extent the absence of coating in a given angular

area of the shell impacts the vibroacoustic behavior of this one. In the previous sections, the removed patch was ranging from 0 to $\pi/4$ rad. In this study, different calculations will be carried out with the same mechanical force as in the previous sections (i.e. $\theta = \pi/2$ rad), and for three other maximal angles for the boundary of the removed patch: $\pi/12$, $\pi/8$ and $\pi/2$ rad. The first two values were chosen beacause, when the impact of a missing patch is evaluated, the concerned missing part of the coating is generally smaller than the one studied in the previous sections. For the last case, $\pi/2$ rad, the aim is to evaluate the impact of removing such a big part of the coating, which should be more important than for the other investigated cases, even if this does not have a practical application in industry.

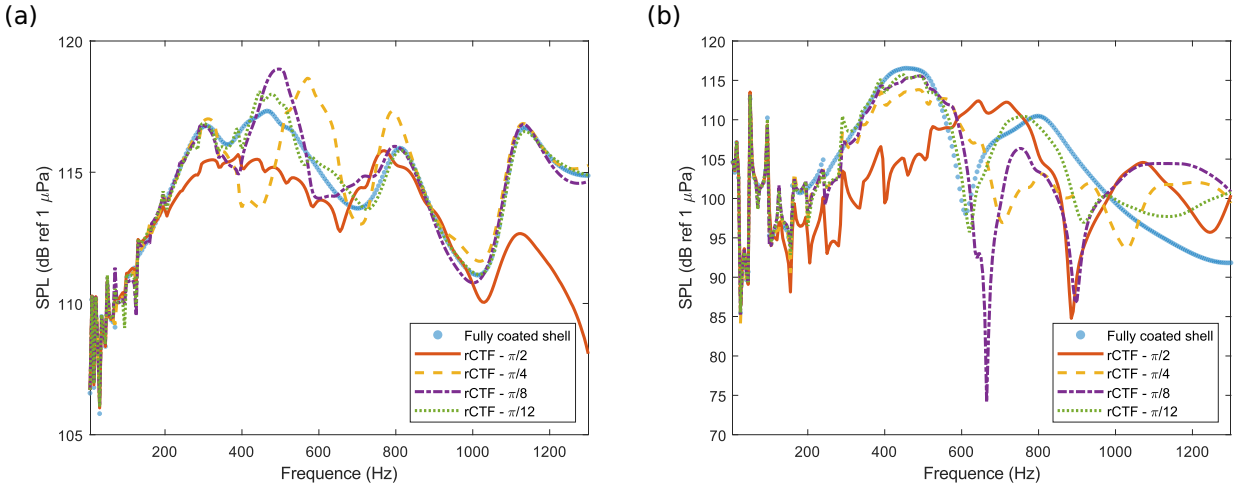

Figure 102: Influence of the angular spreading of the removed patch. (a) 1st point ($\theta = \pi/2$ rad, 1 m away from the shell). (b) 2nd point ($\theta = 0$ rad, 50 cm away from the shell).

The evolution of the pressure at the two previously investigated points in the surrounding fluid for the different sizes of removed patches are shown in figure 102, for a mechanical point force located at an angle of $\pi/2$ rad (as in the previous sections). Firstly, we can remark, as it was also observed in section 5.3, that in the low-frequency range (i.e. below 100 Hz), the size of the removed patch doesn't have any influence, nor the absence of coating. In the remaining parts of the frequency domain, there is no clear tendancy showing that the impact of the absence of coating tends to be higher when the removed patch is bigger. For the 1st point, we can even observe that when the angular spreading of the removed patch is the highest (i.e. for the $\pi/2$ patch), the radiated pressure tends to be lower. Besides, it is important to mention that the difference between the different investigated cases is more important for the 2nd point than for the 1st point. This result was expected as this point is located at the same angle as one boundary of the removed patch, and it is close to the interface between the coating and the surrounding fluid. This point is hence more impacted by the absence of coating, and also necessarily by the difference of size of the removed patches.

To observe clearly this behavior, a cartography is plotted at 640 Hz for the four different

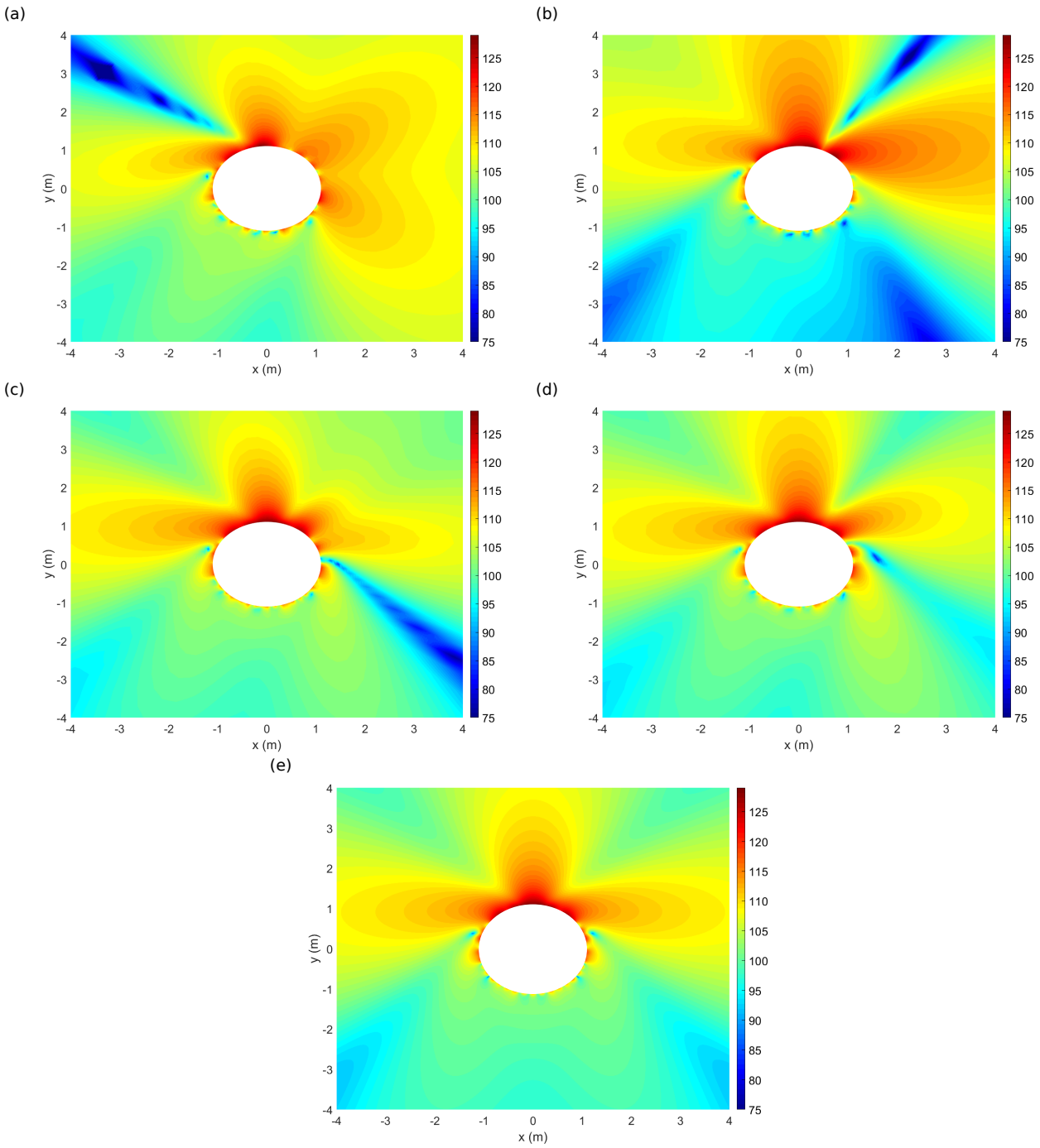

Figure 103: Influence of the angular spreading of the removed patch - cartographies at 640 Hz. (a) $\pi/2$. (b) $\pi/4$. (c) $\pi/8$. (d) $\pi/12$. (e) Fully coated cylindrical shell.

angular spreading configurations in figure 103. At this frequency, we can see in figure 102 that the radiated pressure at the 1st point is close for the four configurations, but more important differences are observed for the 2nd point. Looking at these figures, it is possible to confirm that there is no substantial difference between the four configurations in the angle of application of the mechanical force (i.e. $\pi/2$ rad, at which is located the 1st point). However, other areas are much more impacted by the size of the removed patch, especially those where the radiated pressure diplays minimal values, and in the direct vicinity of the removed patch

(where the 2nd point is located). Besides, it is interesting to notice that, for figures 103b, c and d (corresponding to the $\pi/4$, $\pi/8$ and $\pi/12$ configurations, respectively), the three lobes of maximal pressure are quite distinct, contrary to the figure 103a (corresponding to the $\pi/2$ configuration) where a fourth lobe appears at an angle around $\pi/4$ rad, angle at which the radiated pressure decreases in the other configurations. This is hence clearly the zone where the absence of coating on a large angular area has the more impact. Finally, the radiated pressure field in figure 103d, corresponding to the $\pi/12$ configuration, is almost symmetric with respect to the angle of application of the force. This result shows clearly that this configuration is the closest from the fully coated cylindrical shell, which is displayed in figure 103e as a matter of comparison. These cartographies hence provide meaningful insights on the influence of the size of the removed patch. But they are shown for a single point of application of the force. In the next subsection, two other mechanical excitations will be considered and the results in terms of radiated pressure field will be discussed.

5.4.2 Influence of the location of the external mechanical force

In subsection 5.4.1, as for the previous sections, the calculations have been carried out considering an external mechanical force located at an angle of $\pi/2$ rad. We are interested here in evaluating the difference in the vibroacoustic behavior of the partially coated cylindrical shell when the location of application of the force is modified. To this end, two other external mechanical forces are considered. The first one (F_1 in figure 104) is located at an angle of $\theta = 0$ rad, angle corresponding to a boundary of the removed patch. And the second force (F_2 in figure 104) is located at an angle of $\theta = -\pi/4$ rad, which corresponds to a position where floors of engine foundations can be placed in naval applications, implying mechanical excitations of the shell.

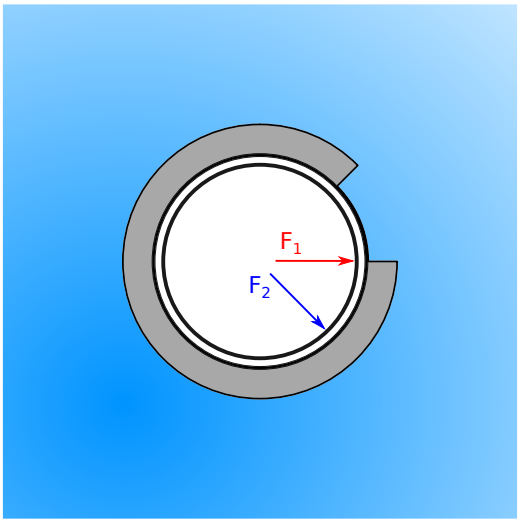

Figure 104: Location of the two external mechanical forces.

For this parametric study, we will focus on analyzing cartographies at a single frequency rather than the evolution of the radiated pressure at isolated points, as it allows a more global vision of the vibroacoustic behavior of the partially coated cylindrical shell. Also, in order to compare with the external mechanical force applied in the previous sections, the same frequency as in subsection 5.4.1 will be investigated (i.e. 640 Hz). In order to avoid displaying too many figures for the sake of clarity, the results will be presented for two different sizes of the removed patches. Firstly, the $\pi/12$ configuration will be investigated in order to see if the modification of point of application of the force has an impact on the almost symmetric nature observed in figure 103d. And secondly, the $\pi/4$ configuration will be investigated in order to have a different behavior than the $\pi/12$ configuration on a case still having an industrial interest, contrary to the $\pi/2$ configuration for example.

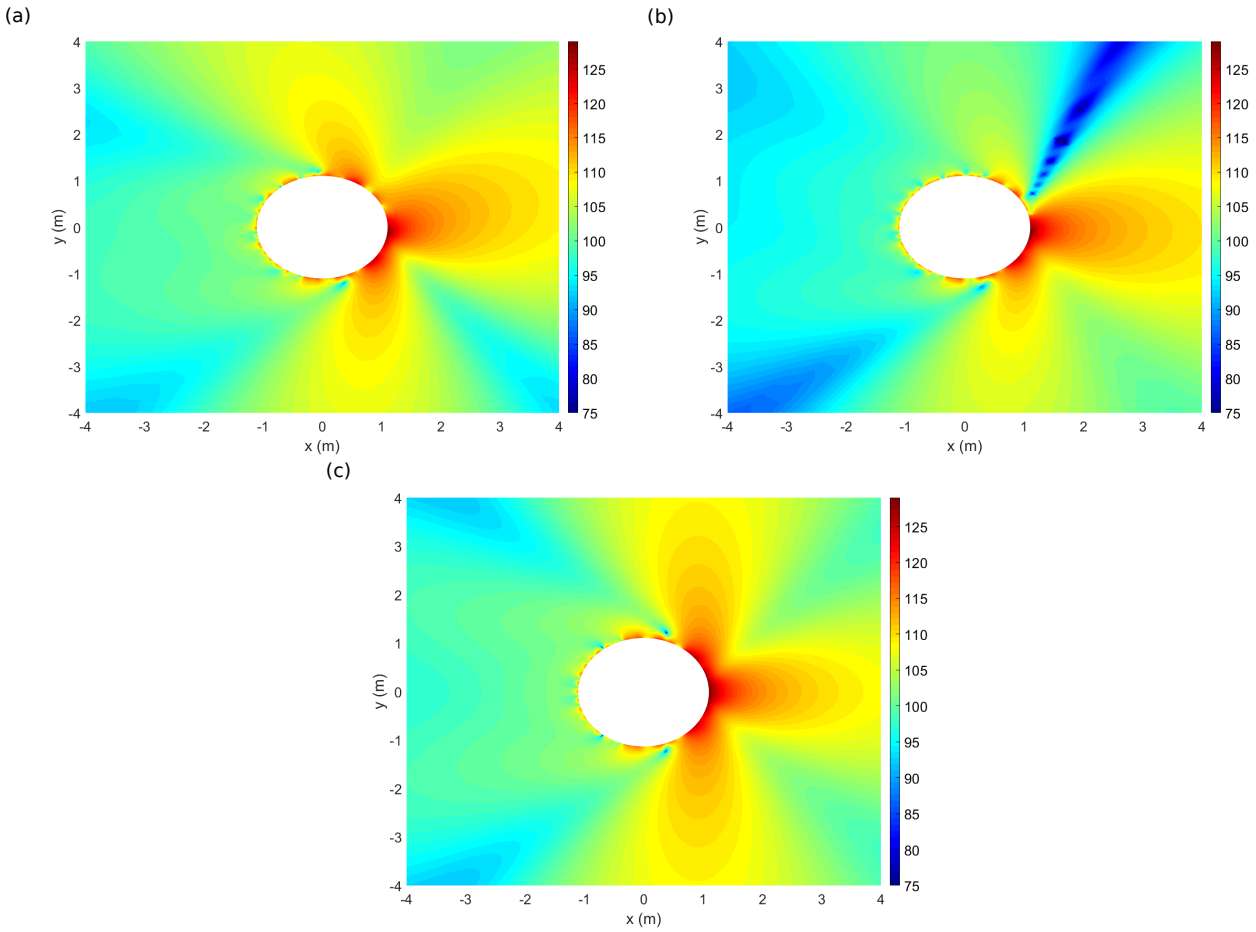

Figure 105: Radiated pressure at 640 Hz when the force is located at $\theta = 0$ rad. (a) $\pi/4$ removed patch configuration. (b) $\pi/12$ removed patch configuration. (c) Fully coated cylindrical shell.

The cartographies when the external mechanical force is located at $\theta = 0$ rad is displayed in figure 105. From this figure, it is clear that applying the force at an angle where the cylindrical shell is not coated exhibits a higher impact on the partial coating than in the case investigated in figure 103. The radiated pressure field in figure 105b, corresponding

to the $\pi/12$ configuration, is much further from being symmetric with respect to the angle of application of the force than in figure 103d. The impact is however less pronounced for the $\pi/4$ configuration (figure 105a), as the displayed behavior is close to the one of the fully coated shell. This means that, depending on the location of application of the force, the ratio between the angular spreading of the removed patch and the whole circumference of the shell plays a role in the vibroacoustic behavior of the partially coated shell, but the impact is not necessarily proportional to this ratio.

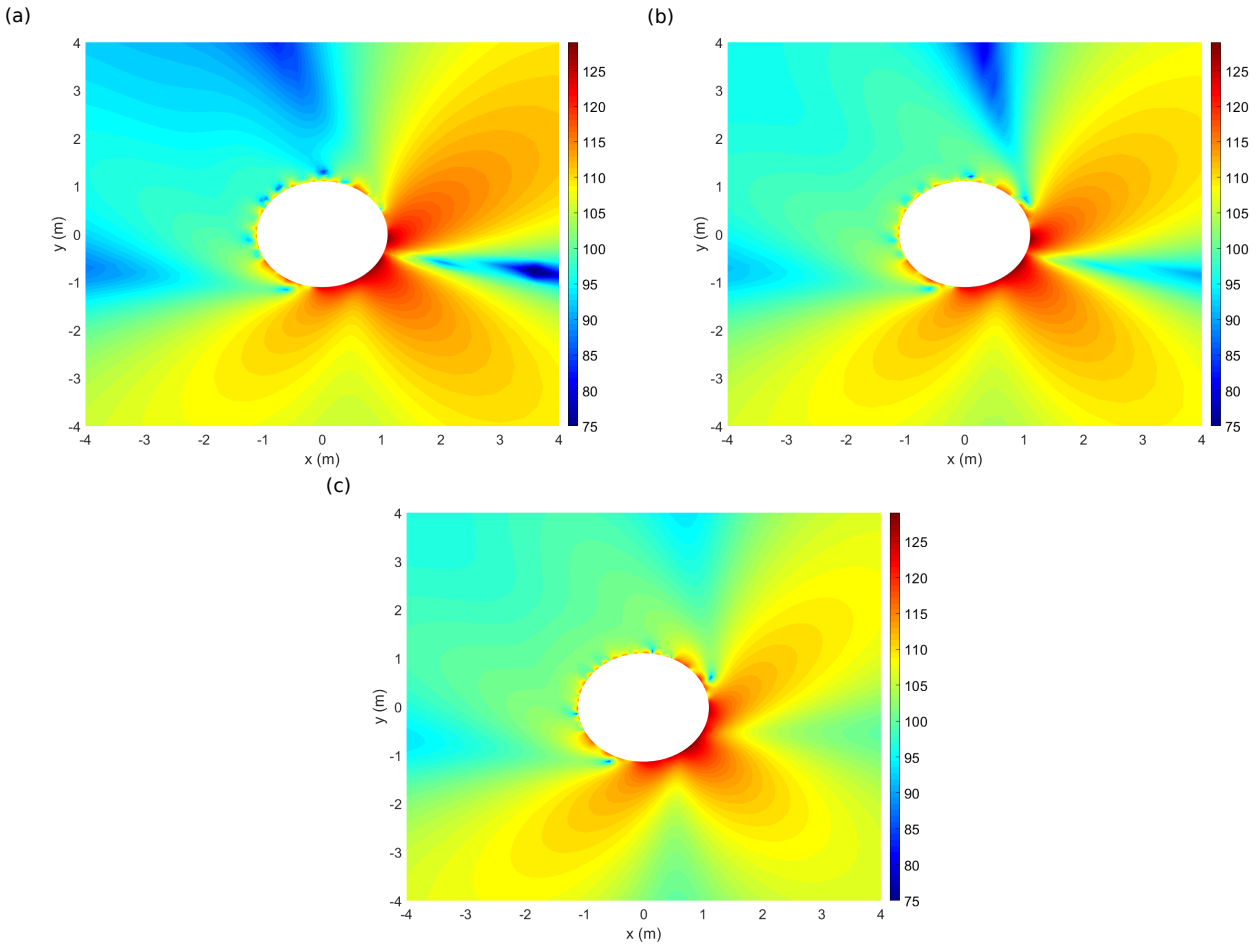

Figure 106: Radiated pressure at 640 Hz when the force is located at $\theta = -\pi/4$ rad. (a) $\pi/4$ removed patch configuration. (b) $\pi/12$ removed patch configuration. (c) Fully coated cylindrical shell.

Concerning the case where the force is applied at $\theta = -\pi/4$ rad, displayed in figure 106, the impact of the partial coating is much less pronounced. The three configurations of partial or full coating ($\pi/4$, $\pi/12$ and fully coated shell, respectively) display a similar behavior, even if the $\pi/12$ configuration is closer from being symmetric with respect to the angle of application of the force than the $\pi/4$ configuration. For this latter, we can see that the behavior is the same than the one in figure 103b, which is normal because the angular distance between the point of application of the force and the closer boundary of the removed patch is equal to $\pi/4$ rad for both cases. We can conclude from this study that the impact

of the partial coating is much more marked when the shell is excited in the vicinity of the removed patch. Following this observation, for practical applications, it should be advised avoiding removing a part of the coating close to locations where the shell can be mechanically excited by the presence of floors, engine foundations, or other internal frames. However, this study needs to be extended in order to draw conclusions with certainty regarding industrial applications of the rCTF method.

5.5 Conclusion

The rCTF method, developed in chapter 3, has been applied in this chapter to an industrial case, in order to study the radiation of a partially coated cylindrical shell. Following the procedure to compute the Condensed Transfer Functions from numerical models developed in chapter 4, a numerical model of the removed part of the coating has been subtracted from a semi-analytical model of a fully coated cylindrical shell immerged in water. This allowed obtaining a partially coated cylindrical shell, for which the removed part of the coating has been replaced by a rigid screen. This model was then coupled to a numerical model of a water tile using the CTF method to obtain the partially coated cylindrical shell immersed in water.

Numerical applications have been presented considering 2-D models, which allowed reducing the complexity of the problem, and gave the possibility of performing a reference FEM calculation to have a meaningful point of comparison. Contrary to the previous chapters, the system studied in this chapter was a vibroacoustical one. Hence, two decoupling boundaries have been considered to perform the decoupling calculations of the rCTF method. A vibroacoustic formulation was then proposed, and the results between the acoustic and vibroacoustic formulation were compared to those of the reference calculation. It appeared that the rCTF calculations considering the acoustic decoupling boundary led to better results, while being easier to implement. It has also been observed that performing decoupling calculations in the vicinity of a vibrating structure can induce large errors, which were reduced by considering smaller segments along the decoupling boundaries of the 2-D models.

Finally, the recoupling procedure, consisting in coupling the model obtained from the rCTF method to a numerical model of a water tile using the CTF method, allowed mitigating the errors induced by the decoupling calculations of the rCTF method. The good results produced by the procedure enabled carrying out a first parametric study on the influence of the size of the removed part of the coating and the position of the external mechanical force. These studies will have to be extended to allow more robust conclusions regarding the impact of the partial coating on the vibroacoustic behavior of the cylindrical shell, but the results obtained in this chapter constitute a meaningful basis on which future works can be

considered.

General conclusions and perspectives

Conclusions

In this work, a substructuring subtractive modelling approach has been developed. Based on a reverse formulation of the Condensed Transfer Function method, it allows decoupling along lines or surfaces a subsystem from a global system. Presented for an acoustical system, it can either be applied to mechanical, acoustical or vibroacoustical problems.

The theoretical fundamentals of this approach have been established. Starting from the coupling problem of the CTF method, the pressures and radial velocities are projected on a set of orthonormal condensation functions, and the CTFs of the uncoupled subsystems can be calculated. Using the superposition principle, along with the pressure continuity and radial velocities equilibrium at the coupling interface, allow deducing the behavior of the coupled system. Then, the formulation is reversed, and the vibroacoustic behavior of the target subsystem can be obtained from information concerning the global system and the subtracted subsystem. This formulation allows predicting the response at any point of the target subsystem, and not only on the decoupling interface. As the global system and the subtracted subsystem are studied separately, they can be characterized by different means (analytical, numerical, experimental). An example has been shown for an academic test case, where the CTFs of the initial (sub)systems were computed analytically at first, allowing the validation of the method. They were then computed from numerical models, which can be based on different methods whether or not the system is bounded. When the studied system is the partially coated, fluid loaded cylindrical shell, the rCTF method can be applied by considering a semi-analytical formulation for the submerged fully coated cylindrical shell, and a FEM calculation for the removed part of the coating.

The sensitivity of the rCTF method to model errors has been evaluated, at first on a 1-D case. It has been highlighted that the rCTF method is particularly sensitive at the common anti-resonances between the global system and the subtracted subsystem. Besides, it tends to exhibit higher errors when the size of the subtracted subsystem increases. On the other hand, if it has been observed that increasing the damping of the materials leads to

better results, particulary around the sensitive anti-resonances of the (sub)systems, other possibilities have been investigated to improve the convergence of the method. Following this, a global decoupling approach has been considered, where the subtracted subsystem is decoupled at two different interfaces from the global system, exhibiting a residual subsystem. This approach presents the combined theoretical interests of reducing the size of the subtracted subsystem and minimizing the number of resonances and anti-resonances of the subsystem in the frequency range of interest. It also has the advantage of a greater flexibility, as the second decoupling interface can be chosen by the user. If the application of the global decoupling approach has given promising results on a 1-D test case, the implementation of the global rCTF approach on the 3-D case consisting in the scattering of a plane wave by a rigid sphere yielded more mitigated results, notably because of the presence of unanticipated resonances in the circumference of the subtracted hollow sphere. By choosing a different second coupling interface, closer to the center of the sphere, and exhibiting a smaller residual sphere, the global rCTF approach produced more interesting results, similar to those of the local rCTF approach when the CTFs were computed from analytical models.

To evaluate the sensitivity of the local and global rCTF approaches to model errors for the 3-D case, the procedure to compute the CTFs from numerical models of the global system and subtracted subsystem has been established. For the global system, a Green formulation was derived allowing computing the CTFs of unbounded domains. As for the subtracted subsystem, a FEM formulation, well adapted for bounded domains of moderate size, was considered. When numerical models were used to compute the CTFs, the local and global rCTF approaches displayed similar results when a moderate discretization size was considered for the global system. The advantages of the global rCTF approach were especially highlighted when a very precise model of the global system was taken into account. However, this gain came with an increased difficulty of application of the method, and, above all, a substantial increase in the required computational effort, hardly compatible with industrial needs.

Following the conclusions drawn from the primary applications of the rCTF method, the local approach was used to study the radiation of a partially coated cylindrical shell immersed in water. The formulation was proposed for a general, 3-D case, but was applied with 2-D models in order to be able to have a reference FEM calculation in a wide frequency range, which would not have been possible considering 3-D models. The rCTF method has shown its ability in dealing with vibroacoustical problems, exhibiting vibroacoustic decoupling interfaces. To study such interfaces, a first possibility is to slightly shift the interface in the acoustic domain, so that the rCTF formulation remains entirely acoustical. The possibility

of considering directly the vibroacoustic interface by defining mechanical excitations and unknowns has been discussed, yielding a vibroacoustic formulation of the rCTF method. The results with the acoustic rCTF formulation showed a better convergence, especially when smaller segments, corresponding to the condensation functions, were considered to address the convergence issues of decoupling near a vibrating structure. Then, it was observed that the process of recoupling the target subsystem with a model of the water occupying the missing part of the coating, using the direct CTF method, tends to mitigate the errors induced by the decoupling process. As a result, the radiated pressure field of the partially coated cylindrical shell was very well described by the rCTF method, in the major part of the frequency range and of the fluid domain. This result hence allowed a first analysis of the impact of the partial coating on the vibroacoustic behavior of the cylindrical shell. It was observed that the influence of the partial coating tends to be reduced when the missing part of the coating is smaller. Besides, the impact of the partial coating is higher when the excitation force is located at the vicinity of the removed tile. If these results could have been expected, this study allowed quantifying them, and constitutes a first step showing the potential applications of the rCTF method for the study of partially coated cylindrical shells.

Further work - perspectives

Many perspectives can now be considered. Firstly, as we saw in chapter 5, some errors subsist when the rCTF method is applied to study the radiation from a partially coated cylindrical shell, in particular in the high-frequency range. The possibility of improving the convergence of the method has already been addressed by dividing the decoupling interface into smaller segments. This study was carried out considering the local rCTF approach, but we saw in chapter 4 that the global rCTF approach can exhibit more robust results, with the disadvantage of being more computationally intensive. As a short-term perspective, we could be interested in applying the global rCTF approach for this case study in order to see if better results can be obtained in the high frequency range and in the vicinity of the removed coating tile. As the local rCTF method yielded very satisfactory results in the major part of the frequency range and of the fluid medium, improving the results with the global rCTF approach could be done without increasing substantially the computation cost, by considering only the parts of the frequency range and of the fluid domain where the local rCTF approach fails to give very accurate results. On the other hand, reducing the size of the segments at the decoupling interface was associated to utilizing gate functions as condensation functions. It has already been observed in other studies [175, 176] that the use of complex exponentials as condensation functions can improve the convergence of the CTF method. It would hence be a possibility to apply these condensation functions when

studying the partially coated cylindrical shell using the rCTF method.

In the medium term, in order to carry out more thorough studies on partially coated cylindrical shells, the rCTF method must be conducted considering 3-D models of the fully coated cylindrical shell and of the removed part of the coating. Indeed, the study with 2-D models allows observing the impact of partial coating along the radial and circumferential coordinates, but there is no information regarding the longitudinal coordinate. Besides, considering 2-D models is equivalent to study a cylindrical shell for which the angular spreading of the partial coating is the same over the length of the shell. In our case, when the impact of a missing tile is evaluated, one must be able to consider non constant geometrical configurations over the length of the shell. The consideration of 3-D models would, in addition, enable the implementation of the rCTF method in a ready-to-use software, allowing the application of the method on the design process of industrial systems.

On another hand, it has been stated in chapter 5 that the coating was modelled as an equivalent fluid having properties close to decoupling coatings (i.e. longitudinal wave speed and damping). This approximation was acceptable as the aim of this thesis was to conduct a first validation of the rCTF method on an industrial case, and equivalent fluids can very well represent the behavior of "soft rubber" materials. However, these materials only represent a part of the materials that can be considered in the naval industry. Hence, in the medium-term future, one could be interested in extending the model to solid coatings where the displacements in the three directions in the material are considered, allowing to take into account both the longitudinal and shear waves. In a similar spirit, different properties for the material could be investigated, in order to study both decoupling and anechoic coatings. And finally, being able to consider different kinds of coating would introduce the possibility of applying the rCTF method to a cylindrical shell coated with both anechoic and decoupling materials (as illustrated in figure 2b). Instead of recoupling the target subsystem with a model of water occupying the missing part of the coating, as it was done in chapter 5, a coating tile having different properties from the initial coating material could be considered for the recoupling. This way, configurations found in the naval industry could be investigated in a relatively simple way.

In the naval industry, cylindrical shells are generally coupled to internal structures as it has been addressed in section 1.1.3. When axisymmetric internal structures such as stiffeners, bulkheads or endcaps are considered, the CAA is well indicated to study such structures. Non-axisymmetric internal structures such as floors or engine foundations can also be taken

into account with the help of the CTF method. By coupling the CAA and CTF methods to the rCTF method, the vibroacoustic behavior of stiffened, non-axisymmetric, partially coated cylindrical shells immersed in water could hence be investigated in a more distant future. As these substructuring approaches are all based on the same assumptions, it is theoretically possible to use them simultaneously for a single system. Besides, the study of chapter 5 is focused on the radiation of the partially coated cylindrical shell, meaning that the considered excitation is a mechanical force applied on the inner surface of the shell. In order to explore further the vibroacoustical properties of such shells, different kinds of excitations could be investigated. Considering an acoustic plane wave excitation would allow studying the scattering from a partially coated cylindrical shell. Random excitations such as TBLs could also be addressed as the understanding of the vibroacoustical behavior of submerged structures under such excitations constitutes a challenging issue in current research. As the CAA and CTF method have already proven their ability in dealing with acoustical and random excitations, extending the rCTF method to such excitations should not be a problem.

Appendix A

Spectral expressions of the Flügge operator and spectral displacements

The spectral Flügge's equations are derived in this appendix, with heavy fluid loading taken into account. The spectral Flügge's system yields

$$\begin{bmatrix} \tilde{\tilde{Z}}_{UU} & \tilde{\tilde{Z}}_{UV} & \tilde{\tilde{Z}}_{UW} \\ \tilde{\tilde{Z}}_{UV} & \tilde{\tilde{Z}}_{VV} & \tilde{\tilde{Z}}_{VW} \\ \tilde{\tilde{Z}}_{UW} & \tilde{\tilde{Z}}_{VW} & \tilde{\tilde{Z}}_{WW} \end{bmatrix} \begin{bmatrix} \tilde{U} \\ \tilde{V} \\ \tilde{W} \end{bmatrix} = \frac{\left(1-\nu^2\right) R^2}{Eh} \begin{bmatrix} -\tilde{L_f} \\ -\tilde{T} \\ \tilde{F} + jk_x\tilde{M} - \tilde{p} \end{bmatrix} \tag{A.1}$$

where

$$\begin{aligned} \tilde{\tilde{Z}}_{UU} &= -R^2k_x^2 - n^2\tfrac{1-\nu}{2}(1+\beta^2) + R^2k_l^2 \\ \tilde{\tilde{Z}}_{UV} &= -R\tfrac{1+\nu}{2}nk_x \\ \tilde{\tilde{Z}}_{UW} &= \mathrm{j}k_x\left(R\nu + \beta^2R^3k_x^2 - \beta^2R\tfrac{1-\nu}{2}n^2\right) \\ \tilde{\tilde{Z}}_{VV} &= -R^2k_x^2\tfrac{1-\nu}{2}(1+3\beta^2) - n^2 + R^2k_l^2 \\ \tilde{\tilde{Z}}_{VW} &= \mathrm{j}n\left(1+\beta^2R^2\tfrac{3-\nu}{2}k_x^2\right) \\ \tilde{\tilde{Z}}_{WW} &= 1+\beta^2\left(R^4k_x^4 + n^2(2R^2k_x^2+2) + n^4 + 1\right) - R^2k_l^2 \end{aligned} \tag{A.2}$$

with $\beta = \frac{h}{R\sqrt{12}}$ and $k_l = \omega\sqrt{\frac{\rho_s(1-\nu^2)}{E}}$. The solutions for the spectral displacements are then

$$\begin{aligned} \tilde{U} = &-\gamma\frac{\tilde{\tilde{Z}}_{VV}(\tilde{\tilde{Z}}_{WW} - \gamma\tilde{\tilde{Z}}_f) - \tilde{\tilde{Z}}_{VW}^2}{\tilde{\tilde{\Delta}}}\tilde{\tilde{L}}_f \\ &-\gamma\frac{\tilde{\tilde{Z}}_{UV}\tilde{\tilde{Z}}_{UW} - \tilde{\tilde{Z}}_{UU}\tilde{\tilde{Z}}_{VW}}{\tilde{\tilde{\Delta}}}\tilde{\tilde{T}} \\ &+\gamma\frac{\tilde{\tilde{Z}}_{UV}\tilde{\tilde{Z}}_{VW} - \tilde{\tilde{Z}}_{VV}\tilde{\tilde{Z}}_{UW}}{\tilde{\tilde{\Delta}}}(\tilde{\tilde{F}} - \mathrm{j}k_x\tilde{\tilde{M}}) \end{aligned} \tag{A.3a}$$

$$\begin{aligned} \tilde{\tilde{V}} = &-\gamma\frac{\tilde{\tilde{Z}}_{VW}\tilde{\tilde{Z}}_{UW} - (\tilde{\tilde{Z}}_{WW} + \gamma\tilde{\tilde{Z}}_f)\tilde{\tilde{Z}}_{UV}}{\tilde{\tilde{\Delta}}}\tilde{\tilde{L}}_f \\ &-\gamma\frac{\tilde{\tilde{Z}}_{UU}(\tilde{\tilde{Z}}_{WW} + \gamma\tilde{\tilde{Z}}_f) - \tilde{\tilde{Z}}_{UW}^2}{\tilde{\tilde{\Delta}}}\tilde{\tilde{T}} \\ &+\gamma\frac{\tilde{\tilde{Z}}_{UW}\tilde{\tilde{Z}}_{UV} - \tilde{\tilde{Z}}_{UU}\tilde{\tilde{Z}}_{VW}}{\tilde{\tilde{\Delta}}}(\tilde{\tilde{F}} + \mathrm{j}k_x\tilde{\tilde{M}}) \end{aligned} \tag{A.3b}$$

$$\begin{aligned}\tilde{\tilde{W}} = &-\gamma\frac{\tilde{\tilde{Z}}_{uv}\tilde{\tilde{Z}}_{vw}-\tilde{\tilde{Z}}_{uw}\tilde{\tilde{Z}}_{vv}}{\tilde{\tilde{\Delta}}}\tilde{\tilde{L}}_f\\ &-\gamma\frac{\tilde{\tilde{Z}}_{uw}\tilde{\tilde{Z}}_{uv}-\tilde{\tilde{Z}}_{vw}\tilde{\tilde{Z}}_{uu}}{\tilde{\tilde{\Delta}}}\tilde{\tilde{T}}\\ &+\gamma\frac{\tilde{\tilde{Z}}_{uu}\tilde{\tilde{Z}}_{vv}-\tilde{\tilde{Z}}_{uv}^2}{\tilde{\tilde{\Delta}}}(\tilde{\tilde{F}}+\mathrm{j}k_x\tilde{\tilde{M}})\end{aligned} \tag{A.3c}$$

where $\gamma = \frac{(1-\nu^2)R^2}{Eh}$, and $\tilde{\tilde{\Delta}}$ is the determinant of the Flügge's matrix taking into account the impedance of the fluid:

$$\begin{aligned}\tilde{\tilde{\Delta}} =&\tilde{\tilde{Z}}_{uw}(\tilde{\tilde{Z}}_{uv}\tilde{\tilde{Z}}_{vw}-\tilde{\tilde{Z}}_{uw}\tilde{\tilde{Z}}_{vv})+\tilde{\tilde{Z}}_{vw}(\tilde{\tilde{Z}}_{uw}\tilde{\tilde{Z}}_{uv}-\tilde{\tilde{Z}}_{vw}\tilde{\tilde{Z}}_{uu})+\\ &(\tilde{\tilde{Z}}_{ww}+\gamma\tilde{\tilde{Z}}_f)(\tilde{\tilde{Z}}_{uu}\tilde{\tilde{Z}}_{vv}-\tilde{\tilde{Z}}_{uv}^2)\end{aligned} \tag{A.4}$$

The spectral tangential rotation is

$$\tilde{\tilde{\varphi}} = \mathrm{j}k_x\tilde{\tilde{W}} \tag{A.5}$$

Appendix B

Analytical expressions of the receptances

B.1 Analytical receptances of the target and residual rods

In order to calculate the receptances of the target rod considered in chapter 2, a harmonic longitudinal force F is applied on the point 1 of the rod, according to the definition of the receptance in Eq. (2.1). The equation of motion corresponding to the problem of a longitudinally vibrating rod is given by

$$ES\frac{\partial^2 U}{\partial x^2} - \rho_s S\frac{\partial^2 U}{\partial t^2} = 0 \tag{B.1}$$

where U is the displacement of the rod. Considering the stationary response of the rod for a harmonic force of angular frequency ω, the rod displacement can be written $u(t,x) = U(x)\mathrm{e}^{\mathrm{j}\omega t}$ and Eq. (B.1) becomes

$$ES\frac{\mathrm{d}^2 U(x)}{\mathrm{d}x^2} + \rho S\omega^2 U(x) = 0 \tag{B.2}$$

The solution of Eq. (B.2) takes the form

$$U(x) = Ae^{\mathrm{j}k_s x} + Be^{-\mathrm{j}k_s x} \tag{B.3}$$

where k_s is the wavenumber ($k_s = \sqrt{\frac{\rho_s}{E}}\omega = c_s\omega$). The unknown coefficients A and B can be found from the boundary conditions of the rod. As the lower end of the target rod is clamped and the upper end is the point of application of the force, it yields

$$\begin{cases} U(x=0) = 0 \\ ES\frac{\mathrm{d}U}{\mathrm{d}x}(x = L_{11}) = F \end{cases} \tag{B.4}$$

Injecting the system of Eq. (B.4) into Eq. (B.3), the displacement field along the target rod can be written

$$U(x) = \frac{F\sin(k_s x)}{k_s ES\cos(k_s L_{11})} \tag{B.5}$$

The receptance α_{11} of the target rod can finally be deduced

$$\alpha_{11} = \frac{U(x = L_{11})}{F} = \frac{\tan(k_s L_{11})}{k_s ES} \tag{B.6}$$

Considering the rod 1 in section 2.2, a residual part appears above the point 2 as shown in figure 22. As there is no physical coupling between points 1 and 2 of the rod 1, the crossed receptances are null

$$\alpha_{12} = \alpha_{21} = 0 \tag{B.7}$$

Finally, the receptance α_{22} of the residual part of rod 1 can be calculated using the same process as for α_{11}. The difference lies in the boundary conditions, as the harmonic longitudinal force is now applied on point 2, and the upper end of the rod is free. In order to respect the sign convention adopted for the calculation of α_{11}, the force applied on point 2 must be in the opposite direction of the force applied on point 1. It yields

$$\begin{cases} ES\frac{\mathrm{d}U}{\mathrm{d}x}(x = 0) = -F \\ ES\frac{\mathrm{d}U}{\mathrm{d}x}(x = L_{12}) = 0 \end{cases} \tag{B.8}$$

The expression of the receptance is then

$$\alpha_{22} = -\frac{1}{k_s ES \tan(kL_{12})} \tag{B.9}$$

B.2 Analytical receptances of the subtracted rod

The receptances of the subtracted rod can be computed with the same process and boundary conditions as for the calculation of α_{22}, as it is a rod with free boundary conditions with a longitudinal force applied at one of its ends. We can then directly derive the direct receptances of the subtracted rod

$$\beta_{11} = -\frac{1}{k_s ES \tan(kL_2)} \qquad \text{and} \qquad \beta_{22} = \frac{1}{k_s ES \tan(kL_2)} \tag{B.10}$$

Once again, the sign difference between β_{11} and β_{22} comes from the sign convention when applying the longitudinal force. As for β_{12}, it can be computed by taking the displacement at the end of the rod which is opposite to the point of application of the force. As the receptance are symmetric based on the reciprocity principle [193], either end can be used to carry on with the calculation. Finally, it yields

$$\beta_{12} = \beta_{21} = \frac{1}{k_s ES \sin(kL_{12})} \tag{B.11}$$

B.2.1 Analytical receptances of the master rod

The process for calculating the receptances of the master rod is a bit more complicated than for the two other rods, as the force must now be applied at a point in the middle of the rod (see [194]).

The rod is separated in two parts at the point of application of the force (which will be point 1 for μ_{11} and μ_{12} and point 2 for μ_{21} and μ_{22}, see figure 22). The displacement of the lower section of the rod will be referred to as U_1, while the displacement of the upper section of the rod will be referred to as U_2. The process will be shown for a longitudinal force applied on point 1, hence the receptances computed here will be μ_{11} and μ_{12}. The process for μ_{21} and μ_{22} is the same and will not be demonstrated here. One has to keep in mind that, as for the receptances of the subtracted rod, the symmetry of the receptances means that μ_{12} equals μ_{21}.

The displacements of the master rod can be written as

$$\begin{cases} U_1(x) = A_1 e^{\mathrm{j}k_s x} + B_1 e^{-\mathrm{j}k_s x}, & x \in [0, L_{11}] \\ U_2(x) = A_2 e^{\mathrm{j}k_s x} + B_2 e^{-\mathrm{j}k_s x}, & x \in [L_{11}, L_{1+2}] \end{cases} \tag{B.12}$$

where A_1, A_2, B_1 and B_2 are the unknowns. As the rod is clamped at its lower end and free at its upper end, the boundary conditions are

$$\begin{cases} U_1(x=0) = 0 \\ ES\frac{\mathrm{d}U_2}{\mathrm{d}x}(x = L_{1+2}) = 0 \end{cases} \tag{B.13}$$

The two other necessary equations to solve the system are given by the displacement continuity and force equilibrium at the point of application of the force

$$\begin{cases} U_1(x = L_{11}) = U_2(x = L_{11}) \\ \frac{\mathrm{d}U_1}{\mathrm{d}x}(x = L_{11}) - \frac{\mathrm{d}U_2}{\mathrm{d}x}(x = L_{11}) = \frac{F}{ES} \end{cases} \tag{B.14}$$

Hence, by solving the systems of Eq. (B.13) and Eq. (B.14), one can deduce the displacement field in the two sections of the master rod

$$U_1(x) = \frac{F\sin(kx)}{k_s ES}\frac{e^{\mathrm{j}k_s L_{11}} + e^{\mathrm{j}k_s(2L_{1+2} - L_{11})}}{1 + e^{2\mathrm{j}k_s L_{1+2}}}, \quad x \in [0, L_{11}] \tag{B.15}$$

$$U_2(x) = \frac{F\sin(k_s L_{11})}{k_s ES}\frac{e^{\mathrm{j}k_s x} + e^{\mathrm{j}k_s(2L_{1+2} - x)}}{1 + e^{2\mathrm{j}k_s L_{1+2}}}, \quad x \in [L_{11}, L_{1+2}] \tag{B.16}$$

Finally, the receptances of the master rod can be deduced

$$\mu_{11} = \frac{\sin(k_s L_{11})}{kES}\frac{e^{\mathrm{j}k_s L_{11}} + e^{\mathrm{j}k_s(2L_{1+2} - L_{11})}}{1 + e^{2\mathrm{j}k_s L_{1+2}}} \tag{B.17}$$

$$\mu_{12} = \frac{F\sin(k_s L_{11})}{k_s ES}\frac{e^{\mathrm{j}k_s(L_{11}+L_2)} + e^{\mathrm{j}k_s(2L_{1+2} - (L_{11}+L_2))}}{1 + e^{2\mathrm{j}k_s L_{1+2}}} \tag{B.18}$$

Following the same process, the final receptance μ_{22} is given by

$$\mu_{22} = \frac{F \sin(k_s(L_{11} + L_2))}{k_s ES} \frac{e^{\mathrm{j}k_s(L_{11}+L_2)} + e^{\mathrm{j}k_s(2L_{1+2}-(L_{11}+L_2))}}{1 + e^{2\mathrm{j}k_s L_{1+2}}} \tag{B.19}$$

Appendix C

Analytical calculation of the condensed transfer functions and condensed pressures for the test case application

C.1 Condensed impedances of the infinite water medium

C.1.1 Local rCTF approach

In order to calculate the condensed impedances of the infinite water domain 1+2 in chapter 3 (see figure 31), and in accordance with its definition in Eq. (3.17), a normal velocity jump φ^j is imposed on the fictitious surface Ω. The resulting pressure on the surface is estimated using a spherical harmonics decomposition [199], considering two domains: D^+, the volume outside the surface of the sphere of radius a, and D^-, the volume inside the surface of the sphere. It is written

$$p^+(R,\theta,\phi) = \sum_{n=0}^{+\infty} \sum_{m=-n}^{n} \psi_{n,m}(\theta,\phi) \left[A^+_{n,m} h_n^{(1)}(k_f R) + B^+_{n,m} h_n^{(2)}(k_f R) \right], \text{ for } R \geqslant a \tag{C.1a}$$

$$p^-(R,\theta,\phi) = \sum_{n=0}^{+\infty} \sum_{m=-n}^{n} \psi_{n,m}(\theta,\phi) \left[A^-_{n,m} j_n(k_f R) + B^-_{n,m} y_n(k_f R) \right], \text{ for } 0 \leqslant R \leqslant a \tag{C.1b}$$

where $h_n^{(1)}$ and $h_n^{(2)}$ are the spherical Hankel functions of the first and second kind, respectively, and j_n and y_n are the spherical Bessel functions of the first and second kind, respectively. k_f is the acoustic wavenumber and $\psi_{n,m}(\theta,\phi)$ are the spherical harmonics defined in Eq. (3.25).

Applying the boundary conditions at infinity (divergent waves) and at the center of the sphere (convergent waves) to the properties of the spherical Hankel and Bessel functions yields

$$\begin{cases} B^+_{n,m} = 0 \\ B^-_{n,m} = 0 \end{cases} \tag{C.2}$$

The pressure fields in the domains D^+ and D^- are thus

$$p^+(R,\theta,\phi) = \sum_{n=0}^{+\infty} \sum_{m=-n}^{n} \psi_{n,m}(\theta,\phi)\, A^+_{n,m} h_n^{(1)}(k_f R), \text{ for } R \geqslant a \tag{C.3a}$$

$$p^-(R,\theta,\phi) = \sum_{n=0}^{+\infty} \sum_{m=-n}^{n} \psi_{n,m}(\theta,\phi)\, A^-_{n,m} j_n(k_f R), \text{ for } 0 \leqslant R \leqslant a \tag{C.3b}$$

A velocity jump δu is imposed on the surface of the sphere, such that the impedance is given by $Z = p/\delta u$. The pressure continuity and velocity equilibrium conditions at the surface of the sphere (i.e. $R = a$) are then written

$$\begin{cases} p^+(a,\theta,\phi) = p^-(a,\theta,\phi) \\ \delta u = u^+(a,\theta,\phi) + u^-(a,\theta,\phi) \end{cases} \tag{C.4}$$

The second equation of C.4 takes into account the orientation of the normals, as in the section 3.2.3, with the normal pointing in the outer-direction of the considered domain. The pressure and the radial velocity are linked by the Euler relation

$$u_n = -\frac{1}{\mathrm{j}\omega\rho_f} \frac{\partial p}{\partial r} \tag{C.5}$$

With the orientation of the normals previously defined, we can write

$$\begin{cases} u^+(a,\theta,\phi) = -u_n \\ u^-(a,\theta,\phi) = u_n \end{cases} \tag{C.6}$$

Furthermore, the spherical Hankel and Bessel functions can be derived with respect to their argument according to the following relation

$$\frac{\partial f_n}{\partial x}(x) = \frac{n}{x} f_n(x) - f_{n+1}(x) \tag{C.7}$$

In the following, and in order to clarify the equations, the spherical Hankel function of the first kind $h_n^{(1)}$ is denoted by h_n. Combining Eq. (C.3a) and Eq. (C.3b) with the relations in Eq. (C.4) and Eq. (C.5) yields

$$\sum_{n=0}^{+\infty} \sum_{m=-n}^{n} \psi_{n,m}(\theta,\phi)\, A^+_{n,m} h_n(k_f a) = \sum_{n=0}^{+\infty} \sum_{m=-n}^{n} \psi_{n,m}(\theta,\phi)\, A^-_{n,m} j_n(k_f a) \tag{C.8a}$$

$$\delta u = \frac{k_f}{\mathrm{j}\omega\rho_f} \sum_{n=0}^{+\infty} \sum_{m=-n}^{n} \psi_{n,m}(\theta,\phi) \left[A^+_{n,m} h'_n(k_f a) - A^-_{n,m} j'_n(k_f a) \right] \tag{C.8b}$$

Using the orthonormal properties of the spherical harmonics (see Eq. (3.28)), we can multiply Eq. (C.8a) and Eq. (C.8b) by $\psi_{\nu,\mu}$ and integrate them on the surface of the sphere to eliminate the sums

$$\begin{cases} A^+_{n,m} h_n(k_f a) = A^-_{n,m} j_n(k_f a) \\ \iint_\Omega \delta u \psi^*_{\nu,\mu}(\theta,\phi) a^2 \sin\theta d\theta d\phi = \frac{k_f a^2}{\mathrm{j}\omega\rho_f} \left[A^+_{n,m} h'_n(k_f a) - A^-_{n,m} j'_n(k_f a) \right] \end{cases} \tag{C.9}$$

where * denotes the complex conjugate. In order to calculate the condensed impedances, the velocity jump must correspond to a condensation function φ^j, which are either weighted spherical harmonics or 2D gate functions, which means

$$\iint_{\Omega} \delta u \psi^*_{n,m}(\theta,\phi) a^2 \sin\theta d\theta d\phi = \iint_{\Omega} \varphi^j \psi^*_{n,m}(\theta,\phi) a^2 \sin\theta d\theta d\phi = \varepsilon^j_{n,m}(a) \tag{C.10}$$

The evaluation of the factor $\varepsilon^j_{n,m}$, which depends on the the radius a of the sphere, will be evaluated for each type of CF. Eq. (C.9) now becomes

$$\begin{cases} A^+_{n,m} h_n(k_f a) = A^-_{n,m} j_n(k_f a) \\ \varepsilon^j_{n,m}(a) = \frac{k_f a^2}{\mathrm{j}\omega\rho_f} \left[A^+_{n,m} h'_n(k_f a) - A^-_{n,m} j'_n(k_f a) \right] \end{cases} \tag{C.11}$$

The resolution of this system of equations enables us to obtain the pressure at the surface of the sphere for the infinite domain

$$p(a,\theta,\phi) = \omega\rho_f k_f \sum_{n=0}^{+\infty} \sum_{m=-n}^{n} \psi_{n,m}(\theta,\phi)\, j_n(k_f a) h_n(k_f a) \varepsilon^j_{n,m}(a) \tag{C.12}$$

For each CF, the pressure must be projected on the CF φ^i to obtain the condensed impedance, according to Eq. (3.17). For the weighted spherical harmonics, it yields

$$Z^{ij}_{1+2} = \begin{cases} \omega\rho_f k_f a^2 j_i(k_f a) h_i(k_f a) & \text{if} \quad i = j \\ 0 & \text{elsewhere} \end{cases} \tag{C.13}$$

The form of this expression is explained by the orthonormal properties of the spherical harmonics, thus resulting in a diagonal condensed impedance matrix. As for the 2D gate functions, the condensed impedances of the global system 1+2 is given by

$$Z^{ij}_{1+2} = \omega\rho_f k_f \sum_{n=0}^{+\infty} \sum_{m=-n}^{n} j_n(k_f a) h_n(k_f a) \varepsilon^j_{n,m}(a) \varepsilon^{i*}_{n,m}(a) \tag{C.14}$$

C.1.2 Global rCTF approach

In order to apply the global rCTF approach, the condensed impedances of the infinite water medium must be considered with the two fictitious surfaces Ω_{int} and Ω_{ext} of the system (see figure 32), and the calculations are carried out using only the patches as condensation functions. Three different cases must hence be explored:

- Case 1: when the excitation and receiving patches are both located at the exterior surface Ω_{ext}.
- Case 2: when the excitation and receiving patches are both located at the interior surface Ω_{int}.

- Case 3: when the excitation and receiving patches are located on different surfaces.

For cases 1 and 2, the developments are the same than those presented in C.1.1. The condensed impedances can thus be obtained directly from Eq. (C.14)

$$Z_{1+2}^{ij} = \omega\rho_f k_f \sum_{n=0}^{+\infty}\sum_{m=-n}^{n} j_n(k_f a_{ext}) h_n(k_f a_{ext}) \varepsilon_{n,m}^{j}(a_{ext}) \varepsilon_{n,m}^{i*}(a_{ext}), \quad \begin{cases} \text{patch } i \in \Omega_{ext} \\ \text{patch } j \in \Omega_{ext} \end{cases} \tag{C.15}$$

$$Z_{1+2}^{ij} = \omega\rho_f k_f \sum_{n=0}^{+\infty}\sum_{m=-n}^{n} j_n(k_f a_{ext}) h_n(k_f a_{int}) \varepsilon_{n,m}^{j}(a_{int}) \varepsilon_{n,m}^{i*}(a_{int}), \quad \begin{cases} \text{patch } i \in \Omega_{int} \\ \text{patch } j \in \Omega_{int} \end{cases} \tag{C.16}$$

For the case 3 however, the reasoning is slightly different. In the following, the developments will be carried out by considering that the incident patch is located on Ω_{ext} while the receiving patch is located on Ω_{int}. The inverse case follows the same principle and will not be explicited here, as the symmetric properties of the condensed impedances do not require to carry out both calculations. Using Eqs. C.3a, C.3b and C.11, the pressure in the domain interior and exterior to Ω_{ext} can be written

$$p^{+}(R,\theta,\phi) = \omega\rho_f k_f \sum_{n=0}^{+\infty}\sum_{m=-n}^{n} \psi_{n,m}(\theta,\phi)\, j_n(k_f a_{ext}) h_n(k_f R) \varepsilon_{n,m}^{j}(a_{ext}), \text{ for } R \geqslant a_{ext} \tag{C.17a}$$

$$p^{-}(R,\theta,\phi) = \omega\rho_f k_f \sum_{n=0}^{+\infty}\sum_{m=-n}^{n} \psi_{n,m}(\theta,\phi)\, j_n(k_f R) h_n(k_f a_{ext}) \varepsilon_{n,m}^{j}(a_{ext}), \text{ for } 0 \leqslant R \leqslant a_{ext} \tag{C.17b}$$

The pressure at the interior surface Ω_{int} can hence be deducted from Eq. (C.18)

$$p(a_{int},\theta,\phi) = \omega\rho_f k_f \sum_{n=0}^{+\infty}\sum_{m=-n}^{n} \psi_{n,m}(\theta,\phi)\, j_n(k_f a_{int}) h_n(k_f a_{ext}) \varepsilon_{n,m}^{j}(a_{ext}), \text{ for } 0 \leqslant R \leqslant a_{ext} \tag{C.18}$$

Finally, the condensed impedances between the incident patch j and the receiving patch i is obtained by projecting Eq. (C.18) on the patch i

$$Z_{1+2}^{ij} = \omega\rho_f k_f \sum_{n=0}^{+\infty}\sum_{m=-n}^{n} j_n(k_f a_{int}) h_n(k_f a_{ext}) \varepsilon_{n,m}^{j}(a_{ext}) \varepsilon_{n,m}^{i*}(a_{int}), \quad \begin{cases} \text{patch } i \in \Omega_{int} \\ \text{patch } j \in \Omega_{ext} \end{cases} \tag{C.19}$$

C.2 Condensed impedances of the water sphere

In order to calculate the condensed impedances of the water sphere for the local rCTF approach (see figure 31), and in accordance with its definition in Eq. (3.2), a normal velocity

is imposed on the spherical surface Ω (where the positive outer-pointing normal points towards the exterior of the sphere), corresponding to a condensation function: $u = \varphi^j$. The calculation process to estimate the resulting pressure is therefore similar to that carried out in C.1.1, except that the calculation is performed only inside the sphere. The pressure inside the sphere is given by Eq. (C.1b), whereas the Euler equation on the surface Ω yields (taking into account the orientation of the outer-pointing normal)

$$\varphi^j = -\frac{1}{\mathrm{j}\omega\rho_f}\frac{\partial p}{\partial r} \tag{C.20}$$

The pressure at the surface Ω of the sphere is easily derived

$$p(a,\theta,\phi) = -\frac{\mathrm{j}\omega\rho_f}{k_f a^2}\sum_{n=0}^{+\infty}\sum_{m=-n}^{n}\psi_{n,m}(\theta,\phi)\frac{j_n(k_f a)}{j_n'(k_f a)}\varepsilon_{n,m}^{j}(a) \tag{C.21}$$

As it was done in C.1.1, and following the definition of the condensed impedances of Eq. (3.2), the condensed impedances at the surface of the sphere for the weighted spherical harmonics are given by

$$Z_2^{ij} = \begin{cases} -\frac{\mathrm{j}\omega\rho_f}{k_f}\frac{j_i(k_f a)}{j_i'(k_f a)} & \text{if} \quad i = j \\ 0 & \text{elsewhere} \end{cases} \tag{C.22}$$

As for the 2D gate functions, the condensed impedances are

$$Z_2^{ij} = -\frac{\mathrm{j}\omega\rho_f}{k_f a^2}\sum_{n=0}^{+\infty}\sum_{m=-n}^{n}\frac{j_n(k_f a)}{j_n'(k_f a)}\varepsilon_{n,m}^{j}(a)\varepsilon_{n,m}^{i*}(a) \tag{C.23}$$

C.3 Condensed impedances of the hollow sphere

In order to calculate the condensed impedances of the hollow sphere for the global rCTF approach (see figure 32), two different calculations must be carried out, wether the incident patch is located on Ω_{ext} or on Ω_{int}. For the former, in accordance with the definition of the condensend impedance in Eq. (3.2), a normal velocity is imposed on the spherical surface Ω_{ext} (where the positive outer-pointing normal points towards the exterior of the hollow sphere), corresponding to a condensation function: $u = \varphi^j$. The velocity at the interior surface Ω_{int} is then null. The pressure inside the hollow sphere is written

$$p(R,\theta,\phi) = \sum_{n=0}^{+\infty}\sum_{m=-n}^{n}\psi_{n,m}(\theta,\phi)\left[A_{n,m}j_n(k_f R) + B_{n,m}y_n(k_f R)\right], \text{ for } a_{int} \leqslant R \leqslant a_{ext} \tag{C.24}$$

The boundary conditions at Ω_{ext} and Ω_{int} can be expressed using the Euler relation

$$\varphi^j = -\frac{1}{\mathrm{j}\omega\rho_f}\frac{\partial p}{\partial r}(a_{ext},\theta,\phi), \quad 0 = \frac{1}{\mathrm{j}\omega\rho_f}\frac{\partial p}{\partial r}(a_{int},\theta,\phi) \tag{C.25}$$

Following developments similar to the ones carried out in C.1.1, the pressure inside the hollow sphere in given by

$$p(R,\theta,\phi) = \frac{\mathrm{j}\omega\rho_f}{k_f}\sum_{n=0}^{+\infty}\sum_{m=-n}^{n}\psi_{n,m}(\theta,\phi)\,\frac{y_n'(k_f a_{int})j_n(k_f R) - j_n'(k_f a_{int})y_n(k_f R)}{j_n'(k_f a_{int})y_n'(k_f a_{ext}) - j_n'(k_f a_{ext})y_n'(k_f a_{int})}\varepsilon^j_{n,m}(a_{ext}), \quad \text{for } a_{int} \leqslant R \leqslant a_{ext} \tag{C.26}$$

In order to obtain the condensed impedance between the incident patch j and the receiving patch i, the relation in Eq. (C.26) is projected on the patch i. If the patch i is located at the exterior surface Ω_{ext}, it yields

$$Z_2^{ij} = \frac{\mathrm{j}\omega\rho_f}{k_f a_{ext}^2}\sum_{n=0}^{+\infty}\sum_{m=-n}^{n}\frac{y_n'(k_f a_{int})j_n(k_f a_{ext}) - j_n'(k_f a_{int})y_n(k_f a_{ext})}{j_n'(k_f a_{int})y_n'(k_f a_{ext}) - j_n'(k_f a_{ext})y_n'(k_f a_{int})}\varepsilon^j_{n,m}(a_{ext})\varepsilon^{i*}_{n,m}(a_{ext}), \quad \begin{cases}\text{patch } i \in \Omega_{ext}\\ \text{patch } j \in \Omega_{ext}\end{cases} \tag{C.27}$$

If the patch i is located at the interior surface Ω_{int}, it yields

$$Z_2^{ij} = \frac{\mathrm{j}\omega\rho_f}{k_f^3(a_{ext}a_{int})^2}\sum_{n=0}^{+\infty}\sum_{m=-n}^{n}\frac{y_n'(k_f a_{int})j_n(k_f a_{ext}) - j_n'(k_f a_{int})y_n(k_f a_{ext})}{\varepsilon^j_{n,m}(a_{ext})\varepsilon^{i*}_{n,m}(a_{int})}, \quad \begin{cases}\text{patch } i \in \Omega_{int}\\ \text{patch } j \in \Omega_{ext}\end{cases} \tag{C.28}$$

For the case where the incident patch is located on Ω_{int}, in accordance with the definition of the condensend impedance in Eq. (3.2), a normal velocity is imposed on the spherical surface Ω_{int} (where the positive outer-pointing normal points towards the interior of the hollow sphere), corresponding to a condensation function: $u = \varphi^j$. The velocity at the exterior surface Ω_{ext} is then null. The boundary conditions at Ω_{ext} and Ω_{int} can be expressed using the Euler relation

$$0 = -\frac{1}{\mathrm{j}\omega\rho_f}\frac{\partial p}{\partial r}(a_{ext},\theta,\phi), \quad \varphi^j = \frac{1}{\mathrm{j}\omega\rho_f}\frac{\partial p}{\partial r}(a_{int},\theta,\phi) \tag{C.29}$$

Following the same developments as before, the condensed impedance between the incident patch j and the receiving patch i can be obtained. For the case where the receiving patch is located on Ω_{ext}, the symmetric properties of the condensed impedances lead to a result corresponding to Eq. (C.28). If the patch i is located at the interior surface Ω_{int}, it yields

$$Z_2^{ij} = \frac{\mathrm{j}\omega\rho_f}{k_f a_{int}^2} \sum_{n=0}^{+\infty} \sum_{m=-n}^{n} \frac{y_n'(k_f a_{ext}) j_n(k_f a_{int}) - j_n'(k_f a_{ext}) y_n(k_f a_{int})}{j_n'(k_f a_{int}) y_n'(k_f a_{ext}) - j_n'(k_f a_{ext}) y_n'(k_f a_{int})} \varepsilon_{n,m}^{j}(a_{int}) \varepsilon_{n,m}^{i*}(a_{int}), \quad \begin{cases} \text{patch } i \in \Omega_{int} \\ \text{patch } j \in \Omega_{int} \end{cases} \tag{C.30}$$

C.4 Condensed impedances of the reference subsystem

The analytical condensed impedances of the infinite fluid domain bounded by the spherical surface Ω (subsystem 1 on figure 31) are calculated to validate and evaluate the ability of the rCTF method. As defined in Eq. (3.2), a normal velocity is imposed on the surface Ω (where the positive outer-pointing normal now points towards the center of the sphere), corresponding to a condensation function: $u = \varphi^j$. The pressure inside the water domain bounded by the surface Ω is described by Eq. (C.1a), whereas the Euler equation on the surface Ω yields (taking into account the orientation of the outer-pointing normal)

$$\varphi^i = \frac{1}{\mathrm{j}\omega\rho_f} \frac{\partial p}{\partial r} \tag{C.31}$$

Again, we derive the pressure at the surface Ω of the sphere

$$p(a,\theta,\phi) = \frac{\mathrm{j}\omega\rho_f}{k_f a^2} \sum_{n=0}^{+\infty} \sum_{m=-n}^{n} \psi_{n,m}(\theta,\phi) \frac{h_n(k_f a)}{h_n'(k_f a)} \varepsilon_{n,m}^{j}(a) \tag{C.32}$$

As with the previous sections, and following the definition of the condensed impedances of Eq. (3.2), the condensed impedances at the surface of the sphere for the weighted spherical harmonics are given by

$$Z_1^{ij} = \begin{cases} \frac{\mathrm{j}\omega\rho_f}{k_f} \frac{h_i(k_f a)}{h_i'(k_f a)} & \text{if} \quad i = j \\ 0 & \text{elsewhere} \end{cases} \tag{C.33}$$

As for the 2D gate functions, the condensed impedances are

$$Z_1^{ij} = \frac{\mathrm{j}\omega\rho_f}{k_f a^2} \sum_{n=0}^{+\infty} \sum_{m=-n}^{n} \frac{h_n(k_f a)}{h_n'(k_f a)} \varepsilon_{n,m}^{j}(a) \varepsilon_{n,m}^{i*}(a) \tag{C.34}$$

Concerning the condensed impedances of the residual subsystem for the case of the global decoupling approach, they correspond to the condensed impedances of a water sphere or radius a_{int}. Their expression is given in Eq. (C.23).

C.5 Calculation of the condensed pressures

The developments in this section are carried out considering the infinite water medium of the local rCTF approach (see subsystem 1+2 in figure 31). For the global rCTF approach, the

developments are the same, but the condensed pressures must be evaluated at both fictitious surfaces Ω_{ext} and Ω_{int} of the subsystem.

C.5.1 Condensed pressure induced by a unit monopole

In order to calculate $\mathbf{P}^{\mathbf{M_1}}_{\mathbf{1+2}}$, the condensed pressure vector induced by a monopole of unit volume velocity located at point M_1 in the infinite water domain 1+2, the expression of the free-space Green's function is expanded in spherical harmonics [8]. The acoustic field pressure at any point $\mathbf{M}(R,\theta,\phi)$ due to a spherical source located at point $\mathbf{M_1}(R_1,\theta_1,\phi_1)$ is given by

$$p_i^{M_1} = \mathrm{j}\omega\rho_f \frac{\mathrm{e}^{\mathrm{j}k_f|\mathbf{M}-\mathbf{M_1}|}}{4\pi|\mathbf{M}-\mathbf{M_1}|} \tag{C.35}$$

where $|\bullet|$ represents the Euclidean norm.

Expanding this expression in spherical harmonics, the pressure induced by the monopole can be rewritten

$$\begin{aligned} p_i^{M_1} = \frac{\omega\rho_f k_f}{4\pi} \sum_{n=0}^{+\infty} \sum_{m=0}^{n} \kappa_m \frac{(n-m)!}{(n+m)!} (2n+1) \cos\left(m(\phi-\phi_1)\right) \\ P_n^m\left(\cos\theta\right) P_n^m\left(\cos\theta_1\right) j_n(k_f R) h_n(k_f R_1) \end{aligned} \tag{C.36}$$

where

$$\kappa_m = \begin{cases} 1 & \text{if} \quad m = 0 \\ 2 & \text{if} \quad m \neq 0 \end{cases} \tag{C.37}$$

According to the definition of the condensed pressure, the pressure at the surface of the sphere (i.e. $R = a$) is projected on the condensation functions according to the scalar product in spherical coordinates defined in Eq. (3.28). For the weighted spherical harmonics as condensation functions, the i^{th} component of $\mathbf{P}^{\mathbf{M_1}}_{\mathbf{1+2}}$ is given by

$$\begin{aligned} P^{M_1}_{1+2,i} = \left\langle p_i, \psi_{\nu,\mu} \right\rangle = \frac{\omega\rho_f k_f}{(4\pi)^{3/2}} \sum_{n=0}^{+\infty} \sum_{m=0}^{n} \kappa_m \frac{(n-m)!}{(n+m)!} (2n+1) \sqrt{(2\nu+1)\frac{(\nu-\mu)!}{(\nu+\mu)!}} \\ P_n^m\left(\cos\theta_1\right) j_n(k_f a) h_n(k_f R_1) \\ \iint_{\Omega} \cos\left(m(\phi-\phi_1)\right) \mathrm{e}^{-\mathrm{j}\mu\phi} P_n^m\left(\cos\theta\right) P_\nu^\mu\left(\cos\theta\right) a \sin\theta \, \mathrm{d}\theta \, \mathrm{d}\phi \end{aligned} \tag{C.38}$$

where $\psi_{\nu,\mu}$ corresponds to the i^{th} condensation function, as defined in Eq. (3.26).

For the 2D gate functions as condensation function, the i^{th} component of $\mathbf{P}^{\mathbf{M_1}}_{\mathbf{1+2}}$ is given by

$$P_{1+2,i}^{M_1} = \left\langle p_{inc}^{M_1}, \varphi^i \right\rangle = \frac{\omega \rho_f k_f}{4\pi} \sum_{n=0}^{+\infty} \sum_{m=0}^{n} \kappa_m \frac{(n-m)!}{(n+m)!} (2n+1) P_n^m (\cos\theta_1)\, j_n(k_f a) h_n(k_f R_1) \frac{1}{\sqrt{\Omega_i}} \iint_{\Omega_i} \cos\left(m(\phi - \phi_1)\right) P_n^m (\cos\theta)\, a^2 \sin\theta \, \mathrm{d}\theta \, \mathrm{d}\phi \tag{C.39}$$

where Ω_i is the area of the patch associated with the condensation function φ^i, according to the definition of the condensation function in Eq. (3.29).

The integrals that appear in these expressions are solved numerically by separating the integrals. The integration over ϕ can be solved analytically, while the integration over θ is evaluated numerically using a global adaptative quadrature and default error tolerances.

C.5.2 Condensed pressure induced by a plane wave

In order to calculate $\mathbf{P_{1+2}}$, the condensed pressure induced by an acoustic plane wave in the infinite water domain 1+2, we consider the expression of the pressure induced by the plane wave expanded in spherical harmonics given in Eq. (3.37). Then, using the definition of the scalar product in spherical coordinates of Eq. (3.28), we project it on the condensation functions. Considering the weighted spherical harmonics as condensation functions, the i^{th} component of the vector $\mathbf{P_{1+2}}$ is given by

$$P_{1+2,i} = \left\langle p_i, \psi_{\nu,\mu} \right\rangle = P_i \sum_{n=0}^{+\infty} (2n+1)\, i^n j_n\left(k_f a\right) \sqrt{\frac{2\nu+1}{4\pi} \frac{(\nu-\mu)!}{(\nu+\mu)!}} \iint_{\Omega} P_n(\cos\theta)\, P_\nu^\mu(\cos\theta)\, \mathrm{e}^{-\mathrm{j}\mu\phi} a \sin\theta \, \mathrm{d}\theta \, \mathrm{d}\phi \tag{C.40}$$

where $\psi_{\nu,\mu}$ corresponds to the i^{th} condensation function, as defined in Eq. (3.26).

For the 2D gate functions as condensation functions, the i^{th} component of $\mathbf{P}_{\mathbf{1+2}}^{\mathbf{M_1}}$ is given by

$$P_{1+2,i} = \left\langle p_i, \varphi^i \right\rangle = P_i \sum_{n=0}^{+\infty} (2n+1)\, i^n j_n\left(k_f a\right) \frac{1}{\sqrt{\Omega_i}} \iint_{\Omega_i} P_n(\cos\theta)\, a^2 \sin\theta \, \mathrm{d}\theta \, \mathrm{d}\phi \tag{C.41}$$

where Ω_i is the area of the patch associated with the condensation function φ^i, according to the definition of the condensation function in Eq. (3.29).

Appendix D

Expression of the pressure radiated by a fully coated cylindrical shell for different kinds of excitations - Application to the calculation of the CTFs, condensed pressures and condensed radial velocities of the fluid-loaded fully coated shell

In this appendix, the formulation to obtain the pressure radiated by a fully coated cylindrical shell in the surrounding fluid medium is derived for three different kinds of excitations:

- A mechanical radial point force applied on the inner surface of the shell;
- A unitary monopole located inside the rubber thickness;
- A unitary monopole located in the surrounding fluid medium.

From the expressions obtained when developing these formulations, the CTFs, condensed pressures and condensed radial velocities of the fluid-loaded fully coated cylindrical shell (which is the global system 1+2 in chapter 5) will be explicited.

When solving the Flügge's equations with heavy fluid loading, the spectral Euler relation of Eq. (1.12), involving the spectral impedance of the fluid $\tilde{\tilde{Z}}_f$, is used. However, when the shell is coated, the presence of the coating modifies the value of the spectral impedance. Thus, as a preamble, we will begin by developing the formulation to obtain the effective spectral impedance of the coating as well as the fluid medium.

D.1 Calculation of the effective spectral impedance of the coating and the fluid medium

In order to compute the effective spectral impedance of the coating and the fluid medium, the pressure inside and outside the rubber must be considered (see figure 107). R corresponds to

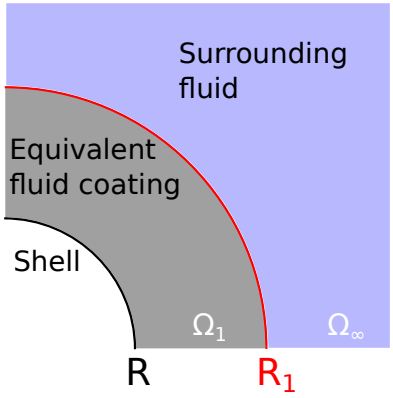

Figure 107: Spectral effective impedance of the coating and the fluid medium.

the radius of the shell, while R_1 denotes the exterior radius of the rubber coating. Ω_1 is the domain corresponding to the thickness of the coating, while Ω_∞ is the exterior fluid domain. For a given point M of coordinates (r, θ, x), the pressure inside the rubber, p^1, and outside the rubber, p^∞, satisfies the Helmholtz equation

$$\begin{cases} \Delta p^1(M) + k_p^2 p^1(M) = 0 \quad \text{if} \quad M \in \Omega_1 \\ \Delta p^\infty(M) + k_f^2 p^\infty(M) = 0 \quad \text{if} \quad M \in \Omega_\infty \end{cases} \tag{D.1}$$

with $k_p = \omega/c_p$ and $k_f = \omega/c_f$. This problem can be solved in the wavenumber domain by the means of a Fourier series decomposition along coordinate θ and a Fourier transform along coordinate x as described in Eq. (1.2). The pressures in Eq. (D.1) can then be written as a linear combination of Bessel and Hankel functions. According to Ricks and Schmidt [50], the most stable formulation reads

$$\tilde{\tilde{p}}^1(r, n, k_x) = A_1^{imp} \frac{H_n(k_{pr} r)}{H_n(k_{pr} R)} + B_1^{imp} J_n(k_{pr} r) H_n(k_{pr} R_1) \quad \text{if} \quad r \leqslant R_1 \tag{D.2a}$$

$$\tilde{\tilde{p}}^\infty(r, n, k_x) = A_\infty^{imp} \frac{H_n(k_r r)}{H_n(k_r R_1)} + B_\infty^{imp} J_n(k_r r) H_n(k_r R_\infty) \quad \text{if} \quad r \geqslant R_1 \tag{D.2b}$$

where $J_n(\bullet)$ denotes the Bessel function of the first kind, $H_n(\bullet)$ the Hankel function of the first kind, $k_{pr}^2 = k_p^2 - k_x^2$, and $k_r^2 = k_f^2 - k_x^2$. The unknowns of this system, A_1^{imp}, B_1^{imp}, A_∞^{imp} and B_∞^{imp} can be obtained from the boundary conditions and continuity relations at the different interfaces. From the boundary conditions, as there is no wave reflection at infinity (i.e. Sommerfeld condition, Eq. (1.11)), B_∞^{imp} must necessarily be 0. The continuity of pressures and velocities at the interface $r = R_1$ yields

$$\tilde{\tilde{p}}^1(r = R_1, n, k_x) = \tilde{\tilde{p}}^\infty(r = R_1, n, k_x) \tag{D.3a}$$

$$\frac{1}{\mathrm{j}\omega\rho_p} \frac{\partial \tilde{\tilde{p}}^1}{\partial r}(r = R_1, n, k_x) = \frac{1}{\mathrm{j}\omega\rho_f} \frac{\partial \tilde{\tilde{p}}^\infty}{\partial r}(r = R_1, n, k_x) \tag{D.3b}$$

The kinematic condition $\frac{\partial \tilde{\tilde{p}}^1}{\partial r}(r = R, n, k_x) = \rho_p \omega^2$ (assumming unit displacement of the shell to calculate the effective spectral impedance of the fluid loaded coating) at the interface between the shell and the coating yields

$$\frac{\partial \tilde{\tilde{p}}^1}{\partial r}(r = R, n, k_x) = \rho_p \omega^2 \tag{D.4}$$

Taking into these relations, it is possible to obtain A_1^{imp}, B_1^{imp}, A_∞^{imp} by solving the following system of equations

$$\begin{bmatrix} -1 & \frac{H_n(k_{pr}R_1)}{H_n(k_{pr}R)} & J_n(k_{pr}R_1)H_n(k_{pr}R_1) \\ -\frac{k_r}{\rho_f}\frac{H_n'(k_rR_1)}{H_n(k_rR_1)} & \frac{k_{pr}}{\rho_p}\frac{H_n'(k_{pr}R_1)}{H_n(k_{pr}R)} & \frac{k_{pr}}{\rho_p}J_n'(k_{pr}R_1)H_n(k_{pr}R_1) \\ 0 & k_{pr}\frac{H_n'(k_{pr}R)}{H_n(k_{pr}R)} & k_{pr}J_n'(k_{pr}R)H_n(k_{pr}R_1) \end{bmatrix} \begin{bmatrix} A_\infty^{imp} \\ A_1^{imp} \\ B_1^{imp} \end{bmatrix} = \begin{bmatrix} 0 \\ 0 \\ \rho_p\omega^2 \end{bmatrix} \tag{D.5}$$

The effective spectral impedance of the coating and the fluid medium is then given by the following expression

$$\tilde{\tilde{Z}}_f(R, n, k_x) = A_1^{imp} + B_1^{imp} J_n(k_{pr}R)H_n(k_{pr}R_1) \tag{D.6}$$

D.2 Radiated pressure for a mechanical radial point force

When the excitation is a radial point force applied on the inner surface of the shell, the Flügge's system that must be solved reads

$$\mathcal{L}(x,\theta)\begin{bmatrix} U(x,\theta) \\ V(x,\theta) \\ W(x,\theta) \end{bmatrix} = \gamma \begin{bmatrix} 0 \\ 0 \\ F(x,\theta) - p(x,\theta) \end{bmatrix} \tag{D.7}$$

where $\gamma = \frac{(1-\nu^2)R^2}{Eh}$ and the elements of the Flügge's operator $\mathcal{L}$ are given in Eq. (1.1). The problem is solved in the wavenumber domain, leading to a spectral Flügge's system

$$\tilde{\tilde{\mathcal{L}}}(k_x, n)\begin{bmatrix} \tilde{\tilde{U}}(k_x,n) \\ \tilde{\tilde{V}}(k_x,n) \\ \tilde{\tilde{W}}(k_x,n) \end{bmatrix} = \gamma \begin{bmatrix} 0 \\ 0 \\ \tilde{\tilde{F}}(k_x,n) - \tilde{\tilde{p}}(k_x,n) \end{bmatrix} \tag{D.8}$$

Using the spectral Euler relation of Eq. (1.12), the radial displacement of the shell can be retrieved according to Eq. (A.3c)

$$\tilde{\tilde{W}}_F(k_x,n) = \frac{\gamma \tilde{\tilde{F}}(k_x,n)\left(\tilde{\tilde{Z}}_{UU}(k_x,n)\tilde{\tilde{Z}}_{VV}(k_x,n) - \tilde{\tilde{Z}}_{UV}^2(k_x,n)\right)}{\Delta(k_x,n)} \tag{D.9}$$

where $\Delta(k_x, n)$ has been explicited in Eq. (A.4). Once the displacement of the shell has been obtained, it is possible to derive the displacement of the exterior coating surface

$$\tilde{\tilde{W}}_F^{coat}(k_x, n) = \frac{k_{pr}}{\rho_p \omega^2} \left(A_1^{imp} \frac{H_n'(k_{pr} R_1)}{H_n(k_{pr} R)} + B_1^{imp} J_n'(k_{pr} R_1) H_n(k_{pr} R_1) \right) \tilde{\tilde{W}}_F(k_x, n) \tag{D.10}$$

The pressure radiated inside the rubber thickness and in the surrounding fluid can then be obtained. For the former, it yields

$$\tilde{\tilde{p}}_F(r, n, k_x) = \left(A_1^{imp} \frac{H_n(k_{pr} r)}{H_n(k_{pr} R)} + B_1^{imp} J_n(k_{pr} r) H_n(k_{pr} R_1) \right) \tilde{\tilde{W}}_F(k_x, n), \quad \text{if} \quad r \leqslant R_1 \tag{D.11}$$

And in the surrounding fluid

$$\tilde{\tilde{p}}_F(r, n, k_x) = \frac{\rho_f \omega^2}{k_r} \frac{H_n(k_r r)}{H_n'(k_r R_1)} \tilde{\tilde{W}}_F^{coat}(k_x, n), \quad \text{if} \quad r \geqslant R_1 \tag{D.12}$$

An example of the pressure radiated by the coated shell in the surrounding fluid medium, when a mechanical radial point force is prescribed on its inner surface is illustrated in figure 108. The mechanical excitation and the two measurement points are the ones presented in figure 79, while the characteristics of the shell, the coating and the fluid medium are presented in table 6.

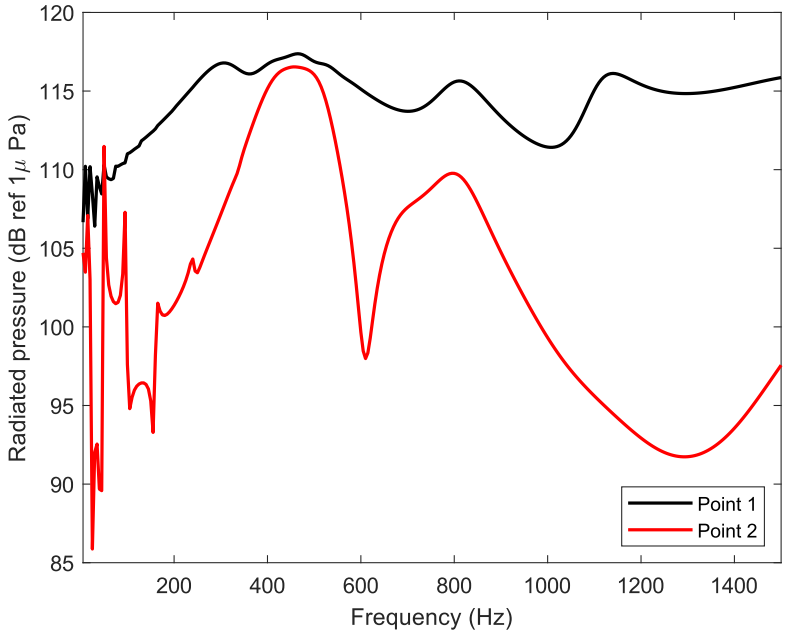

Figure 108: Pressure radiated by the coated shell at 2 points in the surrounding fluid.

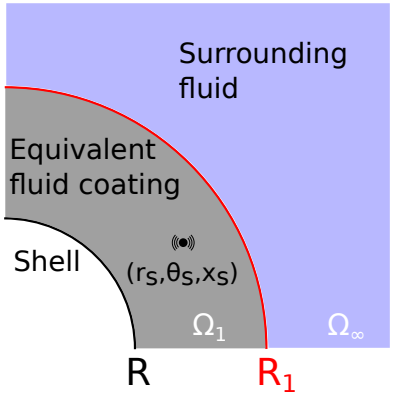

Figure 109: Monopole excitation inside the rubber thickness.

D.3 Radiated pressure for a unit monopole located inside the rubber thickness

When the excitation is a unitary monopole source located inside the rubber thickness at coordinates (r_s, θ_s, x_s) (see figure 109), the Flügge's system reads

$$\mathcal{L}(x,\theta)\begin{bmatrix} U(x,\theta) \\ V(x,\theta) \\ W(x,\theta) \end{bmatrix} = \gamma \begin{bmatrix} 0 \\ 0 \\ -p_e(x,\theta) - p(x,\theta) \end{bmatrix} \tag{D.13}$$

In Eq. (D.13), the total pressure into the fluid domain, p_t, is split into the sum of the monopole blocked pressure p_e, which is the pressure generated by the monopole source on the cylindrical shell, as if the shell was rigid, and the pressure p radiated outwards by the shell's vibrations (i.e. $p_{tot} = p_e + p$).

In order to compute the blocked pressure induced by the monopole source, the pressure inside and outside the rubber must be considered. For a given point M of coordinates (r, θ, x), they satisfy the Helmholtz equation

$$\begin{cases} \Delta p_e^1(M) + k_p^2 p_e^1(M) = \delta_s \quad \text{if} \quad M \in \Omega_1 \\ \Delta p_e^\infty(M) + k_f^2 p_e^\infty(M) = 0 \quad \text{if} \quad M \in \Omega_\infty \end{cases} \tag{D.14}$$

with $k_p = \omega/c_p$, $k_f = \omega/c_f$, and δ_s the Dirac distribution located at the source position. As the monopole source is situated inside the rubber thickness, the pressure in Ω_1 can be decomposed into the sum of the incident pressure, p_i, and the diffracted pressure, p_d^1 ($p_e^1 = p_i + p_d^1$). In the exterior fluid domain, however, as there is no external source, the pressure corresponds to the diffracted pressure: $p_e^\infty = p_d^\infty$. Eq. (D.14) can hence be rewritten

$$\begin{cases} \Delta p_i(M) + k_p^2 p_i(M) = \delta_s \\ \Delta p_d^1(M) + k_p^2 p_d^1(M) = 0 \quad \text{if} \quad M \in \Omega_1 \\ \Delta p_d^\infty(M) + k_f^2 p_d^\infty(M) = 0 \quad \text{if} \quad M \in \Omega_\infty \end{cases} \tag{D.15}$$

The problem is once again solved in the wavenumber domain. Following the same procedure as in section D.1, the pressures in Eq. (D.15) are written as a linear combination of Bessel and Hankel functions

$$\tilde{\tilde{p}}_d^1(r,n,k_x) = A_1 \frac{H_n(k_{pr}r)}{H_n(k_{pr}R)} + B_1 J_n(k_{pr}r) H_n(k_{pr}R_1) \quad \text{if} \quad r \leqslant R_1 \tag{D.16a}$$

$$\tilde{\tilde{p}}_d^\infty(r,n,k_x) = A_\infty \frac{H_n(k_r r)}{H_n(k_r R_1)} + B_\infty J_n(k_r r) H_n(k_r R_\infty) \quad \text{if} \quad r \geqslant R_1 \tag{D.16b}$$

$$\tilde{\tilde{p}}_i(r,n,k_x) = \begin{cases} \mathrm{j}\pi J_n(k_{pr}r_s) H_n(k_{pr}r) \mathrm{e}^{-\mathrm{j}(n\theta_s + k_x x_s)} & \text{if} \quad r_s \leqslant r \leqslant R_1 \\ \mathrm{j}\pi J_n(k_{pr}r) H_n(k_{pr}r_s) \mathrm{e}^{-\mathrm{j}(n\theta_s + k_x x_s)} & \text{if} \quad r \leqslant r_s \leqslant R_1 \end{cases} \tag{D.16c}$$

The procedure to obtain the expressions in Eq. (D.16c) is fully developed in [7]. The unknowns of this system, A_1, B_1, A_∞ and B_∞ can be obtained from the boundary conditions and continuity relations at the different interfaces. From the boundary conditions, as there is not wave reflection at infinity (i.e. Sommerfeld condition), B_∞ must necessarily be 0. The continuity of pressures and velocities at the interface $r = R_1$ yields

$$\tilde{\tilde{p}}_d^1(r = R_1, n, k_x) + \tilde{\tilde{p}}_i(r = R_1, n, k_x) = \tilde{\tilde{p}}_d^\infty(r = R_1, n, k_x) \tag{D.17a}$$

$$\frac{1}{\mathrm{j}\omega\rho_p} \left(\frac{\partial \tilde{\tilde{p}}_d^1}{\partial r}(r = R_1, n, k_x) + \frac{\partial \tilde{\tilde{p}}_i}{\partial r}(r = R_1, n, k_x) \right) = \frac{1}{\mathrm{j}\omega\rho_f} \frac{\partial \tilde{\tilde{p}}_d^\infty}{\partial r}(r = R_1, n, k_x) \tag{D.17b}$$

The radial component of the Euler equation allows expressing the continuity of radial velocities at the interface $r = R$

$$\frac{\partial \tilde{\tilde{p}}_d^1}{\partial r}(r = R, n, k_x) = -\frac{\partial \tilde{\tilde{p}}_i}{\partial r}(r = R, n, k_x) \tag{D.18}$$

Finally, a system similar to the one in Eq. (D.5) is solved to derive A_1, B_1 and A_∞

$$\begin{bmatrix} -1 & \dfrac{H_n(k_{pr}R_1)}{H_n(k_{pr}R)} & J_n(k_{pr}R_1) H_n(k_{pr}R_1) \\ -\dfrac{k_r}{\rho_f} \dfrac{H_n'(k_r R_1)}{H_n(k_r R_1)} & \dfrac{k_{pr}}{\rho_p} \dfrac{H_n'(k_{pr}R_1)}{H_n(k_{pr}R)} & \dfrac{k_{pr}}{\rho_p} J_n'(k_{pr}R_1) H_n(k_{pr}R_1) \\ 0 & k_{pr} \dfrac{H_n'(k_{pr}R)}{H_n(k_{pr}R)} & k_{pr} J_n'(k_{pr}R) H_n(k_{pr}R_1) \end{bmatrix} \begin{bmatrix} A_\infty \\ A_1 \\ B_1 \end{bmatrix} = \begin{bmatrix} -\mathrm{j}\pi J_n(k_{pr}r_s) H_n(k_{pr}R_1) \mathrm{e}^{-\mathrm{j}(n\theta_s + k_x x_s)} \\ -\mathrm{j}\pi \dfrac{k_{pr}}{\rho_p} J_n(k_{pr}r_s) H_n'(k_{pr}R_1) \mathrm{e}^{-\mathrm{j}(n\theta_s + k_x x_s)} \\ -\mathrm{j}\pi k_{pr} J_n'(k_{pr}R) H_n(k_{pr}r_s) \mathrm{e}^{-\mathrm{j}(n\theta_s + k_x x_s)} \end{bmatrix} \tag{D.19}$$

The blocked pressure at the surface of the shell can be obtained with the following expression

$$\tilde{\tilde{p}}_e(r=R,n,k_x) = A_1 + B_1 J_n(k_{pr}R)H_n(k_{pr}R_1) + \mathrm{j}\pi J_n(k_{pr}R)H_n(k_{pr}r_s)\mathrm{e}^{-\mathrm{j}(n\theta_s+k_x x_s)} \quad \text{(D.20)}$$

This expression can be injected in the spectral Flügge system recalled here

$$\tilde{\tilde{\mathcal{L}}}(k_x,n)\begin{bmatrix}\tilde{\tilde{U}}(k_x,n)\\ \tilde{\tilde{V}}(k_x,n)\\ \tilde{\tilde{W}}(k_x,n)\end{bmatrix} = \gamma\begin{bmatrix}0\\ 0\\ -\tilde{\tilde{p}}_e(k_x,n)-\tilde{\tilde{p}}(k_x,n)\end{bmatrix} \quad \text{(D.21)}$$

In order to obtain the radiated pressure $\tilde{\tilde{p}}$ at the surface of the shell, the spectral Euler relation introduced in Eq. (1.12) can be used, with $\tilde{\tilde{Z}}_f$ being the effective spectral impedance of the coating and the fluid medium explicited in Eq. (D.6). Following this, the spectral radial displacement of the shell can be derived

$$\tilde{\tilde{W}}_e(k_x,n) = \frac{\gamma\tilde{\tilde{p}}_e(k_x,n)\left(\tilde{\tilde{Z}}_{UU}(k_x,n)\tilde{\tilde{Z}}_{VV}(k_x,n)-\tilde{\tilde{Z}}^2_{UV}(k_x,n)\right)}{\Delta(k_x,n)} \quad \text{(D.22)}$$

where $\Delta(k_x,n)$ is given in Eq. (A.4). The displacement of the exterior coating surface is then obtained using the same expression as in Eq. (D.10)

$$\tilde{\tilde{W}}_e^{coat}(k_x,n) = \frac{k_{pr}}{\rho_p\omega^2}\left(A_1^{imp}\frac{H_n'(k_{pr}R_1)}{H_n(k_{pr}R)} + B_1^{imp}J_n'(k_{pr}R_1)H_n(k_{pr}R_1)\right)\tilde{\tilde{W}}_e(k_x,n) \quad \text{(D.23)}$$

The spectral radiated pressure $\tilde{\tilde{p}}$ can then be obtained inside the rubber thickness

$$\tilde{\tilde{p}}(r,n,k_x) = \left(A_1^{imp}\frac{H_n(k_{pr}r)}{H_n(k_{pr}R)} + B_1^{imp}J_n(k_{pr}r)H_n(k_{pr}R_1)\right)\tilde{\tilde{W}}_e(k_x,n), \quad \text{if} \quad r \leqslant R_1 \quad \text{(D.24)}$$

And in the surrounding fluid

$$\tilde{\tilde{p}}(r,n,k_x) = \frac{\rho_f\omega^2}{k_r}\frac{H_n(k_r r)}{H_n'(k_r R_1)}\tilde{\tilde{W}}_e^{coat}(k_x,n), \quad \text{if} \quad r \geqslant R_1 \quad \text{(D.25)}$$

And finally, the total pressure inside the rubber thickness is the sum of the spectral blocked pressure and the spectral radiated pressure inside the rubber thickness

$$\begin{aligned}\tilde{\tilde{p}}_{tot} = \tilde{\tilde{p}} + \tilde{\tilde{p}}_e = &\left(A_1^{imp}\frac{H_n(k_{pr}r)}{H_n(k_{pr}R)} + B_1^{imp}J_n(k_{pr}r)H_n(k_{pr}R_1)\right)\tilde{\tilde{W}}_e(k_x,n) + A_1\frac{H_n(k_{pr}r)}{H_n(k_{pr}R)}\\ &+ B_1 J_n(k_{pr}r)H_n(k_{pr}R_1) + \begin{cases}\mathrm{j}\pi J_n(k_{pr}r_s)H_n(k_{pr}r)\mathrm{e}^{-\mathrm{j}(n\theta_s+k_x x_s)} & \text{if} \quad r_s \leqslant r \leqslant R_1\\ \mathrm{j}\pi J_n(k_{pr}r)H_n(k_{pr}r_s)\mathrm{e}^{-\mathrm{j}(n\theta_s+k_x x_s)} & \text{if} \quad r \leqslant r_s \leqslant R_1\end{cases}\end{aligned} \quad \text{(D.26)}$$

And the total pressure in the surrounding fluid is the sum of the spectral blocked pressure and the spectral radiated pressure in the surrounding fluid

$$\tilde{\tilde{p}}_{tot} = \tilde{\tilde{p}} + \tilde{\tilde{p}}_e = \frac{\rho_f \omega^2}{k_r} \frac{H_n(k_r r)}{H_n'(k_r R_1)} \tilde{\tilde{W}}_e^{coat}(k_x, n) + A_\infty \frac{H_n(k_r r)}{H_n(k_{pr} R_1)}, \quad \text{if} \quad r \geqslant R_1 \tag{D.27}$$

D.4 Radiated pressure for a unit monopole located in the surrounding fluid

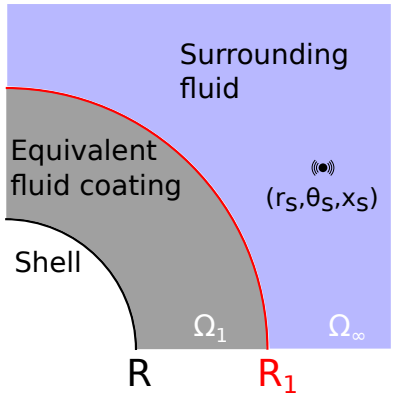

Figure 110: Monopole excitation in the surrounding fluid.

When the excitation is a unitary monopole placed in the surrounding fluid (see figure 110), the procedure is different than the one in section D.3. Indeed, the source is now placed in the surrounding fluid instead of inside the rubber thickness, leading to a different formulation to obtain the blocked pressure at the surface of the shell and in both domains. The Helmholtz equation in both media now yields

$$\begin{cases} \Delta p_e^1(M) + k_p^2 p_e^1(M) = 0 & \text{if} \quad M \in \Omega_1 \\ \Delta p_e^\infty(M) + k_f^2 p_e^\infty(M) = \delta_s & \text{if} \quad M \in \Omega_\infty \end{cases} \tag{D.28}$$

As the monopole source is situated in the surrounding fluid, the pressure in Ω_∞ can be decomposed into the sum of the incident pressure, p_i, and the diffracted pressure, p_d^∞ ($p_e^\infty = p_i + p_d^\infty$). Inside the rubber thickness, however, as there is no external source, the pressure corresponds to the diffracted pressure: $p_e^1 = p_d^1$. Eq. (D.28) can hence be rewritten

$$\begin{cases} \Delta p_d^1(M) + k_p^2 p_d^1(M) = 0 & \text{if} \quad M \in \Omega_1 \\ \Delta p_i(M) + k_f^2 p_i(M) = \delta_s \\ \Delta p_d^\infty(M) + k_f^2 p_d^\infty(M) = 0 & \text{if} \quad M \in \Omega_\infty \end{cases} \tag{D.29}$$

The problem is once again solved in the wavenumber domain, and the spectral pressures yield

$$\tilde{\tilde{p}}_d^1(r, n, k_x) = A_1 \frac{H_n(k_{pr} r)}{H_n(k_{pr} R)} + B_1 J_n(k_{pr} r) H_n(k_{pr} R_1) \quad \text{if} \quad r \leqslant R_1 \tag{D.30a}$$

$$\tilde{\tilde{p}}_d^{\infty}(r,n,k_x) = A_{\infty}\frac{H_n(k_r r)}{H_n(k_r R_1)} + B_{\infty}J_n(k_r r)H_n(k_r R_{\infty}) \quad \text{if} \quad r \geqslant R_1 \tag{D.30b}$$

$$\tilde{\tilde{p}}_i(r,n,k_x) = \begin{cases} \mathrm{j}\pi J_n(k_r r)H_n(k_r r_s)\mathrm{e}^{-\mathrm{j}(n\theta_s+k_x x_s)} & \text{if} \quad R_1 \leqslant r \leqslant r_s \\ \mathrm{j}\pi J_n(k_r r_s)H_n(k_r r)\mathrm{e}^{-\mathrm{j}(n\theta_s+k_x x_s)} & \text{if} \quad R_1 \leqslant r_s \leqslant r \end{cases} \tag{D.30c}$$

Using the continuity of pressures and velocities at the interface $r = R_1$ and the kinematic condition at the surface of the shell, the system to be solved now reads

$$\begin{bmatrix} -1 & \dfrac{H_n(k_{pr}R_1)}{H_n(k_{pr}R)} & J_n(k_{pr}R_1)H_n(k_{pr}R_1) \\ -\dfrac{k_r}{\rho_f}\dfrac{H_n'(k_r R_1)}{H_n(k_r R_1)} & \dfrac{k_{pr}}{\rho_p}\dfrac{H_n'(k_{pr}R_1)}{H_n(k_{pr}R)} & \dfrac{k_{pr}}{\rho_p}J_n'(k_{pr}R_1)H_n(k_{pr}R_1) \\ 0 & k_{pr}\dfrac{H_n'(k_{pr}R)}{H_n(k_{pr}R)} & k_{pr}J_n'(k_{pr}R)H_n(k_{pr}R_1) \end{bmatrix} \begin{bmatrix} A_{\infty} \\ A_1 \\ B_1 \end{bmatrix} = \begin{bmatrix} \mathrm{j}\pi J_n(k_r R_1)H_n(k_r r_s)\mathrm{e}^{-\mathrm{j}(n\theta_s+k_x x_s)} \\ \mathrm{j}\pi\dfrac{k_r}{\rho_f}J_n'(k_r R_1)H_n(k_r r_s)\mathrm{e}^{-\mathrm{j}(n\theta_s+k_x x_s)} \\ 0 \end{bmatrix} \tag{D.31}$$

The blocked pressure at the surface of the shell is then

$$\tilde{\tilde{p}}_e(r = R,n,k_x) = A_1 + B_1 J_n(k_{pr}R)H_n(k_{pr}R_1) \tag{D.32}$$

The displacements of the shell and of the exterior coating surface are the same than those in Eqs. D.22 and D.23, while the radiated pressure inside the rubber thickness and in the surrounding fluid are given by Eqs. D.26 and D.27. Hence, the total pressure inside the rubber thickness is

$$\begin{aligned} \tilde{\tilde{p}}_{tot} = \tilde{\tilde{p}} + \tilde{\tilde{p}}_e = &\left(A_1^{imp}\frac{H_n(k_{pr}r)}{H_n(k_{pr}R)} + B_1^{imp}J_n(k_{pr}r)H_n(k_{pr}R_1) \right)\tilde{\tilde{W}}_e(k_x,n) + A_1\frac{H_n(k_{pr}r)}{H_n(k_{pr}R)} \\ &+ B_1 J_n(k_{pr}r)H_n(k_{pr}R_1) \end{aligned} \tag{D.33}$$

While the total pressure in the surrounding fluid is

$$\begin{aligned} \tilde{\tilde{p}}_{tot} = \tilde{\tilde{p}} + \tilde{\tilde{p}}_e = &\frac{\rho_f\omega^2}{k_r}\frac{H_n(k_r r)}{H_n'(k_r R_1)}\tilde{\tilde{W}}_e^{coat}(k_x,n) + A_{\infty}\frac{H_n(k_r r)}{H_n(k_{pr}R_1)} \\ &+ \begin{cases} \mathrm{j}\pi J_n(k_{pr}r_s)H_n(k_{pr}r)\mathrm{e}^{-\mathrm{j}(n\theta_s+k_x x_s)} & \text{if} \quad R_1 \leqslant r_s \leqslant r \\ \mathrm{j}\pi J_n(k_{pr}r)H_n(k_{pr}r_s)\mathrm{e}^{-\mathrm{j}(n\theta_s+k_x x_s)} & \text{if} \quad R_1 \leqslant r \leqslant r_s \end{cases} \end{aligned} \tag{D.34}$$

D.5 Calculation of the CTFs of the global system 1+2

In subsection 5.1.1, two decoupling boundaries Ω_1 and Ω_2 were considered to compute the CTFs of the system 1+2. Ω_1 exhibits a single acoustic interface, while Ω_2 exhibits an acoustic and a vibroacoustic interface, which means that the CTFs must be computed in different ways whether Ω_1 or Ω_2 is considered.

D.5.1 Case of the decoupling boundary Ω_1 - acoustic interface alone

In order to compute the condensed impedance between two patches of system 1+2 when the decoupling boundary exhibits only acoustic interfaces, an acoustical excitation must be considered on the incident patch (i.e. an array of monopole sources), and the total scattered pressure at each point of the discretization of the receiving patch must be computed. To this end, the formulation when a unit monopole is located inside the rubber thickness, developed in Appendix D.3, must be considered. The total spectral pressure of Eq. (D.26) must be computed for every point in the incident patch j and every point in the receiving patch i. Then, for each spectral pressure obtained, corresponding to the spectral pressure at a single point due to a single monopole excitation, the pressure is computed in the physical space, by the means of a 2-D inverse Fourier transform

$$p_{tot}^{n_i n_j} = \frac{1}{2\pi} \sum_{n=-\infty}^{n=+\infty} \mathrm{e}^{\mathrm{j}n\theta_{n_i}} \int_{-\infty}^{+\infty} \tilde{\tilde{p}}_{tot}^{n_i n_j} \mathrm{e}^{\mathrm{j}k_x x_{n_i}} \, \mathrm{d}k_x \tag{D.35}$$

where $\tilde{\tilde{p}}_{tot}^{n_i n_j}$ is the total spectral pressure at the radius r_{n_i} of point n_i (for which the angular and axial position are θ_{n_i} and x_{n_i}, respectively) when the excitation is a unitary monopole located at point n_j, and $p_{tot}^{n_i n_j}$ is the associated physical quantity. The condensed impedance between these two patches is then obtained according to the procedure in section 4.1.2 by summing these values over the N_j points belonging to the incident patch j and the N_i points belonging to the receiving patch i

$$Z_{1+2}^{ij} = \sum_{n_i=1}^{N_i} \sum_{n_j=1}^{N_j} \frac{p_{tot}^{n_i n_j}}{\sqrt{\Omega_j \Omega_i}} \delta\xi_j \delta\xi_i \tag{D.36}$$

where Ω_j is the area of the incident patch, Ω_i is the area of the receiving patch, and $\delta\xi_j$ and $\delta\xi_i$ represent the discretization step in the incident and receiving patches, respectively. These last values depend on the plan in which the incident and receiving patches are placed (i.e. (r,θ), (r,x) or (θ,x)).

D.5.2 Case of the decoupling boundary Ω_2 - including a vibroacoustic interface

When the decoupling boundary Ω_2 is considered, a distinction must be made between the patches located on an acoustic interface and those located on a vibroacoustic interface. The CTF matrix $\mathbf{H_{1+2}}$ will hence be divided into 4 sub-matrices according to Eq. (5.1). The CTFs are then computed by considering an acoustical excitation when the incident patch is located on an acoustic interface, and a mechanical excitation when the incident patch is located on a vibroacoustic interface.

D.5.2.1 CTFs for an acoustical excitation

When the incident patch is located on an acoustic interface, the excitation is acoustical and the CTFs that are computed are $\mathbf{H_{1+2}^{u_a \delta u_b}}$ and $\mathbf{H_{1+2}^{p_b \delta u_b}}$. The calculation of $\mathbf{H_{1+2}^{p_b \delta u_b}}$ is the same than for $\mathbf{Z_{1+2}}$ in Appendix D.5.1, and the CTF is

$$H_{1+2}^{p_b \delta u_b, ij} = \sum_{n_i=1}^{N_i} \sum_{n_j=1}^{N_j} \frac{p_{tot}^{n_i n_j}}{\sqrt{\Omega_j \Omega_i}} \delta\xi_j \delta\xi_i \tag{D.37}$$

As for $\mathbf{H_{1+2}^{u_a \delta u_b}}$, the spectral radial displacement of the shell must be obtained for each point of the discretization of the receiving patch from Eq. (D.22), for all the monopoles placed on the incident patch. Then, the radial displacement of the shell in the physical space is obtained by the means of a 2-D inverse Fourier transform

$$W_e^{n_i n_j} = \frac{1}{2\pi} \sum_{n=-\infty}^{n=+\infty} \mathrm{e}^{\mathrm{j}n\theta_{n_i}} \int_{-\infty}^{+\infty} \tilde{\tilde{W}}_e^{n_i n_j} \mathrm{e}^{\mathrm{j}k_x x_{n_i}} \, \mathrm{d}k_x \tag{D.38}$$

where $\tilde{\tilde{W}}_e^{n_i n_j}$ is the shell's spectral radial displacement at point n_i when the excitation is a unitary monopole located at point n_j, and $W_e^{n_i n_j}$ is the associated physical quantity. The CTF between the incident patch j and the receiving patch i is then obtained by summing these values over the N_j points belonging to the incident patch j and the N_i points belonging to the receiving patch i

$$H_{1+2}^{u_a \delta u_b, ij} = \sum_{n_i=1}^{N_i} \sum_{n_j=1}^{N_j} \frac{\mathrm{j}\omega W_e^{n_i n_j}}{\sqrt{\Omega_j \Omega_i}} \delta\xi_j \delta\xi_i \tag{D.39}$$

D.5.2.2 CTFs for a mechanical excitation

When the incident patch is located on a vibroacoustic interface, the excitation is mechanical and the CTFs that are computed are $\mathbf{H_{1+2}^{u_a \delta p_a}}$ and $\mathbf{H_{1+2}^{p_b \delta p_a}}$. The formulation to derive the

spectral radial displacement of the shell and the spectral radiated pressure is developed in Appendix D.2.

To obtain $\mathbf{H}_{1+2}^{\mathbf{u_a}\delta\mathbf{p_a}}$, the spectral radial displacement of the shell from a mechanical excitation must be obtained for each point of the discretization of the receiving patch using Eq. (D.9), for all the mechanical point forces placed on the incident patch. Then, the radial displacement of the shell in the physical space is obtained by the means of a 2-D inverse Fourier transform

$$W_F^{n_i n_j} = \frac{1}{2\pi} \sum_{n=-\infty}^{n=+\infty} \mathrm{e}^{\mathrm{j}n\theta_{n_i}} \int_{-\infty}^{+\infty} \tilde{\tilde{W}}_F^{n_i n_j} \mathrm{e}^{\mathrm{j}k_x x_{n_i}} \, \mathrm{d}k_x \tag{D.40}$$

where $\tilde{\tilde{W}}_F^{n_i n_j}$ is the shell's spectral radial displacement at point n_i when the excitation is a mechanical point force located at point n_j, and $W_F^{n_i n_j}$ is the associated physical quantity. The CTF between the incident patch j and the receiving patch i is then obtained by summing these values over the N_j points belonging to the incident patch j and the N_i points belonging to the receiving patch i

$$H_{1+2}^{u_a \delta p_a, ij} = \sum_{n_i=1}^{N_i} \sum_{n_j=1}^{N_j} \frac{\mathrm{j}\omega W_F^{n_i n_j}}{\sqrt{\Omega_j \Omega_i}} \delta\xi_j \delta\xi_i \tag{D.41}$$

As for $\mathbf{H}_{1+2}^{\mathbf{p_b}\delta\mathbf{p_a}}$, the spectral radiated pressure from a mechanical excitation must be obtained for each point of the discretization of the receiving patch using Eq. (D.11), for all the mechanical point forces placed on the incident patch. Then, the radiated pressure in the physical space is obtained by the means of a 2-D inverse Fourier transform

$$p_F^{n_i n_j} = \frac{1}{2\pi} \sum_{n=-\infty}^{n=+\infty} \mathrm{e}^{\mathrm{j}n\theta_{n_i}} \int_{-\infty}^{+\infty} \tilde{\tilde{p}}_F^{n_i n_j} \mathrm{e}^{\mathrm{j}k_x x_{n_i}} \, \mathrm{d}k_x \tag{D.42}$$

where $\tilde{\tilde{p}}_F^{n_i n_j}$ is the spectral radiated pressure at point n_i when the excitation is a mechanical point force located at point n_j, and $p_F^{n_i n_j}$ is the associated physical quantity. The CTF between the incident patch j and the receiving patch i is then obtained by summing these values over the N_j points belonging to the incident patch j and the N_i points belonging to the receiving patch i

$$H_{1+2}^{p_b \delta p_a, ij} = \sum_{n_i=1}^{N_i} \sum_{n_j=1}^{N_j} \frac{p_F^{n_i n_j}}{\sqrt{\Omega_j \Omega_i}} \delta\xi_j \delta\xi_i \tag{D.43}$$

D.6 Calculation of the condensed pressures and condensed radial velocities of the global system 1+2

In order to compute the condensed pressures and condensed radial velocities of the system 1+2, it is necessary to develop the formulation when the external excitation (i.e. mechanical point force) is considered (to compute $\mathbf{\Lambda_{1+2}}$) and when a monopole excitation is considered (to compute $\mathbf{\Lambda^{M}_{1+2}}$).

D.6.1 Condensed pressures and radial velocities from a mechanical excitation

When the excitation is the external mechanical force, the procedure to compute the condensed pressures and condensed radial velocities is close to the one described in Appendix D.5.2.2. The spectral radial displacement of the shell is hence given by Eq. (D.9). The radial displacement of the shell in the physical space at each point of the receiving patch i is then obtained by the means of a 2-D inverse Fourier transform

$$W_F^{n_i} = \frac{1}{2\pi} \sum_{n=-\infty}^{n=+\infty} \mathrm{e}^{\mathrm{j}n\theta_{n_i}} \int_{-\infty}^{+\infty} \tilde{\tilde{W}}_F^{n_i} \mathrm{e}^{\mathrm{j}k_x x_{n_i}} \, \mathrm{d}k_x \tag{D.44}$$

where $\tilde{\tilde{W}}_F^{n_i}$ is the shell's spectral radial displacement at point n_i when the excitation is the external mechanical point force, and $W_F^{n_i}$ is the associated physical quantity. The condensed radial velocity at the receiving patch i is then obtained by summing these values over the N_i points belonging to that patch

$$U_{1+2}(i) = \sum_{n_i=1}^{N_i} \frac{\mathrm{j}\omega W_F^{n_i}}{\sqrt{\Omega_i}} \delta\xi_i \tag{D.45}$$

As for the condensed pressures when the excitation is the external mechanical point force, the spectral radiated pressure in Eq. (D.11) must be used. The radiated pressure in the physical space at each point of the receiving patch i is then obtained by the means of a 2-D inverse Fourier transform

$$p_F^{n_i} = \frac{1}{2\pi} \sum_{n=-\infty}^{n=+\infty} \mathrm{e}^{\mathrm{j}n\theta_{n_i}} \int_{-\infty}^{+\infty} \tilde{\tilde{p}}_F^{n_i} \mathrm{e}^{\mathrm{j}k_x x_{n_i}} \, \mathrm{d}k_x \tag{D.46}$$

where $\tilde{\tilde{p}}_F^{n_i}$ is the spectral radiated pressure at point n_i when the excitation is the external mechanical point force, and $p_F^{n_i}$ is the associated physical quantity. The condensed pressure at the receiving patch i is then obtained by summing these values over the N_i points belonging to that patch

$$P_{1+2}(i) = \sum_{n_i=1}^{N_i} \frac{p_F^{n_i}}{\sqrt{\Omega_i}} \delta\xi_i \tag{D.47}$$

D.6.2 Condensed pressures and radial velocities from a monopole excitation

When the excitation is a unit monopole located in the surrounding fluid at point M, the condensed pressures and radial velocities will be calculated by using the developments in Appendix D.4. The spectral radial displacement of the shell is obtained from Eq. (D.22) (when considering a spectral blocked pressure at the surface of the shell induced by a monopole located in the surrounding fluid). The radial displacement of the shell in the physical space at each point of the receiving patch i is then obtained by the means of a 2-D inverse Fourier transform

$$W_e^{n_i} = \frac{1}{2\pi} \sum_{n=-\infty}^{n=+\infty} \mathrm{e}^{\mathrm{j}n\theta_{n_i}} \int_{-\infty}^{+\infty} \tilde{\tilde{W}}_e^{n_i} \mathrm{e}^{\mathrm{j}k_x x_{n_i}} \, \mathrm{d}k_x \tag{D.48}$$

where $\tilde{\tilde{W}}_e^{n_i}$ is the shell's spectral radial displacement at point n_i when the excitation is a unit monopole located at point M, and $W_e^{n_i}$ is the associated physical quantity. The condensed radial velocity at the receiving patch i is then obtained by summing these values over the N_i points belonging to that patch

$$U_{1+2}^M(i) = \sum_{n_i=1}^{N_i} \frac{\mathrm{j}\omega W_e^{n_i}}{\sqrt{\Omega_i}} \delta\xi_i \tag{D.49}$$

As for the condensed pressures when the excitation is a unit monopole located in the surrounding fluid at point M, the spectral radiated pressure in Eq. (D.33) must be used. The radiated pressure in the physical space at each point of the receiving patch i is then obtained by the means of a 2-D inverse Fourier transform

$$p_{tot}^{n_i} = \frac{1}{2\pi} \sum_{n=-\infty}^{n=+\infty} \mathrm{e}^{\mathrm{j}n\theta_{n_i}} \int_{-\infty}^{+\infty} \tilde{\tilde{p}}_{tot}^{n_i} \mathrm{e}^{\mathrm{j}k_x x_{n_i}} \, \mathrm{d}k_x \tag{D.50}$$

where $\tilde{\tilde{p}}_{tot}^{n_i}$ is the spectral radiated pressure at point n_i when the excitation is a unit monopole located at point M, and $p_{tot}^{n_i}$ is the associated physical quantity. The condensed pressure at the receiving patch i is then obtained by summing these values over the N_i points belonging to that patch

$$P_{1+2}^M(i) = \sum_{n_i=1}^{N_i} \frac{p_{tot}^{n_i}}{\sqrt{\Omega_i}} \delta\xi_i \tag{D.51}$$

Appendix E

Résumé étendu en français

E.1 Contexte de l'étude

Le travail présenté dans cette thèse est le fruit d'une collaboration entre Naval Group, industriel français spécialisé dans le naval de défense, et le Laboratoire Vibrations Acoustique (LVA) de l'INSA de Lyon.

Dans un contexte industriel naval, il est primordial de maîtriser au mieux les performances vibroacoustiques des coques de véhicules sous-marins, et ce dès les premières phases d'étude. Dans le domaine militaire, limiter au maximum le bruit émis par ces véhicules constitue un enjeu d'une importance capitale, et les performances des antennes sonar actuelles impliquent de pouvoir étudier ces systèmes sur une large bande de fréquence. Cela se traduit en termes de capacités opérationnelles par :

- la discrétion acoustique : lorsque la coque est soumise à une excitation mécanique ou acoustique en son intérieur, le bruit émis dans le milieu environnant peut être capté par des sonars passifs qui écoutent la mer grâce à une antenne d'hydrophones.

- l'index de cible : lorsque la coque est soumise à une excitation acoustique venant de l'extérieur, les vibrations induites par cette excitation rayonnent et peuvent être captées par des sonars actifs.

- les performances sonar : les coques de véhicules sous-marins sont généralement équipées d'une antenne sonar, dont les performances dépendent d'un ratio signal sur bruit, qui peut être perturbé par les turbulences générées par le déplacement du véhicule, ou par les excitations internes à la coque (bruit propre).

Afin de maximiser ces performances opérationnelles, des matériaux viscoélastiques, dit revêtements, peuvent être appliqués sur la surface de la coque. Il se séparent en deux grandes catégories. D'un côté, les matériaux de masquage isolent la coque du milieu extérieur en minimisant le bruit rayonné par la coque, permettant de se protéger contre les sonars passifs

et de limiter le bruit propre. D'un autre côté, les matériaux anéchoïques ont pour fonction d'absorder les ondes venant de l'extérieur afin de se protéger contre les sonars actifs. L'étude de ces différents matériaux, ainsi que des coques revêtues, ont fait l'objet de nombreux travaux dans la littérature depuis des décennies. En revanche, beaucoup moins d'attention a été portée à l'étude de coques partiellement revêtues. Comparée à une coque intégralement revêtue, la perte de l'axisymétrie induite par le revêtement partiel entraîne un couplage des ordres circonférentiels de la coque immergée, ce qui empêche l'application des méthodes semi-analytiques généralement utilisées pour étudier des coques cylindriques. En outre, les méthodes numériques à éléments, pouvant en théorie être utilisée afin d'étudier des systèmes à géométrie non-triviale, sont limitées en fréquences du fait de leur important coût numérique, et ne sont par conséquent pas viables dans un contexte industriel au delà de quelques Hz. Pourtant, pouvoir modéliser des coques cylindrique partiellement revêtues peut présenter un grand intérêt pour étudier l'impact de tuiles manquantes, d'une configuration où plusieurs types de revêtements sont appliqués simultanément sur la coque, ou bien d'un mauvais jointement des tuiles, sur les différentes capacités opérationnelles du véhicule sous-marin.

Le but de cette thèse est donc de développer une méthode permettant, à terme, de modéliser des coques cylindriques partiellement revêtues, sur une large gamme de fréquences, tout en ayant un coût numérique raisonnable. En se basant sur la méthode des fonctions de transfert condensées (Condensed Transfer Function, CTF), fruit d'une précédente collaboration entre l'INSA de Lyon et Naval Group, une approche de modélisation vibroacoustique soustractive est proposée : la méthode des fonctions de transfert condensées inversée (reverse Condensed Transfer Function, rCTF). Cette méthode a pour but de modéliser la coque partiellement revêtue un partant d'un modèle de la coque intégralement revêtue, auquel est retiré un modèle de la zone manquante du revêtement, qui est ensuite remplacé par de l'eau.

Après une première étude de la littérature concernant trois domaines en lien avec le sujet de thèse (le rayonnement des coques cylindriques, la modélisation de matériaux acoustiques pour des applications navales, et les méthodes numériques en vibroacoustique), une première étude sur un cas de modélisation soustractive a été réalisée et sera décrite dans le prochain paragraphe.

E.2 Modélisation soustractive sur un système mécanique en une dimension

Dans un premier temps, une étude de modélisation soustractive est menée sur un cas test académique : le découplage de poutres en traction-compression. Le but de cette étude préliminaire est d'obtenir une vision initiale du potentiel de la modélisation soustractive, de sa sensibilité numérique, et de la faisabilité de sa mise en œuvre sur des cas plus complexes.

L'attention est ici portée sur l'estimation des réceptances (c'est-à-dire le déplacement en un point *i* de la poutre lorsqu'elle est excitée par une force harmonique ponctuelle en un point *j*) d'une poutre "cible", à partir des réceptances d'une grande poutre (la poutre "maîtresse") et de celles d'une petite poutre que l'on retire (la poutre "soustraite"). Afin d'avoir une vision nette du problème, le lecteur peut se référer aux figures 13 et 15.

Dans un premier temps, les investigations sont menées sur une approche "locale" du problème, c'est-à-dire que la poutre maîtresse est désassemblée à l'une de ses extrémités par la poutre soustraite, faisant ainsi apparaître un unique point de découplage. En partant du problème direct, à savoir le couplage de la poutre soustraite et de la poutre cible, les réceptances de la poutre maîtresse peuvent être obtenues. Elles sont ensuite inversées afin d'obtenir les réceptances de la poutre cible à partir de celles de la poutre maîtresse et de la poutre soustraite. Une fois le formalisme théorique établi, une étude numérique est menée afin de mettre en application ce cas de modélisation soustractive. Afin de calculer les réceptances des 2 poutres initiales (à savoir la poutre maîtresse et la poutre soustraite), plusieurs possibilités peuvent être envisagées : une formulation analytique (basée sur une méthode de décomposition en ondes forcées), et une modélisation par éléments finis (FEM). Afin de coller au mieux aux applications potentielles de la modélisation soustractive (consistant en la perturbation d'un modèle semi-analytique par un modèle numérique dans le cas de la coque partiellement revêtue), il a été choisi d'étudier ce système en considérant une formulation analytique pour calculer les réceptances de la poutre maîtresse, et un calcul FEM pour les réceptances de la poutre soustraite. La première comparaison entre les réceptances au point de découplage de la poutre cible obtenue via la méthode de découplage et celles de la poutre cible calculées par une formulation analytique montre des résultats globalement très bon sur tout le domaine fréquentiel étudié (entre 100 et 10000 Hz), sauf au niveau de 3 tranches fréquentielles. Après une analyse des erreurs par petites variations permettant d'estimer les cas critiques pour lesquels des erreurs sont le plus susceptibles d'être commises lors du procédé de découplage, il a apparaît que deux cas semblent particulièrement critiques : lorsque les erreurs de modèle sur les réceptances de la poutre soustraite (estimées par FEM) sont importantes, et lorsque les réceptances de la poutre soustraite sont proches de celles de la poutre maîtresse. En traçant ces deux conditions, on observe qu'elles sont toutes deux réunies aux fréquences d'anti-résonance de la poutre soustraite, et que c'est bien dans ces domaines fréquentiels que les erreurs dues au découplage sont les plus importantes. Des études supplémentaires ont ensuite montré que les erreurs peuvent être atténuées en diminuant la taille de la poutre soustraite (car cela fera apparaître moins de résonances et d'anti-résonances dans la gamme de fréquence, ce qui limitera les domaines où les deux conditions critiques sont réunies), ainsi qu'en augmentant l'amortissement structurel du

matériau composant les poutres (car cela a notamment pour effet de diminuer l'amplitude des anti-résonances, et ainsi de limiter les croisements entre les réceptances des deux poutres initiales).

Dans un deuxième temps, une approche de découplage "globale" est étudiée. Le désassemblage de la poutre maîtresse par la poutre soustraite se fait maintenant à une position intermédiaire de la poutre maîtresse, ce qui fait donc apparaître deux points de découplage (voir figure 22). Il est important de souligner que l'on ne s'intéresse ici, en termes de découplage, qu'au comportement de la poutre cible au même point que pour l'approche locale, et que le comportement de la poutre supérieure restante suite au découplage ne fait pas partie du domaine d'intérêt de cette étude. Cette poutre restante sera donc nommée poutre "résiduelle". Contrairement à l'approche locale, où les équations faisaient apparaître une formulation ponctuelle, les deux point de découplage de l'approche globale entraînent nécessairement une formulation matricielle, avec des matrices de réceptances qui font apparaître le calcul des réceptances aux deux points de découplage. Les résultats du découplage via cette approche globale semblent meilleurs que pour l'approche locale, avec un seul domaine d'erreurs (contre trois précédemment), qui semble cette fois-ci apparaître à l'unique résonance dans la poutre soustraite dans le domaine fréquentiel considéré. Si l'on pourrait penser que cette différence avec l'approche locale vient du fait que le découplage ne se fait pas à l'extrémité de la poutre maîtresse (contrairement à ce qui avait été fait précédemment), il apparaît que c'est la nature du problème qui différencie les deux méthodes. En effet, une étude asymptotique où la longueur de la poutre résiduelle est progressivement réduite jusqu'à atteindre 0 m montre que le comportement du découplage global reste le même, à savoir, les erreurs suite au découplage apparaissent à la fréquence de résonance de la poutre soustraite. Le découplage asymptotique de la méthode globale, qui correspond en théorie au même découplage que celui de l'approche locale, montre que les erreurs ont été grandement réduites dans ce cas par rapport à l'approche locale, ce qui souligne une robustesse plus importante de l'approche globale par rapport à l'approche locale. Suite à cette conclusion, il est donc proposé un processus d'optimisation du découplage, où la taille de la poutre soustraite est réduite (ce qui veut dire que le deuxième point de découplage est rapproché du premier point de découplage), afin d'éliminer toute résonance de la poutre soustraite dans le domaine fréquentiel. Le résultat obtenu suite à cette optimisation est excellent et montre aussi un intérêt dans le fait que, la structure soustraite étant plus petite, une modélisation plus fine de son modèle FEM est possible sans que cela n'ait un impact trop important sur le temps de calcul. Les études menées dans ce chapitre ont donc permis de mettre en lumière les potentiels avantages et inconvénients de la modélisation soustractive, et l'approche globale de modélisation soustractive permet d'envisager avec optimisme l'application à des cas plus

complexes.

E.3 Modélisation soustractive sur un système vibroacoustique complexe : principe de la méthode des fonctions de transfert condensées inversée (rCTF)

Dans ce chapitre, le formalisme théorique de la méthode rCTF est développé pour le découplage de deux systèmes acoustiques, en partant de la formulation de couplage de la méthode CTF pour un problème acoustique. Le principe de la méthode CTF directe est illustré sur la figure 29. Un set de fonction orthonormales, appelé fonctions de condensation, est défini sur la surface de couplage Ω entre les sous-systèmes. Les pressions et vitesses normales à la surface Ω pour les deux sous-systèmes sont ensuite décomposées en une combinaison linaire des fonctions de condensations. On peut désigner comme quantité condensée (i.e. pression ou vitesse normale) la projection de cette quantité sur une fonction de condensation au niveau de la surface Ω. Les fonctions de transfert condensées (CTFs), qui seront dans ce cas des impédances condensées, sont ensuite définies comme le rapport d'une pression condensée sur une vitesse normale condensée, pour toutes les combinaisons possibles dans l'ensemble des fonctions de condensation. Par la suite, l'utilisation d'un principe de superposition, de continuité des pression et d'équilibre des vitesses normales permet ensuite d'en déduire les vitesses de couplage entre les deux sous-systèmes, puis de déduire la pression en n'importe quel point du système couplé. Partant de cette équation, on peut alors étudier le problème inverse de découplage décrit par la figure 30, qui consiste en l'obtention d'un sous-système cible à partir d'un système global et d'un sous-système soustrait. A partir d'un principe de réciprocité, on peut calculer le vecteur des impédances condensées ponctuelles du sous-système cible. Ensuite, en considérant un saut de vitesse normale à la surface Ω du système global, on peut obtenir les impédances condensées du système global à partir de celles des sous-systèmes soustrait et cible, avant d'inverser l'équation pour déduire les impédances condensées du sous-système cible via la formule suivante:

$$\mathbf{Z_1} = \mathbf{Z_2} \left(\mathbf{Z_2} - \mathbf{Z_{1+2}}\right)^{-1} \mathbf{Z_{1+2}} \tag{E.1}$$

La pression en n'importe quel point du sous-système cible 1 peut ensuite être obtenue à partir d'informations concernant uniquement les systèmes connus, à savoir le système global 1+2 et le sous-système soustrait 2:

$$\tilde{p}_1(M_1) = p_{1+2}(M_1) + \left(\mathbf{I} + \mathbf{Z_2} \left(\mathbf{Z_2} - \mathbf{Z_{1+2}}\right)^{-1} \mathbf{Z_{1+2}} \mathbf{Z_2}^{-1}\right) \mathbf{P}_{\mathbf{1+2}}^{\mathbf{M_1}} \mathbf{Z_2}^{-1} \mathbf{P_{1+2}} \tag{E.2}$$

Il est important de souligner que cette expression constitue le principal résultat théorique

de la méthode rCTF.

La méthode rCTF est ensuite appliquée à un cas test qui consiste en la diffraction d'une onde plane acoustique par une sphère rigide immergée dans un milieu fluide infini (figure 31). Le problème est étudié sous une forme locale puis sous une forme globale suite aux investigations du chapitre précédent, en considérant un milieu fluide infini (système global) auquel on enlève une sphère pleine (dans le cas de la forme locale) ou creuse (dans le cas de la forme globale) qui correspond au sous-système soustrait. Deux types de fonctions de condensation sont envisagés (pour lesquelles un critère de convergence est défini) : les harmoniques sphériques pondérées, qui par leur propriétés découplent les différentes fonctions de transfert condensées en présentant des matrices diagonales, et les pavés, qui correspondent à des fonctions portes 2D. Les impédances condensées sont calculées à partir de modèles analytiques afin d'avoir une première validation numérique de la méthode sur un cas complexe. En étudiant dans un premier temps le découplage local des impédances condensées (qui correspond à l'équation E.1), il apparaît que les résultats sont excellent sauf à la fréquence d'anti-résonance du sous-système soustrait (la sphère d'eau), mais cet écart peut être corrigé en ajoutant un faible amortissement dans le milieu. Concernant le découplage global des impédances, les résultats sont bien moins bons que ce qui était attendu, notamment à cause de la présence de résonances et d'anti-résonances dans la circonférence du sous-système soustrait (la sphère d'eau creuse) qui n'avaient pas été anticipées. Cependant, en considérant une sphère creuse où le second interface de découplage (i.e. la surface interne de la sphère creuse) est rapproché du centre de la sphère, les résultats sont bien meilleurs et se rapprochent des résultats obtenus avec la méthode globale. Ces impressions sont ensuite confirmées lorsque l'on cherche à obtenir la pression en n'importe quel point du sous-système cible (correspondant à l'équation E.2), en comparant les résultats de la méthode rCTF à un calcul théorique basé sur une décomposition du champ de pression diffracté sur les harmoniques sphériques. Les investigations menées dans ce chapitre ont donc permis de valider la méthode rCTF d'un point du vue numérique en considérant des modèles analytiques pour le calcul des impédances condensées, mais les études menées à ce stade ne permettent pas encore de conclure sur l'intérêt de la méthode globale par rapport à la méthode locale.

E.4 Sensibilité numérique de la méthode des fonctions de transfert condensées inversée

Après avoir été validée, la méthode rCTF est soumise à des erreurs de modèle afin d'en étudier la sensibilité. En effet, si dans le chapitre précédent, les impédances condensées ont été calculées en considérant des modèles analytiques, l'application à des systèmes industriels

requiert de pouvoir appliquer cette méthode en considérant des modèles numériques. Ainsi, dans un premier temps, le processus pour calculer les fonctions de transfert condensées à partir de modèles numériques est décrit en détails, en prenant les pavés décrits au chapitre précédent comme fonctions de condensation.

Pour les systèmes bornés, une formulation FEM est considérée. A partir des matrices de masse et de raideur du système, la matrice dynamique du système peut être obtenue. En associant les nœuds du modèle FEM à leur pavé correspondant, on peut alors définir des excitations correspondant aux fonctions de condensation en excitant seulement les nœuds appartenant au pavé considéré. La matrice dynamique est ensuite inversée, ce qui permet d'obtenir la pression résultante à tous les nœuds du modèle FEM, et de sommer les pressions sur les nœuds du pavé récepteur afin de déduire l'impédance condensée considérée. Concernant les systèmes non bornés, une formulation de Green dérivée de la formulation BEM indirecte est considérée. La surface fictive de découplage est discrétisée en un certain nombre de points qui sont, comme dans le cas du modèle FEM, associés au pavé auquel ils appartiennent. L'excitation est ensuite définie par une couche de sources monopolaires définissant le potentiel de simple couche (et représentant un saut de vitesse normale à la traversée de la surface), placées aux points de discrétisation de la surface de découplage. Les pavés sont donc excités tour à tour grâce aux monopoles les composant, et la réponse aux pavés récepteurs est obtenue grâce à la fonction de Green du système entre les différents points appartenant aux pavés incident et récepteur.

Ces formulations sont ainsi appliquée au cas test du chapitre précédent, à savoir la diffraction de l'onde plane acoustique par une sphère rigide dans un milieu fluide infini. Les impédances condensées du milieu infini sont donc calculées en utilisant la formulation de Green pour les systèmes non bornés, tandis que les impédances condensées de la sphère d'eau pleine (pour la forme locale) et de la sphère d'eau creuse (pour la forme globale) sont calculées en utilisant la formulation FEM pour les systèmes bornés. Dans un premier temps, les impédances condensées du système global et du sous-système soustrait obtenues grâce aux modèles numériques sont comparées à celles obtenues avec une formulation analytique au chapitre précédent. Il apparaît que les modèles FEM des 2 sous-systèmes soustraits doivent être suffisamment précis afin de décrire correctement les résonances et anti-résonances du système, ce qui est crucial dans la mesure où il avait été identifié que ces fréquences sont moins bien conditionnées et plus à même d'être sujettes à des erreurs lorsque les calculs de découplage seront menés. Pour le système global, les calculs sont également plus précis lorsque la discrétisation est plus fine, et l'impact de ces différences de résultats entre une discrétisation fine et une moins contraignante sera évalué lors des calculs de découplages, tant en termes de précision des résultats que de coût numérique.

Dans un premier temps, la sensibilité de la méthode rCTF est évaluée pour le cas du découplage des impédances condensées de l'équation E.1, pour les formes locale et globale du problème. Il apparaît que, pour la forme locale, des erreurs surviennent notamment autour de la fréquence d'anti-résonance de la sphère d'eau, ce qui était anticipé suite aux résultats observés dans les chapitres précédents. De plus, la discrétisation plus ou moins fine de la surface de découplage pour le calcul des impédances condensées du système global ne semble pas avoir un réel impact sur le résultat du découplage. Concernant la forme globale, les erreurs ne sont pas localisées à des fréquences particulières mais sont plus constantes dans le domaine fréquentiel. Là encore, une discrétisation plus fine pour le système global ne semble pas réellement améliorer les résultats. Par la suite, la pression en un point quelconque du sous-système cible est évaluée avec l'équation E.2. Les résultats pour la forme locale du problème font apparaître des erreurs qui n'étaient pas présentes lorsque les modèles analytiques étaient considérés, mais sont globalement largement acceptables dans la majorité du domaine fréquentiel et du milieu fluide infini, dans la mesure où les maxima et minima de pression sont correctement localisés, mêmes aux fréquences où les plus grosses erreurs sont commises. De plus, la discrétisation plus fine pour le système global ne semble, là encore, pas avoir un rôle prépondérant dans les résultats obtenus. Pour la forme globale en revanche, cette discrétisation joue un rôle plus important, dans la mesure où une discrétisation plus fine de la surface de découplage permet d'obtenir de bien meilleurs résultats. Cependant, ce gain en précision est contrebalancé par une augmentation très conséquente des coûts de calcul, ce qui est résumé dans le tableau 5. Par conséquent, et dans la mesure où les résultats obtenus avec la forme locale sont satisfaisants, c'est cette dernière qui est choisi pour l'application finale de la méthode rCTF sur la coque cylindrique partiellement revêtue.

E.5 Rayonnement acoustique d'une coque cylindrique partiellement revêtue avec la méthode rCTF

Finalement, la méthode rCTF est appliquée dans le cas de la coque cylindrique partiellement revêtue dans le dernier chapitre. Pour cela, un modèle de la coque intégralement revêtue est considéré, dans lequel le revêtement est modélisé comme un fluide équivalent. Si les calculs sont présentés dans un cas général 3D, ils sont menés sur des modèles 2D, ce qui permet d'avoir un cas de référence grâce à un calcul FEM qui ne serait pas possible avec des modèle 3D. Les fonctions de transfert condensées à la surface de découplage de la coque intégralement revêtue sont calculées en utilisant une formulation semi-analytique qui est menée dans le domaine spectral, c'est-à-dire après une transformée de Fourier suivant l'axe de la coque, et une décomposition en séries de Fourier suivant la circonférence de la coque (qui se réduit à une décomposition en séries de Fourier suivant la circonférence de la coque

dans le cas 2D). Les équations sont ensuite résolues pour la composante radiale du problème. Les fonctions de condensations considérées sont donc des fonctions portes, et l'interface de découplage est divisée en segments. Contrairement aux cas d'étude précédent, cette interface fait apparaître une frontière vibroacoustique, à la frontière entre la coque et le revêtement. Afin de prendre en compte cette frontière, deux possibilités sont envisagées. La première est de décaler très légèrement cette frontière à l'intérieur du revêtement, afin de ne garder qu'une interface acoustique. La deuxième possibilité est de considérer cette interface vibroacoustique telle quelle, ce qui fera apparaître différents types de fonctions de transfert condensées car les excitations et inconnues à cette interface seront mécaniques. Ces fonctions de transfert condensées sont calculées en considérant la formulation de Green développée au chapitre précédent, en discrétisant l'interface de découplage pour définir des couches de monopoles (ou de forces ponctuelles dans le cas de la frontière vibroacoustique). Les comparaisons entre la formulation spectrale et le calcul FEM de référence montrent que les fonctions de transfert condensées ont été correctement calculées. Les impédances condensées du sous-système soustrait, à savoir la tuile de revêtement manquante, sont elles calculées à partir d'un modèle FEM. Si la frontière vibroacoustique doit être prise en compte, ces impédances condensées sont converties afin de faire correctement correspondre les différentes interfaces.

Les calculs de découplage de la méthode rCTF sont ensuite menés pour prédire le rayonnement acoustique de la coque cylindrique à laquelle une partie du revêtement a été retirée et remplacée par un écran rigide, et les résultats sont comparés au calcul FEM de référence. Une formulation vibroacoustique est également développée afin de prendre en compte la frontière vibroacoustique. Les premiers résultats montrent que le découplage fait apparaître de nombreuses erreurs, notamment dans le domaine des basses fréquences, et surtout lorsque le point examiné est proche de la frontière de découplage. De plus les résultats avec la formulation vibroacoustique semblent moins précis que ceux de la formulation acoustique. Parmi les pistes envisagées afin d'améliorer les résultats du découplage, un test est dans un premier temps réalisé en ne retirant qu'une moitié de l'épaisseur du revêtement, qui n'est pas directement collée à la coque. Les résultats obtenus sont excellents et une étude paramétrique sur la fraction d'épaisseur retirée est ainsi conduite. Il en résulte que, particulièrement lorsque l'on observe les résultats du découplage à un point proche de l'interface de découplage, plus la surface interne de découplage se rapproche de la surface de la coque, plus les erreurs sont importantes. Suite à ces observations, la taille des segments définissant les fonctions de condensation est réduite afin d'évaluer l'impact du critère de définition de la taille des segments en fonction de la longueur d'onde. Il est effectivement observé que, jusqu'à un certain point, réduire la taille des segments a un effet bénéfique sur les résultats du découplage, et un critère en $\lambda/6$ est ainsi retenu, au lieu du critère en $\lambda/2$ précédemment

utilisé.

Si les résultats obtenus avec le découplage n'étaient pas parfaits, il est important de garder à l'esprit qu'ils ne constituaient pas le résultat final de l'étude. En effet, afin de modéliser correctement le comportement vibroacoustique de la coque partiellement revêtue, le système obtenu après découplage doit être à nouveau couplé à un modèle FEM de l'eau occupant l'espace du revêtement manquant. La formulation de ce processus, appelé "recouplage", est développée et le résultat principal afin de décrire la pression rayonnée par la coque partiellement revêtue est le suivant :

$$\begin{aligned} p_{1+2'}(M_1) = p_{1+2}(M_1) + \left(\boldsymbol{I} + \mathbf{Z_2}\left(\mathbf{Z_2} - \mathbf{Z_{1+2}}\right)^{-1}\mathbf{Z_{1+2}}\mathbf{Z_2}^{-1}\right)\mathbf{P}_{\mathbf{1+2}}^{\mathbf{M_1}}\mathbf{Z_2}^{-1}\mathbf{P_{1+2}} \\ - \tilde{\mathbf{P}}_{\mathbf{1}}^{\mathbf{M_1}}\left(\mathbf{Z_1} + \mathbf{Z_{2'}}\right)^{-1}\tilde{\mathbf{P}}_{\mathbf{1}} \end{aligned} \tag{E.3}$$

Le recouplage est ainsi effectué en considérant une taille des segments définie par le critère en $\lambda/6$, et les résultats obtenus sont très bons. Il est ainsi observé que le processus de recouplage semble avoir tendance à limiter les erreurs commises lorsque les calculs de découplage sont effectués, notamment en basses fréquences où le système recouplé fait apparaître moins de résonances et anti-résonances que le système précédemment découplé. Le comportement vibroacoustique de la coque partiellement revêtue est ensuite comparé à celui de la coque intégralement revêtue. Il apparaît que le revêtement partiel est correctement pris en compte dans la mesure où les cartographies tracées montrent un champ de pression rayonné asymétrique, alors qu'il est symétrique dans le cas de la coque intégralement revêtue. On peut également voir qu'en basses fréquences, les configurations de revêtement partiel ou intégral expriment des résultats très similaires, ce qui veut dire que l'impact du revêtement partiel est moindre à ces fréquences. Ces résultats très prometteurs permettent donc de conduire une étude paramétrique sur la taille du revêtement enlevé, ainsi que l'influence de la position de l'excitation mécanique sur la surface de la coque. Il en résulte que plus la zone de revêtement manquante est importante, plus le comportement vibroacoustique du système est différent de celui de la coque intégralement revêtue. De plus, si la force mécanique est localisée proche de la zone non revêtue, l'impact du revêtement partiel sera plus grand. Ces études constituent un premier exemple des possibilités d'application de la méthode rCTF.

E.6 Conclusion et perspectives

Dans cette thèse, une méthode de modélisation vibroacoustique soustractive, la méthode rCTF, a été développée. Elle permet de découpler un sous-système d'un système global le long d'interfaces linéiques ou surfaciques. La formulation théorique de la méthode a été présentée pour un cas acoustique, mais elle peut s'appliquer à des systèmes acoustiques, mécaniques ou vibroacoustiques.

Dans un premier temps, le principe de modélisation soustractive a été appliqué à un cas test mécanique 1D, ce qui a permis d'envisager deux différentes formes de découplage. Un découplage local, qui ne fait apparaître qu'une interface de découplage, particulièrement sensible aux fréquences d'anti-résonance du sous-système soustrait, et un découplage global, faisant apparaître deux interfaces de découplage, et semblant plus robuste face aux erreurs de modèle. Dans un second temps, suite à son développement théorique pour des systèmes (vibro)acoustiques 3D, la méthode rCTF a été mise en application sur un cas test acoustique. En calculant dans un premier temps les fonctions de transfert condensées des différents systèmes avec des modèles analytiques, la méthode a pu être validée d'un point de vue numérique, tant pour la forme locale que pour la forme globale du problème.

Par la suite, les formulations pour calculer les fonctions de transfert condensées à partir de modèles numériques ont été présentées. Lorsque le système est borné, une formulation FEM est utilisée, tandis que lorsque le système est non borné, une formulation de Green est utilisée. L'introduction des erreurs de modèles par le calcul numérique des fonctions de transfert condensées a permis de confirmer les observations effectuées sur le cas test mécanique 1D quant à la sensibilité de la forme locale autour des anti-résonances du sous-système soustrait. La forme globale a, quant a elle, donné des résultats satisfaisants dans le cas où la discrétisation de l'interface de découplage du système global est très fine. Cependant, ce gain en précision étant contrebalancé par une augmentation drastique du temps de calcul, ce qui la rend difficilement applicable dans un contexte industriel.

Ainsi, la méthode rCTF locale a été appliquée afin de prédire le rayonnement acoustique d'une coque cylindrique partiellement revêtue. Les calculs ont été menés sur des modèles 2D mais peuvent être étendus à des modèles 3D. Deux types d'interfaces ont été considérés, la première uniquement acoustique, et la deuxième vibroacoustique, et il est apparu que la formulation contenant l'interface acoustique a montré de meilleurs résultats. Les résultats du découplage se sont montrés intéressants, notamment après avoir réduit la taille des segments définissant les fonctions de condensation, mais certaines erreurs ont subsisté, notamment dans le domaine physique proche de la zone de revêtement manquant. Il a par la suite été observé que recoupler le système obtenue avec un modèle de l'eau occupant la zone manquante de revêtement, à partir de la méthode CTF directe, permet de limiter les erreurs causées par le découplage. Les très bons résultats obtenus ont permis d'étudier le comportement vibroacoustique d'une coque cylindrique partiellement revêtue, et d'observer l'impact de la taille de la zone de revêtement manquante et de la position de l'excitation mécanique sur le rayonnement du système, par rapport à une coque intégralement revêtue.

Les résultats obtenus dans cette thèse permettent d'envisager de nombreuses perspectives. Premièrement, il a été observé que des erreurs subsistaient lorsque la méthode rCTF était

appliquée au cas de la coque cylindrique partiellement revêtue. Afin de limiter ces erreurs, une première possibilité à court terme serait d'envisager l'application de la forme globale de la méthode rCTF, car elle permet d'obtenir des meilleurs résultats que la forme locale dans le cas où les modèles numériques utilisés sont suffisamment précis. Ensuite, une deuxième possibilité serait d'utiliser des fonctions exponentielles complexes comme fonctions de condensation, dans la mesure où il a été observé dans certains travaux qu'elles permettent d'améliorer la convergence de la méthode CTF par rapport aux fonctions portes.

A moyen terme, il sera également nécessaire d'appliquer la méthode rCTF sur des modèles 3D afin d'étudier les coques cylindriques partiellement revêtues. Ceci permettrait en outre d'intégrer les travaux effectués durant cette thèse à un logiciel industriel, et donc d'appliquer cette méthode dans une phase préliminaire de conception de systèmes industriels. La prise en compte de revêtements solides 3D sera également à considérer dans un futur à plus long terme, afin de coller au mieux au matériaux utilisés sur des systèmes industriels. En outre, des études pourront être menées sur des matériaux aux propriétés différentes, ce qui permettra à terme d'utiliser la méthode rCTF pour modéliser des coques cylindriques présentant différents types de revêtements sur leur surface, comme illustré sur la figure 2b. Enfin, il pourrait également être envisagé d'étudier des coques cylindriques partiellement revêtues couplées à des structures internes axisymétriques (en utilisant la méthode CAA) et non-axisymétriques (en utilisant la méthode CTF). Différentes sortes d'excitations pourront également être considérées (excitation acoustique afin d'étudier la diffraction du système, excitations aléatoire de type TBL), afin d'étendre le spectre d'application de la méthode.

Bibliography

[1] A.W. Leissa. *Vibration of Shells*. NASA SP. Scientific and Technical Information Office, National Aeronautics and Space Administration, 1973.

[2] A. E. H. Love. Xvi. the small free vibrations and deformation of a thin elastic shell. *Philos. T. R. Soc. A.*, (179):491–546, 1888.

[3] R. Ruotolo. A comparison of some thin shell theories used for the dynamic analysis of stiffened cylinders. *J. Sound Vib.*, 243(5):847–860, 2001.

[4] W. Flügge. *Statik und dynamik der schalen*. Springer, 1962.

[5] C.R. Fuller. The effects of wall discontinuities on the propagation of flexural waves in cylindrical shells. *J. Sound Vib.*, 75(2):207–228, 1981.

[6] Denis G. Karczub. Expressions for direct evaluation of wave number in cylindrical shell vibration studies using the Flügge equations of motion. *J. Acoust. Soc. Am.*, 119(6):3553–3557, 2006.

[7] E. A. Skelton and J. H. James. *Theoretical acoustics of underwater structures*. Imperial College Press ; Distributed by World Scientific Pub, London : River Edge, NJ, 1997.

[8] M. C. Junger and D. Feit. *Sound, structures, and their interaction*, volume 225. MIT press Cambridge, MA, 1986.

[9] V. Meyer, L. Maxit, Y. Renou, and C. Audoly. Experimental investigation of the influence of internal frames on the vibroacoustic behavior of a stiffened cylindrical shell using wavenumber analysis. *Mech. Syst. Signal Pr.*, 93:104–117, 2017.

[10] A. Harari and B. E. Sandman. Vibratory response of laminated cylindrical shells embedded in an acoustic fluid. *J. Acoust. Soc. Am.*, 60(1):117–128, 1976.

[11] J. E. Manning and G. Maidanik. Radiation properties of cylindrical shells. *J. Acoust. Soc. Am.*, 36(9):1691–1698, 1964.

[12] C. Wang and J.C.S Lai. The sound radiation efficiency of finite length acoustically thick circular cylindrical shells under mechanical excitation i: theoretical analysis. *J. Sound Vib.*, 232(2):431–447, 2000.

[13] M. C. Junger and J. M. Garrelick. Multiple modal resonances of thin cylindrical shells vibrating in an acoustic medium. *J. Acoust. Soc. Am.*, 75(5):1380–1382, 1984.

[14] B. Hamonic. *Contribution à l'étude du rayonnement de transducteurs utilisant les vibrations de coques minces*. PhD thesis, Université des Sciences et Techniques de Lille, 1987.

[15] L. Maxit and J.-M. Ginoux. Prediction of the vibro-acoustic behavior of a submerged shell non periodically stiffened by internal frames. *J. Acoust. Soc. Am.*, 128(1):137–151, 2010.

[16] B. E. Sandman. Fluid-loading influence coefficients for a finite cylindrical shell. *J. Acoust. Soc. Am.*, 60(6):1256–1264, 1976.

[17] R. R. Stepanishen. Modal coupling in the vibration of fluid-loaded cylindrical shells. *J. Acoust. Soc. Am.*, 71(4):813–823, 1982.

[18] B. Laulagnet and J.L. Guyader. Modal analysis of a shell's acoustic radiation in light and heavy fluids. *J. Sound Vib.*, 131(3):397–415, 1989.

[19] D. M. Photiadis. The propagation of axisymmetric waves on a fluid-loaded cylindrical shell. *J. Acoust. Soc. Am.*, 88(1):239–250, 1990.

[20] B. K. Sinha, T. J. Plona, S. Kostek, and S.-K. Chang. Axisymmetric wave propagation in fluid-loaded cylindrical shells. I: theory. *J. Acoust. Soc. Am.*, 92(2):1132–1143, 1992.

[21] B. K. Sinha, T. J. Plona, S. Kostek, and S.-K. Chang. Axisymmetric wave propagation in fluid-loaded cylindrical shells: theory versus experiment. *J. Acoust. Soc. Am.*, 91(4):2470–2470, 1992.

[22] G. Galletly. On the in-vacuo vibrations of simply supported, ring-stiffened cylindrical shells. *Proceedings of the Second U.S. National Congress of Applied Mechanics*, page 225, 1954.

[23] J. L. Sewall and E. Naumann. An experimental and analytical vibration study of thin cylindrical shells with and without longitudinal stiffeners. In *NASA technical note*, 1968.

[24] D. J. Mead and N. S. Bardell. Free vibration of a thin cylindrical shell with discrete axial stiffeners. *J. Sound Vib.*, 111(2):229–250, 1986.

[25] T. Wah and W. C. L. Hu. Vibration analysis of stiffened cylinders including inter-ring motion. *J. Acoust. Soc. Am.*, 43(5):1005–1016, 1968.

[26] A. M. J. Al-Najafi and G. B. Warburton. Free vibration of ring-stiffened cylindrical shells. *J. Sound Vib.*, 13(1):9–25, 1970.

[27] Courtney B. Burroughs. Acoustic radiation from fluid-loaded infinite circular cylinders with doubly periodic ring supports. *J. Acoust. Soc. Am.*, 75(3):715–722, 1984.

[28] C. B. Burroughs and J. E. Hallander. Acoustic radiation from fluid-loaded, ribbed cylindrical shells excited by different types of concentrated mechanical drives. *J. Acoust. Soc. Am.*, 91(5):2721–2739, 1992.

[29] B. Laulagnet and J.L. Guyader. Sound radiation by finite cylindrical ring stiffened shells. *J. Sound Vib.*, 138(2):173–191, 1990.

[30] J. Yan, T.Y. Li, T.G. Liu, and J.X. Liu. Characteristics of the vibrational power flow propagation in a submerged periodic ring-stiffened cylindrical shell. *Appl. Acoust.*, 67(6):550–569, 2006.

[31] J. Yan, T.Y. Li, J.X. Liu, and X. Zhu. Space harmonic analysis of sound radiation from a submerged periodic ring-stiffened cylindrical shell. *Appl. Acoust.*, 67(8):743–755, 2006.

[32] M. Caresta and N. J. Kessissoglou. Structural and acoustic responses of a fluid-loaded cylindrical hull with structural discontinuities. *Appl. Acoust.*, 70(7):954–963, 2009.

[33] G. Maidanik and A.J. Tucker. Acoustic properties of coated panels immersed in fluid media. *J. Sound Vib.*, 34(4):519–550, 1974.

[34] P.J. Gangemi. *Attenuation of the structural and acoustic responses of a submerged hull*. PhD thesis, Univeristy of New South Wales, 2015.

[35] D.G. Crighton. The combined effects of fluid loading and compliant coating on the acoustic and structural fields of an infinite plane elastic surface. *J. Sound Vib.*, 92(2):237–252, 1984.

[36] O. Foin, A. Berry, and J. Szabo. Acoustic radiation from an elastic baffled rectangular plate covered by a decoupling coating and immersed in a heavy acoustic fluid. *J. Acoust. Soc. Am.*, 107(5):2501–2510, 2000.

[37] B. Laulagnet and J. L. Guyader. Sound radiation from a finite cylindrical shell covered with a compliant layer. *J. Vib. Acoust.*, 113(2):267–272, 1991.

[38] J. M. Cuschieri and D. Feit. Influence of circumferential partial coating on the acoustic radiation from a fluid-loaded shell. *J. Acoust. Soc. Am.*, 107(6):3196–3207, 2000.

[39] G. Maidanik, R. Biancardi, and T. Eisler. Use of decoupling to reduce the radiated noise generated by panels. *J. Sound Vib.*, 81(2):165–185, 1982.

[40] Richard F. Keltie. Signal response of elastically coated plates. *J. Acoust. Soc. Am.*, 103(4):1855–1863, 1998.

[41] A. Berry, O. Foin, and J. P. Szabo. Three-dimensional elasticity model for a decoupling coating on a rectangular plate immersed in a heavy fluid. *J. Acoust. Soc. Am.*, 109(6):2704–2714, 2001.

[42] A. J. Hull and J. R. Welch. Elastic response of an acoustic coating on a rib-stiffened plate. *J. Sound Vib.*, 329(20):4192–4211, 2010.

[43] B.R. Mace. Periodically stiffened fluid-loaded plates, i: Response to convected harmonic pressure and free wave propagation. *J. Sound Vib.*, 73(4):473–486, 1980.

[44] B.R. Mace. Periodically stiffened fluid-loaded plates, ii: Response to line and point forces. *J. Sound Vib.*, 73(4):487–504, 1980.

[45] B. A. Cray. Acoustic radiation from periodic and sectionally aperiodic rib-stiffened plates. *J. Acoust. Soc. Am.*, 95(1):256–264, 1994.

[46] M. C. Remillieux and R. A. Burdisso. Vibro-acoustic response of an infinite, rib-stiffened, thick-plate assembly using finite-element analysis. *J. Acoust. Soc. Am.*, 132(1):EL36–EL42, 2012.

[47] Š. Markuš. Damping properties of layered cylindrical shells, vibrating in axially symmetric modes. *J. Sound Vib.*, 48(4):511–524, 1976.

[48] G. C. Gaunaurd. Sonar cross section of a coated hollow cylinder in water. *J. Acoust. Soc. Am.*, 61(2):360–368, 1977.

[49] H. Schmidt and F. B. Jensen. A full wave solution for propagation in multilayered viscoelastic media with application to Gaussian beam reflection at fluid–solid interfaces. *J. Acoust. Soc. Am.*, 77(3):813–825, 1985.

[50] D. C. Ricks and H. Schmidt. A numerically stable global matrix method for cylindrically layered shells excited by ring forces. *J. Acoust. Soc. Am.*, 95(6):3339–3349, 1994.

[51] B. Laulagnet and J. L. Guyader. Sound radiation from finite cylindrical coated shells, by means of asymptotic expansion of three-dimensional equations for coating. *J. Acoust. Soc. Am.*, 96(1):277–286, 1994.

[52] J. M. Cuschieri. The modeling of the radiation and response Green's function of a fluid-loaded cylindrical shell with an external compliant layer. *J. Acoust. Soc. Am.*, 119(4):2150–2169, 2006.

[53] W.Q. Chen, Z.G. Bian, and H.J. Ding. Three-dimensional vibration analysis of fluid-filled orthotropic FGM cylindrical shells. *Int. J. Mech. Sci.*, 46(1):159–171, 2004.

[54] C. Dutrion. *Etude de la faisabilité d'un revêtement pour la furtivité acoustique*. PhD thesis, Institut Supérieur de l'Aéronautique et de l'Espace, 2014.

[55] M. Dana, J. Bernard, and L. Maxit. A spectral global matrix method for modelling the response of a fluid-loaded multilayered cylindrical shell excited by an acoustic plane wave. *J. Acoust. Soc. Am.*, 148(5):2997–3013, 2020.

[56] P. Méresse. *Matériaux absorbants à structure périodique et inclusions résonantes pour l'acoustique sous-marine*. PhD thesis, Institut d'Electronique, de Microélectronique et de nanotechnologie, 2015.

[57] L. Roux. *Acoustic metamaterials for underwater acoustic applications: homogenisation theory, design optimisation and experimental characterisation*. PhD thesis, Institut d'Electronique, de Microélectronique et de nanotechnologie, 2021.

[58] E. Meyer. *Sound absorption and sound absorbers in water*. Technical report, U.S. Bureau of Ships, 1947.

[59] G. Gaunaurd. One-dimensional model for acoustic absorption in a viscoelastic medium containing short cylindrical cavities. *J. Acoust. Soc. Am.*, 62(2):298–307, 1977.

[60] R. Lane. Absorption mechanisms for waterborne sound in Alberich anechoic layers. *Ultrasonics*, 19(1):28–30, 1981.

[61] G. C. Gaunaurd and H. Überall. Theory of resonant scattering from spherical cavities in elastic and viscoelastic media. *J. Acoust. Soc. Am.*, 63(6):1699–1712, 1978.

[62] G. Gaunaurd, K. P. Scharnhorst, and H. Überall. Giant monopole resonances in the scattering of waves from gas-filled spherical cavities and bubbles. *J. Acoust. Soc. Am.*, 65(3):573–594, 1979.

[63] G. C. Gaunaurd and W. Wertman. Comparison of effective medium theories for inhomogeneous continua. *J. Acoust. Soc. Am.*, 85(2):541–554, 1989.

[64] C. Audoly. Acoustic analysis of panels made with viscoelastic materials containing resonant cavities. *Acta Acustica*, 2:393–402, 1994.

[65] A.-C. Hladky-Hennion and J.-N. Decarpigny. Analysis of the scattering of a plane acoustic wave by a doubly periodic structure using the finite element method: Application to Alberich anechoic coatings. *J. Acoust. Soc. Am.*, 90(6):3356–3367, 1991.

[66] P. Langlet, A.-C. Hladky-Hennion, and J.-N. Decarpigny. Analysis of the propagation of plane acoustic waves in passive periodic materials using the finite element method. *J. Acoust. Soc. Am.*, 98(5):2792–2800, 1995.

[67] S. Beretti. Réponse acoustique d'élastomères micro-inclusionnaire soumis à la pression d'immersion. In Société Française d'Acoustique SFA, editor, *10ème Congrès Français d'Acoustique*, Lyon, France, 2010.

[68] A. M. Baird, F. H. Kerr, and D. J. Townend. Wave propagation in a viscoelastic medium containing fluid-filled microspheres. *J. Acoust. Soc. Am.*, 105(3):1527–1538, 1999.

[69] G Lepert, C Aristégui, O Poncelet, T Brunet, C Audoly, and P Parneix. Determination of the effective mechanical properties of inclusionary materials using bulk elastic waves. *J. Phys. Conf. Ser.*, 498:012007, 2014.

[70] G. Ma and P. Sheng. Acoustic metamaterials: From local resonances to broad horizons. *Sci. Adv.*, 2(2):e1501595, 2016.

[71] Z. Liu. Locally resonant sonic materials. *Science*, 289(5485):1734–1736, 2000.

[72] J. Wen, H. Zhao, L. Lv, B. Yuan, G. Wang, and X. Wen. Effects of locally resonant modes on underwater sound absorption in viscoelastic materials. *J. Acoust. Soc. Am.*, 130(3):1201–1208, 2011.

[73] M. S. Kushwaha, P. Halevi, L. Dobrzynski, and B. Djafari-Rouhani. Acoustic band structure of periodic elastic composites. *Phys. Rev. Lett.*, 71(13):2022–2025, 1993.

[74] V. Leroy, A. Bretagne, M. Fink, H. Willaime, P. Tabeling, and A. Tourin. Design and characterization of bubble phononic crystals. *Appl. Phys. Lett.*, 95(17):171904, 2009.

[75] V. Leroy, A. Strybulevych, M. Lanoy, F. Lemoult, A. Tourin, and J. H. Page. Superabsorption of acoustic waves with bubble metascreens. *Phys. Rev. B*, 91(2):020301, 2015.

[76] H. Meng, J. Wen, H. Zhao, L. Lv, and X. Wen. Analysis of absorption performances of anechoic layers with steel plate backing. *J. Acoust. Soc. Am.*, 132(1):69–75, 2012.

[77] F. Zhou, J. Fan, B. Wang, and Z. Peng. Absorption performance of an anechoic layer with a steel plate backing at oblique incidence. *Acoust. Aust.*, 46(3):317–327, 2018.

[78] S. M. Ivansson. Sound absorption by viscoelastic coatings with periodically distributed cavities. *J. Acoust. Soc. Am.*, 119(6):3558–3567, 2006.

[79] S. M Ivansson. Numerical design of Alberich anechoic coatings with superellipsoidal cavities of mixed sizes. *J. Acoust. Soc. Am.*, 124(4):12, 2008.

[80] S. M. Ivansson. Anechoic coatings obtained from two- and three-dimensional monopole resonance diffraction gratings. *J. Acoust. Soc. Am.*, 131(4):2622–2637, 2012.

[81] G. S. Sharma, A. Skvortsov, I. MacGillivray, and N. J. Kessissoglou. Acoustic performance of gratings of cylindrical voids in a soft elastic medium with a steel backing. *J. Acoust. Soc. Am.*, 141(6):4694–4704, 2017.

[82] G. S. Sharma, A. Skvortsov, I. MacGillivray, and N. J. Kessissoglou. Sound absorption by rubber coatings with periodic voids and hard inclusions. *Appl. Acoust.*, 143:200–210, 2019.

[83] Y. Ke, L. Zhang, X. Zhao, and M. Tao. An equivalent method for predicting acoustic scattering of coated shell using identified viscoelastic parameters of anechoic coating. *Appl. Acoust.*, 179:108071, 2021.

[84] A. A. Ferri, J. H. Ginsberg, and P. H. Rogers. Scattering of plane waves from submerged objects with partially coated surfaces. *J. Acoust. Soc. Am.*, 92(3):1721–1728, 1992.

[85] B. Laulagnet and J.L. Guyader. Sound radiation from finite cylindrical shells, partially covered with longitudinal strips of compliant layer. *J. Sound Vib.*, 186(5):723–742, 1995.

[86] S.-X. Liu, M.-S. Zou, L.-W. Jiang, and X.-Y. Zhao. Vibratory response and acoustic radiation of a finite cylindrical shell partially covered with circumferential compliant layers. *Appl. Acoust.*, 141:188–197, 2018.

[87] LMS International. *Numerical acoustics - Theoretical manual*. LMS, 2005.

[88] S. Rubin. Improved component-mode representation for structural dynamic analysis. *AIAA Journal*, 13(8):995–1006, 1975.

[89] J.-F. Sigrist. *Fluid-structure interaction: an introduction to Finite Element coupling*. John Wiley & Sons, Ltd, 2015.

[90] W. C. Hurty. Dynamic analysis of structural systems using component modes. *AIAA Journal*, 3(4):678–685, 1965.

[91] M. Gibanica, T. J.S. Abrahamsson, and D. J. Rixen. A reduced interface component mode synthesis method using coarse meshes. *Procedia Engineering*, 199:348–353, 2017.

[92] G. M. L. Gladwell. Branch mode analysis of vibrating systems. *J. Sound Vib.*, 1(1):41–59, 1964.

[93] R. R. Craig and M. C. C. Bampton. Coupling of substructures for dynamic analyses. *AIAA Journal*, 6(7):1313–1319, 1968.

[94] D. J. Rixen. A dual Craig–Bampton method for dynamic substructuring. *J. Comput. Appl. Math.*, 168(1-2):383–391, 2004.

[95] R. MacNeal. A hybrid method of component mode synthesis. *Comput. Struct.*, 1(4):581–601, 1971.

[96] E. Premat. *Prise en compte d'effets météorologiques dans une méthode d'éléments finis de frontière*. PhD thesis, INSA Lyon, 2000.

[97] S. Amini, P. J. Harris, and David T. Wilton. *Coupled boundary and finite element methods for the solution of the dynamic fluid-structure interaction problem*, volume 77 of *Lecture Notes in Engineering*. Springer Berlin Heidelberg, Berlin, Heidelberg, 1992.

[98] P.J.T. Filippi. Layer potentials and acoustic diffraction. *J. Sound Vib.*, 54(4):473–500, 1977.

[99] C.A. Brebbia and R. Butterfield. Formal equivalence of direct and indirect boundary element methods. *Appl. Math. Model.*, 2(2):132–134, 1978.

[100] J.-P. Berenger. A perfectly matched layer for the absorption of electromagnetic waves. *J. Comput. Phys.*, 114(2):185–200, 1994.

[101] *COMSOL Multiphysics ® v. 5.6*. COMSOL AB, Stockholm, Sweden, 2020.

[102] P. Bettess. Infinite elements. *Int. J. Numer. Methods Eng.*, 11(1):53–64, 1977.

[103] R. J. Astley, G. J. Macaulay, J-P. Coyette, and L. Cremers. Three-dimensional wave-envelope elements of variable order for acoustic radiation and scattering. part i. formulation in the frequency domain. *J. Acoust. Soc. Am.*, 103(1):49–63, 1998.

[104] R. J. Astley, G. J. Macaulay, J-P. Coyette, and L. Cremers. Three-dimensional wave-envelope elements of variable order for acoustic radiation and scattering. part ii. formulation in the time domain. *J. Acoust. Soc. Am.*, 103(1):64–72, 1998.

[105] Q. Zhou and P.F. Joseph. A numerical method for the calculation of dynamic response and acoustic radiation from an underwater structure. *J. Sound Vib.*, 283(3-5):853–873, 2005.

[106] L. H. Chen and D. G. Schweikert. Sound radiation from an arbitrary body. *J. Acoust. Soc. Am.*, 35(10):1626–1632, 1963.

[107] M. Caresta and N. J. Kessissoglou. Acoustic signature of a submarine hull under harmonic excitation. *Appl. Acoust.*, 71(1):17–31, 2010.

[108] M. Caresta and N. J. Kessissoglou. Free vibrational characteristics of isotropic coupled cylindrical–conical shells. *J. Sound Vib.*, 329(6):733–751, 2010.

[109] S. Merz, R. Kinns, and N. J. Kessissoglou. Structural and acoustic responses of a submarine hull due to propeller forces. *J. Sound Vib.*, 325(1-2):266–286, 2009.

[110] S. Merz, N. J. Kessissoglou, R. Kinns, and S. Marburg. Minimisation of the sound power radiated by a submarine through optimisation of its resonance changer. *J. Sound Vib.*, 329(8):980–993, 2010.

[111] H. Peters, N. J. Kessissoglou, and S. Marburg. Modal decomposition of exterior acoustic-structure interaction problems with model order reduction. *J. Acoust. Soc. Am.*, 135(5):2706–2717, 2014.

[112] M. Zampolli, A. Tesei, F. B. Jensen, N. Malm, and J. B. Blottman. A computationally efficient finite element model with perfectly matched layers applied to scattering from axially symmetric objects. *J. Acoust. Soc. Am.*, 122(3):1472–1485, 2007.

[113] A. L. Hale and L. Meirovitch. A general procedure for improving substructures representation in dynamic synthesis. *J. Sound Vib.*, 84(2):269–287, 1982.

[114] J.-L. Guyader. Statistical energy analysis : une description floue de la compléxité structurale. In *13ème Congrès Français d'Acoustique*, pages 329–335, 2016.

[115] C. B. Burroughs, R. W. Fischer, and F. R. Kern. An introduction to statistical energy analysis. *J. Acoust. Soc. Am.*, 101(4):1779–1789, 1997.

[116] R. H. Lyon and G. Maidanik. Power flow between linearly coupled oscillators. *J. Acoust. Soc. Am.*, 34(5):623–639, 1962.

[117] P. W. Smith. Response and radiation of structural modes excited by sound. *J. Acoust. Soc. Am.*, 34(5):640–647, 1962.

[118] L. Maxit. *Extension et reformulation du modèle SEA par la prise en compte de la répartition des énergies modales*. PhD thesis, INSA Lyon, 2000.

[119] A. J. Keane. *Statistical Energy Analysis of engineering structures*. PhD thesis, Department of Mechanical Engineering, Brunel University, 1988.

[120] L. Maxit and J.-L. Guyader. Estimation of sea coupling loss factors using a dual formulation and fem modal information, part i: theory. *J. Sound Vib.*, 239(5):907–930, 2001.

[121] H. Li, N. Totaro, L. Maxit, and A. Le Bot. Ergodic billiard and statistical energy analysis. *Wave Motion*, 87:166–178, 2019.

[122] G. Maidanik. Some elements in statistical energy analysis. *J. Sound Vib.*, 52(2):171–191, 1977.

[123] L. Maxit and J.-L. Guyader. Extension of SEA model to subsystems with non-uniform modal energy distribution. *J. Sound Vib.*, 265(2):337–358, 2003.

[124] V. Cotoni, R.S. Langley, and P.J. Shorter. A statistical energy analysis subsystem formulation using finite element and periodic structure theory. *J. Sound Vib.*, 318(4-5):1077–1108, 2008.

[125] R. S. Langley and P. Bremner. A hybrid method for the vibration analysis of complex structural-acoustic systems. *J. Acoust. Soc. Am.*, 105(3):1657–1671, 1999.

[126] R. S. Langley and J. A. Cordioli. Hybrid deterministic-statistical analysis of vibro-acoustic systems with domain couplings on statistical components. *J. Sound Vib.*, 321(3):893–912, 2009.

[127] L. Maxit and J.-L. Guyader. Estimation of sea coupling loss factors using a dual formulation and fem modal information, part ii: numerical applications. *J. Sound Vib.*, 239(5):931–948, 2001.

[128] V. Cotoni, P. Shorter, and R. Langley. Numerical and experimental validation of a hybrid finite element-statistical energy analysis method. *J. Acoust. Soc. Am.*, 122(1):259–270, 2007.

[129] G. Tanner. Dynamical energy analysis—determining wave energy distributions in vibro-acoustical structures in the high-frequency regime. *J. Sound Vib.*, 320(4):1023–1038, 2009.

[130] D. J. Chappell and G. Tanner. Solving the stationary liouville equation via a boundary element method. *J. Comput. Phys.*, 234:487–498, 2013.

[131] R. Bernhard and J. E. Huff. Structural-acoustic design at high frequency using the energy finite element method. *J. Vib. Acoust.*, 121:295–301, 1999.

[132] N. Vlahopoulos, L. O. Garza-Rios, and C. Mollo. Numerical implementation, validation, and marine applications of an energy finite element formulation. *J. Ship Res.*, 43:143–156, 1999.

[133] W. Zhang, A. Wang, and N. Vlahopoulos. An alternative energy finite element formulation based on incoherent orthogonal waves and its validation for marine structures. *Finite Elem. Anal. Des.*, 38(12):1095–1113, 2002.

[134] V. Meyer, C. Audoly, D. Liu, N. Kessissoglou, and L. Maxit. Bridging the frequency gap for vibro-acoustic prediction of a submerged shell. In *Proceedings of WESPAC 2018*, page 6, New Delhi, India, 2018.

[135] L. Maxit and C. Audoly. Hydrodynamic noise prediction inside a sonar dome : injected power estimation from the wavevector - frequency spectrum of turbulent wall pressure. In *Proceedings of NOVEM 2005*, page 12, St Raphael, France, 2005.

[136] C. Jong and B. Petersson. Resonant underwater radiation revisited. In *17th International Congress on Acoustics, ICA 2001*, Rome, Italy, 2001.

[137] Y. Qiao, H. B. Chen, and J. L. Luo. Estimation of shell radiation efficiency using a fem-smeda algorithm. *J. Vibroengineering*, 15(3):1130–1146, 2013.

[138] W. Zhang, N. Vlahopoulos, and W. Kuangcheng. An energy finite element formulation for high-frequency vibration analysis of externally fluid-loaded cylindrical shells with periodic circumferential stiffeners subjected to axi-symmetric excitation. *J. Sound Vib.*, 282(3-5):679–700, 2005.

[139] C. Audoly. Introducing decoupling coatings in sea models – physical interpretation and results on simple models. In *Proceedings of Noise-Con 97*, pages 21–26, The Pennsylvania State University, 1997.

[140] C. Audoly. Prediction of the efficiency of a decoupling coating partially covering a cylindrical hull using the sea method. In *Proceedings of UDT 97*, pages 293–297, Hamburg, Germany, 1997.

[141] L. Maxit. Analysis of the modal energy distribution of an excited vibrating panel coupled with a heavy fluid cavity by a dual modal formulation. *J. Sound Vib.*, 332(25):6703–6724, 2013.

[142] F.A. Firestone. The mobility method of computing the vibration of linear mechanical and acoustical systems: mechanical-electrical analogies. *J. Appl. Phys.*, 9(6):373–387, 1938.

[143] P. Gardonio and M.J. Brennan. On the origins and developpement of mobility and impedance methods in structural dynamics. *J. Sound Vib.*, 249:557–573, 2002.

[144] S. Rubin. Transmission matrices for vibration and their relation to admittance and impedance. *J. Eng. Ind.*, 86(1):9–21, 1964.

[145] G.J. O'Hara. Mechanical impedance and mobility concepts. *J. Acoust. Soc. Am.*, 41(5):1180–1184, 1967.

[146] B. Petersson and J. Plunt. On effective mobilities in the prediction of structure-borne sound transmission between a source structure and a receiving structure, part II: Procedures for the estimation of mobilities. *J. Sound Vib.*, 82(4):531–540, 1982.

[147] B. Petersson and J. Plunt. On effective mobilities in the prediction of structure-borne sound transmission between a source structure and a receiving structure, part I: Theoretical background and basic experimental studies. *J. Sound Vib.*, 82(4):517–529, 1982.

[148] B. Petersson. An approximation for the point mobility at the intersection of two perpendicular plates. *J. Sound Vib.*, 91(2):219–238, 1983.

[149] B. Petersson. A thin-plate model for the moment mobility at the intersection of two perpendicular plates. *J. Sound Vib.*, 108(3):471–485, 1986.

[150] I.D. Wilken and W. Soedel. The receptance method applied to ring-stiffened cylindrical shells: Analysis of modal characteristics. *J. Sound Vib.*, 44(4):563–576, 1976.

[151] D.T. Huang and W. Soedel. Natural frequencies and modes of a circular plate welded to a circular cylindrical shell at aribtrary axial positions. *J. Sound Vib.*, 162(3):403–427, 1993.

[152] S.M. Kim and M.J. Brennan. A compact matrix formulation using the impedance and mobility approach for the analysis of structural-acoustic systems. *J. Sound Vib.*, 223(1):97–113, 1999.

[153] L. Maxit. Circumferential admittance approach for vibro-acoustic prediction of a submerged cylindrical shell with rib aperiodicity and transversal bulkheads. *J. Acoust. Soc. Am.*, 123(5):3060–3060, 2008.

[154] L. Maxit. Scattering model of a cylindrical shell with internal axisymmetric frames by using the Circumferential Admittance Approach. *Appl. Acoust.*, 80:10–22, 2014.

[155] L. Maxit, O. Guasch, V. Meyer, and M. Karimi. Noise radiated from a periodically stiffened cylindrical shell excited by a turbulent boundary layer. *J. Sound Vib.*, 466:115016, 2020.

[156] L. Maxit, M. Karimi, and O. Guasch. Spatial coherence of pipe vibrations induced by an internal turbulent flow. *J. Sound Vib.*, 493:115841, 2021.

[157] S. Kassab, S. Serbout, F. Michel, and L. Maxit. Acoustic source detection inside a pipe using vibro-acoustic beamforming: assessment of the array gain from virtual experiments. In *Proceedings of the 23rd International Congress on Acoustics*, page 9, 2019.

[158] M. Ouisse, L. Maxit, C. Cacciolati, and J.-L. Guyader. Patch transfer function as a tool to couple linear acoustic problems. *J. Vib. Acoust.*, 127:pp. 458–466, 2005.

[159] A.J. Jerri. The Shannon sampling theorem - Its various extensions and applications: A tutorial review. In *Proceedings of the IEEE*, volume 65, pages 1565–1596, 1977.

[160] G. Veronesi, C. Albert, E. Nijman, J. Rejlek, and A. Bocquillet. Patch transfer function approach for analysis of coupled vibro-acoustic problems involving porous materials. In *SAE Technical Paper*, pages 2014–01–2092, 2014.

[161] J. Rejlek, G. Veronesi, C. Albert, E. Nijman, and A. Bocquillet. A combined computational-experimental approach for modelling of coupled vibro-acoustic problems. In *SAE 2013 Noise and Vibration Conference and Exhibition*, pages 2013–01–1997, 2013.

[162] J.-D. Chazot and J.-L. Guyader. Prediction of transmission loss of double panels with a patch-mobility method. *J. Acoust. Soc. Am.*, 121(1):267–278, 2007.

[163] J.-D. Chazot and J.-L. Guyader. Transmission loss of double panels filled with porogranular materials. *J. Acoust. Soc. Am.*, 126(6):3040–3048, 2009.

[164] L. Maxit, C. Yang, L. Cheng, and J.-L. Guyader. Modeling of micro-perforated panels in a complex vibro-acoustic environment using patch transfer function approach. *J. Acoust. Soc. Am.*, 131(3):2118–2130, 2012.

[165] X. Yu, L. Cheng, and J.-L. Guyader. Modeling vibroacoustic systems involving cascade open cavities and micro-perforated panels. *J. Acoust. Soc. Am.*, 136(2):659–670, 2014.

[166] X. Zhang and L. Cheng. Acoustic silencing in a flow duct with micro-perforated panel liners. *Appl. Acoust.*, 167:107382, 2020.

[167] M. Aucejo, N. Totaro, and J.-L. Guyader. Identification of source velocities on 3D structures in non-anechoic environments: Theoretical background and experimental validation of the inverse patch transfer functions method. *J. Sound Vib.*, 329(18):3691–3708, 2010.

[168] D. Vigoureux, N. Totaro, J. Lagneaux, and J.-L. Guyader. Inverse Patch Transfer Functions Method as a tool for source field identification. *J. Vib. Acoust.*, 137(2):021006, 2015.

[169] S. Forget, N. Totaro, J.L. Guyader, and M. Schaeffer. Source fields reconstruction with 3D mapping by means of the virtual acoustic volume concept. *J. Sound Vib.*, 381:48–64, 2016.

[170] M. Aucejo, L. Maxit, N. Totaro, and J.-L. Guyader. Convergence acceleration using the residual shape technique when solving structure–acoustic coupling with the Patch Transfer Functions method. *Comput. Struct.*, 88(11):728–736, 2010.

[171] L. Maxit, M. Aucejo, and J.-L. Guyader. Improving the Patch Transfer Function approach for fluid-structure modelling in heavy fluid. *J. Vib. Acoust.*, 134(5):051011, 2012.

[172] V. Meyer, L. Maxit, J.-L Guyader, T. Leissing, and C. Audoly. A condensed transfer function method as a tool for solving vibroacoustic problems. *Proceedings of the Institution*

of Mechanical Engineers, Part C: Journal of Mechanical Engineering Science, 230(6):928–938, 2016.

[173] V. Meyer, L. Maxit, J.-L. Guyader, and T. Leissing. Prediction of the vibroacoustic behavior of a submerged shell with non-axisymmetric internal substructures by a condensed transfer function method. *J. Sound Vib.*, 360:260–276, 2016.

[174] V. Meyer, L. Maxit, and C. Audoly. A substructuring approach for modeling the acoustic scattering from stiffened submerged shells coupled to non-axisymmetric internal structures. *J. Acoust. Soc. Am.*, 140(3):1609–1617, 2016.

[175] Z. Hu, L. Maxit, and L. Cheng. Piecewise convergence behavior of the condensed transfer function approach for mid-to-high frequency modelling of a panel-cavity system. *J. Sound Vib.*, 435:119–134, 2018.

[176] Z. Hu, L. Maxit, and L. Cheng. Mid-to-high frequency piecewise modelling of an acoustic system with varying coupling strength. *Mech. Syst. Signal Pr.*, 134:106312, 2019.

[177] Z. Hu, Laurent M., and L. Cheng. Acoustic design and analyses of a double Skin Façade system. *Appl. Acoust.*, 173:107727, 2021.

[178] D. T. Soedel and W. Soedel. Synthesizing reduced systems by complex receptances. *J. Sound Vib.*, 179(5):855 – 867, 1994.

[179] C. Gontier and M. Bensaibi. Time domain identification of a substructure fromin situanalysis of the whole structure. *Mech. Syst. Signal Pr.*, 9(4):379–396, 1995.

[180] W D'Ambrogio and A Fregolent. Decoupling of a substructure from modal data of the complete structure. In *Proceedings of ISMA2004: International Conference on Noise and Vibration Engineering*, page 15, Leuven, Belgium, 2004.

[181] W D'Ambrogio and A Fregolent. Promises and pitfalls of decoupling procedures. In *26th IMAC: Conference and Exposition on Structural Dynamics*, page 8, Orlando, United States, 2008.

[182] W. D'Ambrogio and A. Fregolent. The role of interface DoFs in decoupling of substructures based on the dual domain decomposition. *Mech. Syst. Signal Pr.*, 24(7):2035–2048, 2010.

[183] P. Sjövall and T. Abrahamsson. Substructure system identification from coupled system test data. *Mech. Syst. Signal Pr.*, 22(1):15–33, 2008.

[184] S.N. Voormeeren and D.J. Rixen. A family of substructure decoupling techniques based on a dual assembly approach. *Mech. Syst. Signal Pr.*, 27:379–396, 2012.

[185] O. Tuysuz and Y. Altintas. Frequency domain updating of thin-walled workpiece dynamics using reduced order substructuring method in machining. *J. Manuf. Sci. E-T. Asme*, 139(7):071013, 2017.

[186] S. Bi, M. Ouisse, E. Foltête, and A. Jund. Virtual decoupling of vibroacoustical systems. *J. Sound Vib.*, 401:169–189, 2017.

[187] D. T. Huang and Edward C. Ting. Vibration of plates with sub-structural deduction: a reverse receptance approach. *J. Sound Vib.*, 271(1-2):177–207, 2004.

[188] D. T. Huang. A reverse receptance approach for analysis of vibration of grooved plates. *Int. J. Mech. Sci.*, 53(12):1084–1102, 2011.

[189] D. T. Huang. The effects of in-plane loading on vibration and buckling of the grooved plates. *Int. J. Mech. Sci.*, 60(1):34–45, 2012.

[190] D. T. Huang. Effects of constraint, circular cutout and in-plane loading on vibration of rectangular plates. *Int. J. Mech. Sci.*, 68:114–124, 2013.

[191] D. S. Cho, N. Vladimir, and T. M. Choi. Numerical procedure for the vibration analysis of arbitrarily constrained stiffened panels with openings. *Int. J. Nav. Archit*, 6(4):763–774, 2014.

[192] D. S. Cho, B. H. Kim, J.-H. Kim, N. Vladimir, and T. M. Choi. Frequency response of rectangular plates with free-edge openings and carlings subjected to point excitation force and enforced displacement at boundaries. *Int. J. Nav. Archit*, 8(2):117–126, 2016.

[193] F. J. Fahy. Some applications of the reciprocity principle in experimental vibroacoustics. *Acoust. Phys.*, 49(2):217–229, 2003.

[194] J.-L. Guyader. *Vibration des milieux continus*. Hermes Sciences, 2002.

[195] SDTools. *Structural Dynamics Toolbox (for use with MATLAB)*. Paris, 1995-2020.

[196] F. Dumortier, L. Maxit, and V. Meyer. Vibroacoustic subtractive modeling using a reverse condensed transfer function approach. *J. Sound Vib.*, 499:115982, 2021.

[197] C. Marchetto, L. Maxit, O. Robin, and A. Berry. Vibroacoustic response of panels under diffuse acoustic field excitation from sensitivity functions and reciprocity principles. *J. Acoust. Soc. Am.*, 141(6):4508–4521, 2017.

[198] *Altair Hypermesh ®*. CAE Altair HyperWorks, Troy MI, United States, 2017.

[199] T. Valier-Brasier. *Rayonnement acoustique [Acoustic radiation]*. Université Pierre et Marie Curie, 2017.

[200] *LiveLink^{TM} for MATLAB ®*. COMSOL AB, Stockholm, Sweden, 2018.

[201] M. Berton. *Modélisation de la réponse vibro-acoustique d'une structure excitée par une couche limite turbulente en présence d'un gardient de pression statique*. PhD thesis, Ecole Centrale de Lyon, 2014.

FOLIO ADMINISTRATIF

THESE DE L'UNIVERSITE DE LYON OPEREE AU SEIN DE L'INSA LYON

NOM : DUMORTIER
(avec précision du nom de jeune fille, le cas échéant)

DATE de SOUTENANCE : 30/11/2021

Prénoms : Florent, Thomas

TITRE : Principle of vibroacoustic subtractive modelling and application to the prediction of the acoustic radiation of partially coated submerged cylindrical shells

NATURE : Doctorat

Numéro d'ordre : 2021LYSEI082

Ecole doctorale : Mécanique – Energétique – Génie Civil - Acoustique

Spécialité : Acoustique

RESUME : Modelling the vibroacoustic behavior of submerged cylindrical shells has been a challenging issue for the last decades in the naval industry. The application of viscoelastic coatings on submarine hulls allows reducing the noise radiated and scattered by the shell and is thus of paramount importance for their acoustic furtivity. These coatings can generally be decomposed into two categories. Decoupling coatings isolate the hull from the surrounding medium and reduce the radiated noise, serving as a protection against passive sonars, while anechoic coatings serve as a protection against active sonars by reducing the acoustic scattering from the hull. If fully coated cylindrical shells have been intensively studied in the literature, few works can be found on partially coated cylindrical shells. Modelling the vibroacoustic behavior of such structures may be useful for predicting the impact of missing coating tiles, or for studying cylindrical shells with several kinds of coatings. Compared to fully coated cylindrical shells, partial coating induces a coupling of the circumferential orders of the submerged shell, leading to prohibitive calculation costs for numerical methods and the impossibility of applying classical semi-analytical methods.
In this work, a subtractive modelling approach is developed to circumvent this issue. It is based on a reverse formulation of the Condensed Transfer Function method, a substructuring approach that has already proven its ability in dealing with complex vibroacoustic problems. Considering this approach, the partially coated cylindrical shell can be studied considering the model of a fully coated cylindrical shell, from which a model of the missing part of the coating is removed. The theoretical framework of the method is explored for 1-D and 3-D problems before being applied to several test cases to evaluate the method's accuracy and its sensitivity to model errors. Finally, the partially coated cylindrical shell is studied using this subtractive modelling approach.

MOTS-CLÉS : Vibroacoustic– Subtractive modelling – Substructuring approach – Acoustic coating – Partial coating – Subermerged cylindrical shell

Laboratoire (s) de recherche : Laboratoire Vibrations Acoustique

Directeur de thèse: Laurent Maxit

Président de jury : Morvan Ouisse

Composition du jury : Christian Audoly, Orial Guasch, Nicole Kessissoglou, Laurent Maxit, Valentin Meyer, Morvan Ouisse